III-Nitride nanostructures for UV emitters

Chalermchai Himwas

UNIVERSITÉ DE GRENOBLE

THÈSE

Pour obtenir le grade de

DOCTEUR DE L'UNIVERSITÉ DE GRENOBLE

Spécialité : **Physique / Nanophysique**

Arrêté ministériel : 7 août 2006

Présentée par

Chalermchai HIMWAS

Thèse dirigée par **Rudeesun SONGMUANG** et **Eva MONROY**

préparée au sein du **Laboratoire Nanophysique et Semi-Conducteurs (CNRS / Institut Néel et CEA / INAC / SP2M)**
dans **l'École Doctorale de Physique**

Nanostructures à base de semi-conducteurs nitrures pour l'émission ultraviolette

Thèse soutenue publiquement le **27 janvier 2015**
devant le jury composé de :

M Guillaume CASSABOIS
Rapporteur
M Fabrice SEMOND
Rapporteur
M Le Si DANG
Président
Mme Eva MONROY
Membre
M Stephen PURCELL
Membre
M Henning RIECHERT
Membre
M Martin STRASSBURG
Membre
Mme Rudeesun SONGMUANG
Membre

Université Joseph Fourier / Université Pierre Mendès France / Université Stendhal / Université de Savoie / Grenoble INP

Acknowledgement

This Thesis originated as a part to fulfill the requirements for the Doctoral degree of Physics, reporting three years research that I have performed in the group of “Nanophysics and Semiconductors (NPSC)”. During this period, I have enjoyed working on my topic with the guidance and assistance of various people both inside the laboratory and collaborators. It is a pleasure to take this opportunity to convey my gratitude to all the members who have contributed to my success.

Foremost, I would like to express my deep appreciation to my research advisors, Dr. Rudeesun Songmuang for selecting me for this Ph.D. position and her instruction on the nanowire topic, Dr. Eva Monroy for her promptness for all the questions/troubles with a problem-solving mind, and also to Prof. Le Si Dang for his insight explanations which have contributed to broaden my knowledge in the field of study. I appreciate all of your guidance, support and encouragement through these three years, and feel so fortunate to have been in this team.

My sincere thanks go to Prof. Henri Mariette, Director of the group NPSC, for the fruitful discussions on my topic, and also to Prof. Jean-Michel Gérard, Director of the division of “Physics of Materials and Microstructures (SP2M)”. Their leadership has created a positive and learning environment for all the members of the laboratory.

I convey my thanks to the members of the jury: The President Prof. Le Si Dang (Institut Néel-CNRS, Grenoble), Referees Prof. Guillaume Cassabois (Université Montpellier II, Montpellier) and Dr. Fabrice Semond (CRNS-CRHEA, Valbonne), and Examiners Prof. Stephen Purcell (Institut Lumière Matière, Lyon), Prof. Henning Riechert (Paul Drude Institut, Berlin), and Dr. Martin Strassburg (OSRAM opto Semiconductors, GmbH) for accepting to serve as the jury, despite their busy schedules. This Thesis improved a lot with your constructive comments.

Regarding the external collaborations, I would like to thank Prof. S.T. Purcell and his team (Dr. M. Choueib, K. Naji) at Université Claude Bernard Lyon1, G. Tocu and Dr. H. Lin from Newstep Technologies, for their excellent cooperation to achieve common goals. I also extend my thanks to Prof. N. Cote-Pattat, Director of the MAP laboratory at Université Claude Bernard Lyon1 for assisting in the E-coli bacteria purification test.

I would like to thank Dr. M. den Hertog for providing high-quality TEM images and useful interpretations, Dr. E. Bellet-Amalric for x-ray diffraction measurements that allow comprehending the complex structures, Dr. F. Donatini for CL training and his assistance when I encountered CL problems. L. Notin for AFM training and his experimental aid, Dr. B. Gayral for PL instructions and his suggestions on such measurements, and Dr. J. Bleuse for his time-resolved PL measurements.

I would like to acknowledge the former members of the team: Aparna and Yulia for transferring your experience and support which help me start my research with ease, Fernando and Manos for their comments on my work, my presentations, and also for their mental support, Giang –my officemate– and Anna for their suggestions on daily life in France which helped me a lot. Also for the current members of the team: Sirona, Mark, Luca, Jonas, Caroline, Akhil, and Siew, it is such a pleasure to know all of you, thanks for everything we have shared, and I wish you all success in achieving your goals. I would like to thank as well the previous and current colleagues at NPSC for creating a nice atmosphere in the laboratory: Karine, Diane, Damien, Aurélie, Pamela, Thomas, Emmanuel, Thibault, Zhihua, Matthias, Agnès, Xin, Martin, Thobias etc.

I gratefully acknowledge the financial support from the ANR “UVLamp” project (ANR-2011 NANO-027).

Finally, I wish to thank my family and friends in Thailand for their support and encouragement towards my pursuit of higher education in France.

Chalermchai HIMWAS (buk)

Resumé

Ce manuscrit de these, intitulé “Nanostructures à base de semi-conducteurs nitrures pour l'émission ultra-violette”, concerne l'élaboration de matériaux actifs pour l'émission de lumière dans la gamme spectrale de l'ultraviolet profond, dite UV-C. Plus spécifiquement, ces travaux de thèse s'inscrivent dans le programme de travail du projet ANR « UVLamp » dont l'objectif est de fabriquer une source UV-C pompée électriquement pour la purification de l'eau. Dans ce projet, le pompage électrique est réalisé par une source externe d'électrons à base de nanotubes de carbone, qui excite ensuite une couche active à base d'AlGaN. Mes travaux de thèse abordent la problématique de l'émission de lumière dans l'UV profond, avec une contribution intéressante comparant boîtes quantiques auto-organisées et nanodisques intégrés dans des nanofils.

Ce manuscrit de these est composé de six chapitres. Un premier chapitre d'introduction generale expose le context et la motivation de l’étude. Le chapitre deux rappelle les propriétés opto-électroniques de base des semiconducteurs nitrures composés d'éléments de la colonne III et d'azote (III-N). Le texte commence par une description des différentes structures cristallines, suivie de celle des propriétés électroniques : sont ainsi passées en revue les structures de bandes, les masses effectives dans les matériaux GaN et AlN, ainsi que leurs constantes élastiques et piézo-électriques. Ce chapitre se termine avec une presentation des défauts structuraux dans le semi-conducteurs nitrures.

Le chapitre trois est focalisé sur les techniques expérimentales mises en oeuvre pendant cette these, en commençant par l'épitaxie, au coeur de ce travail de doctorat. Je explique par ailleurs, comment, en parallèle de l'épitaxie, une caractérisation par diffraction d'électrons de haute énergie (RHEED) peut être effectuée in-situ, élément tout à fait essentiel au contrôle de la croissance. En préambule des deux chapitres suivants, j’indique les conditions de croissance dans plusieurs configurations de base : GaN, AlN et AlGaN massifs crus suivant l'axe (0001), boîtes quantiques GaN en conditions riche métal (mode Frank-van der Merve) et riche azote (mode Stranski-Krastanov), et enfin nanofils GaN sur substrats sapphir ou silicium (111). Les différents types de substrat possibles (saphir, silicium(111) et SiC) sont ensuite décrits et comparés. Ce chapitre se termine avec une revue des techniques de diffraction X, microscopie à force atomique, microscopie électronique à balayage, cathodoluminescence, photoluminescence et transmission infra-rouge qui permettront de réaliser une caractérisation détaillée des échantillons fabriqués.

Le chapitre quatre est centré sur les échantillons de boîtes quantiques AlGaN/AlN. Les épaisseurs de la couche active et de la barrière sont étudiées et caractérisées avec soin avant d'aborder le problème de l'accord en longueur d'onde, qui est étudié en fonction de la température du substrat, du rapport des flux Al/métal et enfin de l'épaisseur d'alliage AlGaN déposé. En faisant varier ces paramètres, je montre qu'il est possible d'atteindre une longueur d'émission de 235 nm avec un rendement quantique interne de l'ordre de 30 % à température ambiante. Dans un deuxième temps, je m'intéresse à maximiser l'émission de la couche active à température ambiante en jouant sur l'épaisseur d'AlGaN déposé, ce qui conduit à la définition d'un compromise entre la densité des boîtes quantiques et leur rendement quantique interne, ce compromise étant trouvé pour environ cinq monocouches déposées. Une autre stratégie est ensuite abordée consistant à modifier la longueur d'onde d'émission à épaisseurd'alliage donnée, en faisant varier le rapport des flux Al et métal. De fait, une longueur d'onde d'émission de 260 nm est atteinte. Enfin, ce chapitre termine avec la description des essais de polissage et métallisation pour augmenter l'extraction de la lumière, ainsi que par la presentation d'un essai de croissance sur substrat SiC, qui sera utilisé dans le prototype de lampe UV décrite dans le dernier chapitre.

Le chapitre cinq est consacré au deuxième type d'échantillons fabriqués, consistant en des nanodisques AlGaN/AlN sur nanofils GaN. Dans la géométrie nanofils, l'aspect croissance deviant bien plus complexe. Tout d'abord, je describe l'épitaxie de ciyces éoausses d'AlGa? sur des nanofils GaN. Les variations du flux d'Al en fonction des flux de Ga et N sont étudiées, mettant ainsi en évidence des inhomogénéités importantes de la composition de l'alliage AlGaN le long du nanofil. Je montre que c'est la relaxation de la contrinte qui est à l'origine de ces inhomogénéités de composition, et donc de la localization des porteurs. La conception d'hétérostructures AlGaN/AlN est ensuite étudiée dans les régimes métal-riche et azote-riche, ce dernier cas étant le seul à montrer des signatures dans le spectre d'émission dépendant de la composition de l'alliage. Température de croissance, concentration en Al et épaisseur des nanodisques déposés permettent ainsi de couvrir la gamme spectrale 240-350 nm. Enfin, une configuration originale de croissance de nanodisques dans les conditions de croissance de boîtes quantiques auto-organisées est testée en parallèle sur une couche d'AlN et sur un échantillon de nanofils, aboutissant à des résultats radicalement différents.

Dans le dernier chapitre avant de conclure, je décris brièvement un prototype de source UV-C utlisant l'approche optimisée du chapitre 4, à savoir des boîtes quantiques AlGaN/AlN

déposées sur substrat SiC. Les résultats de purification d'eau obtenus avec cette lampe sont presentés.

Contents

Chapter 1

1 Introduction and targets

This chapter starts with a historical introduction to III-nitride semiconductors, including a presentation of their optoelectronic and electronic applications. Subsequently, the motivation of using III-nitrides to fabricate ultraviolet emitters is described, followed by the definition of the targets of this work. Finally, the chapter finishes with a description of the organization of the manuscript.

1.1 Historical introduction to III-nitride semiconductors

Wurtzite III-nitride semiconductors (GaN, AlN, InN, and their ternary and quaternary compounds) are direct band gap materials that can cover a large spectral range, from near infrared (~0.65 eV for InN), visible, to ultraviolet (UV) (6.2 eV for AlN), as illustrated in Figure 1.1. In addition, the high thermal conductivity, chemical inertness, and mechanical stability of such semiconductors make them able to compete with Si or GaAs in application fields requiring extreme operation conditions.

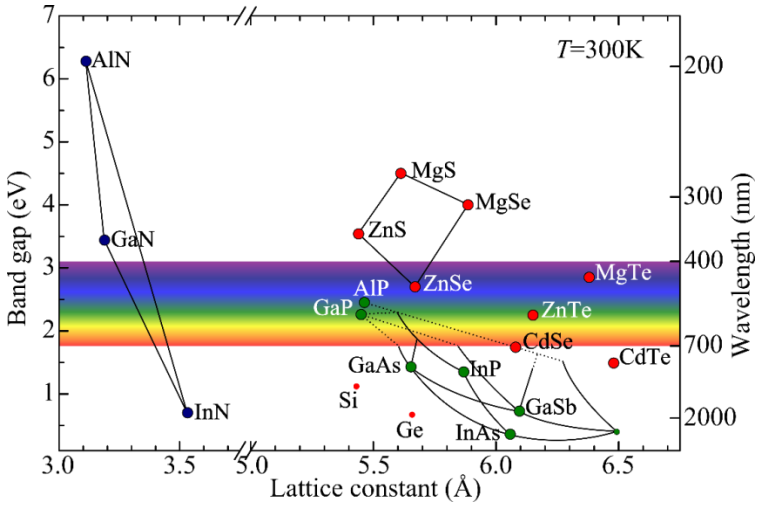

Figure 1.1: Bandgap energy versus lattice constant of the most common semiconductors.

The growth of polycrystalline AlN [1], GaN [2], and InN [3] was first reported in 1907, 1932, and 1938, respectively. By the end of the 60's, the developments in chemical vapor phase epitaxy resulted in GaN [4] and AlN [5] with improved crystalline quality. In the 70's,

we find the first reports of III-nitrides grown by metalorganic vapor phase epitaxy (MOVPE) [6] and molecular beam epitaxy (MBE) [7]. However, at that time, the high defect densities and high n-type residual doping hampered the development of III-nitride devices. A major breakthrough came in 1986, when *Amano et al.* [8] proposed the use of an AlN buffer layer prior to the GaN growth, which successfully improved the crystalline quality. A few years later, the same team achieved *p*-type GaN by doping with Mg [9].

III-nitride research progressed rapidly after the first demonstration of high efficient blue light emitting diodes (LEDs) in 1994 [10], and laser diodes in 1996 [11]. Nitride-based blue and green LEDs, commercialized since 1995, are a basic technology for full color displays, and the GaN blue laser diode (405 nm) have become a new standard for data storage (Blue-ray technology). Furthermore, the combination of the blue LED with phosphors has revolutionized the lighting industry, offering an efficient and environmentally friendly alternative to the white light bulb.

Beside the success of LEDs and laser diodes, III-nitride materials are attractive for a number of optoelectronic and electronic devices, such as high-electron-mobility transistors (HEMTs) or UV photodetectors. AlGaN/GaN HEMTs were first developed in 1994 [12] by taking benefit of the high electron mobility (~2000 cm^2/Vs) in a two-dimensional electron gas. By exploiting the robustness of GaN, there have been reports on HEMTs with unprecedented breakdown voltages [13], [14] which pave the way for high-voltage and high-power switching applications, such as the electric drive system used in hybrid electric vehicles. Several critical advancements make this application prospect increasingly realistic, including the progress in GaN-on-Si substrates, development of normally-off gate structures, and suppression of current collapse phenomenon. On the other hand, visible-blind ultraviolet photodetectors [15], [16] based on GaN have also found broad public outreach as a cheap solution to assess the potential erythema damage, for instance incorporated in wrist watches.

Beyond the above described commercial devices, the properties of III-nitrides have drawn attraction for applications such as solar cells, intersubband devices and UV emitters. Because of the extraordinary range of the band gap of InGaN, which covers almost the complete solar spectrum (from 0.65 to 3.42 eV), InGaN has been recently investigated for solar energy conversion [17]–[19]. InGaN solar cells show promising results in terms of open-circuit voltage (~2V) and fill factor (up to 80%). Although the energy conversion efficiency remains low (below 3.4% [20]) due to the high defect density in high-indium-

content InGaN films.

On the other hand, the large conduction band offset of III-nitride semiconductors is highly interesting for the applications in the mid- and far-infrared regions using intersubband (ISB) transitions [21], a technology where the operation wavelength is defined by band gap engineering in quantum structures. Typically, ISB detectors and lasers are based on III-As-P materials [22], [23]. The advantages of III-nitrides lie, on the one hand, on the large GaN/AlN conduction band offset which can extend the ISB optical response to the fiber-optics telecommunication range (1.3-1.5 μm), and on the other hand, the large LO-phonon energy of III-nitride materials which should allow operation in the THz spectral range (λ = 30-1000 μm) at room temperature.

One important issue in the development of the III-nitride technology is the difficulty to obtain lattice-matched substrates. Most often, III-nitride materials are still grown on foreign substrates such as sapphire, SiC or Si(111). The different lattice parameters and thermal expansion coefficients between the grown III-N and the substrates result in high dislocation densities (10^7-10^{10} cm^{-2}). Today, bulk GaN substrates are produced by hydride vapor phase epitaxy (HVPE) [24], [25] or by ammonothermal methods [26]. However, these substrates remain much more expensive than the commercial sapphire-based GaN templates.

Regarding the growth techniques, commercial III-N devices are grown by MOVPE. However, MBE presents several advantages over MOVPE for the fabrication of structurally-demanding devices, in spite of the lower production throughput. The relatively low MBE growth temperature (~700-800°C for GaN, to be compared to >1000°C when grown by MOVPE) makes it possible to achieve chemically sharp GaN/AlGaN/AlN interfaces. The ability to control the growth rates in the order of monolayer-per-second (ML/s) enables the formation of homogeneous nanofilms. Furthermore, adequate tuning of the growth conditions opens the possibility of synthesizing three dimensional nanostructures (quantum dots, nanowires) in a broad compositional range.

1.2 III-nitrides for UV emitters: Motivation and targets

UV emitters are used in a number of industrial applications, for instance water/air purification, bio-detection, phototherapy, or resist curing. They consist mostly of mercury (Hg) vapor lamps, whose emission spectrum spans from mid-UV until infra-red regions as exhibited in Figure 1.2.

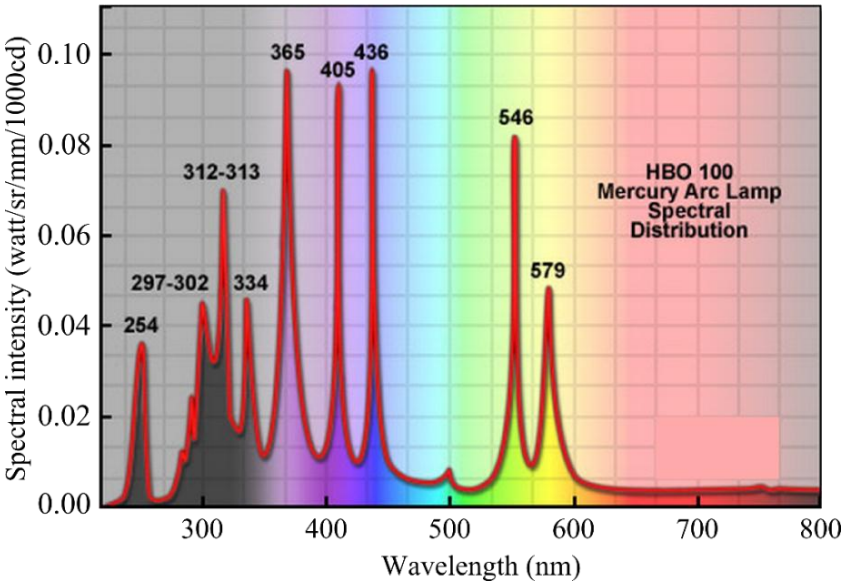

Figure 1.2 Mercury emission spectrum [27].

The electrical/optical energy conversion efficiency for the Hg lamp is ~10% [28]. Furthermore, the emission spectrum of the Hg lamp shows a variety of lines, and usually a single line is selected for the corresponding application, so that only a small percentage of the emitted optical power is used. For instance, the 365 nm line (i-line UV-A) represents 1.5% of the emission spectrum [29], and thus, taking the reported electrical-optical energy conversion into account, the efficiency of the Hg lamp at 365 nm cannot exceed 0.15%. Moreover, Hg and its compounds are toxic materials. These facts have motivated research on the replacement of the Hg lamp by a solid-state alternative, especially in the medical domain.

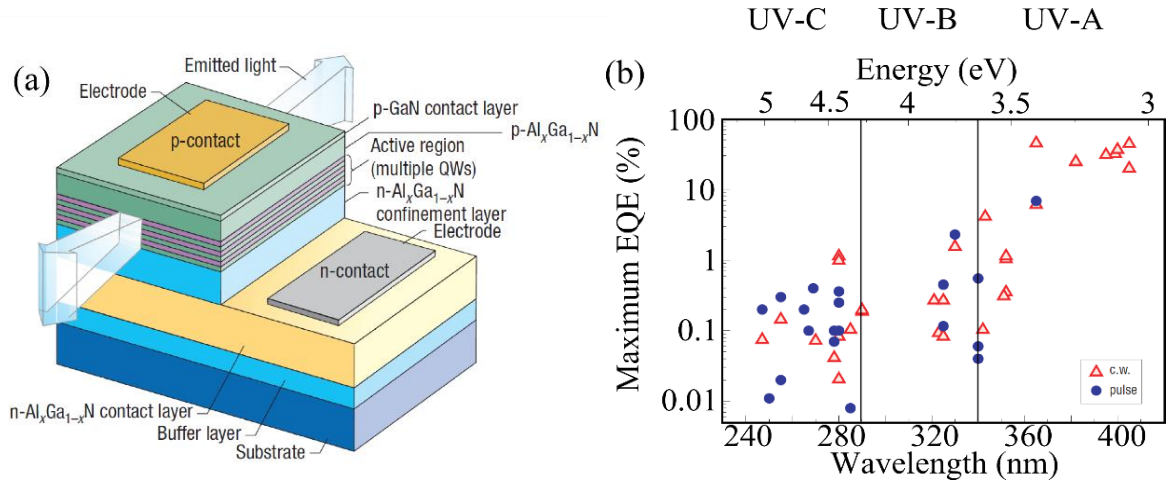

Figure 1.3: (a) Schematic of a typical UV LED based on III-nitride semiconductors. (b) Plot of the maximum external quantum efficiency UV reported for continuous wave (c.w.) (open triangles) and pulsed (closed circles) UV LEDs by different research groups [30].

III-nitride semiconductors are a promising choice for such replacement due to the band gap that can span over the entire Hg spectral range. Band gap engineering of AlInGaN alloys allows tuning the peak emission wavelength to minimize the problems of unwanted heat and non-useful optical emission. For the long wavelength UV-A region (365-400 nm), most of the commercially available LEDs with high performance are fabricated using InGaN quantum wells (QWs).

Generally, the performance of the photon emitters is probed by the external quantum efficiency (EQE) which is expressed by:

$$EQE=CIE\times IQE\times LEE \tag{1.1}$$

where the carrier injection efficiency (CIE) is the ratio between the number of electron-hole pairs generated in the active region and the number of carriers injected into the device, the internal quantum efficiency (IQE) is the ratio between the number of photons emitted by the active region and the number of electron-hole pairs generated in the active region, and the light extraction efficiency (LEE) is the ratio between the number of photons emitted in free space to the number of photons emitted by the active region.

If we look at the performance of UV LEDs reported by various research groups [Figure 1.3(b)], a degradation occurs when approaching $\lambda = 365$ nm from visible band, which corresponds to the band gap of GaN [31], [32]. In order to further blue shift, Al must be introduced into the active region, which results in lower EQE than that of LEDs fabricated by InGaN/GaN QWs due to a number of key parameters, such as the stronger quantum confined Stark effect [33], the absence of In-rich-InGaN alloy clustering which assists in confining carriers away from threading dislocations, or the absorbing coefficients (of SiC and sapphire based templates) that further increase with decreasing wavelength.

To enter UV-B (320-280 nm) and UV-C (280-150 nm) regions, high Al contents are introduced, which results in higher dislocation densities (10^{10}-10^{11} cm^{-2} compared to ~10^{8} cm^{-2} in the GaN case). Other challenges are the high resistivity of *n*-contact AlGaN layer, the difficulty of making and contacting a *p*-type AlGaN layer [34]. Kneissl *et al*. [35] reported that EQE usually drops to lower than 1% for the $\lambda < 320$ nm. Currently, to our knowledge there is only one company: Sensor Electronic Technology (SET) Inc., in USA, who offers commercial UV-C LEDs.

The efficiency of short-wavelength emitters can be improved by using the electron-pumped UV (EPUV) emitter concept [36]. Although the presence of threading dislocations

in the system is inevitable due to the lack of lattice matched substrates, the *p*-type doping issue can be avoided by injecting carriers directly to the active region using an electron gun [36]. However, the efficiency of electron-hole generation when injecting the electron beam into semiconductors cannot exceed 1/3 (CIE<1/3) [37], limiting the maximum EQE of EPUV devices at 33%. For this reason, it is only worth fabricating EPUV emitters in UV-B and UV-C region, where the problems of doping and contacts introduce a dramatic limitation for current LED technology. EPUV devices have been formerly studied by a couple of Japanese teams (National Institute of Material Science [38] and Kyoto University [36]) using AlGaN QWs as active region.

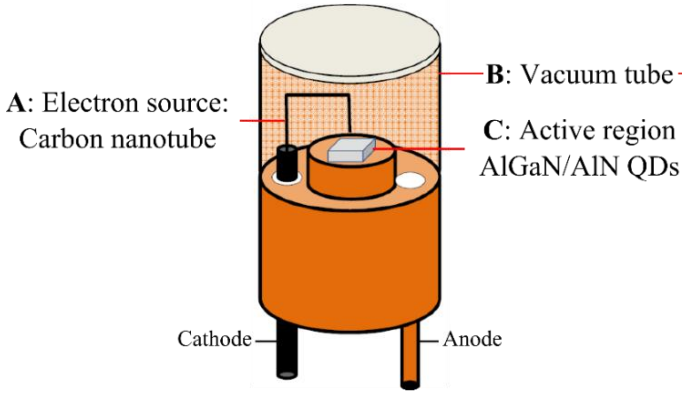

Figure 1.4 UV emitter schematic, showing major components including, A: the cabon nanotube field emission source, B: Vacuum tube, and C: AlGaN/AlN active region.

This manuscript is my contribution to the "UVLamp" project (ANR-2011-NANO-027), which aims at developing EPUV emitters. The targeted wavelength is set at 260 nm for the application of water purification. Carbon nanotubes (CNT) were selected as electron injecting sources, due the small source size, low energy consumption, low voltage turn-on, high current stability and current density. One challenge to fabricate electron based devices is the requirement of operation under high vacuum. To this fact, a special vacuum tube needs to be designed. AlGaN/AlN nanostructures were selected to be used as an active medium since their spectral response fits the targeted wavelength, and the efficiency of the materials can be enhanced by heterostructuring.

The project consists of three partners who are responsible for different tasks, namely the excitation source, vacuum tube, and active medium. The CNT excitation source (Figure 1.4: A) has been studied and optimized under the supervision of Prof. S. Purcell at Université Claude Bernard Lyon1. The vacuum tube (10^{-6} Torr) (Figure 1.4: B) has been provided by

NEWSTEP technologies. The last part, the active medium fabricated using AlGaN/AlN nanostructures (Figure 1.4: C), has been studied and optimized at INAC/SP2M-CEA and Institute Néel-CNRS and sets the basis of this PhD work.

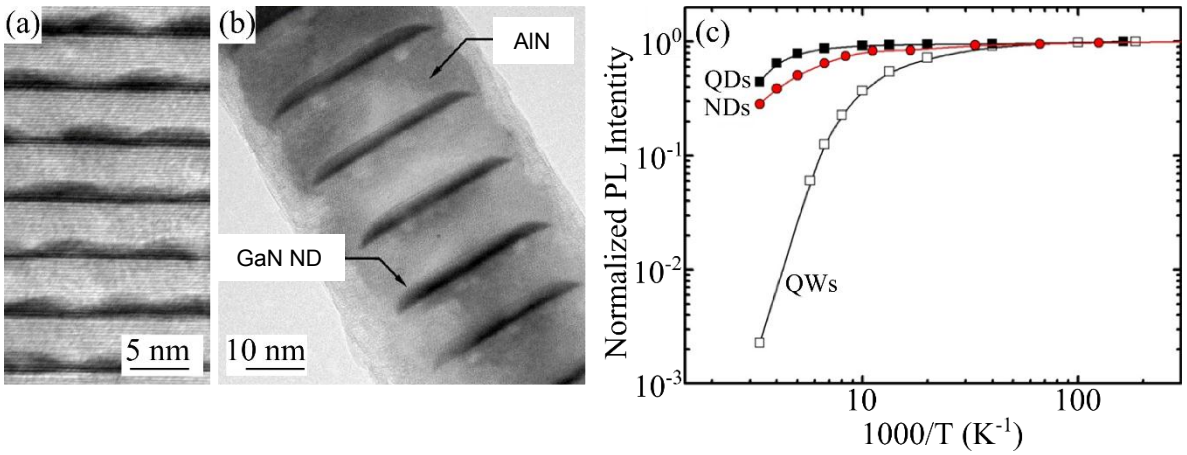

Figure 1.5: Transmission electron microscope images of (a) a multilayer of self-assembled GaN/GaN QDs, and (b) GaN/AlN NDs embedded along the wire axis grown by MBE. (c) Variation of integrated PL intensity from QDs, NDs, and QWs with temperatures.

Although the CIE value in EPUV devices is limited at 33%, the EQE can be improved by using the nanostructures with high IQE at room temperature as an active medium. The IQE can be probed by the ratio between integrated photoluminescence (PL) intensities at room temperature (300K) and at low temperature (~5K). Figure 1.5(c) shows the PL evolution with temperature for three kinds of GaN/AlN nanostructures, namely QWs, quantum dots (QDs) and nanodisks (NDs) in nanowires (NWs). Assuming that 100% of the electron-hole pairs generated at low temperature do emit the photons, the IQE of QDs and NDs are ~30-40% derived from the luminescence intensity from Fig.1.5(c), which is higher than that of QWs (~0.2%). The difference between QDs/NDs and QWs is due to the three dimensional carrier confinement which prevents carriers from reaching nonradiative recombination centers. In the case of GaN/AlN nanostructures, reaching the targeted wavelength would imply decreasing the thickness of GaN heterostructures down to two monolayers, which correspons to the thickness of the wetting layer of GaN QDs. The growth of such very thin layers is hard to control and generally results in a degradation of the optical quality. Therefore, incorporation of Al in the active nanostructures is considered as an alternative solution to approach the targeted 260 nm emission. Two types of nanostructures, AlGaN/AlN QDs and AlGaN/AlN NDs on GaN NWs, are chosen to be developed in this project.

The target of my PhD work was to study the epitaxial growth of AlGaN/AlN QDs and AlGaN/AlN NDs on GaN NWs using plasma-assisted MBE, in order to assess their capability as active media of EPUV lamps. To the best of my knowledge, this is the first attempt to incorporate Al in GaN QDs, to reduce the emission wavelength. Efforts were dedicated to understanding of the growth, the structural properties and the optical performance of such nanostructures, and to adapt the design of the sample to the targeted application.

During my PhD, my work has concerned the MBE growth of AlGaN/AlN QDs and NDs on GaN NWs, and their characterization using *in situ* reflection high energy electron diffraction, atomic force microscopy, photoluminescence, cathodoluminescence and Fourier transform infrared spectroscopy. Additional data on the structural properties was provided by transmission electron microscopy performed by Dr. Martien den Hertog (Institut Néel, Grenoble), and by x-ray diffraction measured by Dr. Edith Bellet-Amalric. The characterization of the samples under electron pumping using CNT guns was performed by our collaborators at Université Claude Bernard Lyon1 (Prof. S. Purcell).

1.3 Organization of the manuscript

After this introductory chapter, where I have presented the targets of this work, chapter 2 reviews the basic properties of III-nitride semiconductors, in order to understand the nature of the materials. The crystal properties, namely, the crystal structure and the crystal polarity are introduced in the first part of the chapter, followed by the description of their electronic properties i.e. the band structure and effective masses. Afterwards, the concepts of the strain and the intrinsic nature of spontaneous and piezoelectric polarization are displayed. The chapter finishes with a description of the structural defects that can be found in the III-nitride material system.

The aim of the third chapter is first to review the growth of III-nitrides via plasma-assisted MBE. With this purpose, I start with a description of the concepts of growth thermodynamics and kinetics. Then, the growth of the relevant materials for this work, i.e. GaN, AlN, AlGaN, GaN/AlN QDs, and GaN NWs, is presented, followed by the specification of different types of substrate utilized in this work. In the second part of this chapter, the principles of the various experimental techniques used to determine the structural and optical properties of the grown nanostructures are discussed.

The fourth chapter begins with a brief introduction including the challenges of UV emitter fabrication and the reason of using the quantum dot nanostructure as an active medium. Followed by the systematic designs of the active region which are divided into the report of the total active region thickness, AlN barrier thickness, and the amount of deposited AlGaN QDs. In order to have an efficient active media, approaching the targeted wavelength is demonstrated by fixing the optimized amount of AlGaN QDs and methodically adjusting the Al-to-metal flux ratio and substrate temperature. After all the growth optimization, some post-growth processes are displayed that can enhance the light extraction. Finally, the growth on SiC is shown that can be done without any degradation with respect to that performed on sapphire-based substrates.

The fifth chapter concentrates on the growth of NW heterostructures, starting with a study of AlGaN sections on GaN NWs, in order to use this know-how as a foundation for the study of AlGaN/AlN NDs. I generally find that the main challenge for nanowire heterostructuring is the ternary alloy inhomogeneity, which is governed by the misfit strain relaxation in the structure.

In chapter 6, I firstly describe the characterization of the active QD structure used for the first prototype EPUV emitter. Then, the process of fabrication and characterization of the EPUV emitter is described. To complete the study, a final test is set by exposing the E-coli bacteria with the prototype EPUV emitter in order to evaluate the purification ability of the device.

Finally, chapter 7 contains the conclusions of this work, and a view on the perspectives.

Chapter 2

2 Properties of III-nitride semiconductors

This chapter describes the basic properties of III-nitride semiconductors in order to understand the nature of the materials and properly utilize them for each application. The crystal properties, namely, crystal structure and crystal polarity are presented in the first part of the chapter, followed by their electronic properties which are divided into band structure and effective mass. Afterwards, the concepts of stress, strain and intrinsic natures of spontaneous and piezoelectric polarization are displayed. Finally, the defects that can be found in III-nitride system are introduced.

2.1 Crystal properties

There are three types of crystal structure for group III-nitride semiconductors, namely wurtzite (α-phase, with hexagonal symmetry), zinc-blende (β-phase, with cubic symmetry) and rock salt (γ-phase). However, only the first two structures can be epitaxially grown, whereas the last appears only at very high pressures and not stable [39]. In order to understand the representations of the hexagonal and cubic unit cells, each unit cell system is illustrated with their base vectors in Figure 2.1.

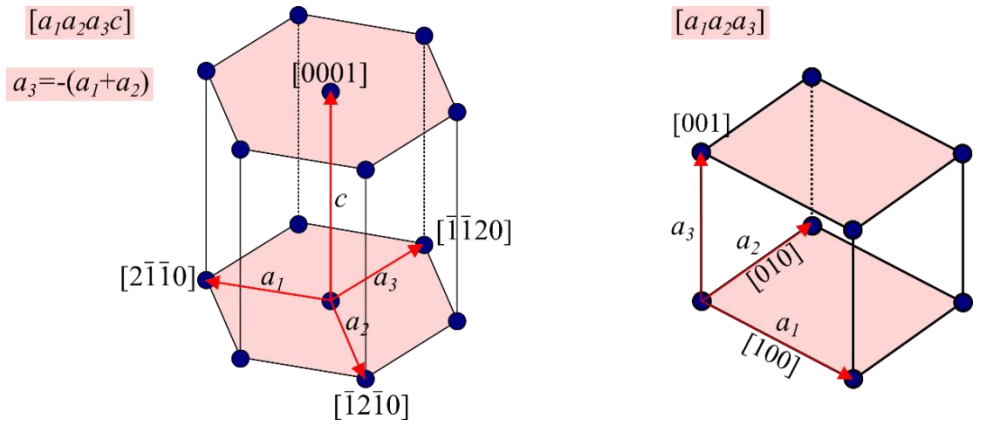

Figure 2.1: (a) Hexagonal unit cell with the base vectors a_1, a_2, a_3, and c (b) Cubic unit cell with the base vectors a_1, a_2, a_3.

To describe the position of a plane in a hexagonal symmetry, the notation system uses a set of 4 integers called "Miller-Bravais indices", which are denoted by the letters *h k i l* is

utilized. The first three indices represent three basal axes a_1, a_2, and a_3, which make 120° to each other, as illustrated in Figure 2.1(a). Note that the summation of the first three indices must be equal to zero, i.e. -(h+k)=i. The fourth index represents the vertical c-axis. In case of cubic unit cell, the notation system uses a set of 3 integers, which are denoted by the letters h k l. The three direction indices represent three axes, a_1, a_2, and a_3 that are perpendicular to each other as illustrated in Figure 2.1(b).

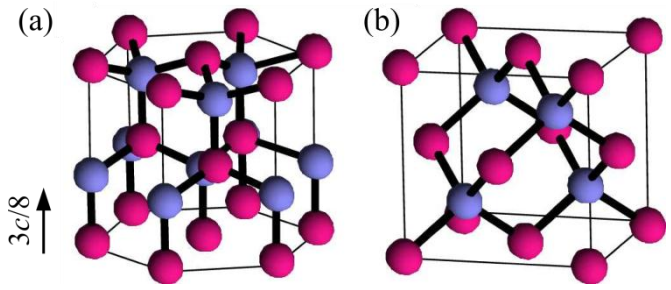

Figure 2.2: Schematic representation of (a) the wurtzite and (b) zinc-blende structures. The red and blue spheres indicate metal and N atoms, respectively.

The wurtzite structure consists of two hexagonal compact sublattices shifted by $\frac{3}{8}c$, as shown in Figure 2.2(a), whereas the zinc-blende structure consists of two interpenetrating face-centered cubic sublattices with the second sublattice shifted by $\frac{\sqrt{3}}{4}[111]$ with respect to the first sublattice as shown in Figure 2.2(b).

Each atom from wurtzite or zinc-blende structure is tetrahedrally coordinated. When one performs a rotation of 60° around [111] axis of the zinc-blende structure, the [0001] wurtzite structure is obtained. Figure 2.3 depicts the periodicity of both structures. For wurtzite structure, the oriented sequence is AB-AB-AB-… along [0001] axis and for zinc-blende structure, the oriented sequence is ABC-ABC-ABC-… along [111] axis.

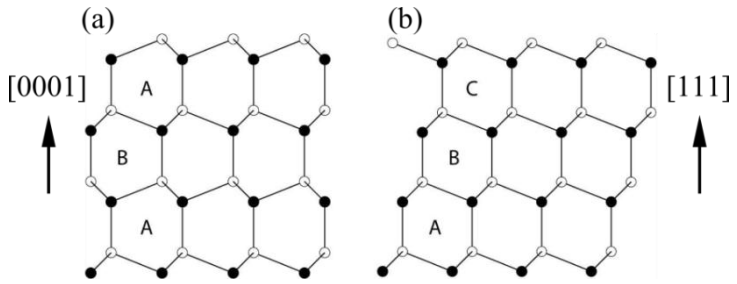

Figure 2.3: Stacking sequence of (a) (0001) planes in wurtzite (seen along the [11-20] azimuth), and (b) (111) planes in zinc-blende (seen along the [1-10] azimuth).

The wurtzite structure is more thermodynamically stable than the zinc-blende structure. The difference of the energy to form these two structures is in the range of -20 to -10

meV/atom [40]. The zinc-blende III-N can be grown by using specific conditions [41], [42] or appears as stacking faults in the wurtzite segments [43]. In this work, the substrates and the growth conditions are selected in such the way that they promote the wurtzite phase.

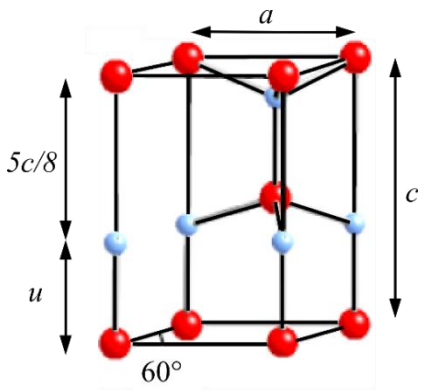

Figure 2.4: Wurtzite unit cell, where c and a are lattice constants and u is the anion-cation bond length.

Figure 2.4 shows the parameters that define the wurtzite unit cells which are the edge of hexagon (*a*), the height of hexagon (*c*) and the anion-cation bond length (*u*) along the [0001] direction. For the ideal wurtzite structure, the *c/a* and *u/c* ratios are 1.633 and 0.375, respectively. Deviation from these ratios, which change in experimental measurements of GaN and AlN (Table 2.1), reflects the distortion of the real lattice structure.

	GaN	AlN
c (Å)	5.185	4.982
a (Å)	3.189	3.112
c/a	1.626	1.600
u/c	0.377	0.382
Reference	[44], [45]	[44], [45]

Table 2.1: Lattice parameters of bulk GaN and AlN.

In the case of ternary alloys, all the lattice parameters can be approximated by using Vegard's law, that is, by linear interpolation from the parameters of the binary compounds:

$$a(Al_xGa_{1-x}N)=x\cdot a(AlN)+(1-x)\cdot a(GaN) \quad (2.1)$$

$$c(Al_xGa_{1-x}N)=x\cdot c(AlN)+(1-x)\cdot c(GaN) \quad (2.2)$$

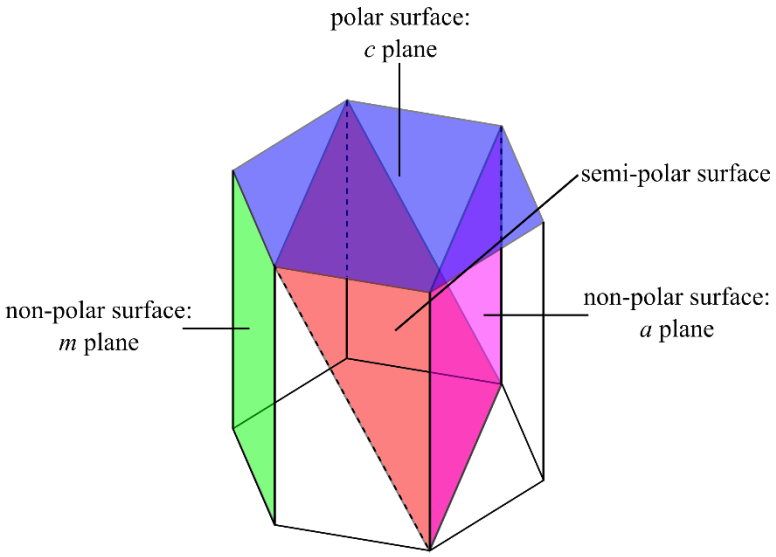

Figure 2.5: Schematic view of polar, non-polar, and semi-polar plane.

In the wurtzite system, the [0001] *c* axis is known as the "polar direction". The {0001} planes or *c* planes (blue in Figure 2.5) are the polar planes, which has only group III or nitrogen atoms at the surface layer. Surfaces parallel to the *c* axis, which contain equal number of group III and nitrogen atoms, are called "non-polar surfaces". Among them, the {11-20} plane family is called *a* plane, and the {1-100} plane family is called *m* plane (pink and green planes illustrated in Figure 2.5, respectively). Planes that form an angle different than 0° and 90° with the *c* axis are called "semi-polar", e.g. the {11-22} plane family (orange plane in Figure 2.5).

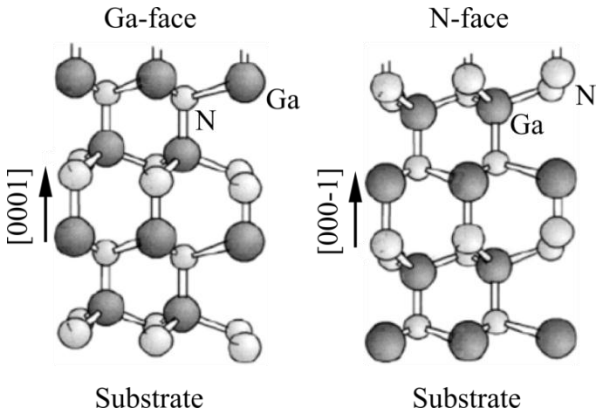

Figure 2.6: The polarity in GaN: (a) Ga-polar along [0001], (b) N-polar along [000-1] [46].

Due to the asymmetry of the wurtzite structure, the [0001] and [000-1] directions are different. The [0001] and [000-1] directions are determined by the vector associated to the metal-nitrogen bond along the <0001> axis. The [0001] direction is the direction where the vector points from a metal atom to a nitrogen atom, and the [000-1] is the direction where

the vector points from a nitrogen atom to a metal atom, as illustrated in Figure 2.6. Arbitrarily, the material is metal-polar if it is grown along [0001] direction, and nitrogen-polar if it is grown along [000-1] direction.

The polarity strongly affects the surface properties and it is important for the design and the fabrication of electronic devices. To determine the polarity of GaN films, various analytical tools have been used, such as x-ray photoemission spectroscopy [47], Auger spectroscopy [48], x-ray photoelectron diffraction [49], resonant X-ray diffraction [50]–[52], convergent beam electron diffraction [53] or ion channeling techniques [54]. The chemical etching with KOH or NaOH has also been used to determine the polarity since the N-polar face is chemically reactive [55]. The choice of polarity depends on the nature of the substrate and the growth conditions. In the case of metalorganic vapor phase epitaxy (MOVPE), GaN grown on sapphire is systematically Ga-polar. For molecular beam epitaxy (MBE), the polarity depends on the substrate preparation and on the nature of buffer layers. For example, Ga-polar GaN can be grown on an AlN buffer layer on (0001) sapphire while N-polar GaN can be obtained by nucleating GaN buffer layer directly on (0001) sapphire under heavily Ga-rich conditions. On the other hand, Ga-polar GaN can be converted to N-polar GaN during the growth by exposure the substrate to Mg [56].

2.2 Electronic properties

2.2.1 Band Structure

The band structures of GaN and AlN shown in Figure 2.7 were calculated by using the density-functional theory via the local-density approximation method [57]. As illustrated, the conduction band minimum and the valence band maximum locate at the center of Brillouin zone (Γ-point, k=0).

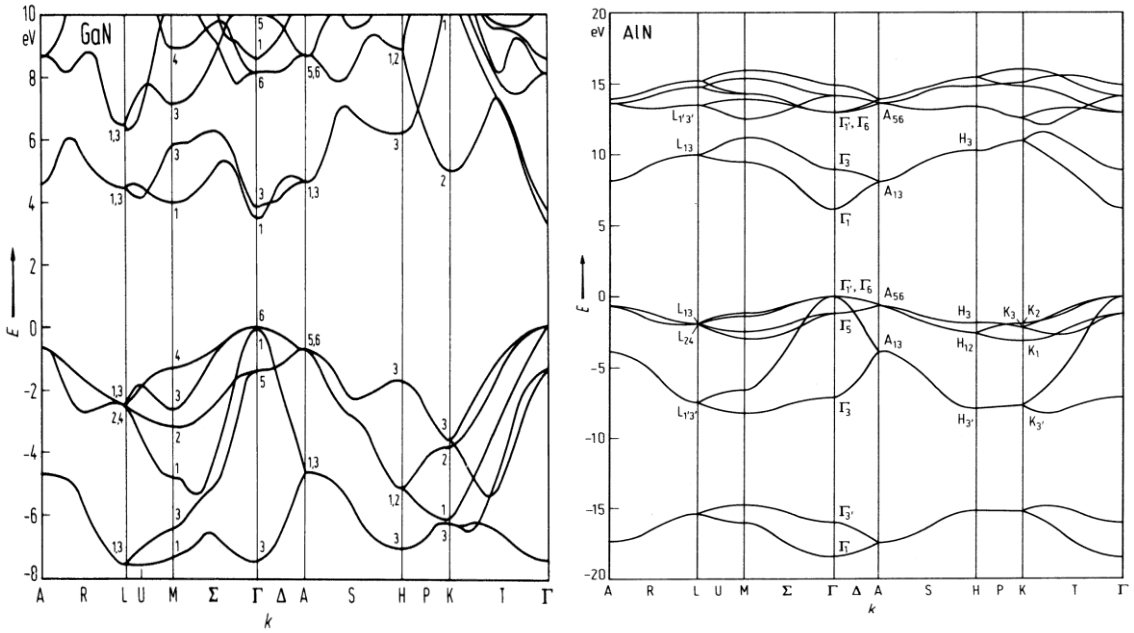

Figure 2.7: Calculated band structure of GaN (left) and AlN (right) [57].

Because of the asymmetric nature of wurtzite structure, the crystal-field splitting (Δ_{cf}) and spin-orbit splitting (Δ_{SO}) result in broken valence band degeneracy, which provides three different energy level subbands. As illustrated in Figure 2.8, the heavy-hole (HH), light-hole (LH), and crystal field split-off hole (CH) subbands are separated. The subband symmetry at the Γ-point is Γ_9 for HH and Γ_7 for LH, and CH. The reported value of Δ_{cf} for GaN = 10 meV [58], resulting in the splitting of subbands as illustrated in Figure 2.8. In the case of AlN, Δ_{cf} = -169 meV [58], i.e. the energy of the top of the LH subband is higher than the energy of HH subband.

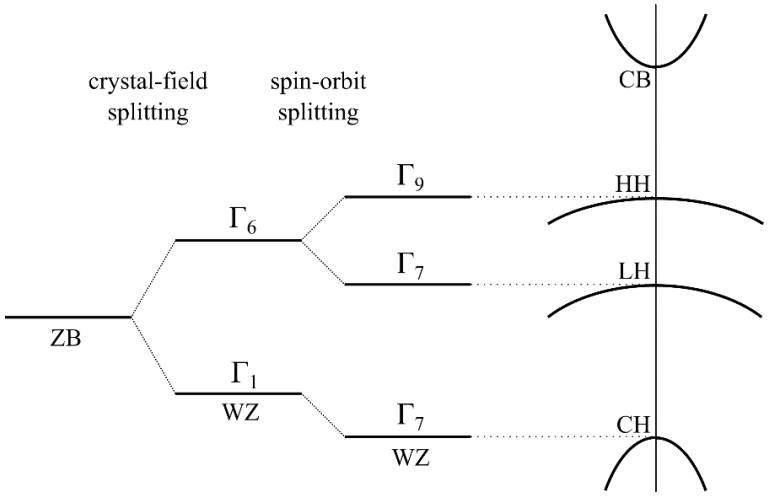

Figure 2.8: Schematic illustration of the spin-orbit splitting and crystal-field splitting in wurtzite (WZ) materials compared to zinc-blende (ZB) materials [58].

	E_g(T=0K) (eV)	E_g(T=300K) (eV)	α (meV/K)	β (K)	References
GaN	3.47 3.492	3.411 3.426	0.590 0.531	600 432	[59] [60]
AlN	6.126	6.030	1.799	1462	[61]

Table 2.2: Band parameters of GaN, and AlN.

The band gap of ternary alloys can be found using equation (2.3), where *b* is the bowing parameter which accounts for the deviation from a linear interpolation between the binary compounds (A and B). The reported *b* for AlGaN has the value in the range of 0-1.5 eV [62], [63].

$$E_g^{(AB)} = xE_g^{(A)} + (1-x)E_g^{(B)} - x(1-x)b \tag{2.3}$$

The semiconductor band gap changes with temperature due to the lattice expansion and electron-lattice interaction. The evolution of the band gap can be modelled by equation (2.4, which was proposed by *Varshni et al*. [64], where α and β are fitting parameters known as Varshni's thermal coefficients.

$$E_g = E_g(T=0) - \frac{\alpha T^2}{\beta + T} \tag{2.4}$$

2.2.2 Effective mass

The carriers in a crystal interact with their periodic potential of the lattice, and thus their "wave-particle" motion is different from electron in free space. The effective mass is inversely related to the curvature of the (*E,* $\boldsymbol{k}$) relationship, and can be derived from equation (2.5) by assuming a parabolic curvature of the (*E,* $\boldsymbol{k}$).

$$\frac{d^2E}{d^2\boldsymbol{k}} = \frac{\hbar^2}{m} \tag{2.5}$$

Thus, the effective mass has smaller value for the bands with higher degree of curvature (for example, the Γ-valley of GaN in comparison to the K-valley and M-L-valleys, as illustrated in Figure 2.9).

In approximations, the bands are assumed parabolic and the average effective masses are taken from different experimental measurements, such as infrared reflectivity, Hall effect [65], cyclotron resonance [66], and picosecond time-resolved photoluminescence [67]. The commonly used effective masses of electrons and holes of wurtzite GaN and AlN are summarized in Table 2.3.

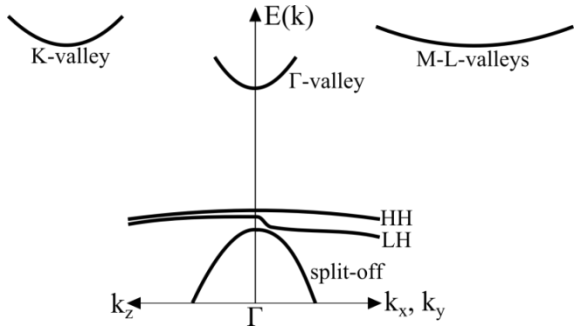

Figure 2.9: Valence band structure of GaN, indicating the anisotropy [68].

	Electron effective mass	Hole effective mass
GaN	0.2 m_0 [65], [66]	0.3 m_0 [69] 2.2 m_0 [67] 0.54 m_0 [70] 0.8 m_0 [71] 1.0 m_0 [72]
AlN	0.32 m_0 [66], [72]	1.41 m_0 [73]

Table 2.3: Effective masses of wurtzite GaN and AlN.

2.3 Elastic properties

III-nitride materials are mainly synthesized on sapphire, SiC, or Si substrates. The lattice and thermal expansion mismatch between substrate and epitaxial layer imposes a stress on the epitaxial layer which can profoundly affect its optical and electronic properties. The magnitude of the effect depends on the degree of stress. For small stress, the lattice reacts elastically through a shape transition (strain). For large deformations, the relaxation occurs plastically, i.e. introducing dislocations or cracks.

2.3.1 Strain and stress

In a linear elasticity regime, the stress (σ_{ij}) applied to a material is related to the strain (ε_{kl}) by Hooke's law:

$$\sigma_{ij} = \sum_{kl} C_{ijkl} \cdot \varepsilon_{kl} \tag{2.6}$$

where C_{ijkl} is the fourth-order elastic tensor.

To simplify the notation especially that of the fourth-order tensor C_{ijkl} , we introduce the indices {1, 2, 3, 4, 5, 6}, which replace the pairs of indices.

$$\varepsilon_1 = \varepsilon_{xx} \qquad \sigma_1 = \sigma_{xx}$$
$$\varepsilon_2 = \varepsilon_{yy} \qquad \sigma_2 = \sigma_{yy}$$
$$\varepsilon_3 = \varepsilon_{zz} \qquad \sigma_3 = \sigma_{zz}$$
$$\varepsilon_4 = \varepsilon_{yz}, \varepsilon_{zy} \qquad \sigma_4 = \sigma_{yz}, \sigma_{zy}$$
$$\varepsilon_5 = \varepsilon_{zx}, \varepsilon_{xz} \qquad \sigma_5 = \sigma_{zx}, \sigma_{xz}$$
$$\varepsilon_6 = \varepsilon_{xy}, \varepsilon_{yx} \qquad \sigma_6 = \sigma_{xy}, \sigma_{yx}$$

For hexagonal symmetry, the elastic tensor contains six elastic modules, five of which are independent and $C_{66}=(C_{11}-C_{12})/2$ as illustrated in equation (2.7):

$$\begin{pmatrix} \sigma_1 \\ \sigma_2 \\ \sigma_3 \\ \sigma_4 \\ \sigma_5 \\ \sigma_6 \end{pmatrix} = \begin{pmatrix} C_{11} & C_{12} & C_{13} & 0 & 0 & 0 \\ C_{12} & C_{11} & C_{13} & 0 & 0 & 0 \\ C_{13} & C_{13} & C_{33} & 0 & 0 & 0 \\ 0 & 0 & 0 & C_{44} & 0 & 0 \\ 0 & 0 & 0 & 0 & C_{44} & 0 \\ 0 & 0 & 0 & 0 & 0 & C_{66} \end{pmatrix} \begin{pmatrix} \varepsilon_1 \\ \varepsilon_2 \\ \varepsilon_3 \\ \varepsilon_4 \\ \varepsilon_5 \\ \varepsilon_6 \end{pmatrix} \tag{2.7}$$

Calculated and experimental values of the C_{ij} parameters of GaN and AlN are summarized in Table 2.4.

	C_{11}	C_{12}	C_{13}	C_{33}	C_{44}	References
GaN	374	106	70	379	101	[74] exp.
	390	145	106	398	105	[75] exp.
	365	135	114	381	109	[76] exp.
	370	145	110	390	90	[77] exp.
	396	144	100	392	91	[78] The.
	367	135	103	405	95	[79] The.
AlN	411	149	99	389	125	[80] exp.
	410	140	100	390	120	[77] exp.
	398	140	127	382	96	[78] The.
	396	137	108	373	116	[79] The.

Table 2.4: Experimental and theoretical stiffness constants of GaN and AlN in GPa.

When performing heteroepitaxy of III-nitrides on the (0001) plane, biaxial stress occurs, i.e. the in-plane stress is uniform ($\sigma_{11}=\sigma_{22}=\sigma$) and there is neither stress along the *c*-axis nor shear stress. In that particular case (biaxial strain configuration), the Hooke's law is simplified:

$$\begin{pmatrix}\sigma\\ \sigma\\ 0\end{pmatrix}=\begin{pmatrix}C_{11} & C_{12} & C_{13}\\ C_{12} & C_{11} & C_{13}\\ C_{13} & C_{13} & C_{33}\end{pmatrix}\begin{pmatrix}\varepsilon_1\\ \varepsilon_2\\ \varepsilon_3\end{pmatrix} \tag{2.8}$$

Due to the lattice symmetry, the strain components ε_1 and ε_2 are equal:

$$\varepsilon_1 = \varepsilon_2 = \varepsilon_{xx} = -(a_{epi}-a_{sub})/a_{sub} \tag{2.9}$$

where a_{epi} and a_{sub} are the lattice constants of the epilayer, and substrate, respectively. Consequently, the biaxial strain induces a strain ε_3 with the opposite sign of ε_{xx} along the [0001] axis perpendicular to the surface, which is given by:

$$\varepsilon_3 = \varepsilon_{zz} = -2(C_{13}/C_{33})\,\varepsilon_{xx} \tag{2.10}$$

2.3.2 Spontaneous and Piezoelectric polarization

Spontaneous polarization (P_{sp}) is an intrinsic property of III-nitride materials, due to the asymmetry in hexagonal wurtzite structure. A non-zero dipole moment of III-N orients along [0001] direction, different from high symmetry cubic structure where the dipole moments cancel each other. Bernardini *et al*. performed *ab initio* calculations of III-nitride spontaneous polarization using the Berry-phase approach to polarization in solids, obtaining P_{sp} = -0.029 and -0.081 C/m^2 for GaN and AlN, respectively [33]. A later report using the generalized gradient approximation corrected these values to P_{sp} = -0.034 and -0.090 C/m^2 for GaN and AlN, respectively [81]. In the case of the $Al_xGa_{1-x}N$ ternary alloy, the spontaneous polarization can be calculated as [82], [83]:

$$P_{SP}(Al_xGa_{1-x}N) = xP_{SP}(AlN) + (1-x)P_{SP}(GaN) + bx(1-x) \tag{2.11}$$

where P_{SP} is the spontaneous polarization and b = 0.019 C/m^2 is the bowing parameter for the spontaneous polarization in AlGaN [83], [84].

The piezoelectric polarization (P_{pz}) exists when applying stress to the system. The direction of P_{pz} depends on the strain state, e.g. in case of tensile biaxial strain of polar material the piezoelectric vector points along [000-1] direction whereas compressive biaxial strain of polar material, the vector points along [0001] direction. The piezoelectric polarization III-N can be calculated with the following equation:

$$P_{PZ} = \begin{pmatrix} 0 & 0 & 0 & 0 & e_{15} & 0 \\ 0 & 0 & 0 & e_{15} & 0 & 0 \\ e_{31} & e_{31} & e_{33} & 0 & 0 & 0 \end{pmatrix} \times \begin{pmatrix} \varepsilon_{xx} \\ \varepsilon_{yy} \\ \varepsilon_{zz} \\ \varepsilon_{yz} \\ \varepsilon_{xz} \\ \varepsilon_{xy} \end{pmatrix} \tag{2.12}$$

where e_{ij} are the piezoelectric coefficients of the material and ε_{ij} are the stress tensor. The values of the piezoelectric coefficients for GaN and AlN are summarized in Table 2.5.

	GaN	AlN	Ref.
e_{15}(C/m^2)	-0.30	-0.48	[85]
e_{31}(C/m^2)	-0.49	-0.60	[33]
e_{33}(C/m^2)	0.73	1.46	[33]

Table 2.5: Calculated piezoelectric coefficients e15, e31, e33 for GaN, and AlN.

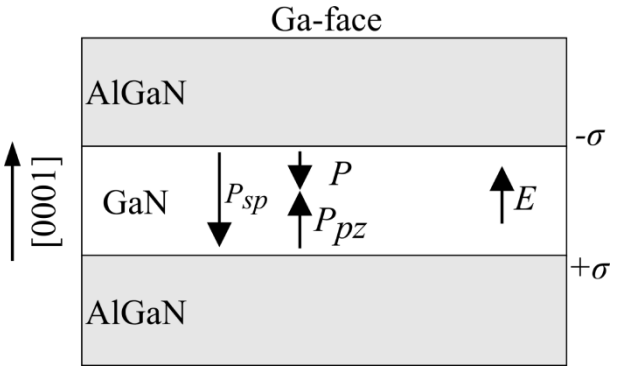

Figure 2.10: Polarization (spontaneous, piezoelectric and total polarization) in a quantum well consisting of a pseudomorphic GaN layer embedded in relaxed AlGaN. The interface charge (σ) is caused by the different total polarization in the GaN and AlGaN films [46].

In order to demonstrate the effect of polarization, the structure of a Ga-polar *AlGaN/GaN/AlGaN* quantum well is depicted in Figure 2.10. The GaN is assumed to be grown pseudomorphically on the AlGaN. The lattice constants *a* and *c* of the GaN quantum well decrease and increase respectively due to the biaxial compressive stress. Piezoelectric polarization can be calculated as:

$$P_{PZ} = e_{33}\varepsilon_{zz} + e_{33}(\varepsilon_{xx}+\varepsilon_{yy}) \tag{2.13}$$

where e_{13} *and* e_{33} are the piezoelectric coefficients. Assuming a biaxial strain configuration, and hence combining equations (2.10) and (2.13), the piezoelectric polarization can be determined by:

$$P_{PZ} = 2\left(e_{31} - e_{33}\frac{C_{13}}{C_{33}}\right)\varepsilon_{xx} \tag{2.14}$$

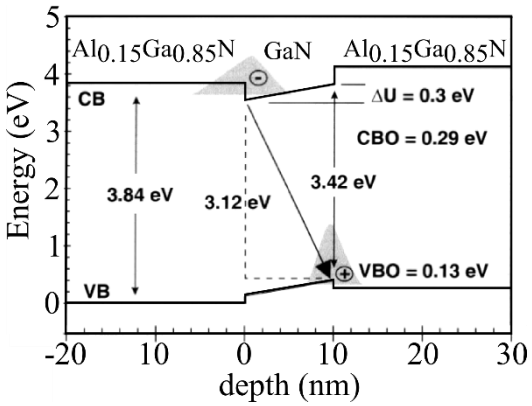

Figure 2.11: Conduction and valence band edges of a pseudomorphic growth $Al_{0.15}Ga_{0.85}N/GaN/Al_{0.15}Ga_{0.85}N$. The arrow indicates radiative recombination of an electron and hole, which is red-shifted in comparison to the bandgap energy due to the Stark effect [46].

Considering the structure in Figure 2.10, the different total polarization in GaN and AlGaN layers induce charge densities ($-\sigma$, and $+\sigma$) at the GaN/AlGaN interfaces, and consequently generate an internal electric field (E) across the GaN epilayer. Figure 2.11 shows the corresponding conduction and valence bands of the structure depicted in Figure 2.10. The bands are bent due to the Stark effect, which separates the electron and hole wavefunctions along the growth axis and reduces the energy of the band-to-band transition [67].

2.4 Structural Defects

Structural defects are any interruption of the crystal translation system, and can be classified into point defects, line defects, and planar defects. Point defects are defects generated only at or around a lattice point, so that the lattice distortion is rather local. Point defects can be vacancies, interstitial defects, or substitutional defects, as illustrated in Figure 2.12. Vacancies are lattice sites which should be occupied in the perfect crystal but are vacant. Interstitial defects are atoms that occupy some sites in the structure where, usually, there should not be an atom. A pair of nearby vacancy and interstitial atom can be called "Frenkel defect". Substitutional defects are the types of atoms that should not be in the lattice structure but they are, by occupying the vacant sites in the lattice. Hence they can be called "impurities". Such substitutional atom can be either smaller (substitutional smaller atom) or larger (substitutional larger atom) than the fundamental atom.

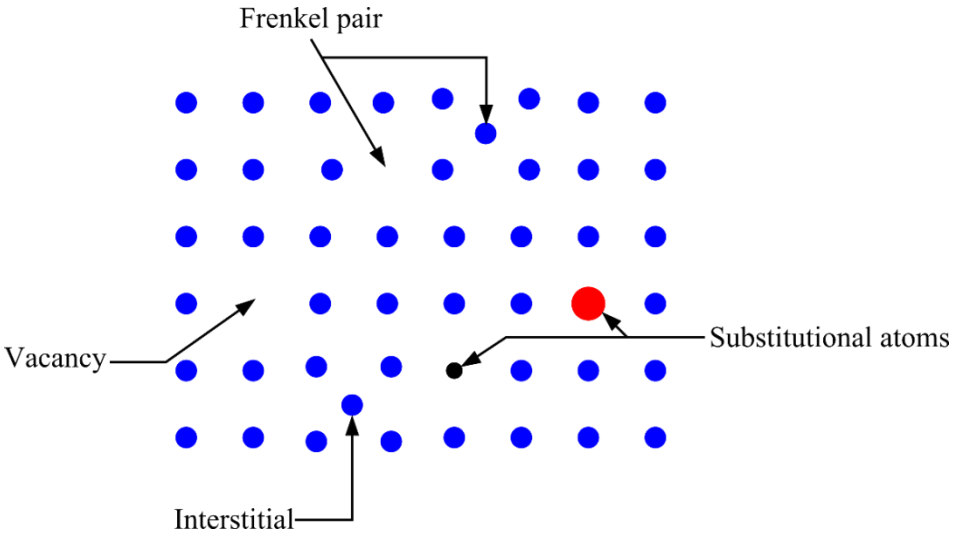

Figure 2.12: Schematic illustration of point defect types in crystal structure.

Line defects and planar defects are called in general "extended defects", and they are systematically present in III-nitride materials due to the growth on foreign substrates. The grown epilayers release the misfit-induced strain via generation of dislocations [53], [86], [87], cracks[88]–[90], or stacking faults [91, p. 1998], [92], [93]. These extended defects can affect the material properties causing non-radiative recombination, carrier scattering, and enhanced diffusion of dopants and impurities [94], [95].

The dislocations in the III-nitride system have been studied by *Wu et al.* [86]. They reported that ~70% of such defects are perfect pure edge dislocations (*a*-type) with burgers vector of 1/3<11-20>, consistent to the dislocation vector reported elsewhere [96]–[98]. The edge-type threading dislocations are generated at the first stage of the growth when islands coalesce and then propagate along the growth direction [99], [100]. Other perfect dislocations have also been observed, i.e. mixed screw-edge dislocation (*a*+*c* type) and screw dislocation (*c*-type) with burgers vectors of 1/3<11-23> and <0001>, respectively. In addition to perfect dislocations, Shockley and Frank partial dislocations are observed close to the epilayer-substrate interface.

Apart from dislocations, there are other mechanisms to release the stress from epilayer system, e.g. cracks and stacking faults. For the cracks, it was reported that they are generated by the tensile growth stresses once a critical thickness is reached [88]. The cracks are reported in nitride system grown on many types of substrate, such as on sapphire [88], on Si [89], and on SiC [90]. Another extended defect in III-nitride materials is stacking faults (SFs). Generally, they are terminated at each end with partial dislocations. Transmission

electron microscopy studies have reported a high density of basal SFs near the epilayer-substrate interface [86], [101]–[103]. Basal SFs in III-nitride materials are separated into type I, type II, and extrinsic SFs [104], which differ in the arrangement of the stacking sequence. From theoretical calculations, the formation energy of type I SF is lower than type II and extrinsic SF, respectively. The SFs can be considered as quantum-well liked region of zinc-blende surrounded by the wurtzite host. Other than the basal stacking fault, which occur perpendicularly to the growth axis, another type of SF, namely prismatic SF, can generate parallel to the growth axis. The prismatic SF is believed to occur when III-nitrides are grown on foreign substrates such as SiC or sapphire [91]. Furthermore, prismatic SFs can be generated when basal SFs fold onto the prism plane within epilayers. A summary of the typical dislocation and stacking faults found with their burgers vectors (**b**) and displacement vectors (**R**) are summarized in Table 2.6 [105].

Dislocations		
b	Type	Character
1/3<11-20>	*a*	Perfect
1/3<11-23>	*a*+*c*	Perfect
<0001>	*c*	Perfect
1/3<1-100>		Shockley partial
1/6<20-23>		Frank-Shockley partial
1/2<0001>		Frank partial
Stacking faults		
R	Type	SS or plane
1/3<1-100>	B-I_1	AB<u>ABC</u>BCB
1/6<20-23>	B-I_2	AB<u>ABCA</u>CA
1/2<0001>	B-E	AB<u>ABCAB</u>AB
1/2<1-101>	P	{11-20}
1/6<20-23>	P	{11-20}

Table 2.6: Dislocations and stacking faults in hexagonal structure. P: prismatic, B: basal, and SS: stacking sequence [105].

Chapter 3

3 Experimental techniques

The aim of this chapter is to introduce the concept of epitaxial growth and the information concerning the growth of III-Nitrides (GaN, AlN, AlGaN, GaN/AlN quantum dots, GaN nanowires, and GaN/AlN nanodisks on GaN nanowires) via plasma-assisted molecular beam epitaxy. The ending part of the chapter describes the characterization techniques that I used for determining the structural and optical properties of the grown samples.

3.1 Epitaxial growth

The process of material deposition onto a crystalline substrate is called *"epitaxy"* if the crystallographic arrangement of the deposited material is aligned with the substrate lattice. When the deposited material is the same as the substrate, the process is called *"homoepitaxy"*, which is generally performed when a purified layer is required or when a different doping level is needed. When the deposited material is different from the substrate, the process is called *"heteroepitaxy"*, which is used either to grow crystalline materials for which bulk crystals cannot be obtained, i.e. no substrate available for homoepitaxy, or to integrate crystalline layers of different materials (heterostructuring).

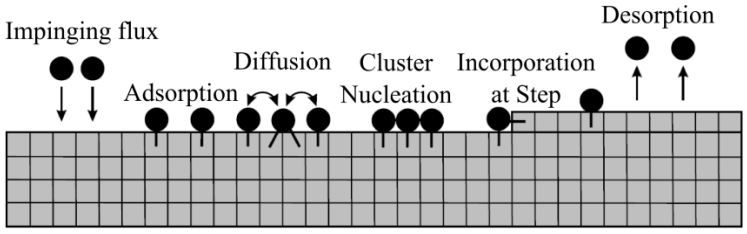

Figure 3.1: Schematic of different atomic processes occurred on the surface during the growth.

Figure 3.1 depicts different atomic processes namely adsorption, diffusion, nucleation, incorporation and desorption that can take place at the growing surface. The growth process depends not only on thermodynamic models, but also on the adatom kinetics [106]–[110] which is affected mainly from the substrate temperature.

In the case of lattice mismatched heteroepitaxy, Daruka and Barabàsi discriminated three thermodynamic growth modes, namely *Frank van de Merve*, *Stranski-Krastanov*, and

Volmer-Weber growth modes [111][112]:

- *Frank van der Merve* (*FM*) growth mode: Adatoms attached preferentially to the surface sites due to the comparative lattice constants (very low misfit ε) resulted in atomically smooth surface. Misfit dislocations appear above a critical thickness.
- *Stranski-Krastanov* (*SK*) growth mode: Due to the mediate misfit ε affect to the primitive growth layer is strained layer-by-layer growth, continuous growth of the layer until the height is higher than critical thickness resulted in relaxation of the layer and generated three-dimensional islands. Continuation of the growth can result in the formation of misfit dislocations *(SK-MD)*
- *Volmer-Weber* (*VW*) growth mode: Adatom-adatom interactions are stronger than that of adatom-surface interactions due to huge misfit ε resulted in three-dimensional clusters or islands.

In the case of the GaN/AlN material system, tuning of the growth conditions allows switching between FM and SK growth modes. The choice of growth mode is given by the minimum free energy per unit area, understood as $E = E_{\text{strained epilayer}} + E_{\text{surface}}$, for a certain film thickness h (h > 1 monolayer (ML)). If we compare (1) coherent two-dimensional (2D) growth (FM), (2) SK growth mode, (3) 2D growth with misfit dislocations (FM-MD), and (4) SK growth mode with misfit dislocations (SK-MD), the free energies per unit of area can be written as [113]:

$$E_{FM}\,(h) = M(\Delta a/a)^2 h + \gamma \tag{3.1}$$

$$E_{SK}\,(h) = (1-\alpha)M(\Delta a/a)^2 h + \gamma + \Delta\gamma \tag{3.2}$$

$$E_{FM-MD}\,(h) = -\frac{E_{MD}(h)^2}{[M(\Delta a/a)^2 d_0^2 h))M]} + \frac{2E_{MD}(h)}{d_0} + \gamma \tag{3.3}$$

$$E_{SK-MD}\,(h) = -\frac{E_{MD}(h)^2}{[(1-\alpha)M(\Delta a/a)^2 d_0^2 h]} + \frac{2E_{MD}(h)}{d_0} + \gamma + \Delta\gamma \tag{3.4}$$

where M is the film's biaxial modulus, $\Delta a/a$ is the lattice mismatch between the epilayer and the substrate: $(a_{subs}\text{-}a_{epi})/a_{epi}$, γ is the film's surface energy ($<\gamma_{subst}$), α is the elastic gain by accommodating the film's strain through the formation of partly relaxed SK islands, $\Delta\gamma$ is the surface energy cost by the formation of the facets, d_0 is the distance for a fully relaxed epilayer, and E_{MD} is the energy cost per unit length of forming a MD. The equations (3.3) and (3.4) are only defined when the film thickness (h) is thicker than the critical plastic

thickness (h_c^{MD}):

$$h_c^{MD} = E_{c-MD}/(M(\Delta a/a)^2 d_0) \quad (3.5)$$

where $E_{c\text{-}MD}$ is the MD energy formation at the critical plastic thickness (h_c^{MD}). Another critical thickness is the critical thickness of SK quantum dot (QD) generation (h_c^{SK}), which can be expressed from the equations (3.1) and (3.2) as:

$$h_c^{SK} = \Delta\gamma/(\alpha M(\Delta a/a)^2) \quad (3.6)$$

For a given epilayer thickness, the equilibrium growth mode is the one that exhibits the minimum energy. The comparison between the energies deduced from the equations (3.1), (3.2), (3.3), and (3.4) would, therefore, allow us to predict the expected growth mode.

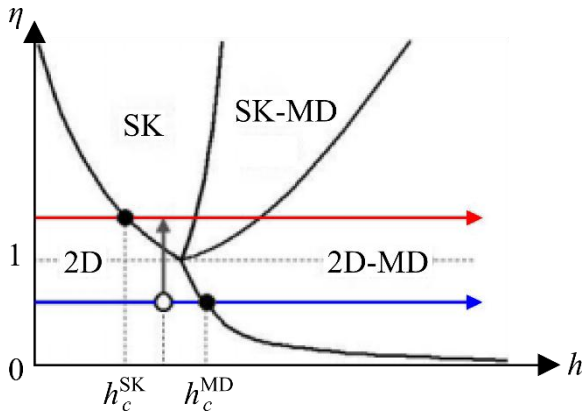

Figure 3.2: Phase diagram showing the expected growth mode as a function of the deposited thickness (h) and the critical thickness ratio (η) [113].

Figure 3.2 is the phase diagram showing the expected growth mode derived from the minimized formation energy as a function of the deposited thickness and the ratio between the two critical thicknesses η:

$$(\eta = h_c^{MD}/h_c^{SK}) \quad (3.7)$$

When considering a specific η in equation (3.7), for example η <1, i.e. $h_c^{MD}<h_c^{SK}$, the system favors plastic relaxation, i.e. the growth evolves along the blue arrow (shown in Figure 3.2), which render 2D growth mode in a primitive layer and start generating dislocations when deposited film is thickner than the h_c^{MD}. However, the h_c^{SK} can be lowered by decreasing the surface energy $\Delta\gamma$ for creating facets, consequently transforms the η ratio to be more than unity, thus the growth proceeds along the red arrow (displayed in Figure 3.2). The modification induces the SK transition instead of the plastic relaxation as exhibited as the shift of white circle, at the same deposited thickness, in Figure 3.2 from the 2D to SK

region.

The formation of SK QDs in III-As system such as InAs/GaAs is driven by the large lattice mismatch ($\varepsilon = \Delta a/a \approx 7\%$) of the system. However, in II-VI system which also has large lattice mismatch ($\varepsilon \approx 6\%$), no clear islands are reported. On the other hand, GaN/AlN system with lower lattice mismatch ($\varepsilon \approx 2.4\%$) is known for exhibiting a clear 2D-3D transition. Hence, it is obvious that the growth mode depends not only on the lattice mismatch between the grown layer and substrate but also on the dislocation formation energy and surface energy. These facts emphasize the validity of the equilibrium model presented above.

3.2 Plasma-assisted molecular beam epitaxy

Epitaxial growth can be performed by various techniques, such as by metalorganic vapor phase epitaxy (MOVPE), liquid phase epitaxy (LPE), hydride vapor phase epitaxy (HVPE), and molecular beam epitaxy (MBE). The latest is the method used in this work, which was developed in the late 60s for the growth of III-V semiconductors in Bell Telephone Laboratories [114]. It requires ultra-high vacuum (UHV = 10^{-10}-10^{-11} Torr) to ensure that the mean free path of the precursor molecules is much longer than the distance between the source cells and the substrate. Thus, the crystal growth is mostly governed by the kinetics of the surface processes rather than the thermodynamic equilibrium. The relatively low growth temperatures (600-700 °C) in MBE compared to other growth techniques allow a wide range of alloys to be synthesized even though they are rarely miscible under thermodynamic equilibrium. The UHV environment of MBE makes the real-time *in situ* surface characterization by reflection high energy electron diffraction (RHEED) possible. This measurement technique allows the grower to determine the surface mechanism and to atomically control the layer thickness by observing RHEED intensity oscillations.

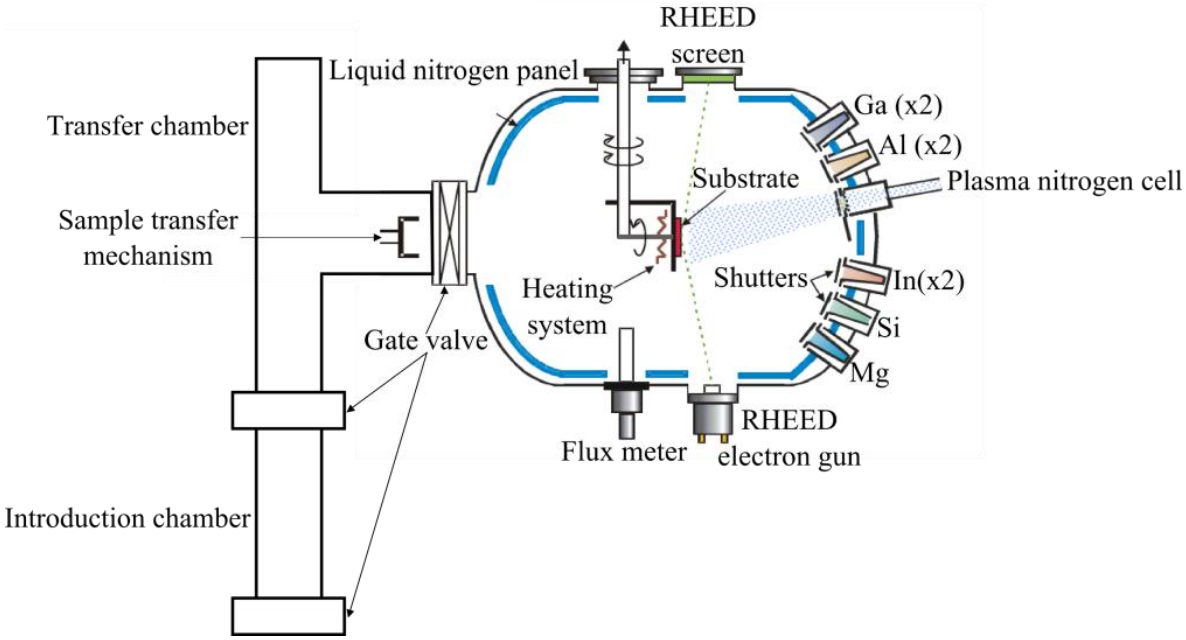

Figure 3.3: Schematic of the PA-MBE machine.

Figure 3.3 depicts the schematic of the plasma-assisted MBE (PA-MBE) used in this work. The system consists of 3 chambers, i.e. introduction chamber, transfer chamber and growth chamber. Samples are loaded into the system through the introduction chamber. The pressure of this chamber is normally kept ~10^{-8} Torr. While loading the samples into the system, the pressure of the introduction chamber is increased to atmospheric pressure by nitrogen gas, which keeps supplying during the transfer process to reduce the contamination that is coming from air atmosphere. The samples are transferred from the introduction chamber to the transfer chamber through a gate valve. The transfer chamber pressure is constantly kept in the 10^{-10} Torr range by an ionic pump. This chamber is used as a buffer between the introduction chamber that is often exposed to atmospheric pressure and the growth chamber that need to be kept in UHV conditions, since the structure synthesis is performed in the growth chamber. The fluctuation of the pressure may disturb the synthesis. The background pressure of the growth chamber is kept in the range of 10^{-10}-10^{-11} Torr by the cryogenic pump, the pressure rises to ~10^{-6} Torr during the deposition. Once the sample is transferred to this chamber, it is mounted onto a manipulator and is then adjusted to the growth position. During the growth, the substrate holder can be rotated in-plane to have a homogeneous deposition.

In the case of III-N PA-MBE, the metallic III elements (In, Ga, and Al) and doping elements (Si, Mg) are normally obtained from solid sources. In contrast, the nitrogen

molecules, N_2 cannot be thermally dissociated into mono-atomic nitrogen. Generally, there are two possibilities to create active N atoms, either by using radio-frequency plasma cell or NH_3 source. In the first case, the active N is produced by a dissociation of N_2 molecules which pass through a lightning of plasma generated by radio-frequency (RF) discharge. Hence, such system is called "plasma-assisted MBE". In the latter case, the active N atoms are created from NH_3 molecules in which the bound of nitrogen atom is weaker than that in N_2. GaN is obtained by reaction of NH_3 with Ga adatoms through a surface decomposition process shown in equation (3.8).

$$2NH_3 + 2Ga \rightleftharpoons 2GaN + 3H_2 \tag{3.8}$$

The presence of NH_3 on the surface can prevent GaN from dissociating and evaporating. As a consequence, GaN can be grown at higher temperatures than the one grown by PA-MBE. In our case, PA-MBE is selected for the growth of III-N nanostructures. The system is equipped with a radio-frequency (RF) plasma cell HD25 supplied by Oxford Applied Research, as illustrated in Figure 3.4. High purity N_2 is introduced into a pyrolytic boron nitride (PBN) cavity. The N_2 molecules are dissociated into active N atoms by the plasma, which is generated by inductively-coupled RF excitation. The stability of N atom flux is controlled by an optical feed-back loop.

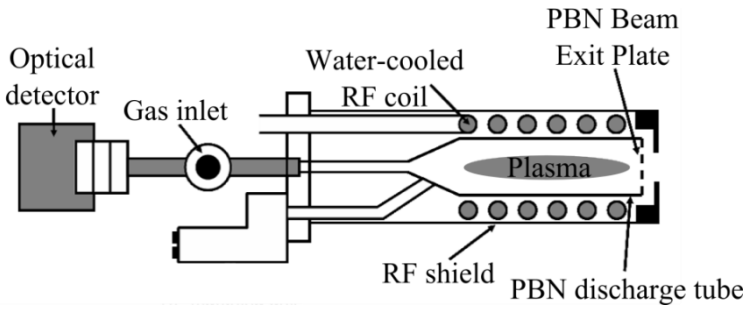

Figure 3.4: Schematic of the RF plasma cell mounted to PA-MBE system.

3.3 Reflection high energy electron diffraction

As PA-MBE growth is performed under UHV conditions, the system can be equipped with RHEED which allows *in-situ* and real-time monitoring the surface evolution. Figure 3.5 depicts the schematic description of the RHEED system. Electrons are generated by injecting current to a filament and then they are accelerated by high voltage (current = 1.5 A, acceleration voltage V = 32 kV in our system). The electron beam strikes on the substrate surface at a small grazing angle (2-3°). This driving voltage (V) determines the wavelength

of the electron (λ) as:

$$\lambda = \frac{h}{\sqrt{2m_0 eV(1 + \frac{eV}{2m_0 c^2})}} \tag{3.9}$$

The reflected and diffracted beams from the surface impinge onto the fluorescent screen and generate the interference pattern that corresponds to the reciprocal space view of the surface structure.

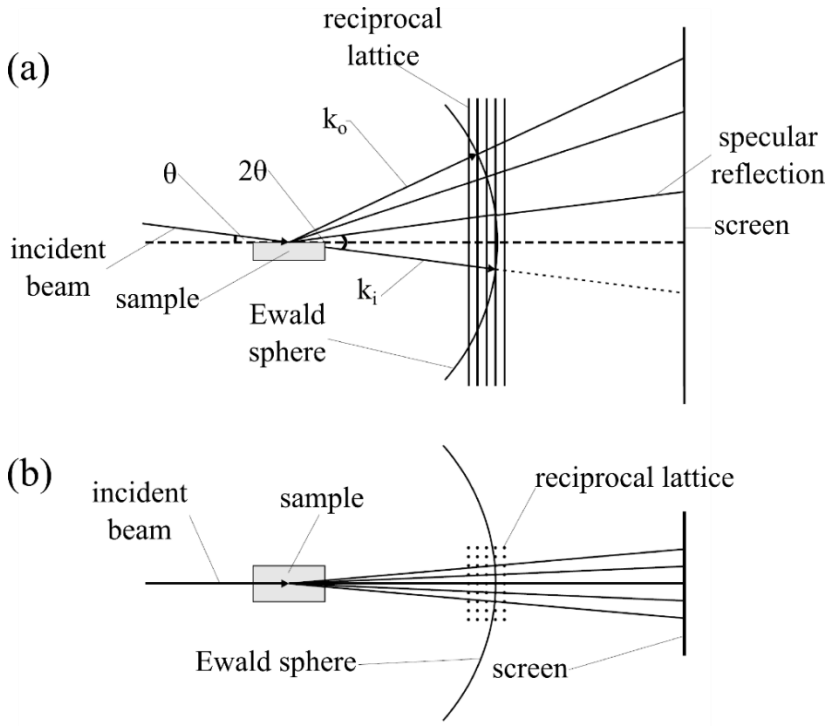

Figure 3.5: (a) Side-view and (b) Top-view schematic descriptions of the RHEED.

By analyzing the RHEED patterns, the following information can be extracted:

– *Determination of the in-plane lattice constant*. As illustrated in Figure 3.6, for a small incident angle, the in-plane lattice distance d_u is given by:

$$d_u = L\lambda/t \tag{3.10}$$

where L is the distance from the normal surface to the fluorescence screen, λ is the electron wavelength, and t is the horizontal distance between two fringes (or two arrays of spots) of the RHEED pattern. By this concept, we could *real-time* monitor the lattice parameter evolutions and deduce the strain relaxation process during the growth of strained layer.

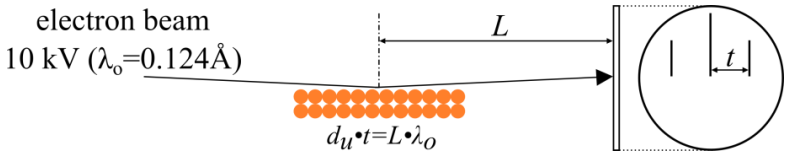

Figure 3.6: Schematic description of the procedure to determine the in-plane lattice constant.

– *Surface morphology*. The RHEED pattern is highly sensitive to the surface morphology and the crystal quality. However, the interpretation from the RHEED pattern towards different surface morphology is not easy due to the "non-idealities" which arise from both the substrate and the electron beam [115]. There are some common interpretations from the well-known patterns, such as the streaky pattern indicates an atomically flat surface, the spotty pattern that moves with the sample rotation indicates the roughness with large terrace size, and the stationary spot pattern indicates 3D growth.

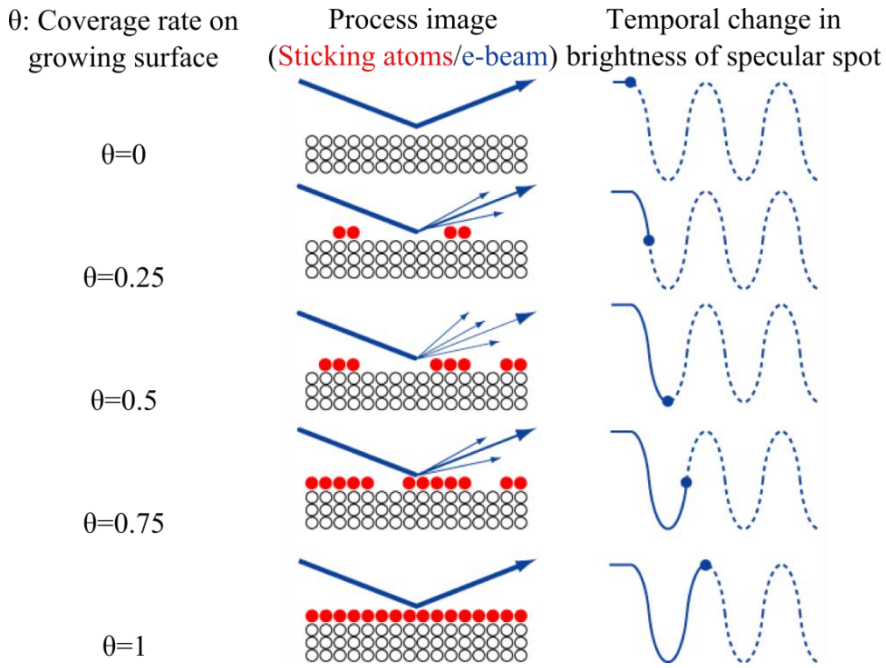

Figure 3.7: Schematic description of the procedure to determine the growth rate from the variation of the RHEED intensity.Red dots represent adatoms that form during the layer formation process, white dots represent adatoms in deep layers that are not involve in RHEED intensity, and blue arrows represent the electron beam that projects onto the surface.

– *Determination of the growth rate* [116]. The growth rate is defined from the coverage of 1 ML divided by the interval time spent from θ = 0 to 1 ML as shown in Figure 3.7. The RHEED intensity depends on the surface roughness. For a flat surface (coverage θ = 0 ML) the RHEED intensity is maximum. Then, the RHEED intensity decreases for incomplete coverage due to the electron diffusion and reaches a minimum intensity at

$\theta = 0.5$ ML, where the surface roughness is maximum. After that, the space between the nucleating sites gets filled, resulting in intensity recovering until $\theta = 1$ ML, where the intensity returns to maximum. In the case of III-nitrides, the fluctuation of the RHEED intensity is observed under nitrogen rich conditions where the growth occurs in layer-by-layer fashion, whereas under metal rich conditions, the mobility of the adsorbed species is much larger and the growth proceeds in the step-flow layer-by-layer mode. Thus, the RHEED intensity remains constant.

3.4 Plasma-assisted molecular beam epitaxy of III-nitrides

The PA-MBE growth of III-nitrides is performed under constant nitrogen flux which sets the maximum growth rate. The key parameters which control the crystal quality and the growth kinetics are the substrate temperature and the metal/nitrogen flux ratio. In this section, the growth of 2D GaN(0001), AlN(0001), and AlGaN(0001), zero-dimensional (0D) GaN/AlN QDs, one-dimensional (1D) GaN nanowires (NWs), and GaN/AlN NW heterostructures are presented, respectively.

3.4.1 Growth of GaN (0001)

The growth of GaN on GaN (0001) performed by PA-MBE at specific growth temperatures may result in various surface morphologies which drastically depend on the III/V ratio. As discussed in literatures [117]–[119], the GaN layer presents a facetted surface when the growth is performed under N-rich conditions. In order to achieve atomically flat GaN layers a certain Ga excess is required, i.e. the GaN growing surface must be covered by an adsorbed layer of Ga atoms. Figure 3.8 shows the Ga coverage as a function of impinging Ga flux, 4 regimes can be distinguished [117]:

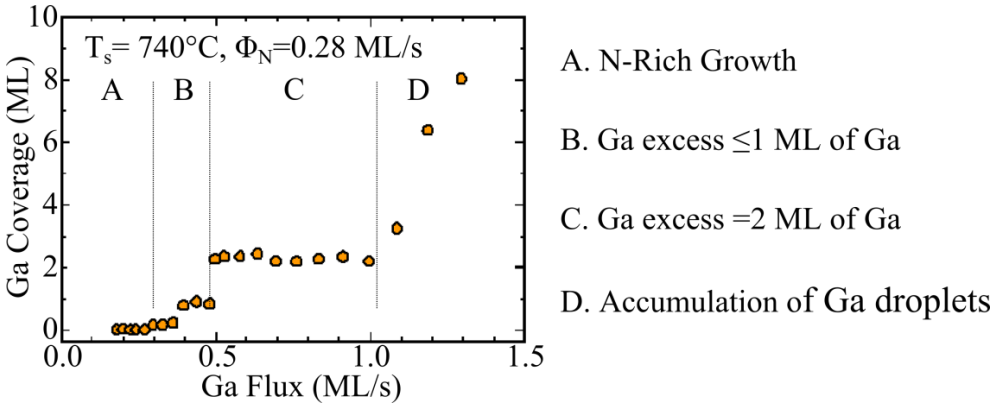

Figure 3.8: Ga coverage on top of the GaN (0001) surface as a function of the supplied Ga flux, measured at substrate temperature T_s=740°C and under N flux =0.28 ML/s [117].

- A: For Φ_{Ga} < 0.3 ML/s, the Ga coverage presented on the surface can be ignored.
- B: For 0.3 ML/s < Φ_{Ga} < 0.5 ML/s, there is >1 ML of Ga presented on the surface.
- C: For 0.5 ML/s < Φ_{Ga} < 1 ML/s, there are 2 ML of Ga presented on the surface.
- D: For Φ_{Ga} > 1 ML/s, the system reach the Ga accumulation regime, forming Ga droplets on the surface.

It is noteworthy that the above described experiment was performed at 740°C, since performing at different temperatures might affect Ga desorption characteristics and thus changing the stated boundaries, as illustrated in Fig. 3.9 [119].

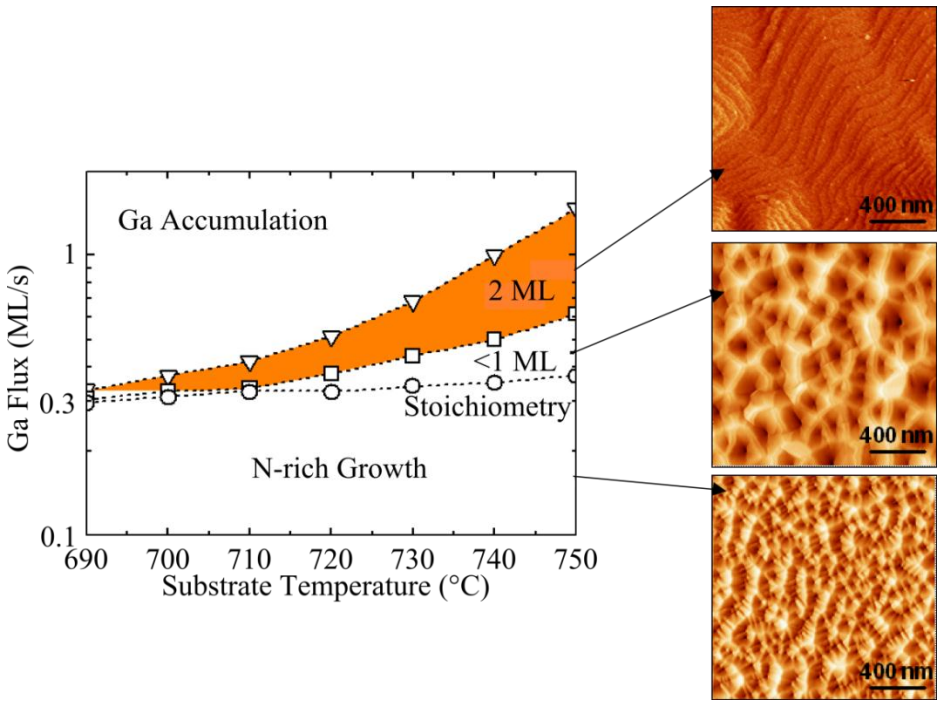

Figure 3.9: Ga coverage regimes as a function of both substrate temperature and impinging Ga flux. On the right side, AFM images of the surface of GaN layers grown at different values of Ga flux [119].

The benefit of the Ga excess becomes obvious in view of the morphology of the GaN surfaces grown with different Ga coverage, (see Figure 3.9). The AFM images show that if GaN is grown with a Ga coverage of less than 2 ML it presents a rough surface, whereas atomic steps can be seen when GaN is grown under Ga excess. The appearance of Ga bilayers reduces the (0001) surface energy thus favoring 2D growth. The 2 ML regime consists of two Ga layers on top of the Ga-terminated GaN(0001) surface [120], [121], following the laterally-contracted Ga bilayer model proposed [122] as shown in Figure 3.10.

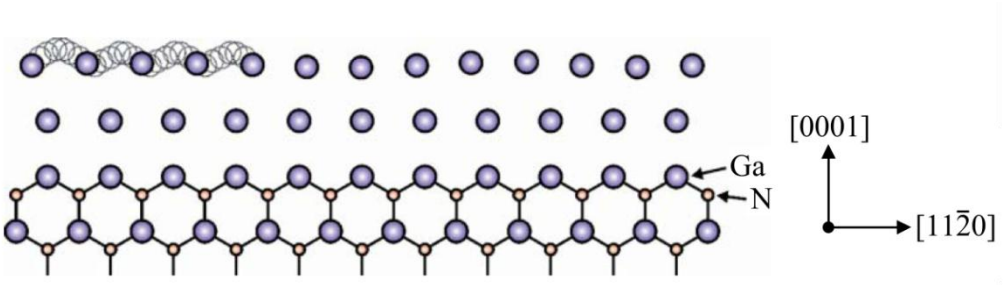

Figure 3.10: Schematic view of the laterally-contracted Ga bilayer model [122].

Even though a relatively large stability window for the Ga bilayer on the GaN surface can be obtained, the 2D growth of heterostructures requires identifying Φ_{Ga} at the transition between 2 ML of Ga coverage and Ga accumulation conditions, to prevent the formation of pits associated to threading dislocations [119], [123].

3.4.2 Growth of AlN (0001)

The growth of 2D AlN also requires metal-rich conditions as in the 2D GaN growth. At the standard growth temperature of III-N system (>800°C [124]), Al atoms do not desorb from the surface, thus causing Al excess condition. The excess Al can be noticed by the shadow lines in RHEED pattern taken along <11-20> azimuth occur, as shown in Figure 3.11. These shadow lines are an evidence of metal-Al, with reduced lattice constant in comparison to that of AlN. Since Al cannot desorb, in order to get rid of the excess Al, one needs to perform a growth interruption under N atmosphere, to capture excess Al forming AlN on the surface. The consuming time is an interval time from the closure of Al shutter until the shadow lines disappear. The time required to consume the excess Al can be used to calculate the Al cell temperature which provides Al:N stoichiometric growth conditions.

Since the Al-N binding energy is much higher than the Ga-N binding energy, it results in preferential Al-N incorporation in presence of Al, Ga, and N. This fact can be taken as an advantage when growing AlN at stoichiometry, by using the additional Ga flux as a surface

surfactant to improve mobility of adatoms at the growing surface, thus promoting a smooth surface morphology, without Ga incorporation into the AlN layer [125].

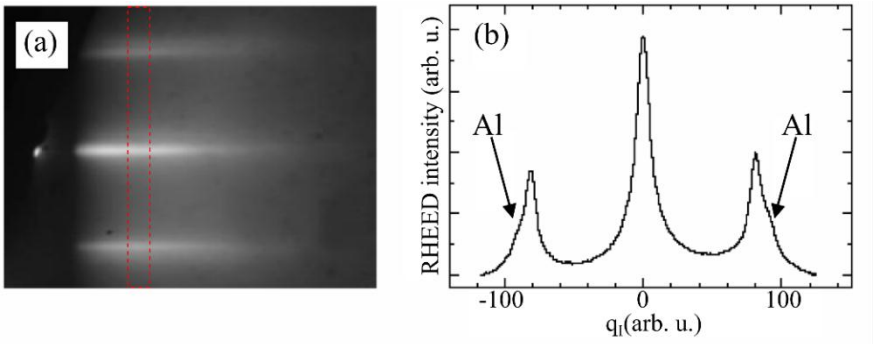

Figure 3.11: RHEED image of an Al-rich AlN surface (azimuth<11-20>). (b) Intensity profile along the <11-20> direction of the region delimited by a dashed rectangle in (a). The extra streaks due to the Al excess are indicated by the arrows.

3.4.3 Growth of AlGaN (0001)

Similar to the cases of GaN and AlN, the growth of 2D AlGaN requires metal-rich conditions [125], [126]. Some additional difficulties are triggered by the differences in Ga-N and Al-N binding energies, and in the mobility of Al and Ga adatoms on the growing surface. The strong Al-N bond allows Al to primarily incorporate in the AlGaN alloy, i.e. the sticking coefficient of Al is unity. This information can be applied to the growth of AlGaN, where the required Al content is calculated from the Al/N flux ratio, and an additional Ga flux is used to generate the metal excess to obtain the self-surfactant effect that favors 2D growth. However, all the explained procedure is valid only for low Al content regime (Al/N<0.4). For the high Al content regime, another parameter, i.e. substrate temperature (T_s), needs to be considered in order to maintain 2D growth. Decreasing T_s helps balancing the diffusion barrier between Al, Ga, and N. In addition, indium (In) can be added in the AlGaN system during the growth as a surfactant to smoothen the surface of AlGaN without incorporating in the AlGaN layer [125].

3.4.4 Growth of GaN/AlN quantum dots

As described in figure 3.2, the formation of a 3D structure requires an enhancement of the (0001) surface energy to favor the relaxation by faceting instead of creating dislocations. The means to achieve high (0001) surface energy are either to perform a growth interruption in vacuum to evaporate the metal excess or to grow under N-rich conditions.

a) *Ga-rich GaN QDs*: GaN QDs can be achieved by depositing them in Ga-rich conditions followed by a growth interruption in vacuum [127]–[129]. In this method, a GaN layer is grown under Ga excess ($\Phi_{Ga} > \Phi_N$) under the Frank-van der Merve growth mode, then the layer re-arranges into 3D nanostructures due to the increase in (0001) surface energy when the Ga excess is evaporated. The high mobility of adatoms when growing under Ga-rich conditions results in low density (10^{10}-10^{11} cm^{-2}) and large (2-5 nm high) GaN QDs as illustrated in Figure 3.12.

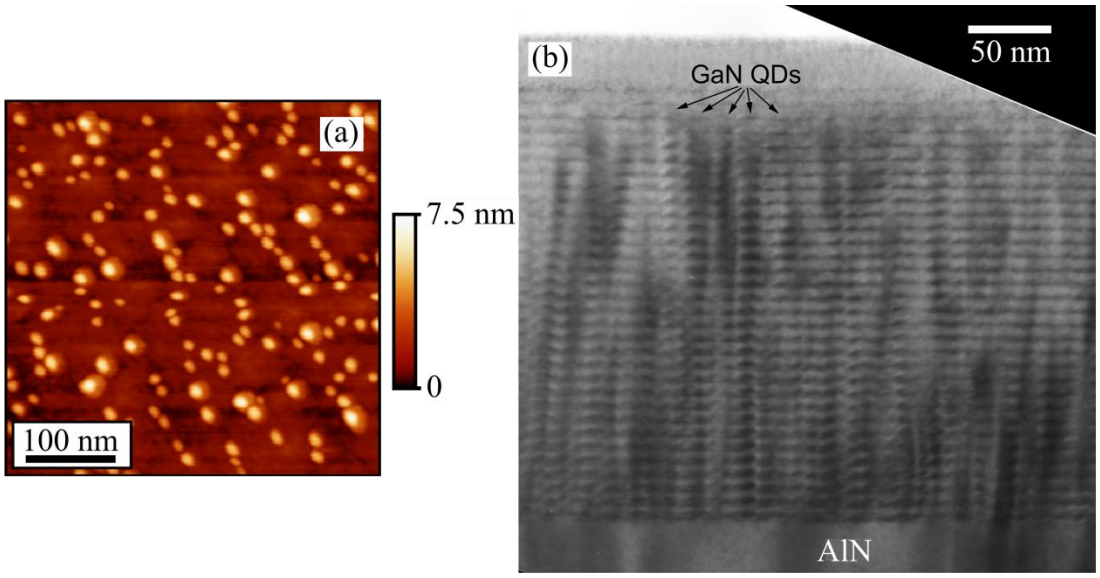

Figure 3.12: (a) Typical AFM image [130] and (b) Cross-section TEM bright-field image of GaN QDs grown under Ga-rich conditions (TEM image from Prof. Ph. Komninou, Aristotle University of Thessaloniki).

b) *N-rich GaN QDs*: GaN QDs under N-rich conditions can also be achieved [131], since a III/N flux ratio < 1 increases the surface energy of the (0001) plane [120]. Hence, the growth favors the formation of 3D faceted structures. Under these conditions, the growth starts 2D until the deposition of a ~2-ML-thick wetting layer (critical thickness). Further depositing GaN leads to the formation of 3D islands via the Stranski-Krastanov growth mode [54], [131]. N-rich growth implies a low mobility of adatoms which results in a high density (10^{11}-10^{12} cm^{-2}) and small (1-2 nm high) GaN QDs as illustrated in Figure 3.13.

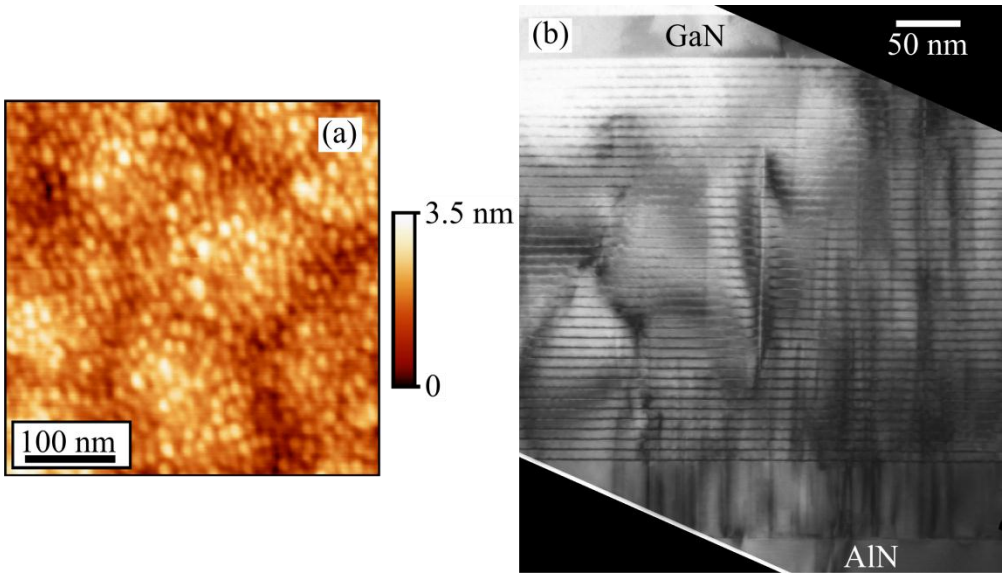

Figure 3.13 (a) Typical AFM image [130] and (b) Cross-section TEM bright-field image of GaN QDs grown under N-rich conditions (TEM image from Prof. Ph. Komninou, Aristotle University of Thessaloniki).

3.4.5 Growth of GaN nanowires

III-nitride NWs have recently emerged as a promising structure for novel optoelectronic applications owing to their advantages. For instance, NWs possess reduced dislocation density due to the efficient elastic relaxation through their free surface [132]. One dimensional structure of NW could enhance the light extraction efficiency because of the waveguide effect [133]. NW heterostructuring offers an alternative pathway to synthesize zero dimensional nanostructures, and simplicity to perform band gap engineering. In addition, modulating electrical conductivity can be achieved by adjusting impurities along the nanowire axes. The flexibility of material combination in nanowires also opens the way to integrate high quality semiconductor materials on low cost mainstream Si technology. Utilizing the mentioned superior features, the prototype of several nanowire based devices have successfully demonstrated, e.g. light emitting diodes, lasers or photodetectors [134]–[137].

To synthesize NWs, vapor-liquid-solid (VLS) catalyst-induced or catalyst-free approaches can be used. The NW growth via VLS mechanism was first demonstrated by Wagner *et al*. [138] for the growth of Si NWs in 1964. They used Si contained ($SiCl_4$) *vapor* as a source which reacts at the *liquid* catalyst-substrate (Au-Si) interface. The chemical reaction leads to the formation of a *solid* Si wire. The advantage of the VLS growth is that

the diameter and the density of the NW can be adjusted by controlling those parameters of the catalyst. This mechanism has been used widely in the NW synthesis of III-V (MBE: [139]–[141], MOVPE: [142]–[145]), and II-VI compounds (MBE: [146]–[149], MOVPE: [150]–[152]). For the catalyst-induced NWs, there are various metal catalysts which can be used as an initiator such as Ni, Fe and Au [139], [143]–[145]. Lately, Geelhaar *et al*. [139] presented the MBE growth of Ni induced GaN NWs (Figure 3.14). Ni seeds were sputtered onto a *c-plane* sapphire substrate and used as a catalyst to induce the NW formation. The NW growth occurred at the interface between the supersaturated Ni droplets and the substrate via the VLS process. However, the presence of catalyst could induce unwanted contaminations in the NWs because of the metal catalyst diffusion, causing a difficulty to adjust the electrical conductivity via doping. The problem concerning the contamination in NWs can be avoided by using catalyst-free growth.

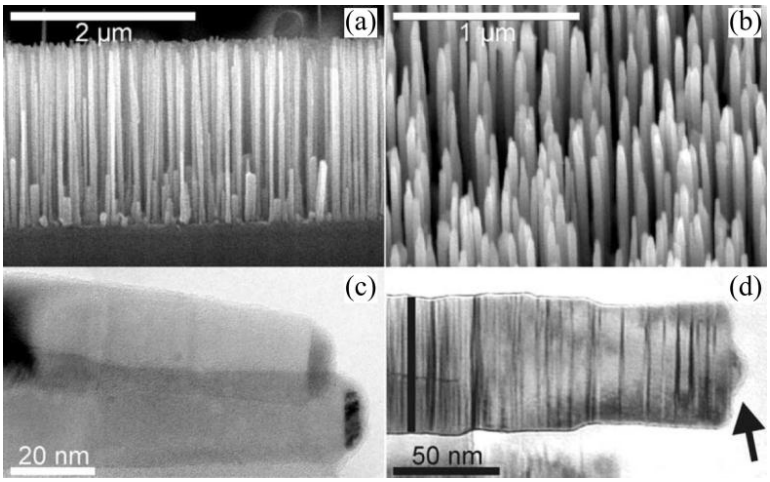

Figure 3.14: Ni-induced GaN NWs grown by MBE on sapphire. Scanning electron microscopy images that were acquired at an angle of (a) 90° and (b) 45° normal to the surface. (c) Cross-sectional transmission electron microscopy (XTEM) image of two NWs. (d) XTEM image of a NW that resulted from Ga-rich growth after initially N-rich growth. The seed particle is indicated by an arrow. The vertical lines across the NW are attributed to stacking faults [139].

Catalyst-free GaN NWs can be synthesized by using various growth techniques. For examples, Koester *et al*. reported that the growth of catalyst-free GaN NWs by MOVPE was achieved on *c*-plane sapphire substrates [153]. In this case, a thin SiN_x layer (~2 nm) was created prior to the NW growth in order to favor GaN seed nucleation and assist the vertical growth of GaN NWs. PA-MBE is another technique which allows the formation of catalyst-free GaN NWs on both sapphire [154], [155] and Si(111) substrates [156]. The latter substrate is highly of interest because of its compatibility with the electronic industrial mainstream.

The growth of GaN NWs by PA-MBE can be achieved by direct depositing Ga and N fluxes onto Si(111). However, this growth process possibly generates amorphous SiN_x [157], which might lead to the formation of disoriented GaN NWs. A thin AlN buffer layer was reported to assist the vertically alignment of the wires [158]. Songmuang *et al*. [158] demonstrated an improvement of the vertical orientation of GaN wires after inserting a thin AlN layer on Si(111) substrate prior to the NW growth. This is attributed to a favorable formation of AlN in a presences of Al, N, and Si [159] due to the higher binding energy of Al-N than that of Si-N. For PA-MBE, the key parameters to synthesize the GaN NWs are III/N flux ratio (Φ_{Ga}/Φ_N) and substrate temperature. As described in section 3.4.4, Ga-rich conditions ($\Phi_{Ga}>\Phi_N$) promote 2D growth whereas N-rich conditions ($\Phi_{Ga}<\Phi_N$) would introduce 3D growth which is a basis of the SK QDs and NWs formation [160]–[162]. In addition to the N-rich conditions, relatively higher temperature than those used for 2D growth is also mandatory for the NW formation [158], [162].

In this thesis, GaN NWs are grown by depositing Ga and N fluxes in N-rich conditions on Si(111) substrate at various flux ratios and growth temperatures. As the flux calibration is presented (see 3.3), here, I present the Si(111) substrate temperature calibration by measuring the Ga desorption time from the substrate surface. This calibration method provides a better reproducibility of the growth temperature than by using a thermocouple, since it is the measurement of physical dynamics on the substrate surface.

Before introducing Si(111) into PA-MBE system, it was chemically degreased to eliminate contamination, and was dipped in HF 5% for a few minutes to remove native oxide from the surface. In the growth chamber, the Si(111) substrate was heated ~800°C (thermocouple temperature) for ~30 min to thermally clean the surface. The cleaned surface was proved by (7×7) reconstruction as illustrated in Figure 3.15(c), which is generally observed at 600-850°C [163]–[165].

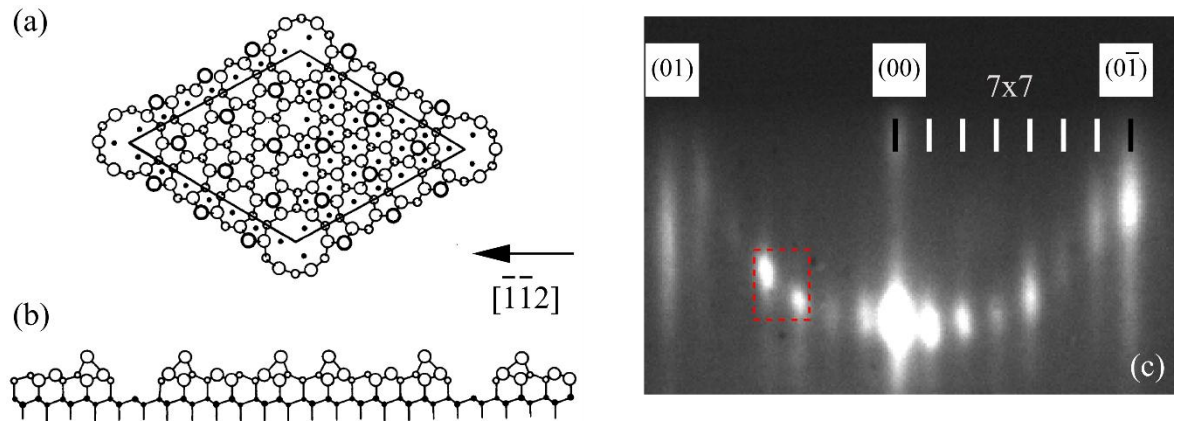

Figure 3.15: (a) top view and (b) side view of the Si(111) (7x7) reconstruction [166]. (c) 7x7 surface reconstruction observed by RHEED along [-1-12] azimuth.

Takayanagi *et al*. [166] proposed the orientation of Si atoms on the topmost surface as shown in Figure 3.15(a) and (b). The periodicity of the topmost surface orientation is 7 times larger than that of the bulk Si atoms. Thus, the reconstruction pattern of the topmost surface periodicity is 7 times smaller than the pattern of bulk Si atoms. The RHEED pattern of the topmost surface is displayed in Figure 3.15(c), the black marked lines correspond to the periodicity of bulk Si atoms while the white marked lines (7 times narrower in width to that of the black marked lines) correspond to the topmost atoms which form the reconstruction.

In order to calibrate the growth temperature, the evolution of RHEED intensity was recorded from the red rectangular delimited area in Figure 3.15(c) during the deposition of Ga flux. Exposing the surface to Ga results in the abrupt drop of RHEED intensity at $t = 0$ s in Figure 3.16(a). When the Ga shutter was closed after 10 s of Ga deposition, Ga adatoms would desorb from Si(111) surface, leading to the recovery of the RHEED intensity. The time required for the RHEED intensity recovering can be used as a reference for the temperature calibration since the Ga desorption rate depends on the substrate temperature.

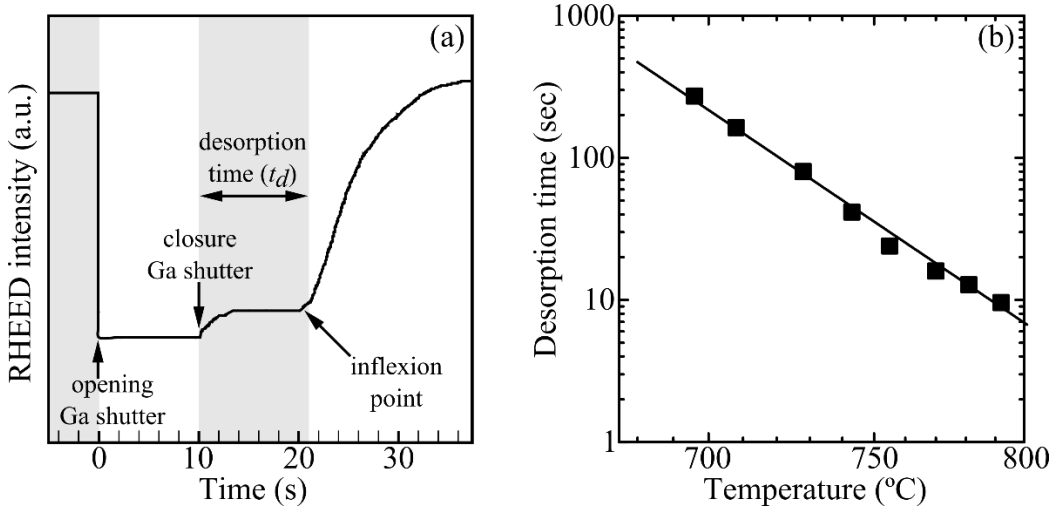

Figure 3.16: (a) RHEED intensity recovery profile taken at the red rectangular delimited area in Figure 3.15(c). At time t=0s, the Ga shutter is opened, at t=10s, the Ga shutter is closed. The interval time between the closure of the Ga and the first inflexion point is defined as the Ga desorption time. (b) Substrate temperature (measured by the thermocouple in contact with Si(111) wafer as a function of Ga desorption time).

Figure 3.16(a) presents the evolution of the RHEED intensity taken at the area defined by a red rectangle in Figure 3.15(c). The desorption time (t_d) is defined as the time interval between the closure of Ga shutter (at t = 10s) and the inflexion point. The desorption time corresponds to the time spent of Ga adatoms for desorbing from the surface, which is strongly affected by the substrate temperature.

Figure 3.16(b) shows evolution of the desorption time as a function of substrate temperature which was measured by thermocouple. The accuracy of the plot was assured by averaging few calibration sets. As exhibited, the desorption time exponentially decays with linearly increasing of the substrate temperature, described by Arrhenius relationship for the temperature reproducibility. Ga desorption calibration was performed prior the growth on Si(111) for every sample. Then, the growth temperature is found using the plot shown in Figure 3.16(b).

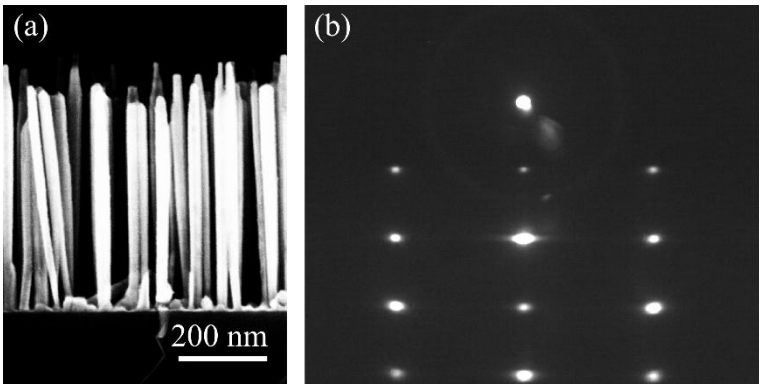

Figure 3.17: (a) SEM image of GaN nanowires grown on thin AlN layer on Si(111) substrate and (b) their corresponding RHEED pattern.

In this manuscript, GaN NWs are used as a starting point for studying the growth of $Al_xGa_{1-x}N$ sections and $Al_xGa_{1-x}N$/AlN NDs grown on GaN NWs. The GaN NWs grown by PA-MBE were synthesized by using the same method over the entire manuscript. Prior to the growth of GaN NWs, a thin AlN (~0.5nm) was deposited at T_s = 840°C (corresponding t_d = 2 s) in order to suppress the SiN_x formation. Subsequently, T_s was decreased to 795°C (corresponding t_d = 8 s) to grow GaN NWs under N-rich conditions (Φ_{Ga}/Φ_N ~0.5) for 2.5 hours. The presence of NW structure was confirmed *in*-situ by RHEED. The general structure of GaN NWs and its corresponding RHEED pattern are shown in Figure 3.17(a) and Figure 3.17(b), respectively.

The formation of GaN NW can be described into two major steps, namely the nucleation and the NW growth. Several teams have suggested that NWs develop from GaN islands at the initial stage of the deposition, and then transform into wire-like structure [158], [161], [167], [168]. During the nucleation stage, the density of NWs increases rapidly to $>10^{10}$ cm^{-2} [169]. The wire nucleation was elaborately studied by Consonni *et al*. [168]. They reported the structural evolution observed by high-resolution TEM, describing how GaN 2D metastable nuclei [170] evolve to truncated pyramids with {1-103} side facets (Figure 3.18(b)), to full pyramids (Figure 3.18(c)), and to NWs (Figure 3.18(d)). The shape transition to truncated pyramids with {1-103} side facets which are the facets mentioned in SK GaN QDs, is attributed to their smaller surface energy compared to the {0001} planes [171], [172]. The shrinking of the {0001} top facet and the progresses of the {1-103} lateral facets are due to the minimization of the free energy per unit volume [173], [174] of the structure, resulting in the shape transition from the truncated pyramids to full pyramids. Further deposition of GaN triggers the plastic relaxation process and then promotes the NW growth [175].

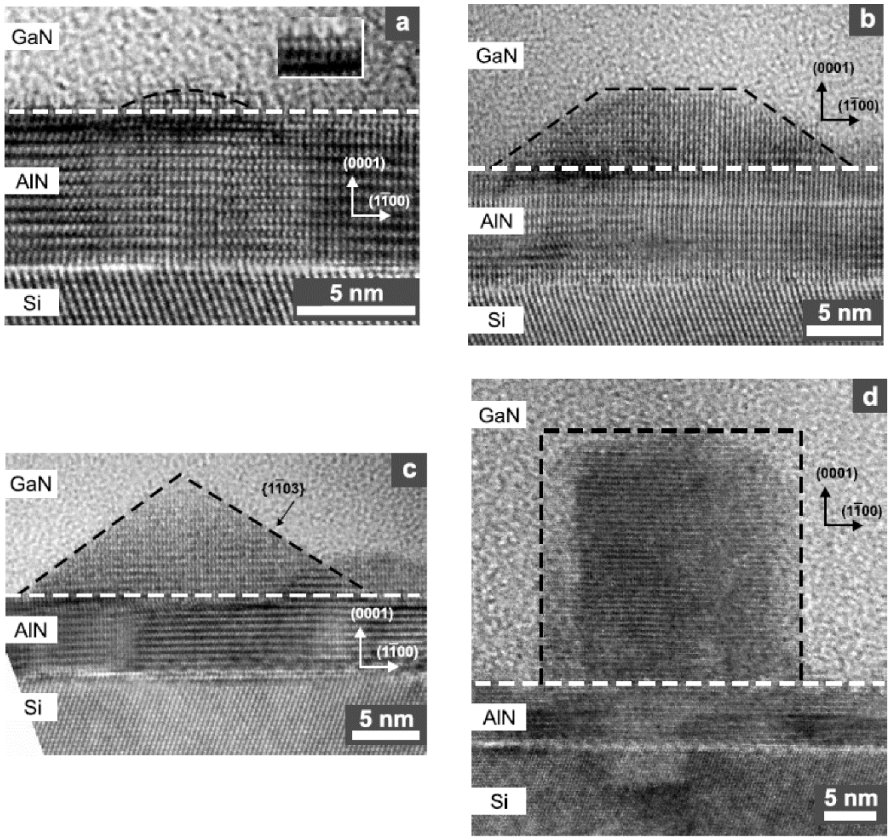

Figure 3.18: High-resolution TEM images collected on dedicated samples grown during 4.5, 6, 9, 10, and 15 min, revealing the following respective GaN island shapes at the onset of the nucleation process: (a) spherical-cap-shaped island with an inset representing a high magnification of the first AlN monolayers at the interface, (b) truncated-pyramid-shaped island, (c) full-pyramid-shaped island, and (d) NW [168].

After the nucleation stage, it was found that the deposited material only increases the volume of each NW, i.e. only enlarges the NW diameter and length. The growth behavior of III-N NWs was studied using a marker technique. Figure 3.19(a) depicts a scanning TEM (STEM) image of the GaN NWs (dark contrast) with AlN marker layers (bright contrast). The evolution of the GaN growth rate in NWs ($R_{GaN,NW}$) as a function of Ga cell temperature (T_{Ga}) was plotted as a green line in Figure 3.19(b). The 2D growth rate (R_{2D}) deduced from RHEED oscillation was plotted in comparison shown in Figure 3.19(b). The grey line (black line) represents the R_{2D} measured at 745°C (790°C).

Figure 3.19(b) shows 2 different growth regimes of GaN NWs. For the first regime (T_{Ga} < 940°C), $R_{GaN,NW}$ is systematically higher than R_{2D}. This observation evidences that besides the Ga atoms that impinged to the wire top, there are contributions of Ga diffusing along the NW sidewalls to the vertical growth. In principle, Ga adatoms can diffuse in any direction with different diffusion lengths depending on the diffusion barriers set by the potential

energy surface distribution along the different crystallographic axis. The theoretical work of Lymperakis *et al*. suggests that only Ga adatoms adsorbing at the sidewall in a proximity to the top of the NW are able to participate in the axial growth [176]. Those atoms which can reach the NW top can be easily incorporated due to the larger number of adatom adsorption sites at the NW top (*c*-plane) in comparison to the sidewall (*m*-plane). The NW growth could occur when these two contributions (the direct deposition and the diffusion) overcome the Ga desorption and GaN dissociation processes which are significant at the high growth temperatures.

For the second regime, the $R_{GaN,NW}$ saturates at the value close to the N-limited value, pointing out that only the N atoms impinged on the NW participate in the wire growth. On the other hand, the N diffusion can be neglected. This fact agrees with theoretical work which shows that the diffusion barrier of N atoms is higher than that of Ga atoms [177].

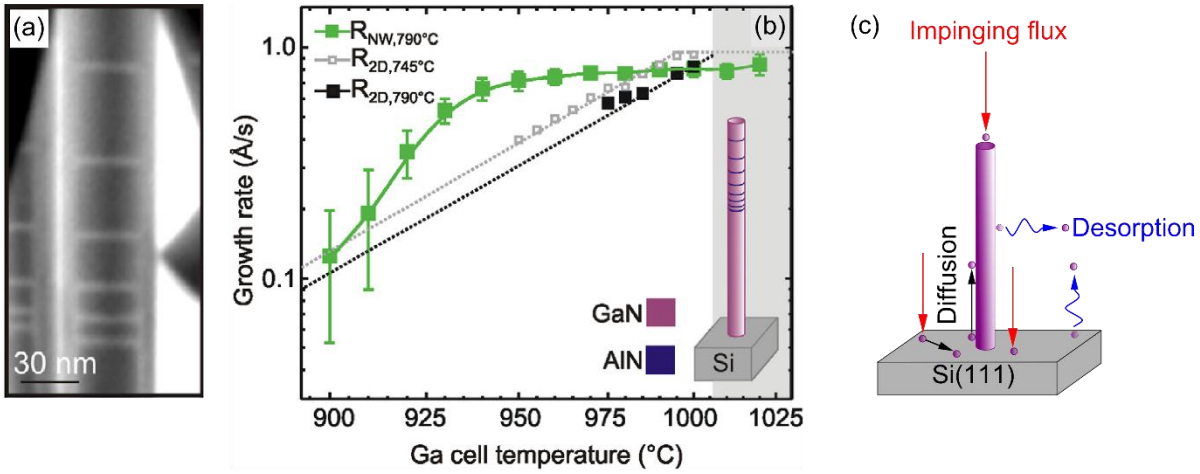

Figure 3.19: (a) STEM image of GaN with AlN marker layers. The Ga flux was progressively increased before depositing (black contrast) among AlN thin marker layer (white contrast). (b) Growth rate comparison between GaN in NWs ($R_{GaN, NW}$) growth at T_{sub} = 790°C and that in a 2D layer ($R_{GaN, 2D}$) as a function of T_{Ga}. $R_{GaN, 2D}$ was measured at T_{sub} = 745 and 790°C. The grey shading represents the regime where the impinging Ga flux is higher than the active N flux at T_{sub} = 790°C. The inset of (b) is a schematic illustration of the sample shown in (a) [178]. (c) Schematic of the MBE growth process of NWs in which the relevant processes, such as adsorption, desorption, and diffusion are included.

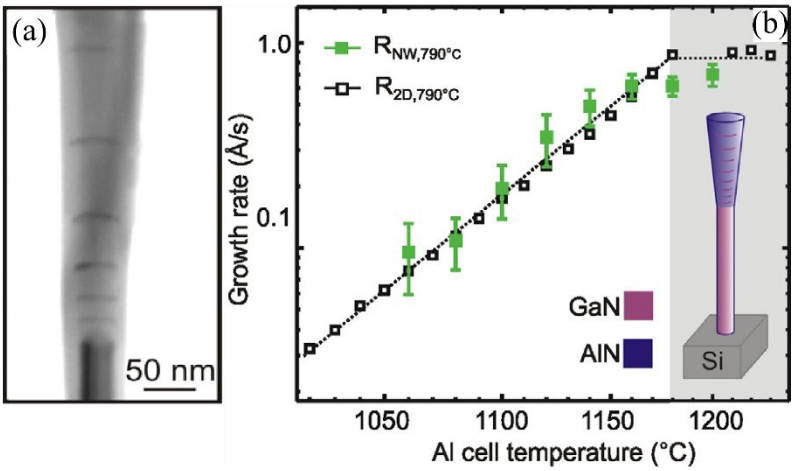

Figure 3.20: (a) STEM image of AlN with GaN marker layers. The Al flux was progressively increased before depositing (white contrast) among GaN thin marker layer (black contrast). (b) Growth rate comparison between AlN in NWs ($R_{AlN,\ NW}$) growth at T_{sub} = 790°C and that in a 2D layer ($R_{AlN,\ 2D}$) as a function of T_{Al}. R_{2D} was measured at 790°C. The grey shading represents the regime where the impinging Al flux is higher than the active N. The inset of (b) is a schematic illustration of the sample shown in (a) [178].

This section describes the growth of AlN in NWs which was studied by using the marker technique in order to further apply for NW heterostructuring. Figure 3.20(a) shows STEM image of AlN (bright contrast) with GaN (dark contrast) grown on top of GaN NW. The wire shows a cone-like shape with gradually increasing diameter from ~30 to ~200nm. This shape suggests a non-negligible lateral growth of AlN. The AlN growth rate ($R_{AlN,NW}$) was obtained by averaging 20 wires measurements. Then the evolution of $R_{AlN,NW}$ as a function of Al cell temperature (T_{Al}) was plotted (green squares) in Figure 3.20(b) in comparison with 2D growth rate (R_{2D}) which was deduced from RHEED oscillation at the same growth temperature (black dash line). In contrast to the growth of GaN NWs, $R_{AlN,NW}$ and R_{2D} of AlN are similar at different T_{Al} as displayed in the figure. Most of the Al and N atoms which arrive at the top and sidewall of the NWs would directly incorporate to the NWs. The different growth behavior between AlN and GaN in NWs is due to the shorter diffusion length of Al atoms in comparison to Ga atoms at the wire growth temperatures [169], [178].

3.4.6 Growth GaN/AlN NW heterostructures

The understanding of GaN and AlN NW growth is considered as a basis for the fabrication of NDs and superlattices in NWs. In catalyst-free growth, by switching the deposition of GaN and AlN on the NWs results not only in material alternation along the wire axis but also in the formation of a radial heterostructures around the GaN NWs [169],

[178]. However, the superlattices of GaN/AlN grown by MBE are mostly reported in an axial direction [178]–[181]. The difficulty to implement the radial GaN/AlN heterostructures is because of the high NW density (>10^{10} cm^{-2}) [158], which induces a shadowing effect, preventing the lateral deposition on the NW sidewall [182], [183].

Despite the difficulty, *Carnevale et al.* [184] demonstrate a possibility to produce both vertical and coaxial GaN/AlN heterostructures on GaN NWs as illustrated in Figure 3.21. The vertical heterostructures were achieved by the alternation of Ga and Al fluxes [178]–[181], whereas the coaxial heterostructures were achieved by reducing the NW density to suppress the shadowing effect. Subsequently, GaN/AlN heterostructures were deposited at low growth temperature to minimize the diffusion of group III materials from the surface.

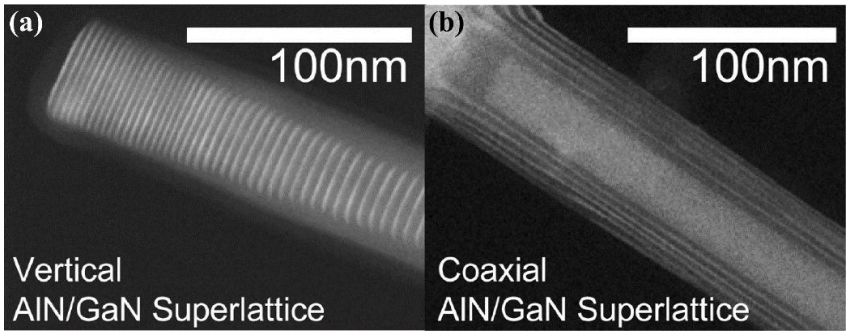

Figure 3.21: STEM images of three-dimensional GaN/AlN heterostructures. (a) Fifty-period vertically-aligned GaN/AlN superlattice. (b) Five-period coaxially-aligned GaN/AlN heterostructures [184].

3.5 Substrates

Today GaN substrates are commercially available. However, the target of this thesis being AlN/AlGaN nanostructures, AlN substrates would be the more adequate choice. Bulk AlN exists in the market, but its crystalline quality is not compatible with homoepitaxial growth by MBE. Therefore, growth needs to be performed on foreign substrates. The selection of substrate for III-N heteroepitaxy should be made by considering the parameters such as lattice constant, thermal expansion coefficient, requirement of III-N epilayer orientation, defect density, purity. Possible choices of substrate which can be provided for the growth of III-N are sapphire-, Si(111)-, and SiC-based substrates. The lattice constants and thermal expansion coefficients of GaN, AlN and their possible substrates are illustrated in Table 3.1. In the case of conventional SK QDs, there are two types of substrate that we used, i.e. GaN and AlN on sapphire while III-N NDs on GaN NWs were grown on Si(111).

	Space group symmetry	Lattice constant (Å)	Thermal expansion coefficient ($x10^{-6}$ K^{-1})
GaN	$P6_3mc$	*a*=3.189, *c*=5.185 [45]	3.34, 3.43 [185]
AlN	$P6_3mc$	*a*=3.112, *c*=4.982 [45]	3.48, 4.35 [185]
Al_2O_3	R3*c*	*a*=4.7589, *c*=12.991	7.3, 8.5
Si	Fd-3m	5.431	2.6
6H-SiC	$P6_3mc$	*a*=3.0806, *c*=15.1173	4.46, 4.16

Table 3.1: Space group symmetry, lattice constants, and thermal expansion coefficients for substrate materials (Al_2O_3, Si, SiC) comparing to those of epitaxial layer (GaN, AlN) [46].

3.5.1 Sapphire-based substrates

The sapphire (α-Al_2O_3) structure can be described using either a rhombohedral unit cell as shown in Figure 3.22 or a hexagonal unit cell. By using the hexagonal unit cell, the lattice parameters are *a*=4.765 Å and *c*=12.982Å. The growth of GaN or AlN epitaxial layer on *c*-plane sapphire results in *c*-plane oriented film with in-plane orientation of 30° respect to the sapphire(0001) substrate to reduce the lattice mismatch between the epitaxial layer and the sapphire (13.9%). The epitaxial GaN layer can also be grown on *a*-plane sapphire [11], [186] which results in the lower lattice mismatch (2%). However the *c*-axis of GaN film grown on an *a*-plane sapphire has a non-zeroinclenation, thus crystal twinnings, which is one of the lattice deformations, might generate in the structure. This is the main disadvantage of an *a*-plane comparing to *c*-plane sapphire substrates. The *a*-plane (11-20) AlN or GaN can be produced by growing the epitaxial layer on *r*-plane (1-102) sapphire [187]. By growing GaN or AlN films on (10-10) *m*-plane sapphires, the grown layers could have (10-10), (10-13), or (11-22) orientations, depending on the growth technique and growth conditions [188]–[190].

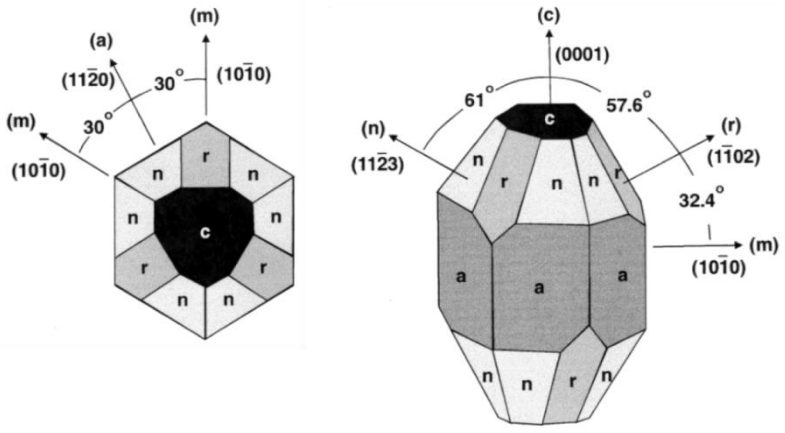

Figure 3.22: Rhombohedral structure and surface planes of sapphire [46].

The sapphire-based substrates used in this thesis are separated into two templates, i.e. GaN(0001)-on-sapphire and AlN(0001)-on-sapphire templates. The GaN(0001)-on-sapphire

templates are supplied by LUMILOG, consisting of 4-µm-thick GaN on *c*-sapphire grown by MOCVD with a dislocation density of ~10^8 cm^{-2}. The AlN(0001)-on-sapphire templates are supplied by DOWA consist of ~1µm-thick AlN deposited by MOCVD on *c*-sapphire with a dislocation density ~10^9 cm^{-2}. Atomic force microscopy (AFM) images as illustrated in Figure 3.23 reveal the atomically flat surface of GaN (Figure 3.23 (a)) and AlN (Figure 3.23 (b)) templates.

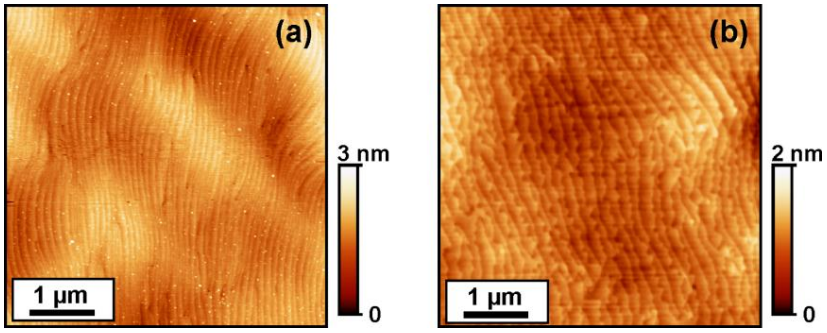

Figure 3.23: AFM images of (a) the GaN-on-sapphire and (b) the AlN-on-sapphire templates.

3.5.2 Si(111)-based substrates

Silicon is widely used in mainstream semiconductor electronic industry since it has many advantages, e.g. low prices, large scale productions support, and good thermal/electrical conductivity. The common crystal structure for Si substrate is a diamond structure with a lattice parameter, a_{si} =5.431 Å as illustrated in Figure 3.24. Its (111) surface presents a hexagonal geometry which can be compared with hexagonal system, that is $a_{Si}^{hex} = \frac{a_{Si}\sqrt{2}}{2} = 3.840$ Å and $c_{Si}^{hex} = a_{Si}\sqrt{3} = 9.407$ Å.

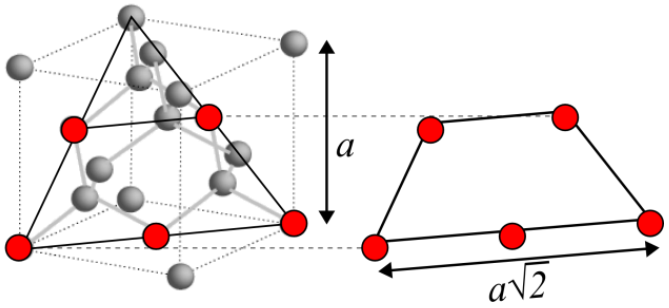

Figure 3.24: Silicon diamond crystalline structure compare with hexagonal structure.

Using Si(111) as a substrate for III-nitride materials has faced many challenges. The greater thermal expansion coefficient than the one of III-N materials induces a strain

generating cracks during the cooling down process. Furthermore, the Si(111) surface exhibits 17% lattice mismatch to GaN and 19% lattice mismatch to AlN. As a result, the defect density of III-N-on-Si templates is significantly higher than the one grown on sapphire or SiC. Hence, we mainly used sapphire-based substrates for the growth of 2D III-nitride materials. On the other hand, Si(111) substrate is used for particular geometries of nanostructures where the differences of lattice parameters do not degrade the crystal quality, such as the growth of NWs.

3.5.3 SiC-based substrates

4H-, 6H-SiC configurations can be used as a substrate for III-N system because of their comparable lattice *a* parameter to that of AlN. The higher thermal conductivity of SiC than sapphire-based substrate, thus providing a better heat dissipation, is another interesting parameter driving the use of SiC-based substrate for III-N system. However, the main factor that limits the wider use of SiC is the high cost of these substrates.

3.6 Characterization techniques

Two major properties of nanostructures, i.e. structural and optical properties were investigated. The structural characterizations were performed using X-ray diffraction (XRD), scanning electron microscopy (SEM), and Atomic Force Microscopy (AFM) whereas the optical characterizations were performed using Photoluminescence (PL), Time-resolved PL Cathodoluminescence (CL), and Fourier Transform Infrared spectroscopy (FTIR).

3.6.1 X-ray diffraction

X-ray diffraction (XRD) is a versatile structural characterization technique which is an indispensable method to determine composition, crystal orientation, strain state, grain size, and crystal quality. XRD utilizes the constructive interference of monochromatic x-ray diffracted by the crystalline structure. The beam-sample interaction produces the constructive interference of the diffracted x-ray at specific angles which satisfy Bragg's Law:

$$2d \sin\theta = n\lambda \tag{3.11}$$

where n (an integer) is the order of reflection, λ is the wavelength of the x-rays, d is the interplanar spacing of the reflecting planes, and θ is the angle of the incidents which are

specified only some angles. There are no signals perceived by the detector for all the other angles that undergo destructive interference. The interplanar spacing of the crystal, d can be obtained from the eq. (3.11) after specifying the angle, θ.

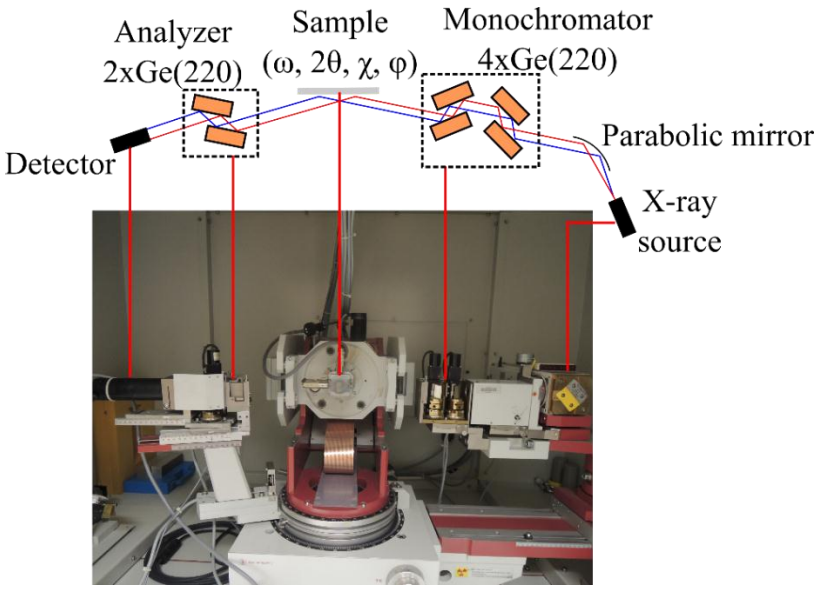

Figure 3.25: Illustration of the X-ray diffraction system used in this work.

XRD measurements in this study were performed on a Seifert XRD 3003 PTS system, illustrated in Figure 3.25, which uses the Cu $K_{\alpha 1}$ wavelength (λ=0.154056 nm). XRD consists of three parts: an x-ray beam generator, sample holder (goniometer), and x-ray detector. X-rays are generated by applying an accelerating high voltage (15-60 kV) to accelerate the electrons that are released from a hot cathode. These electrons subsequently collide with a metal target (anode) and create x-ray emission. The emission beam is reflected by a parabolic mirror to transform into parallel beam and increase its intensity by one order of magnitude. The beam passes through two monochromators (each of them consists of two mounted Ge(220) monocrystals, thus they are called "4-crystal" scheme) for reducing the angular and wavelength divergences of the beam. The improved resolution of the beam after passing through the monochromators is $\Delta\theta$=0.0033° and $\Delta\lambda/\lambda=1.4\text{x}10^{-4}$.

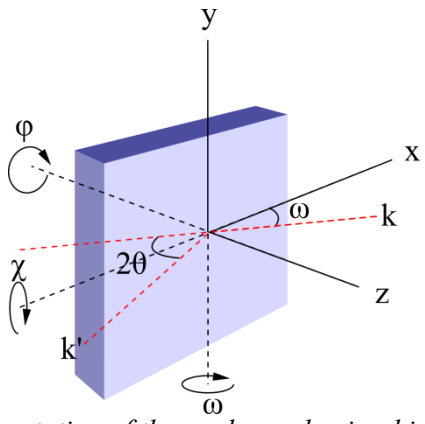

Figure 3.26: Schematic representation of the angles and axis which allow positioning the sample.

The x-ray beam is injected into the sample which is mounted on a goniometer (sample holder), allowing us to select the plane family of orientation. The goniometer can independently rotate in 4 angles, i.e. ω, 2θ, φ, and χ, as shown in Figure 3.26. The angle ω is the angle between the incident x-ray beam and the surface, 2θ is the angle between the incident beam and the reflect beam from the surface, φ is the rotate angle around z-axis, and χ is the rotate angle normal to z-axis. For each reflection, we can measure *ω, 2θ, ω-2θ* scans or a 2D scan around a reflection i.e. a 2D map of the reciprocal space.

The detector has an aperture of ≤2°. The slits might be inserted in order to improve the resolution of the diffracted beam which results in decreasing the aperture and thus decreasing the signal. For high resolution XRD measurements, an analyzer (two pieces of Ge(220) monocrystals) is placed between the sample and the diffracted beam to improve the angular precision of the diffracted beam (≤0.001°).

3.6.2 Atomic force microscopy

Atomic force microscopy (AFM) is one type of scanning probe microscopies, which is used for probing the surface morphology of the sample. As no current flow is needed, in contrast with scanning tunneling microscopy, AFM can be used for characterizing the surface of various types of samples, i.e. conductors, semiconductors, and insulators. Figure 3.27(a) depicts the schematic of AFM setup. The bending of the cantilever, which is proportional to the force on the cantilever, is measured by the deviation of a laser beam position on the detector. The applied force is kept constant by a feedback circuit by changing the tip-sample distance using piezoelectric actuator which also drives the lateral movement of the measured sample.

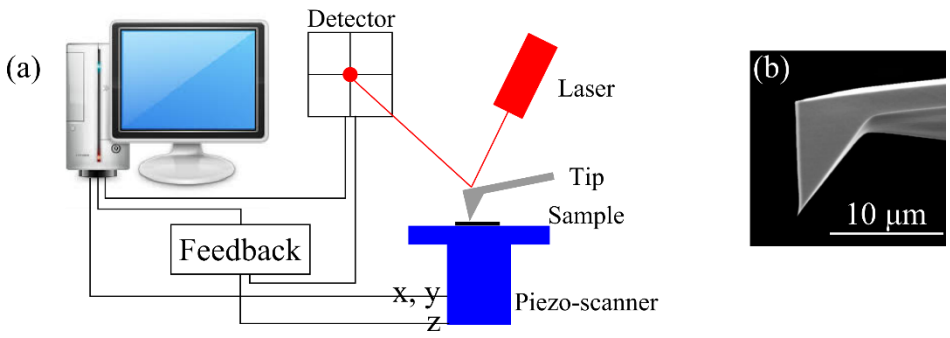

Figure 3.27: (a) Schematics of an AFM system, (b) AFM tip.

The AFM tip, illustrated in Figure 3.27(b), has a couple of microns length and less than 100 Å-diameter. The AFM tip and cantilever are fabricated from Si or Si_3N_4. The type and magnitude of the interaction force between the tip and the sample directly depend on the distance between the tip and the sample [191]. Thus, the variation of the interaction force between the sample and the tip mirrors the variation of the surface height; that is, the surface morphology.

The AFM can be operated in 3 different modes, which are contact, non-contact, or tapping mode, as illustrated in Figure 3.28 and described below:

1. *Contact mode*: The measurement is done by keeping the repulsive force constant. In this mode, the cantilever is kept very close to the surface (few angstroms above the surface) throughout the measurement hence the measurement is done with huge frictional and adhesive forces that can damage the sample surface and distort the measured image.
2. *Non-contact mode*: The interaction force between the surface and the tip in this mode is attractive Van der Waals force which is a force occurring when the distance between the sample and the tip is in the order of ten to hundreds of angstrom. In this mode, the cantilever can oscillate with large amplitudes near the tip resonance frequency. Thus, the non-contact mode measurement typically provides low resolution and the measured image can be hampered by the natural oscillations. However, it is very useful for measuring the morphology which is soft or liquid.
3. *Tapping mode*: This mode combines the advantages of the contact and non-contact mode. In this mode, the force between the surface and the tip is kept near "0" to avoid the surface damage problems, occurring in the contact-mode and to provide better resolution than that performed by the non-contact mode. This mode was used to measure all the samples in this thesis.

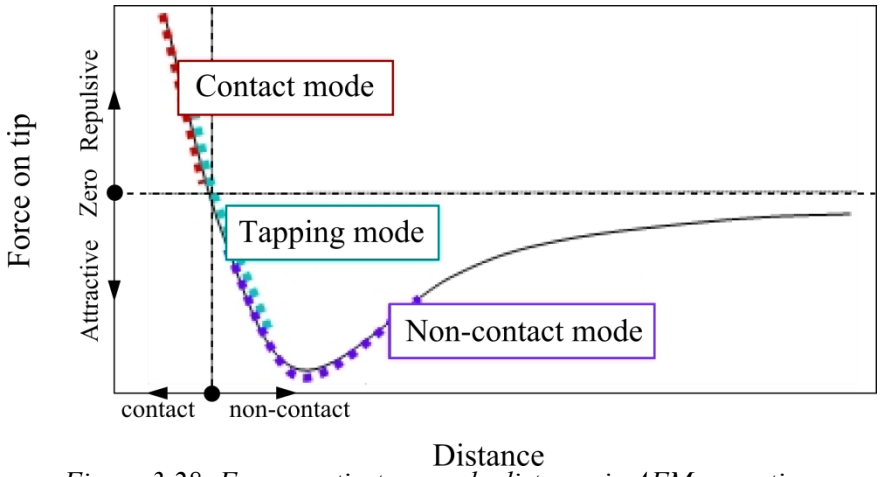

Figure 3.28: Force vs. tip-to-sample distance in AFM operation.

In tapping mode, the tip operates near its resonant frequency, ω_0. The high resonance frequency ($\omega_0 >> 1$kHz) is advantageous, since it allows us to decouple the tip oscillating frequency from the low-noise frequency induced by the mechanical vibrations. ω_0 is defined with:

$$\omega_0 = \sqrt{k/m} \tag{3.12}$$

where k and m are the force constant and the mass of the tip. When the tip is close to the surface (<100 angstrom), it exposes to a Van der Waals interaction gradient. This gradient affects to the resonance frequency of the tip, that is:

$$\omega = \omega_0 \sqrt{1 - \frac{1}{k}\frac{\partial F}{\partial z}} \tag{3.13}$$

In this mode, the oscillating amplitude (the tip-sample distance) is kept constant using a piezo-electronic actuator and a PID regulator to minimize the force gradient, $\frac{\partial F}{\partial z}$. The minimal detectable force gradient is given by [192]:

$$\frac{\partial F}{\partial z} = \frac{1}{A}\sqrt{\frac{4B\kappa k_B T}{\omega_0 Q}} \tag{3.14}$$

where A is the root mean square oscillation amplitude, B is the detection bandwidth, and $Q=\Delta\omega/\omega$ is the quality factor of the resonance. Hence there are four main parameters to optimize the sensitivity. The force constant (κ) should be small which requires the minimization of the cantilever mass while the quality factor of the resonance (Q) should be high. Measuring at low temperature is usually preferred. In addition, the oscillation amplitude (A) which is limited by the experimental setup should be large.

The spatial resolution of AFM measurement depends on the shape and size of the tip. The actual tip that is not ideally sharp might generate the effect called “tip-evolution” which consequently differentiate the measured image and the real topology of the object. The convolution occurred when the radius of the tip is comparable with or larger than the size of measured object [193]. As shown in Figure 3.29, where the semi-spheres represent the tips and the trapezoids represent the islands. The diameter of the island, which measured from Figure 3.29(a), is larger than the real island size whereas the heights of the islands, which measured from Figure 3.29(b), are shorter than the real island height due to the convolution effect. The accurate convolution of the tip is hard to compensate since the effective tip shape might change during measurements. Furthermore, the influencing factors affected to the resolution are the non-linear response of the piezo-scanner and environmental noise interference.

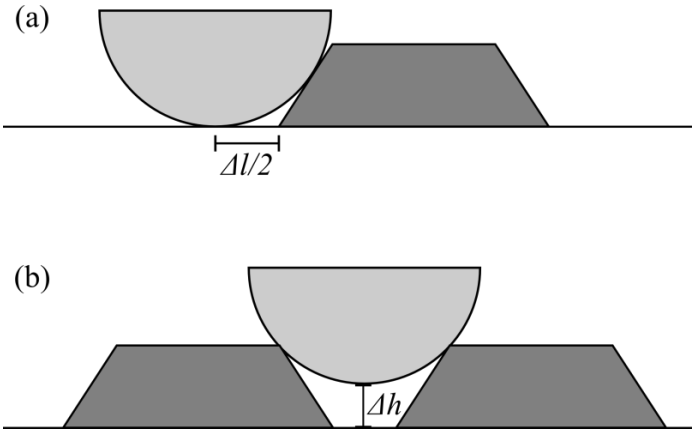

Figure 3.29: (a) Increase of lateral island size with respect to the real island size and (b) Decrease of the island height when two islands are closer to each other than the tip diameter.

3.6.3 Scanning Electron Microscopy

Scanning electron microscopy (SEM) is an imaging magnification which results from the measuring of secondary electrons while the specimen is scanned with an electron beam. The interaction of the electron beam with the specimen results in the generation of a number of secondary particles, for example secondary electron, backscattered electrons, x-rays, photons and phonons (heat) as illustrated in Figure 3.30. The secondary electrons are most valuable for showing morphology and topology of the specimen whereas the backscattered electrons are most valuable for imaging contrasts in composition in a multi-phase specimen. The process of photon measuring when the specimen is excited by electron beam, is called cathodoluminescence (CL, which is explained in 3.6.4)

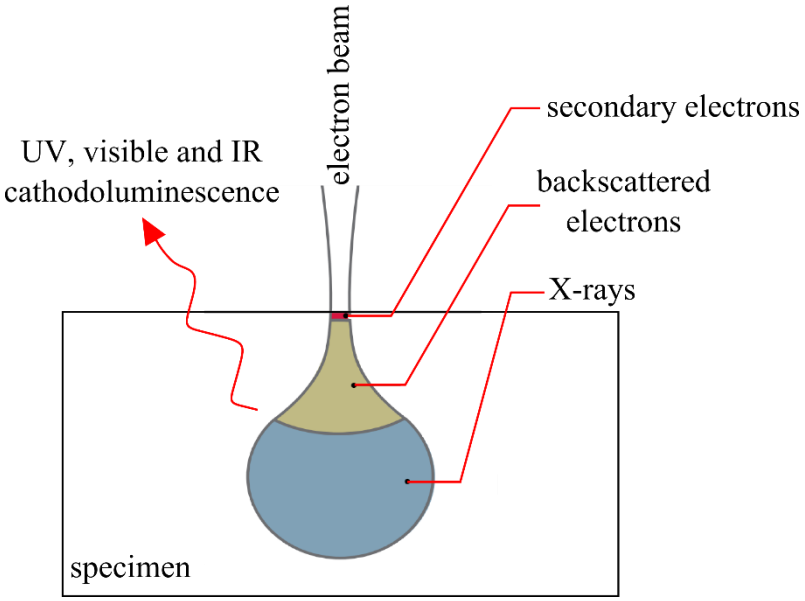

Figure 3.30: Signals that result from electron beam-specimen interaction [194].

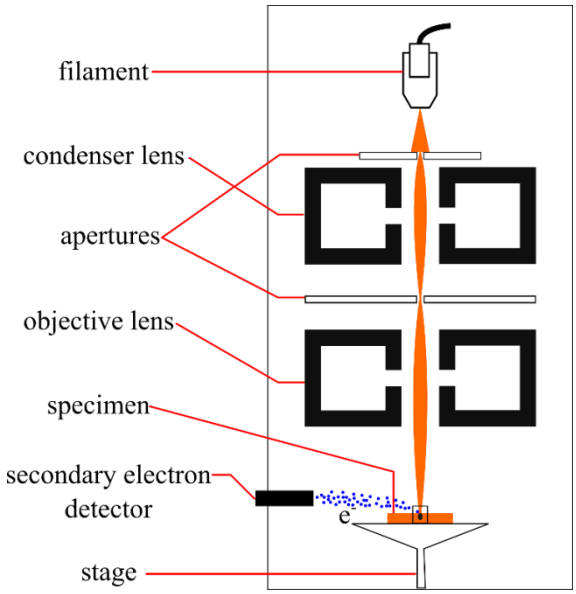

Figure 3.31: (a) Schematic diagram of an SEM.

Figure 3.31(a) illustrates the schematic of SEM. Electron gun is located at the top of the column where free electrons are generated by a tungsten filament, and an acceleration voltage projects them onto a specimen. The electron beam is converged by condenser lens, which focus the beam into a small aperture which determines spot size of the electron beam. Decreasing spot size would provide a better resolution [195]. The scanning system is processed by rastering the electron beam across the specimen. Only secondary electrons, resulted from inelastic collision and scattering of incident electrons, are attracted to the detector by a positive charge. Since the SEM is regarding the characteristics at and near the

surface of the specimen, as displayed in Figure 3.30, an acceleration voltage < 50 kV is utilized for revealing the surface of the material with a resolution better than 10 nm [194], allowing magnification of the image from 10× to 100,000×.

3.6.4 Cathodoluminescence spectroscopy

Cathodoluminescence (CL) is the process of the light emission resulting from the electron injection (0.2-30 kV) into the material, which is one of the generated signals via this excitation method as illustrated in Figure 3.30. CL has a wide variety of applications since its system can be assembled with electron imaging techniques. The advantage of CL over photoluminescence (PL) is the small size of electron beam (in the order of 100 nanometers), which allows us to characterize a very specific area of a sample. By varying the electron beam energy, the volume of excitation especially along the depth can be changed.

The CL is known to be an above band gap excitation method, that is all the materials within the excitation volume is excited no matter how much the band gap energies are, differing from the PL where the excitation laser can excite some parts in the materials which have the band gap energies lower than the excitation photon whereas the other part remains transparent. For instance, to measure PL of GaN/AlN SLs, the excitation laser (E_{photon} = 5.08eV, in our case) can excite only GaN (E_g = 3.51 eV [72]) while AlN (E_g = 6.23 eV [72]) let photons passing through.

In our study, CL characterization is performed on FEI quanta 200. An aluminium parabolic mirror is placed between the sample stage and the electron beam pole as illustrated in Figure 3.32. The electrons pass through the hole in the parabolic mirror and then penetrate into the sample which is placed at the focal point of the mirror. The mirror reflects the emission from the sample into a parallel beam which is focused onto a Jobin Yvon HR460 monochromator. The monochromator scans over a specific range to project photons on to a detector. There are 2 detectors equipped to the monochromator, i.e. charge-couple device (CCD) camera and photomultiplier tube (PMT) detector. The CCD camera is used to acquire photons as a function of wavelength that is changed by the grating in monochromator. The PMT is used to obtain the CL intensity mapping at one specific wavelength by synchronizing it to the raster electron beam.

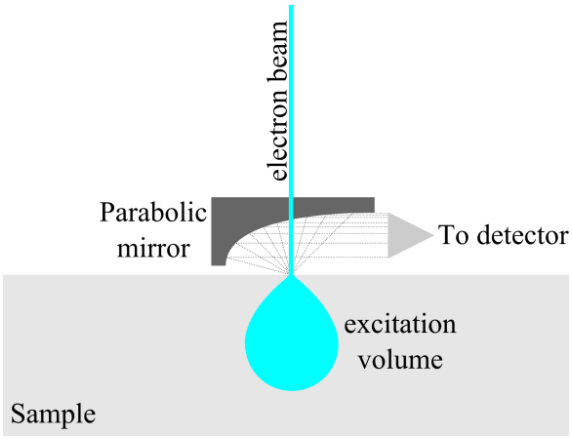

Figure 3.32: Schematic representation of the detection of light with the parabolic mirror from the CL system.

3.6.5 Photoluminescence spectroscopy

PL spectroscopy is a method to measure the light emission induced by excitation and recombination of electron-hole pairs, as depicted in Figure 3.33. Incoming photon energy must exceed the band gap energy (E_g) of semiconductor to allow material to absorb (process-(a)) and create an electron-hole pair. The excess excitation energy holes and electrons will thermally relax to the edges (**process-(b)**) of conduction and valence bands, respectively by releasing the energy in the form of longitudinal optical (LO) phonons. The direct recombination (**process-(c)**) occurs as the electron recombines to the hole in the valence band, giving a photon with specific energy (approximately equal to the E_g). In addition to the free exciton recombination, there are other processes, namely donor bound (**process-(d)**), acceptor bound (**process-(e)**), and donor-acceptor pair (**process-(f)**). These processes can emit photons, resulting from additional donor band (E_d) and acceptor band (E_a) appear in the band diagram. The E_d and E_a can either unintentionally appear because of the impurities /the lattice defects or they can be intentionally generated by doping. The recombination of electron hole pairs does not necessarily lead to the photon emission. Non-radiative recombination to the mid-gap level (E_t) (**process-(g)**) is another relaxation path via phonons, i.e. the heating of the crystal. The origin of mid-gap level might attribute to vacancies, dislocations, impurities, or surface dangling bonds.

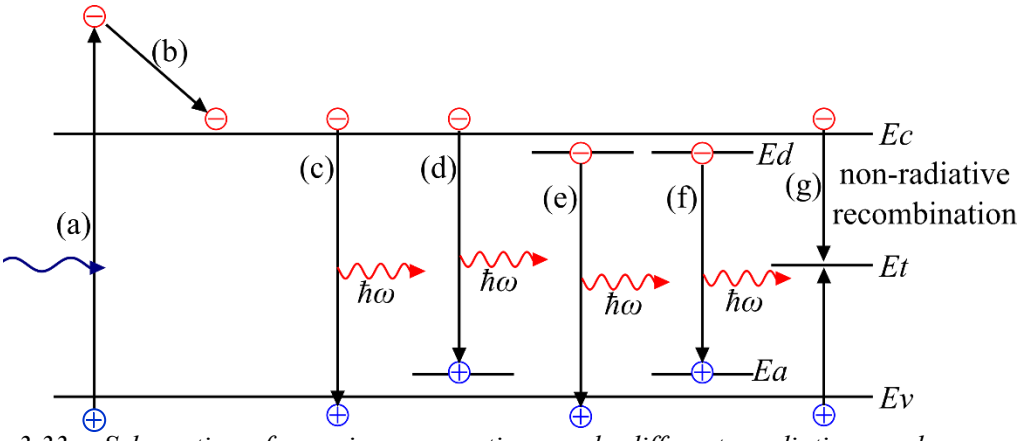

Figure 3.33: Schematic of carrier generation and different radiative and non-radiative recombination paths in semiconductors.

Time-resolved PL (TR-PL) is also used in our experiments to measure decay times which provide information about the nature of transition in the material. TR-PL is a method where the sample is excited with a light pulse and then the intensity of photoluminescence as a function of time is recorded. At low temperature where the non-radiative processes are suppressed, the luminescence decay time is, thus, associated to the radiative decay time. This decay time provides information concerning the overlapping of the electron and hole carrier distribution in the conduction and valence band. Furthermore, the evolution of the decay time as a function of temperature would also provide knowledge of the temperature where the non-radiative recombination processes start playing a role on decay time, hence giving the localization efficiency of the structure.

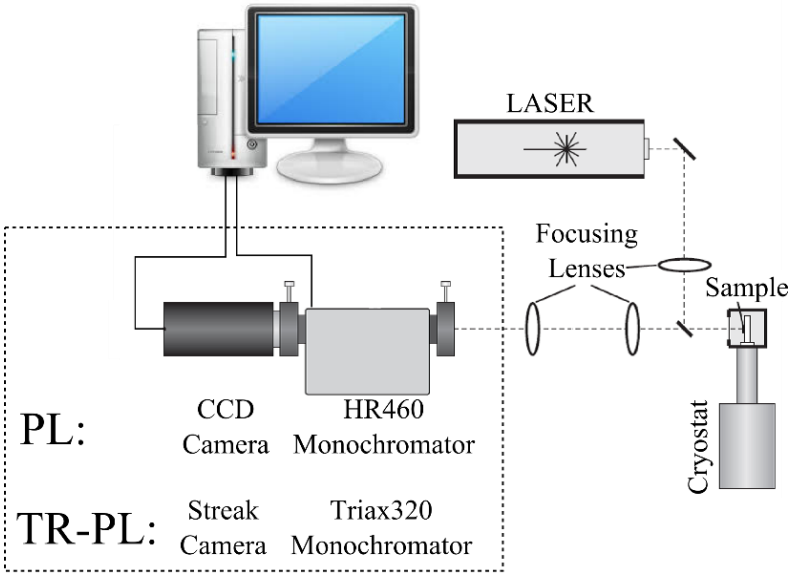

Figure 3.34: (Time-resolved) photoluminescence setup

Figure 3.34 shows the PL setup used in this work. The excitation source is frequency-doubled continuous wave Ar+ laser (λ=244 nm). After exciting the sample which is placed in the cryostat, the photon emission was collected by focusing lenses to project on a Jobin Yvon HR460 monochromator equipped with a UV-enhanced CCD camera. For the time-resolved PL (TR-PL) setup, the schematic is quite similar to that shown in Figure 3.34. the excitation source is a frequency-tripled Ti:sapphire laser (λ=270 nm) with pulse width of 200 fs and repetition rate that can be adjusted in the range of 0.9-76MHz. The luminescence from the sample was dispersed into a Triax320 monochromator and was detected by a streak-camera using a 2.2 ns window, giving a system response of about 25 ps, allowing us to characterize the measured signal in both frequency (*x*-axis) and time (*y*-axis) aspects.

3.6.6 Fourier Transform Infrared Spectroscopy

Fourier transform infrared spectroscopy (FTIR) is an optical measurement used for measure transmission or absorption characteristics of the material as a function of wavelength in the infrared (IR) region with a very fast scan rate due to the specific design of excitation source. A very fast scan rate is achieved by the allowance of simultaneously measuring all of the IR frequencies, without progressively scan the sample characteristic as a function of IR wavelengths, but by encoding a various frequencies into an encoded interferogram and use it as an excitation object. The source-interferogram excitation signal is created using the Michelson interferometer (Figure 3.35(a)), which consists of a beam splitter, fixed mirror and moving mirror. As the moving mirror travels back and forth, various wavelengths of beam go in and out of phase, which provide a specific interferogram as illustrated in Figure 3.35(b).

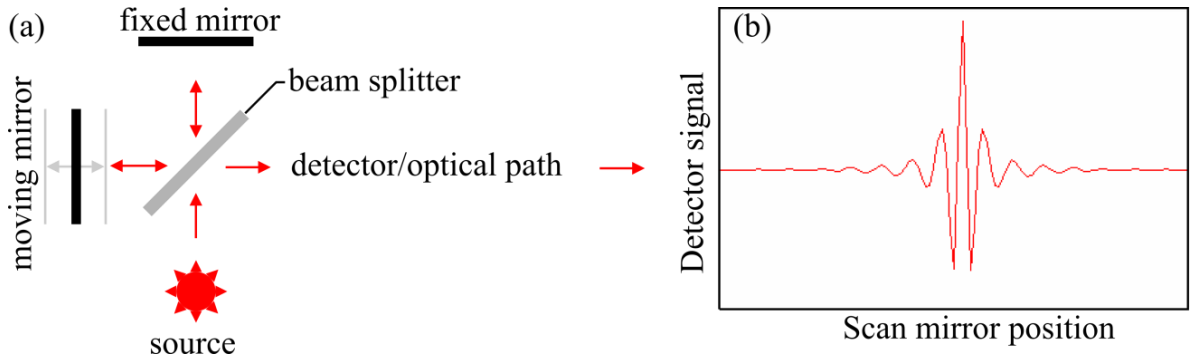

Figure 3.35: (a) Schematic of the interferometer. (b) Interferogram obtained by the detector.

The source-interferogram passes through the characterized material, which changes the characteristic of interferogram due to the absorption/transmission characteristic of the material, and projects onto the specific detector for interferogram measurement. After the output interferogram is detected, the analysis cannot be instantly performed from the obtained interferogram. The signal is digitized and is Fourier transformed to frequency domain, resulting in an IR absorption/transmission spectrum. For instance, the Fourier transform of the detected interferogram in Figure 3.35 (b) with no sample on the sample compartment give a spectrum as in Figure 3.36, which shows many absorption lines due to presence of molecules which exist in atmosphere, such as H_2O, CO_2, ….

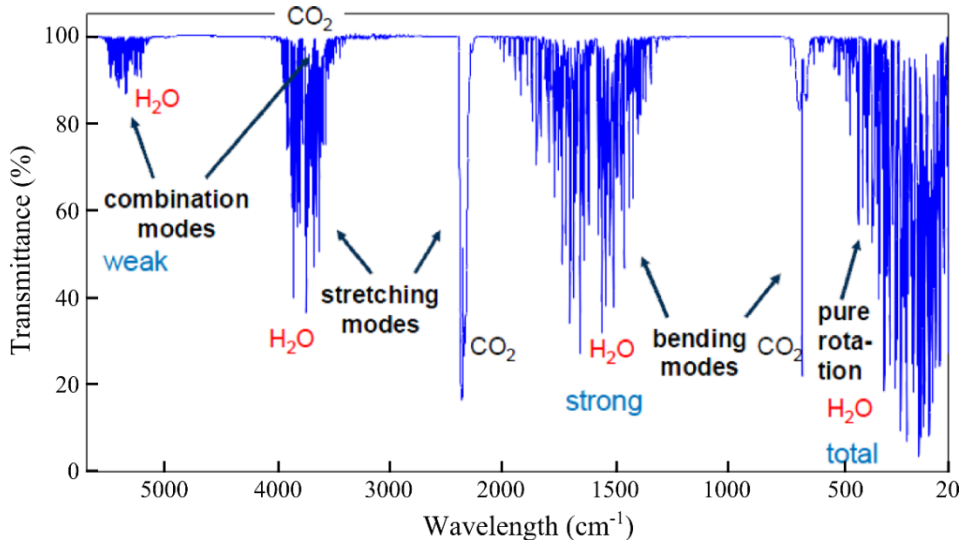

Figure 3.36 Air vapor IR spectrum.

In this work, FTIR spectroscopy was performed by Bruker Vertex 70v, which is able to perform in vacuum. Thus, the detrimental atmospheric effects can be minimized, which eliminates the unwanted absorption spectra that can be observed as a noisy signal. The schematic of the FTIR machine is illustrated in Figure 3.37.

The source-interferogram, in our experiments, was convoluted with a polarizer in order to probe the excited electronic levels in the conduction band under transverse-magnetic (TM) and transverse-electric (TE) polarized excitation. The signature of intra-band is the transition between the ground state of the conduction band, *s*, and the first excited electronic state confined along the growth axis, p_z, under TM-polarized excitation and the transition between the *s* and the first excited electronic state due to the lateral confinement, p_x and p_y under TE-polarized excitation. However, all the transition that takes place at >4 μm is masked by the sapphire absorption.

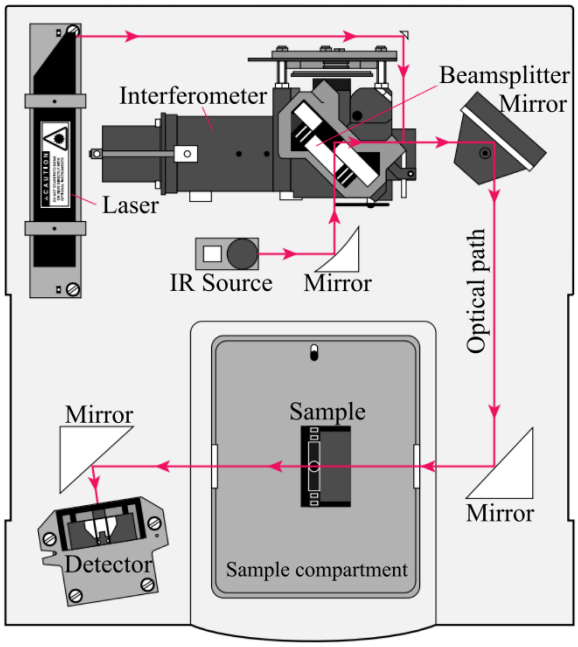

Figure 3.37: Schematic configuration and optical path in the FTIR spectrometer.

Chapter 4

4 AlGaN/AlN Quantum Dots

The chapter begins with a brief introduction describing the challenges of the fabrication of an ultraviolet emitter, and the reason to use quantum dot nanostructures as active medium. Then, I introduce the design of the active region of an electron-pumped quantum-dot-based ultraviolet emitter, addressing the calculation of the total active region thickness, optimum AlN barrier thickness, and the amount of deposited AlGaN in each quantum dot layer which provides the maximum luminescence. The targeted wavelength is tuned by methodically adjusting the Al-to-metal flux ratio and substrate temperature. After the growth optimization, I propose some post-growth processes that can enhance the light extraction. Finally, I show that the technological transfer to 6H-SiC substrates can be performed without any performance degradation.

4.1 Introduction

AlGaN/AlN quantum wells (QWs) with a broad dispersion in internal quantum efficiency (IQE~5-50%) have been reported [196]–[199], but there is a general agreement that high IQE values are associated to in-plane carrier localization [198]–[200]. To fully exploit the advantages of carrier localization, Stranski-Krastanov (SK) quantum dots (QDs) are proposed in this work, since their size and density can be adjusted thanks to the control-by-growth of the nanostructure. Excitons trapped in QDs are expected to be much more insensitive to non-radiative recombination than those in QW structures, as demonstrated in GaN/Al(Ga)N system [130], [201]. Thus, various groups have proposed using GaN QDs as active layers for ultraviolet (UV) light emitting diodes (LEDs) to reduce non-radiative recombination [202]–[205]. However, GaN/AlN QD LEDs have a limitation in emission wavelength and must face the challenges of *p*-type doping and contacting high-Al-content layers. In this thesis, an AlGaN/AlN QD electron-pumped UV (EPUV) source was proposed. The choice of AlGaN/AlN QDs as active media was made in order to blue shift the peak emission wavelength to the targeted position (λ=260-270 nm) for water purification, whereas the EPUV approach allows circumventing the LED-related difficulties. To my knowledge, here is the first systematic study of AlGaN/AlN SK QDs.

4.2 Active region design

Figure 4.1 depicts the general AlGaN/AlN QDs structure which I have synthesized during my PhD for the fabrication of EPUV sources. The active region (Figure 4.1-A) consists of a certain number of AlGaN QD layers (Figure 4.1-B), each QD layer is separated by AlN barrier (Figure 4.1-C). The active region is grown directly on the substrate, which is generally a commercial 1-µm-thick AlN-on-sapphire template. Three parameters of the structure must be optimized:

- The minimum active region thickness, which is given by the electron penetration depth. The acceleration voltage (V_{ac}) of the EPUV emitter has been set, in our case, at 5 kV in order to minimize x-ray emission from the active region. Thus, the first experiment aimed at identifying the penetration depth of the electrons in such conditions (section 4.2.1).
- The AlN barrier thickness, which should be thick enough to recover two-dimensional growth before the following QD layer, and thin enough to prevent carrier diffusion loses (section 4.2.2).
- The amount of AlGaN in each QD layer, which can affect the QD density and size, and the Al/Ga flux ratio and growth temperature can further modify the structural and optical properties of the QDs. These parameters are discussed in sections 4.3 and 4.4.

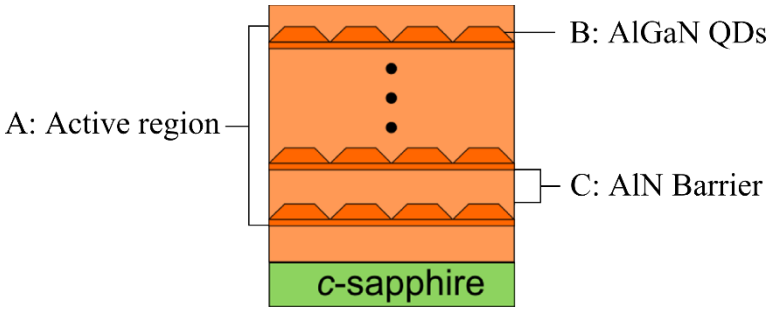

Figure 4.1: Schematic of the AlGaN/AlN QD structure, illustrates the (A) active region which consists of (B) multilayers of AlGaN QDs and (C) AlN barriers separate between each QD layer.

4.2.1 Active layer thickness

When electrons impinge onto the structure, they can penetrate a certain depth which depends on the acceleration voltage (V_{ac}) and the type of material. An empirical equation to describe the electron penetration depth (R_e) was developed by Kanaya *et al*. [206] which

predicts the maximum penetration depth of electrons. At a given acceleration voltage, the maximum penetration depth is given by [206]:

$$R_e = \frac{0.0276A}{\rho Z^{0.889}} V_{ac}^{1.67} \ (\mu m) \qquad (4.1)$$

where A is the atomic weight of the sample in g/mol, ρ is the density in g/cm^3, and Z is the atomic number. For instance, if V_{ac} = 5 kV is applied on GaN bulk, the maximum penetration depth of electrons, which is calculated from (4.1), is ~300 nm, whereas the maximum penetration depth of electron in AlN bulk, using the same acceleration voltage, is ~600 nm. Hence, following this empirical equation, to cover all the area that electron can reach through when accelerating with 5 kV, an active region of ~600 nm should be grown.

Apart from the empirical method presented above, Monte Carlo simulations [207] of electron beam interaction with solid structures can precisely predict the volume of material that electrons can penetrate through. Such simulations require the material density, the energy of electron beam as input parameters, and then the collision events are computed until all the electrons come to a rest and an energy loss curve is generated. CASINO [208]–[210] is a Monte Carlo simulator that is extensively used to model electron penetration depth. As illustrated in Figure 4.2, for V_{ac} = 5 kV, the maximum electron penetration depths are 250 and 350 nm for GaN and AlN, respectively. Therefore, the active region thickness for the EPUV source should be > 350 nm, in order to cover the whole electron penetration depth, and hence maximize the photon emission.

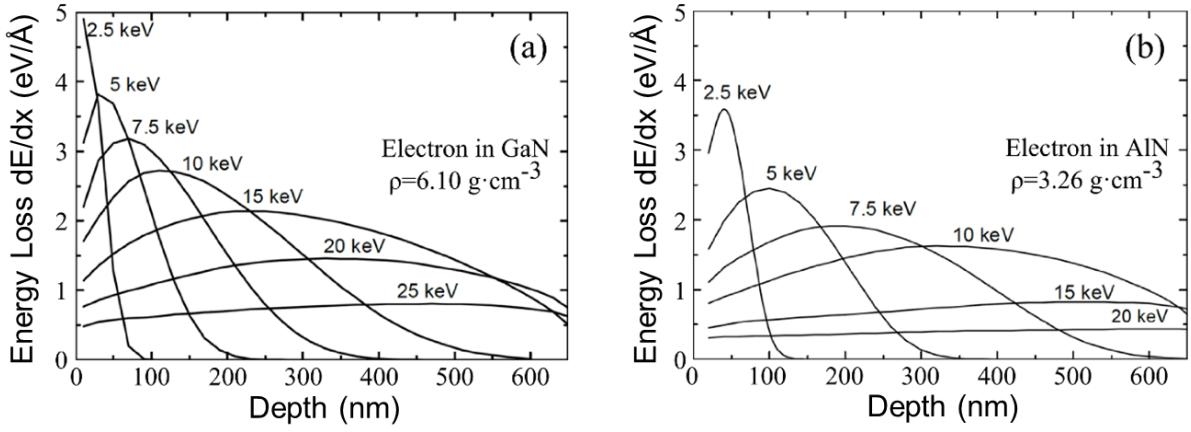

Figure 4.2: Depth dependent CL spectra of as a function of electron kinetic energy at the surface for (a) bulk GaN and (b) bulk AlN.

As an experimental verification, I have determined the minimum active region thickness by growing a series samples containing a single layer of GaN QDs with various AlN capping

thicknesses (100, 300, and 500 nm for samples E2900, E2901, and E2902, respectively) via PA-MBE. The flux of active nitrogen (Φ_N) was set at 0.34 monolayers per second (ML/s). The growth of GaN QDs was performed under N-rich conditions ($\Phi_{Ga}/\Phi_N \sim 0.75$). The thickness of GaN QDs was fixed at 3 ML over entire samples in the series. The QDs were Si-doped in the 10^{19} cm^{-3} range to favor charge evacuation. After the growth, they were measured by cathodoluminescence (CL) at V_{ac} = 5 kV. The schematics of the samples are depicted in Figure 4.3.

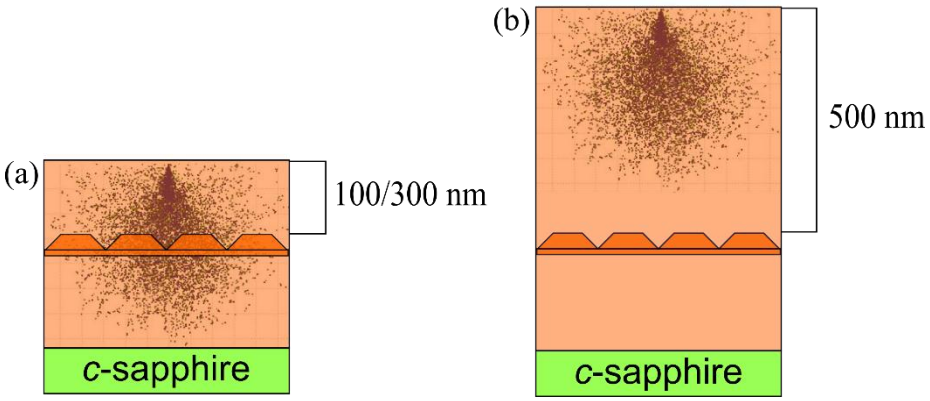

Figure 4.3: Schematics of samples consisting of a single GaN QD layer grown in an AlN matrix, and illustration of the electron trajectories when measuring CL. (a) Thin AlN cap layer thicknesses (100 and 300 nm AlN) where electrons penetrate beyond the QD layer, and (b) thick AlN cap layer thickness (500 nm AlN) where electrons do not reach QD layer.

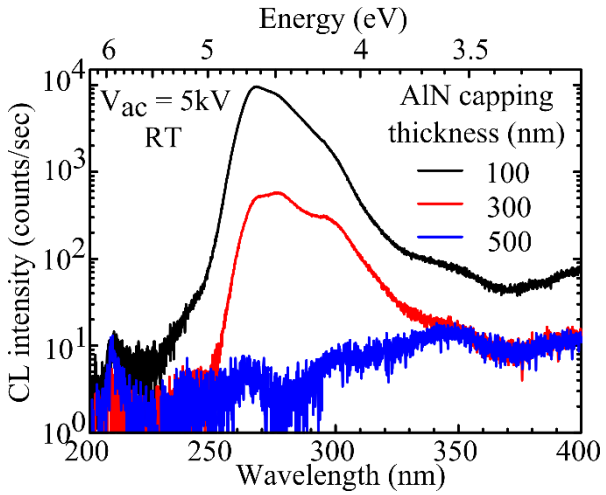

Figure 4.4: Luminescence intensity from the samples with capping thicknesses of 100, 300, and 500 nm probed by cathodoluminescence with acceleration voltage of 5kV.

As illustrated in Figure 4.4, the maximum CL intensity is obtained from the sample with 100 nm cap layer, whereas the emission decreases by almost one order of magnitude for the sample with a 300 nm thick cap layer, and there is no signal of GaN QDs probed from the sample with a cap layer thickness of 500 nm, which means that for V_{ac} = 5 kV the electrons

cannot penetrate 500 nm in the structure. From this experiment, I extract that the minimum active region thickness (for V_{ac} = 5 kV) is ~400 nm. This experimental value is lower than the maximum active region thickness of ~600 nm which was defined using empirical equation, and is in the same range of the maximum active region thickness of 350 nm simulated by the Monte Carlo method presented in Figure 4.2.

4.2.2 Maximum barrier thickness

The maximum AlN barrier thickness was determined by the measurements of carrier diffusion length. With this purpose, a sample consisting of 10 layers of GaN QDs was grown by plasma-assited molecular beam epitaxy (PA-MBE), each QD layer separated by 50 nm of AlN barrier. Then the sample was characterized by CL performed in a STEM microscope at the Otto-von-Guericke-University in Magdeburg (Germany) by the group of Prof. Christen. The CL-detection unit is integrated in a FEI STEM Tecnai F20 equipped with a liquid helium transmission electron microscopy (TEM) cryo-sample holder (T = 10K/300K). The emitted CL light is collected by a parabolic mirror above the sample and focused onto the entrance slit of the grating monochromator system Gatan MonoCL4. In scanning-TEM (STEM) mode the electron beam is convergent and either kept at a single position for local spectra or scanned over the region of interest in imaging mode. Panchromatic as well as spectrally resolved CL imaging is used. The CL-intensity is collected simultaneously to the STEM signal at each pixel.

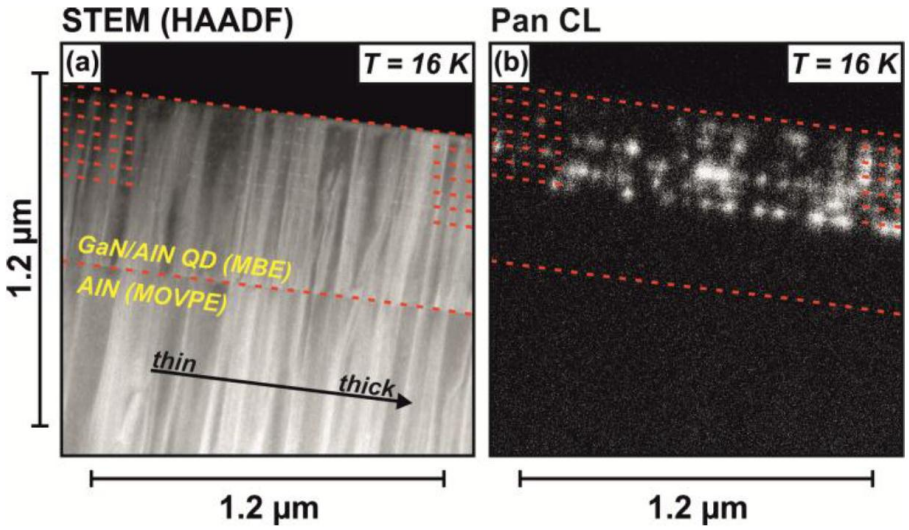

Figure 4.5: Low temperature panchromatic STEM-CL mapping in overview shows (a) high angle annular dark field contrast of the upper GaN QD layers, and (b) panchromatic spot like CL-intensity within the upper marked QD layers; red dashed lines mark the interface between the AlN-on-sapphire template (MOVPE) and the the AlN grown by MBE, the formed QD layers and the surface.

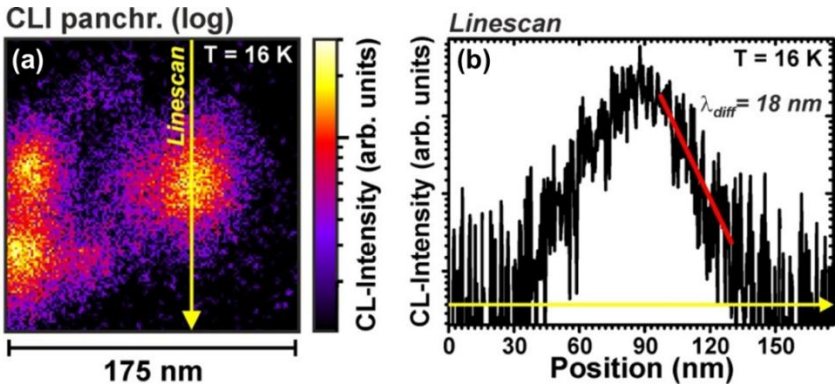

Figure 4.6: (a) Spot-like panchromatic CL intensity distribution at 16K (b) A linescan over spot-like emission shows the QD carrier capture length of 18 nm.

The cross-section STEM image clearly shows the interface between the AlN-on-sapphire template, grown by metalorganic vapor phase epitaxy (MOVPE) and the AlN grown by molecular beam epitaxy (MBE) containing the GaN QD layers (Figure 4.5(a)). Originating from the AlN sapphire interface, vertically running threading dislocations show up in the high angle annular dark field contrast (HAADF). The comparison of the HAADF-STEM images with the simultaneously recorded panchromatic CL mappings (Figure 4.5(b)) at 16 K exhibits a spot like luminescence distribution in the QD layers.

To investigate the CL distribution of single QDs, an area of 175×175 nm^2 was scanned in panchromatic mode (see Figure 4.6(a)). A line scan (yellow arrow) was performed across the center of the QD emission and plotted as a variation of the QD emission intensity as a function of position (Figure 4.6(b)). From the logarithm decay, a carrier diffusion length of 18 nm was extracted from the experimental curve.

Carrier diffusion length measurements set a maximum barrier thickness while the minimum barrier thickness is determined by the requirement of a flat surface before the growth of the subsequent QD layer. Deposition of the second QD layer before complete planarization leads to the vertical correlation of the QDs, as a result of the non-homogenous strain state of AlN capping layer [211]. Vertical correlation affects both the structural [212] and optical properties of the dots: the QD density decreases, the QD diameter and height increases, and the emission wavelength red-shifts with the number of QD periods [211]. Therefore, to get small QDs and uniform emission along the active region, vertical correlation should be avoided.

The minimum AlN thickness to achieve planarization depends on the QD size and density. For instance, the small QDs need less thickness of AlN barrier for surface flattening

whereas the big QDs need more AlN barrier thickness. The minimum AlN barrier thickness has been determined experimentally by the recovery of a streaky reflection high energy electron diffraction (RHEED) pattern after the QD formation. To flatten QDs that are grown under N-rich conditions with QD thicknesses in the 3-7 ML range, minimum AlN barrier thicknesses are in the range of 4-5 nm. It is noteworthy that the thickness of 4-5 nm of AlN barrier is much smaller than the maximum AlN barrier thickness of 18 nm that was defined above, so that it is possible to achieve a good carrier collection with planar interfaces.

4.3 Wavelength tunability: Substrate temperature, Al-to-metal flux ratio, and the amount of AlGaN in each QD layer

In this section, I describe the structural and optical properties of AlGaN/AlN QD superlattices (SLs) synthesized by PA-MBE, with the target to assess the range of emission wavelengths accessible by AlGaN QDs. The samples were designed so as to adapt to the requirements of EPUV sources: they consisted of 100 periods of AlGaN QDs with 4-nm-thick AlN barriers (i.e. active region > 400 nm) deposited on 1-μm-thick (0001)-oriented AlN-on-sapphire templates. The Φ_N was fixed at 0.32 (ML/s). The growth of AlGaN QDs was performed under N-rich conditions, i.e. the total metal flux ($\Phi_{metal} = \Phi_{Al} + \Phi_{Ga}$) was lower than Φ_N. The QDs were Si-doped in the 10^{19} cm^{-3} range, in order to favor charge evacuation in EPUV modules. As reported for GaN QDs [131], [213]. Under these conditions, the growth starts two-dimensionally, with a transition into three-dimensional (3D) islands (SK growth mode) when the deposited material is beyond a certain critical thickness. The growth kinetics was analyzed *in situ* by reflection high-energy electron diffraction, which confirmed the formation of a 3D surface after the deposition of the QD layers, and the subsequent planarization during the growth of the AlN barriers. The choice of N-rich conditions is motivated by the target of short wavelength emission: the nitrogen excess reduces the mobility of adsorbed species during growth, resulting in a high density of small QDs (10^{11} cm^{-2}), which contributes to the luminescence blue shift thanks to the carrier confinement. The QD deposition was followed by a 10-s growth interruption in vacuum, before capping with 3-4 nm of AlN grown under slightly Al-rich conditions to achieve a good planarization before the next QD layer. The purpose of this interruption is to have the time to visually confirm the QD formation after deposition of every QD layer –the RHEED pattern was not permanently visible since the substrate kept rotating to achieve good in-plane

homogeneity. It is known that QDs in vacuum undergo morphological changes with time, known as Ostwald ripening [214]. However, in this work I have verified that growth interruptions up to 15 s have no influence on the QD emission spectra at this relatively low growth temperature.

In the samples under study, I tuned the emission wavelength by adjusting three parameters, namely the substrate temperature (T_S), Al-to-metal flux ratio (Φ_{Al}/Φ_{metal}), and the amount of AlGaN in each QD layer. Table 4.1 presents a summary of the growth parameters of the samples under study.

Sample	T_s (ºC)	Φ_{Al}/Φ_{metal}	Amount of AlGaN in the QD layer (ML)	Emission wavelength (nm)	IQE(%)	Measuring technique
QD-1, E1761	720	0	4	320	60	PL, CL
QD-2, E2816	720	0.14	5	287	40	PL, CL
QD-3, E2817	720	0.24	6	280	39	PL, CL
QD-4, E2818	720	0.33	6	274	38	PL, CL
QD-5, E2820	720	0.42	7	268	42	PL, CL
QD-6, E2368	745	0.12	4	256	40	CL
QD-7, E2366	745	0.21	4	245	40	CL
QD-8, E2999	745	0.12	1.6	235	26	CL

Table 4.1: Description of the AlGaN QD samples under study: growth parameters, peak emission wavelengths at room temperature, IQEs, and measuring techniques (photoluminescence or cathodoluminesce.

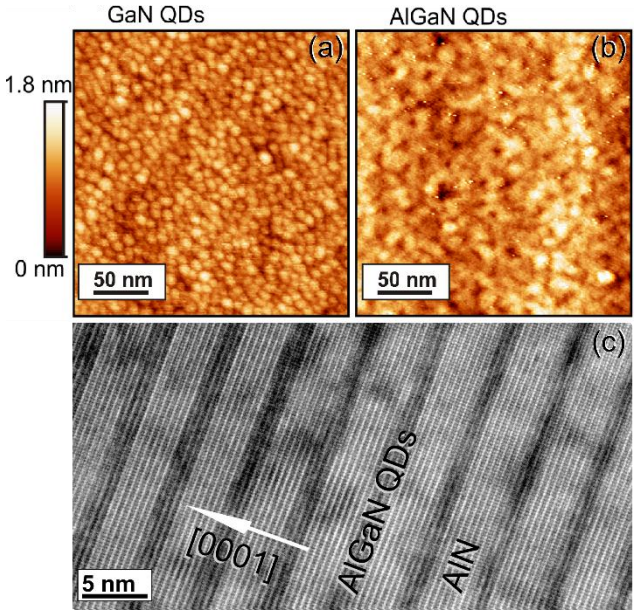

Figure 4.7: AFM images of (a) GaN/AlN QDs synthesized by deposition of 4 ML of GaN under N-rich conditions (Φ_{Ga}/Φ_N~0.8), and (b) AlGaN/AlN QDs synthesized by deposition of ML of AlGaN under N-rich conditions (Φ_{Ga}/Φ_N~0.8), and (c) TEM micrograph corresponds to the AlGaN/AlN QDs shown in (b).

To verify the presence of QD structures *ex situ* via atomic force microscopy (AFM) characterization, an additional QD plane was deposited on the sample surface. Figure 4.7(a) and (b) depict the surface of SLs containing GaN and AlGaN ($\Phi_{Al}/\Phi_{metal} = 0.33$) QDs, respectively when Figure 4.7(c) shows corresponding high-resolution transmission electron microscopy (HRTEM) image of AlGaN QDs in Figure 4.7(b). In both cases, the QD height is 1-2 nm above the wetting layer, their base diameter is < 10 nm, and the QD density is 10^{11}-10^{12} cm^{-2}. HRTEM image of the sample reveals the presence of 3D structures with a base dimension ~7 nm and a height ~1.5 nm, consistent with AFM observations. However, the high QD density results in the superimposition of several QDs in the HRTEM images, which hinders the clear identification of the QD facets and a precise measurement of the thickness of the wetting layer. It is noteworthy that a 2D/3D transition is obtained for flux ratios as high as $\Phi_{Al}/\Phi_{metal} = 0.42$, which implies a lattice mismatch between the QD material and the underlying AlN layer lower than 1.7%. Therefore, I attribute the SK transition in this semiconductor system not only to the accumulation of elastic energy due to lattice mismatch, but also to the high surface energy of the (0001) plane in presence of nitrogen [215].

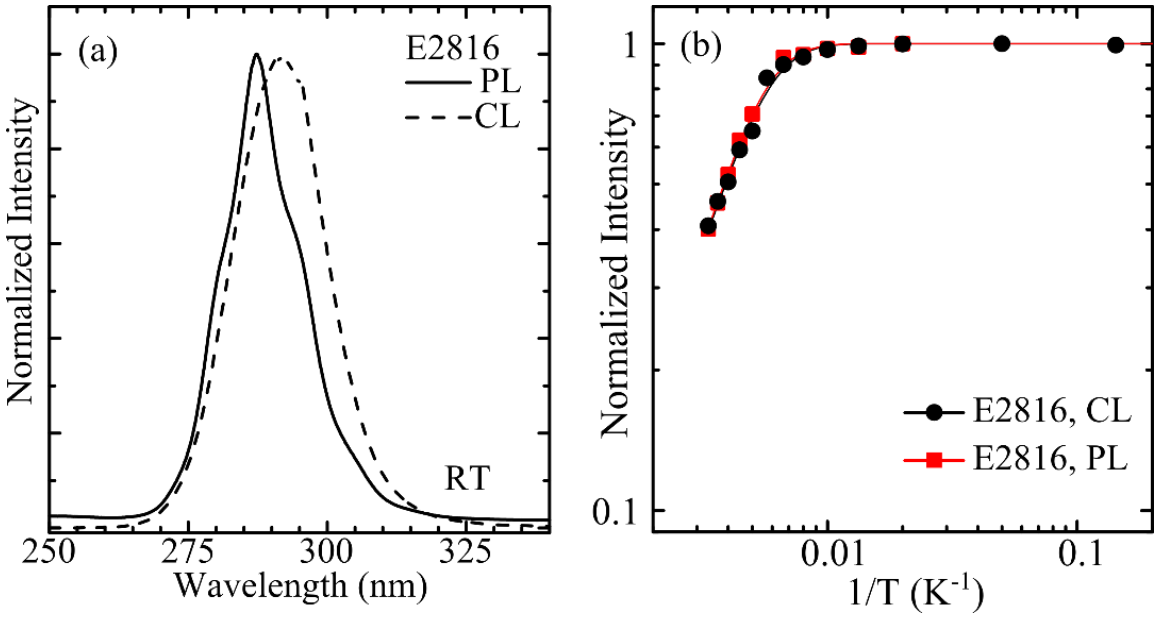

Figure 4.8: (a) Room-temperature emission from E2816 measured by PL (solid line) and CL (dash line). (b) Variation of fitted integrated luminescence intensity (black scatters correspond to CL data and red scatters correspond to PL data) from E2816 as a function of temperature.

The choice of optical characterization by photoluminescence (PL) or CL is made among samples because PL technique works by exciting with Ar laser ($\lambda = 244$nm), thus can probe only the sample with $\lambda > 250$ nm. On the contrary, there is no wavelength limitation when

characterize using CL technique. The optical characterizations were probed both by CL and PL. Figure 4.8(a) shows a comparison of both techniques, the CL spectrum is slightly red shift from the one measured by PL, which might relate to a certain in-plain inhomogeneity among QD layers. However both spectra render a similar linewidths. PL measurement shows a superimposed Fabry-Perot interferences associated to the total nitride layer thickness (~1.5 μm). This interference does not occur in CL measurements, where high-energy electron injection results in a Gaussian-like profile. The IQEs probed, by the variation of the integrated emission intensity as a function of temperature, from PL and CL show the same characteristics as illustrated Figure 4.8(b). This experiment assures us that the comparisons between IQEs extracted from PL and CL that report elsewhere in the manuscript are valid.

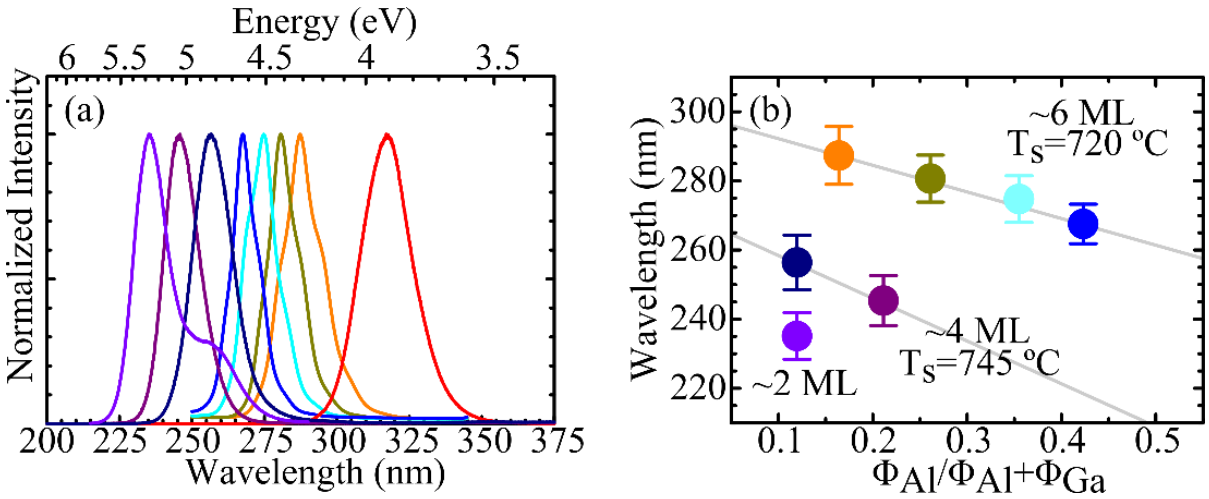

Figure 4.9: (a) Room-temperature emission from AlGaN/AlN QDs. Spectra peaking at λ>265 nm were measured by PL and the ones at λ < 265 nm were measured by CL. (b) Variations of the peak emission wavelength as a function of the growth parameters.

Figure 4.9(a) shows the emission of the samples at room temperature. Spectra from samples peaking at $\lambda = 340$ nm and $\lambda < 265$ nm were measured by CL, and the rest of the spectra were obtained by PL. By varying Φ_{Al}/Φ_{metal}, T_S, and the amount of AlGaN in each QD layer as stated in Figure 4.9(b), the peak emission wavelength can be tuned down to 235 nm. The full width at half maximum (FWHM) of the luminescence is in the range of 0.19-0.26 eV (spectral width $\Delta\lambda/\lambda = 4$-6%).

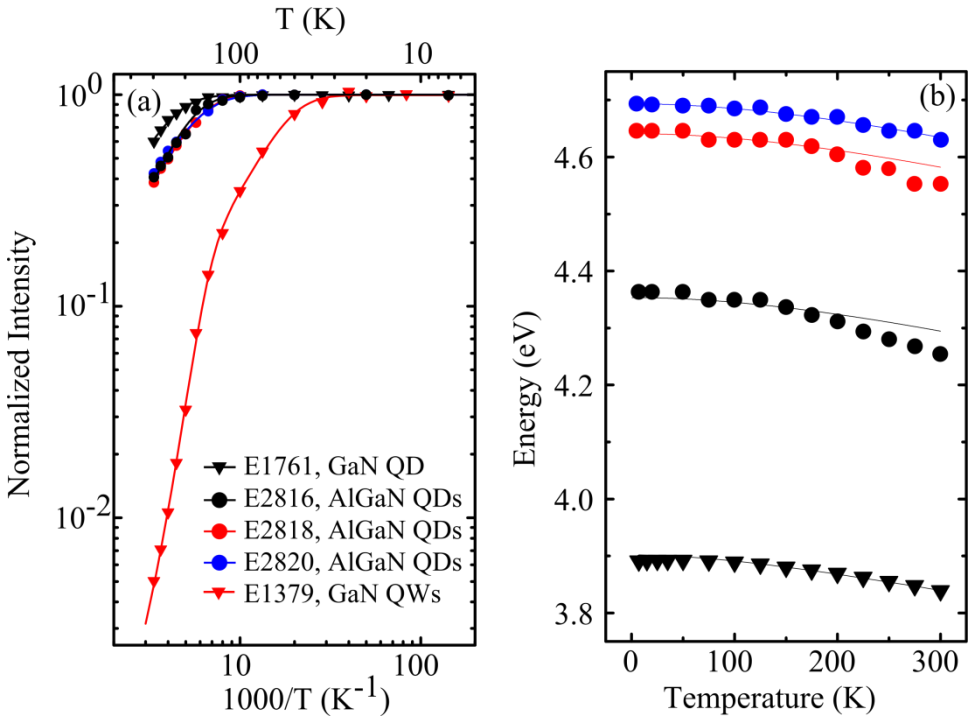

Figure 4.10: Variation of the integrated intensity from (Al)GaN/AlN QDs with temperature. Data from GaN/AlN QWs emitting at 310 nm is included for comparison. (b) Temperature dependence of the luminescence peak position for (Al)GaN/AlN QDs. The solid lines represent the expected evolution following Varshni's equation. Varshni's parameters for AlGaN samples were obtained by linear interpolation between the AlN [61] and GaN [59].

The emission efficiency has been evaluated via PL measurements as a function of temperature. Let us remind that the IQE is defined as:

$$IQE=\tau_R^{-1}/(\tau_R^{-1}+\tau_{NR}^{-1}) \qquad (4.2)$$

where τ_R and τ_{NR} are the radiative and nonradiative carrier lifetimes, respectively. For thermally activated non-radiative recombination centers, i.e. for $\tau_{NR}=\tau_0 e^{Ea/kT}$ with E_a being the nonradiative activation energy, kT being the thermal energy, and τ_0 being a constant prefactor, the IQE can be expressed as:

$$IQE=1/(1+ae^{-Ea/kT}) \qquad (4.3)$$

where $a = \tau_R/\tau_0$ [130], [216].

Figure 4.10(a) presents the integrated emission intensity as a function of temperature normalized to its value at low temperature ($T = 5$ K) for various AlGaN/AlN QDs. Data corresponding to GaN/AlN QDs (E1761) and to GaN/AlN QWs (E1379, consisting of 40 periods of 1.2nm GaN / 3nm AlN, with peak emission at 310 nm) are included for

comparison. Keeping in mind that the PL intensity remains stable below ~70 K for all the QD samples, and below ~30 K for the QW sample, the data presented in Figure 4.10(a) should correspond directly to the IQE as a function of temperature. In all the samples under study, the IQE at room temperature remained higher than 25%. The values of E_a and a extracted from fits to equation 4.3 (solid lines in the figure) are summarized in Table 4.2. The value of a remains in the 9-17 range for all the QD samples, which could be an indication that the introduction of Al in the AlGaN QDs does not modify significantly the non-radiative recombination path, i.e. the density and nature of the defects remain stable. On the contrary, the value of E_a is maximum for GaN/AlN QDs (78±5 meV), and decreases monotonically when increasing Φ_{Al}/Φ_{metal}, i.e. when reducing the band offsets. This activation energy is the potential barrier that the carriers have to overcome to reach the non-radiative recombination centers, which is significantly higher for QDs than for QWs, thanks to the 3D carrier confinement. The in-plane carrier confinement in QWs is only associated to thickness or alloy fluctuations.

Sample	Emission wavelength at 300K (nm)	E_a (meV)	a	Decay time at 5K (ps)	s-p_z (μm)
QD-1, E1761	320	78±5	13±3	770	1.45
QD-2, E2816	287	64±4	17±3	500	1.57
QD-3, E2818	274	57±2	14±2	400	1.78
QD-4, E2820	268	49±2	9±2	360	2.02
QW-1, E1379	310	E_{a1}=15±3 (*) E_{a2}=110±15		280	

Table 4.2: PL data of various samples: peak emission wavelength at room temperature, thermal activation energy, and exponential prefactor in Eq. (4.3), PL decay time measured at T=5K, and s-p_z intra-conduction-band transition wavelength at room temperature.
(*) In the case of QWs, I systematically identify two activation energies, as described in Ref. [130]. The smaller one is associated to the onset of the PL decay at low temperatures (~30K in Figure 4.10)

The PL spectral shifts with temperature, which can provide information concerning the carrier localization in potential fluctuations in the AlGaN/AlN QDs, are shown in Figure 4.10(b). All the samples present a red shift of the PL with increasing temperature which fits well with the expected evolution of the AlGaN band gap calculated using Varshni's equation (solid lines in the figure) [59], [61]. Therefore, I conclude that the effect of potential fluctuations inside the QDs is negligible. This is in contrast with the results in GaN/InGaN QDs and in nonpolar GaN/AlN QDs, which present a strong S-shaped evolution of the PL with temperature attributed to intra-dot potential fluctuations associated to alloy inhomogeneities [130], [217] or to the presence of stacking faults [218]. S-shaped PL-

behavior has also been reported in AlGaN thin films [125], [219]–[221] and AlGaN/GaN QWs [222], [223], which points out that the AlGaN inhomogeneities originating from potential fluctuations are larger than the exciton Bohr radius (~ 2 nm in bulk GaN). The fact that these fluctuations do not have an effect on the spectral response of AlGaN QDs is an indication of the strong carrier localization imposed by both the band offsets and the polarization-induced electric fields in these 3D nanostructures.

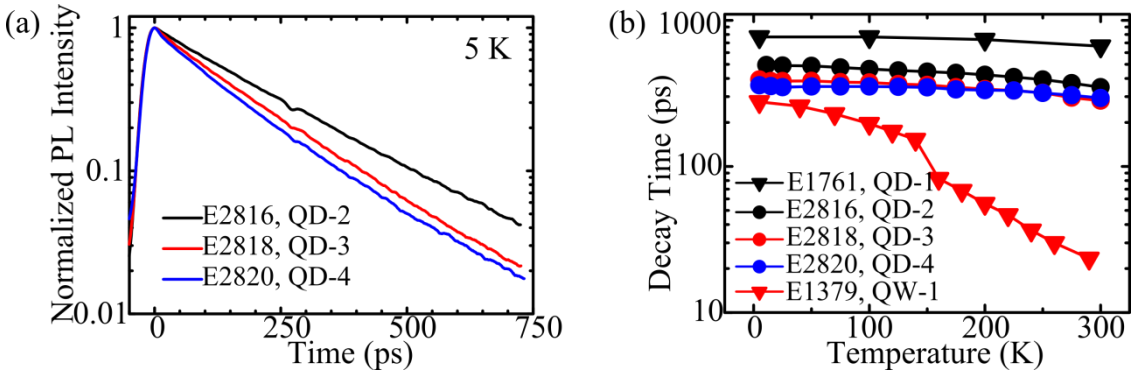

Figure 4.11: (a) Time-resolved PL of AlGaN/AlN QDs at 5K. (b) Evolution of the decay time as a function of temperature. The decay time is fit in the range where the PL intensity decreases from 90% to 10% of its maximum value.

The radiative recombination efficiency of QD samples has also been assessed by time-resolved PL. As shown in Figure 4.11 and Table 4.2, the decay time of the AlGaN QD samples is mono-exponential at low temperature ($T = 5$ K), with decay times evolving from 500 to 360 ps with increasing Al content, possibly due to the reduction of the polarization-induced internal electric field. For all the samples, the decay times decrease by less than 30% between $T = 5$ K and $T = 300$ K, confirming that the carriers are efficiently localized in the QD and hence relatively insensitive to non-radiative recombination centers. In contrast, the decay time in the QW sample decreases by more than one decade in the same temperature range, due to the in-plane carrier mobility, as previously observed [201].

As a further verification of the electronic structure and optical quality of AlGaN QDs, I have studied their excited electronic levels in the conduction band using FTIR spectroscopy. Figure 4.12(a) displays the TM-polarized absorption of AlGaN/AlN QDs measured at room temperature, showing a dip in the 1.6-2 μm wavelength range, which does not appear for TE polarization. This is a signature of an intraband transition between the ground state of the conduction band, *s,* and the first excited electronic state confined along the growth axis, p_z. The lateral confinement in the QDs should give rise to additional transitions under TE-

polarized excitation. However, taking into account the lateral dimension of the QDs ~7 nm, the s-p_x and s-p_y transitions should be masked by the sapphire absorption for $\lambda > 4$ µm. The s-p_z transition red shifts for increasing Al mole fraction in the QDs as a result of the reduction of the band offset. A comparison with theoretical calculations using the 8-band k·p Schrödinger-Poisson Nextnano[3] solver [119], [224] with a one-dimensional approximation provides an excellent fit with the experimental results, as illustrated in the inset of Figure 4.12 which supports the Al incorporation in the QDs in levels close to the nominal values.

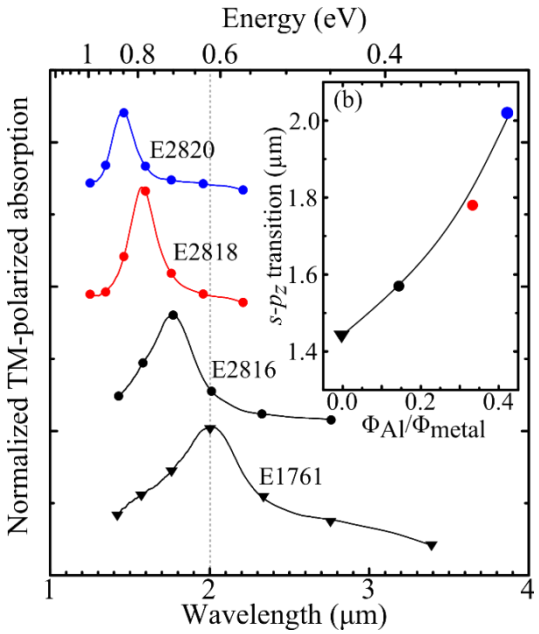

Figure 4.12: Room temperature infrared absorption spectra for TM-polarized light measured in AlGaN/AlN QDs. Inset: Evolution of the s-p_z intraband transition wavelength as a function of the Al mole fraction in the nanostructures. Scatters correspond to experimental measurements and the solid line is a theoretical calculation using the 8-band k·p Schrödinger-Poisson Nextnano[3] solver. The calculation considers a one-dimensional approximation with the material parameters in [119], a QD height of 1.4 nm, and the Al mole fraction in the nanostructures as the only variable parameter.

In conclusion, I have demonstrated the PA-MBE growth of AlGaN/AlN QD SLs displaying room-temperature emission down to 235 nm wavelength with IQE higher than 25%. The spectral evolution of the PL with temperature presents no indications of intra-dot carrier localization. The efficient carrier confinement is confirmed by the stability of the PL decay time as a function of temperature up to 100 K. Above this threshold, the PL intensity decreases and the radiative lifetime increases due to carrier thermalization. Using Fourier transform infrared (FTIR) spectroscopy, I have identified the intraband electronic transition between the ground level of the conduction band and the first excited state confined along the growth axis. The evolution of the intraband transition with the Al-to-metal flux ratio is in good agreement with theoretical calculations confirms the incorporation of Al in the QDs.

4.4 Effect of the amount of AlGaN on the IQE and morphology

In this section, I describe the identification of an optimum deposited amount of AlGaN in AlGaN/AlN QDs to achieve maximum luminescence at room temperature. Such thickness is given by a compromise between the thicknesses providing maximum IQE and maximum QD density. To perform this study, I grew stacks of 19 periods of AlGaN/AlN QDs on 1-µm-thick (0001)-oriented AlN-on-sapphire templates. The structures of all the samples are illustrated in Figure 4.13.

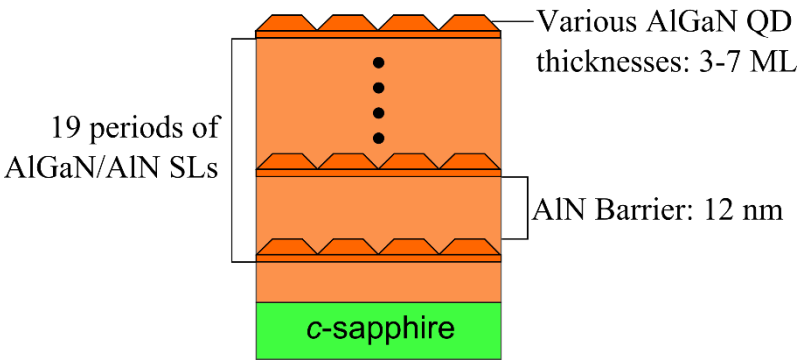

Figure 4.13: The structure of the grown samples for section 4.4, which consists of 19 periods of AlGaN/AlN QD SLs. The thickness of AlN barrier was set at 12 nm while the thicknesses of AlGaN QD is varied from 3 to 7 ML, which associate to the sample number as shown in Table 4.3.

The growth of AlGaN QDs was performed under N-rich conditions [131], [213], i.e. the total metal flux ($\Phi_{metal} = \Phi_{Al} + \Phi_{Ga}$) was lower than the active nitrogen flux Φ_N which was set at 0.44 ML/s. The QDs were Si-doped in the 10^{19} cm^{-3} range in order to improve the conductivity, hence preventing the charging effect that might occur in electron-injection measurements. The substrate temperature remained at T_S=720°C, the Al-to-metal flux ratio was fixed at $\Phi_{Al}/\Phi_{metal} = 0.09$, and the amount of AlGaN in each QD layer was varied from 3 to 7 ML. The synthesis of each AlGaN QD layer is followed by a 10 s growth interruption under vacuum, during which additional reflections corresponding to the QD facets are visible in the RHEED pattern when the total amount of AlGaN is larger than 4 ML. The QDs were capped with 12 nm of AlN grown under slightly Al-rich conditions. The reason for such large barriers in comparison with the experiments described in section 4.3 is that I wanted to guarantee surface planarization after the growth of the barrier even in the samples with thicker QDs (deposition of 7 ML). Table 4.3 presents a summary of the growth parameters of the samples under study.

Sample	Amount of AlGaN (ML)	QD density ($\times 10^{11}$cm^{-2})	λ_{RT} (nm)	IQE (%)	E_a	a	s-p_z (μm)
E3180	3	2.4±0.3	256	38	38±3	6±1	--
E3179	4	2.9±0.3	276	60	74±3	11±2	1.50
E3178	5	7.3±0.3	296	52	45±3	5±1	1.51
E3177	6	9.5±0.5	311	31	22±3 89±20	2.1±0.7 19±14	1.55
E3175	7	9.0±0.5	322	22	18±2 102±7	1.1±0.2 90±20	1.59

Table 4.3: Description of the AlGaN QD samples under study: amount of AlGaN in the QD layers, QD density, room temperature peak emission wavelength (λ_{RT}), IQE, thermal activation energy (E_a), exponential prefactor (a) in Eq. (4.3), and intraband transition energy (s-p_z).

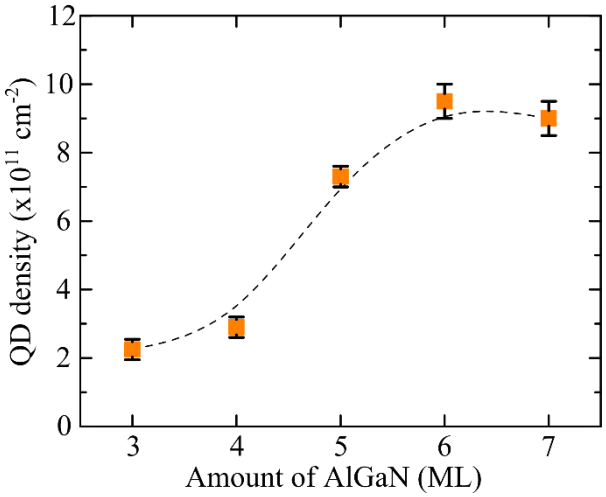

Figure 4.14: Variation of QD density as a function of the amount of AlGaN deposited to form each QD layer.

The QD densities were extracted from AFM measurements and plotted in Figure 4.14. When progressively increasing the amount of AlGaN in the QDs from 3 to 7 ML, the QD density increases monotonously from $(2.4\pm0.3)\times10^{11}$ cm^{-2} (E3180) to $(9\pm1)\times10^{11}$ cm^{-2} (E3175). However, the base diameter and height cannot be straightforwardly extracted since the AFM tip radius (~7 nm) is comparable to the size of the measured objects [193]. This relatively high QD saturation density, compared to previous literature [129], [225]–[227], is achieved due to the low growth temperature (T_S = 720°C) and short ripening time (10 s), which reduces the material capture radius around the QD nucleation site [131]. Figure 4.15 (a)-(c) show a cross-sectional HAADF-STEM image of 3, 5, 7-ML AlGaN QDs. The QDs appear closely packed for the 5 and 7 ML QDs when they are scarcely seen for 3 ML QDs since the deposited thickness is close to the thickness ~2 ML of wetting layer. The extracted base-diameter D_{QD} and height h_{QD} of 5 ML AlGaN QDs are 6.5±1.0 nm and 4±1 ML when those of 7 ML AlGaN QDs are 7.5±1.0 nm and 6±1 ML.

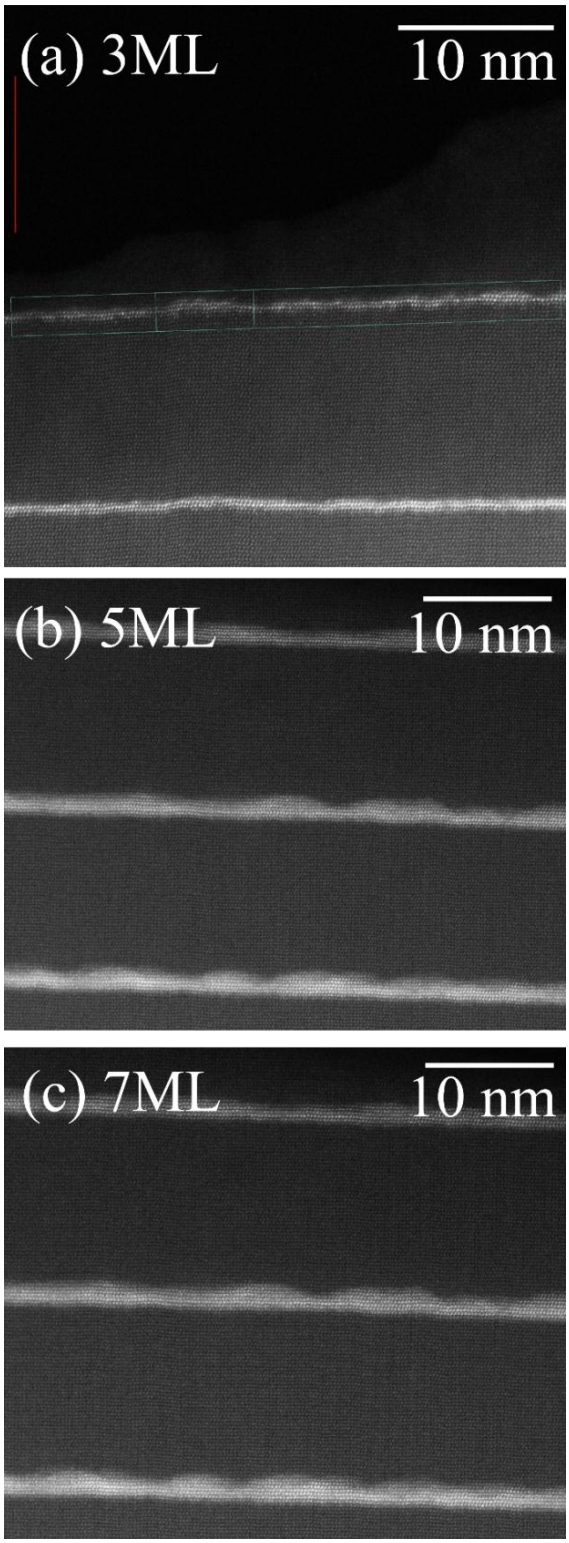

Figure 4.15: Cross-sectional HAADF-STEM images of (a) 3 ML, (b) 5 ML, and (c) 7 ML QDs taken along the <11-20> axis. White contrast is provided by Ga atoms.

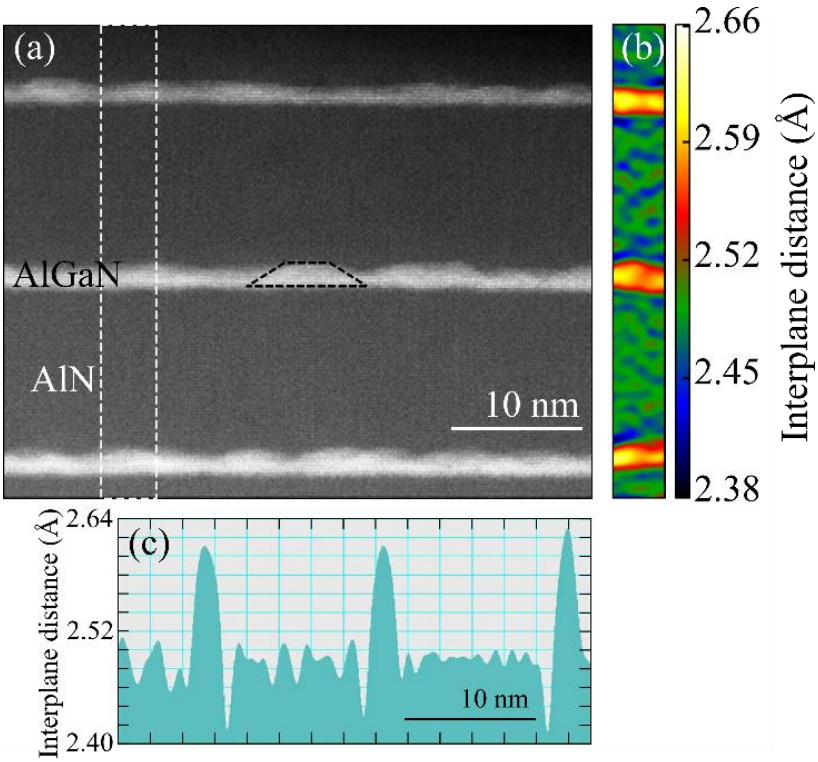

Figure 4.16: (a) Cross-sectional HDAAF-STEM image of 7 ML AlGaN QDs (E3175) taken along the <11-20> axis, showing 3 AlGaN QD layers. White contrast is provided by Ga atoms. (b) Map of the (0001) interplanar distance obtained by GPA of the region delimited by a dashed rectangle in (a). The AlN area is considered as a reference lattice assuming it relaxed (average AlN interplanar distance = 2.491 Å). (c) Variation of the (0001) interplanar distance along the growth axis obtained by horizontal averaging of (b).

In order to verify the incorporation of Al in the QDs, geometrical phase analysis (GPA) [228] was performed on Figure 4.16 (a) to analyze the variation of the (0001) interplane distance [see color mapping in Figure 4.16(b)]. For the GPA analysis, scan distortions were removed using the AlN as reference region [229]. Figure 4.16(c) shows the interplane distance profile extracted by horizontal averaging of Figure 4.16(b). At the AlGaN QD layers, the (0001) interplane distance reaches 2.61±0.01 Å, which corresponds to an Al composition of 12±7% assuming that the QDs are pseudomorphic on AlN and applying the biaxial strain approximation ($e_{zz}/e_{xx} = -2c_{13}/c_{33} \approx -0.537$, e_{zz} and e_{xx} being the strain along <0001> and <11-20>, respectively, and the elastic constants c_{13} = 106 GPa and c_{33} = 398 GPa for GaN [75] and c_{13} = 108 GPa and c_{33} = 373 GPa for AlN [79]).

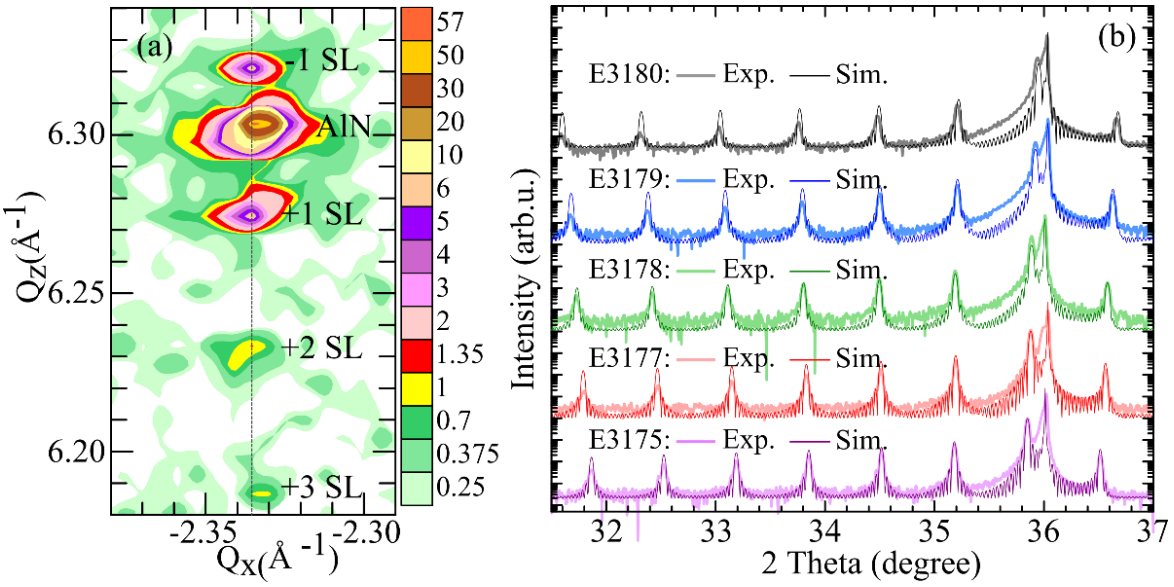

Figure 4.17: (a) Reciprocal space map around the asymmetric (-1015) reflection for E3175, Q_x and Q_z are the reciprocal space vectors in $Å^{-1}$. (b) High-resolution XRD θ-2θ scans of the symmetric (0002) reflections of samples E3180, E3179, E3178, E3177, and E3175. The simulations superimposed on the experimental scans were performed using the X'Pert Epitaxy 40 software from Philips Analytical, assuming that the structures are fully strained on the AlN substrates, and using the data in Table 4.3 (biaxial strain configuration).

Reciprocal space maps around the (-1015) asymmetrical reflection (shown in Figure 4.17(a)) confirm that the QDs are pseudomorphic on AlN within the error bar of the characterization technique, i.e. the relaxation of the *a* lattice parameter is smaller than 1%. Relaxation here is defined as $R = (a - a_{AlN})/(a_0 - a_{AlN})$, where *a* is the measured average in-plane lattice parameter, a_0 is the average lattice parameter of the relaxed AlGaN SLs and a_{AlN} is the lattice parameter of the AlN matrix. From the maps, I assume that the structures are fully strained on the AlN substrate. Figure 4.17(b) shows x-ray diffraction (XRD) θ-2θ scans around the (0002) reflection of all the samples, together with simulations using the X'Pert Epitaxy software from Panalytical. From such diffractograms, I extract the superlattice (SL) period, d_p, and average SL *c* lattice parameter, $<c_{SL}>$, which are summarized in Table II for the samples under study. From all these data, the average *c* lattice parameter in the QD layer, $<c_{QD}>$, can be calculated from the equation:

$$< c_{SL} > d_p = c_{AlN}(d_p - d_{QD}) + < c_{QD} > d_{QD} \quad (4.4)$$

where c_{AlN} is the lattice parameter of relaxed AlN, and the average thickness of the QD layer, d_{QD}, is given by:

$$d_{QD} = (\Phi_{Al} + \eta_{Ga}\Phi_{Ga})t_d \quad (4.5)$$

where Φ_{Ga} (Φ_{Al}) are deposited Ga (Al) flux, η_{Ga} (<1)* is the Ga sticking coefficient. Note that the nominal QD thicknesses are already corrected to take into account the 0.05 ML/s Ga desorption rate, the Al sticking coefficient is considered as 1, and t_d is the QD deposition time. The average Al composition, x of the QD layer can be obtained from:

$$x = \frac{\Phi_{Al} t_d}{d_{QD}} = \frac{c'_{GaN} - < c_{QD} >}{c'_{GaN} - c_{AlN}} \quad (4.6)$$

where I assume pseudomorphic growth, and thus the Vegard's law is modified so that c'_{GaN} is the lattice parameter of GaN biaxially strained on AlN. Combining Eqs. (4.4) and (4.6), I extract x = 12.0% and d_{QD} = 5.2 ML for E3175, in good agreement with the microscopic-scale calculation performed by GPA on HAADF-STEM. The calculated x and d_{QD} for all the samples assuming biaxial strain configuration are summarized in Table 4.4. However, this picture of biaxially strained QD SLs is oversimplified. The biaxial deformation assumes identical stress along the <11-20> directions and no stress along <0001>. In a 3D structure like AlGaN/AlN QDs, the surrounding AlN matrix imposes a compressive stress on the QD facets with a component along <0001> which might not be negligible. Therefore, a complete 3D modeling of actual strain distribution is required for precise determination of the Al composition, as it is described below.

Sample	d_p (nm)	$<c_{SL}>$ (nm)	Biaxial strain configuration		e_{zz}/e_{xx}	3D strain calculation	
			x (%)	d_{QD} (ML)		x (%)	d_{QD} (ML)
E3180	12.7	0.4994	11.7	2.4	-	-	-
E3179	13.0	0.4997	11.0	3.2	-0.236	9.6	3.6
E3178	13.3	0.5000	11.6	3.9	-0.267	10.4	4.4
E3177	13.6	0.5003	11.9	4.7	-0.337	11.0	5.1
E3175	13.9	0.5005	12.0	5.2	-0.375	11.4	5.5

Table 4.4: SL period (d_p) and average SL c lattice parameter ($<c_{SL}>$) measured by XRD in the AlGaN QD samples under study. Extracted average Al composition (x) and thickness (d_{QD}) of the QD layer assuming biaxial strain configuration. Strain ratio e_{zz}/e_{xx} in the center of the QDs obtained from calculations of the 3D strain distribution in the structure. Extracted values of x and d_{QD} using the 3D strain calculation.

* At 720°C, the desorption of adsorbed Ga on a GaN surface happens at a rate of 0.05 ML/s. Taking into account that our impinging Ga flux is in the range of 0.3 ML/s, the Ga sticking coefficient is only 0.83 in absence of other factors that can further reduce this value (for instance, strain).

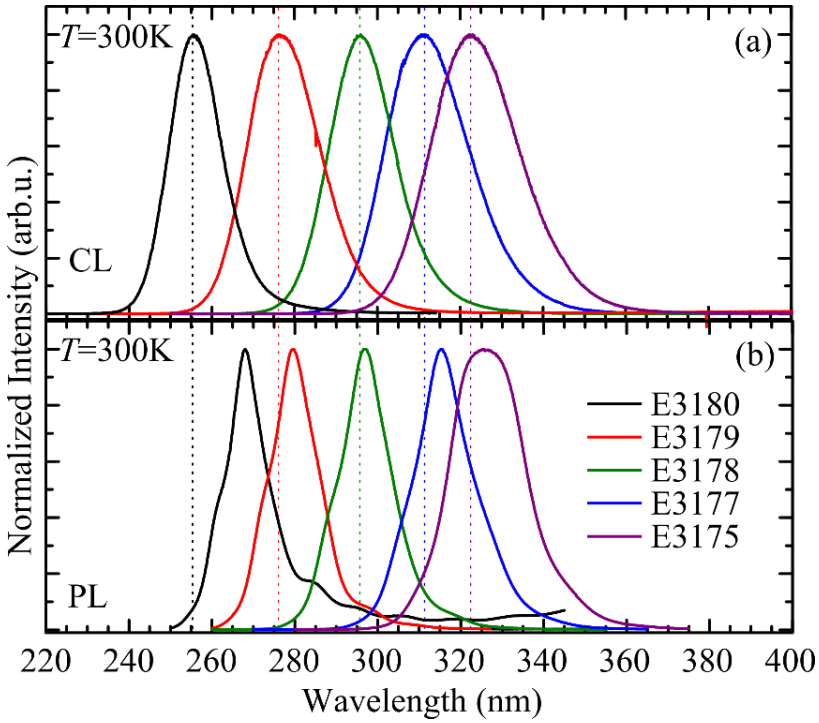

Figure 4.18: Normalized room-temperature CL spectra of AlGaN QDs obtained by deposition of different amoutns of AlGaN in Table 4.3.

The luminescence of each sample was characterized as a function of temperature using CL and PL. Normalized CL spectra at room temperature are displayed in Figure 4.18(a), and the emission peak wavelengths (λ_{RT}) are summarized in Table 4.3, whereas the peak emission spectra measured by PL as shown in Figure 4.18(b) are red-shift from those measured by CL in the range of 14-51 meV. Except the spectrum of E3180, which shows a huge deviation (217 meV). Such deviation is attributed the fact that the smaller QDs are not active for PL measurements since they cannot be excited by the laser. Increasing the amount of AlGaN in each QD layer from 3 to 7 ML, results in a CL red shift from 256 to 323 nm which associated to a weaker confinement effect. CL from the wetting layer could be expected around 240 nm for the alloy composition under consideration. However, features associated to the wetting layer are only observed in the case of highly diluted QDs (for instance, as reported by simeonov *et al*. [230] for GaN/AlN with maximum QD density of 5×10^{10} cm^{-2}). For high QD density, a good transfer of the free carriers to the QDs, enhanced by the internal electric field, quenches the emission associated to the wetting layer. In cases of quasi-coalescence, like 6 or 7 ML QDs (E3177 or E3175), the electronic level of the wetting layer is strongly perturbed by the presence of the dots. A 3D calculation of the electronic structure, considering both the QDs and the wetting layer, is required to identify the electronic levels.

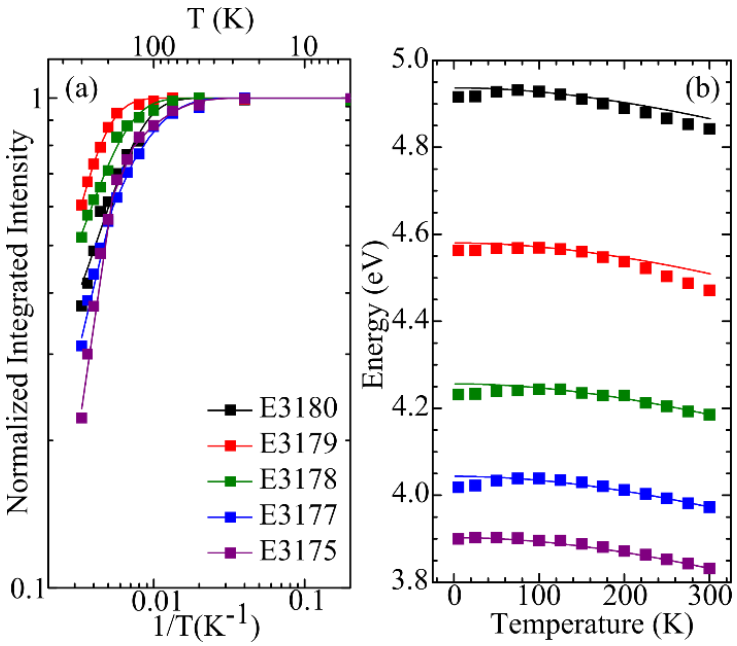

Figure 4.19: (a) Evolution of the integrated CL intensity from AlGaN/AlN QDs with temperature. Solid lines are fits to Eq.(4.3). (b) Temperature dependence of the CL peak position of AlGaN/AlN QDs. Solid lines represent the evolutions of the emission with temperature following Varshni's equation. Varshni's parameters of AlGaN samples were obtained by linear interpolation between the AlN [61] and GaN [59] values.

Figure 4.19(a) presents the integrated emission intensity as a function of temperature normalized to its value at low temperature (T = 5 K) for various AlGaN QD samples. In all cases the CL intensity remains stable at low temperatures (T < 30 K). Therefore, the IQE can be approximated by Eqs.(4.2) or/and (4.3).

Solid lines of 3 to 5 ML QDs are fit to Eq.(4.3). The calculated values of E_a and a are summarized in Table 4.3. The maximum E_a corresponds to 4 ML QDs (E3179). Let us remind that increasing the amount of deposited AlGaN results in an increase of the QD density, which reaches saturation at 6 ML, as confirmed in Figure 4.23(c). When the QDs get closer, the hole wavefunction, which is located at the base of the dot due to the polarization-induced internal electric field, gets delocalized, and the probability of carriers to escape via the wetting layer increases, which explains the monotonous decrease of IQE from 5 to 7 ML QDs. In addition, in high density QDs (6 and 7 ML QDs) the variation of IQE with temperature do no longer follows Eq. (4.3); a second activation energy is required to obtain a good fit, similar to the case of GaN/AlN QWs [130]. This provides additional evidence that 6 and 7 ML QDs start losing the character of QDs and their wetting layers start playing role as non-radiative recombination path.

The CL spectral shifts with temperature, which can provide information concerning

carrier localization in intra-dot potential fluctuations, are shown in Figure 4.19(b). All the samples present a red shift with very slight S-shaped evolution of the CL with increasing temperature which fit with the expected evolution of the AlGaN band gap calculated using Varshni's equation (solid lines in the figure) [59], [61]. Therefore, I conclude that the effect of potential fluctuations inside the QDs is negligible, which agree with our previous results in section 4.3 [231].This is in contrast with the results in InGaN/GaN QDs and in nonpolar GaN/AlN QDs, which present a strong S-shaped evolution of the PL with temperature attributed to intra-dot potential fluctuations associated to alloy inhomogeneities [130], [217] or to the presence of stacking faults [218], respectively.

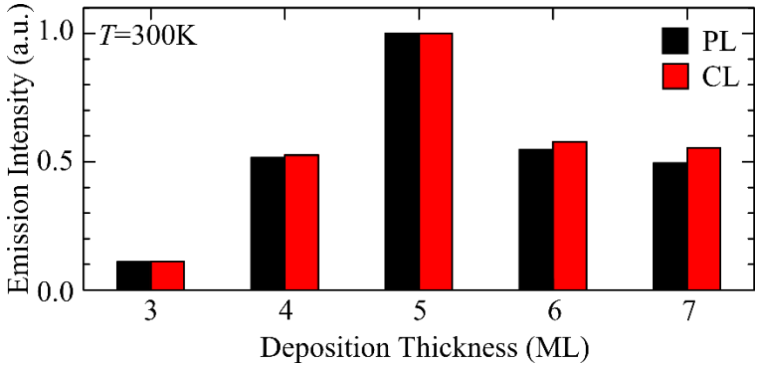

Figure 4.20: Variation of the room-temperature integrated CL/PL intensity as function of amount of AlGaN in the QD layer. In case of PL, the intensity is corrected to account for the different absorption volume.

Figure 4.20 shows the room-temperature emission intensity of each sample measured by PL and CL and normalized to the maximum value. The PL data are corrected by the amount of AlGaN in the samples, to account for the incomplete excitation absorption – PL measurements used an Ar Laser (244 Nm) as excitation source, so that photons could only be absorbed in the AlGaN QD layers, while the AlN barriers were optically transparent. Therefore, a correction by the amount of AlGaN is required to account for the different absorption in the various samples. In contrast, the generation of electron-hole pairs by CL should be comparable in all the samples, since they have approximately the same density. The variation of emission intensity shows the same trend in both cases (CL and PL). Initially, the intensity increases with the amount of AlGaN due to the improved IQE and the increased QD density. Maximum emission intensity is observed for 5 ML QDs (E3178), where the slight decrease of IQE with respect to 4 ML QDs (E3179) is compensated by the higher QD density. The marked decrease in 6 and 7 ML QDs emission intensity can be directly related to the drop in IQE (Figure 4.19(a)) and the saturation of the QD density.

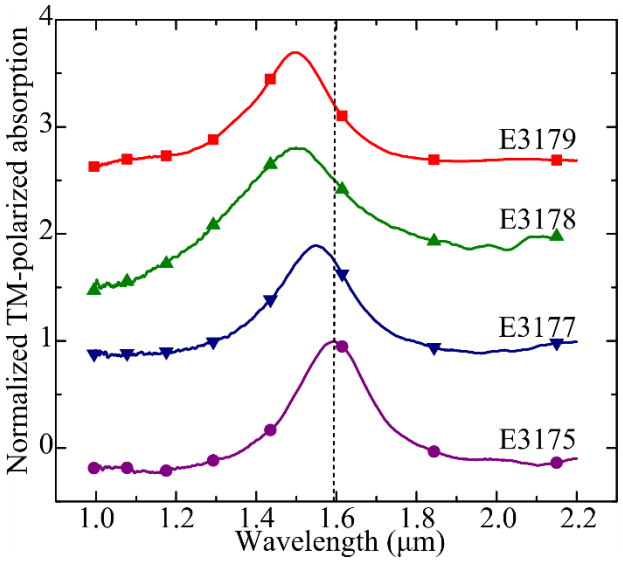

Figure 4.21: Room-temperature infrared absorption spectra for TM-polarized light measured in AlGaN/AlN QDs.

Further information on the electronic structure of the AlGaN QDs was obtained by studying the excited electronic levels in the conduction band using FTIR spectroscopy. Figure 4.21 displays the normalized absorption of transverse-magnetic (TM) polarized light measured in AlGaN/AlN QDs at room temperature. No transverse-electric (TE) polarized absorption was observed for any of the samples. The absorption peak energies, summarized in Table 4.3, red shift when increase the amount of AlGaN in the QD layer. These absorption lines are assigned to intra-band transitions between the ground state of the conduction band, *s*, and the first excited electronic state confined along the growth axis, p_z. The lateral confinement in the QDs can give rise to additional transitions under TE-polarized excitation. However, taking into account the lateral dimension of the QDs ~7.5 nm, the *s*-p_x and *s*-p_y transitions should be masked by the sapphire absorption for $\lambda > 5$ μm.

For interpretation and correlation of the interband and intraband optical data, I have performed 3D calculations of the QD strain state, band diagram and quantum confined states by using the Nextnano^3 Schrödinger-Poisson equation solver [224] with the GaN and AlN parameters in ref. [119] and neglecting the AlGaN bowing parameters. The simulated structure consisted of 10 periods of $Al_{0.1}Ga_{0.9}N$ QDs separated by 10-nm-thick AlN barriers grown on bulk AlN. In each layer, the QDs were defined as a hexagonal truncated pyramids with {10-13} facets [212], connected by a 0.5-nm-thick wetting layer. A schematic view of the structure is presented in Figure 4.22(a)-(b) In this example, the $Al_{0.1}Ga_{0.9}N$ QDs have a base diameter of 8.3 nm and a height of 1.5 nm.

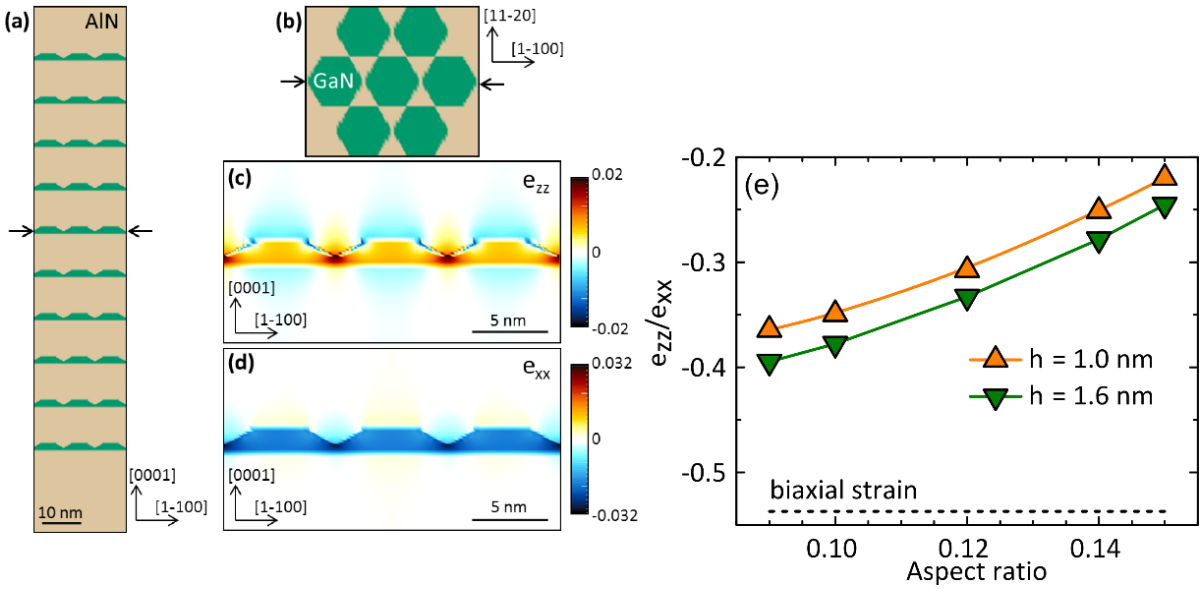

Figure 4.22: (a) Cross-section and (b) plane-view of a schematic material description of the structure simulated with Nextnano[3]. In this example, $Al_{0.1}Ga_{0.9}N$ QDs have a base diameter of 8.3 nm and a height of 1.5 nm, and are separated by 10 nm AlN barriers. Cross-sectional views of the (c) e_{zz} and (d) e_{xx} strain components in a QD layer. (e) Evolution of the e_{zz}/e_{xx} ratio as a function of the aspect ratio in QDs with a height of 1 nm and 1.6 nm. The dashed line indicates the value for biaxial strain.

The 3D strain distribution was calculated by minimization of the elastic energy through the application of periodic boundary conditions along the <1-100> and <11-20> directions. Figure 4.22(c) and (d) display cross-sectional views of the strain components along the <0001> direction, e_{zz}, and along the <1-100> direction, e_{xx}, for three QDs passing through the center of the simulated structure. In this example, the ratio between e_{zz} and e_{xx} at the QD center, $e_{zz}/e_{xx} = -0.337$, is significantly smaller than the theoretical value in the biaxial strain configuration ($e_{zz}/e_{xx} \approx -0.537$). This confirms that the AlN matrix results in the application of a uniaxial compressive stress along <0001> which adds up to the biaxial strain configuration, hence reducing the value of e_{zz}. Note that the value of e_{zz}/e_{xx} is sensitive to the QD aspect ratio (τ = QD height / base diameter), as illustrated in Figure 4.22(e).

For the calculation of the band profiles, the spontaneous and piezoelectric polarizations and the band gap deformation potentials were taken into account. Figure 4.23(a) displays a cross section view of the conduction band in the structure in Figure 4.22, and Figure 4.23(b) describes a conduction band profile along <0001> passing through the center of the QDs. The $Al_{0.1}Ga_{0.9}N$/AlN sequence presents the saw-tooth profile characteristic of III-nitride, due to spontaneous and piezoelectric polarizations. In this example, the magnitude of the electric field in the center of the QDs is 6.7 MV/cm, to be compared with 7.1 MV/cm expected in an $Al_{0.1}Ga_{0.9}N$/AlN QW with the same thickness.

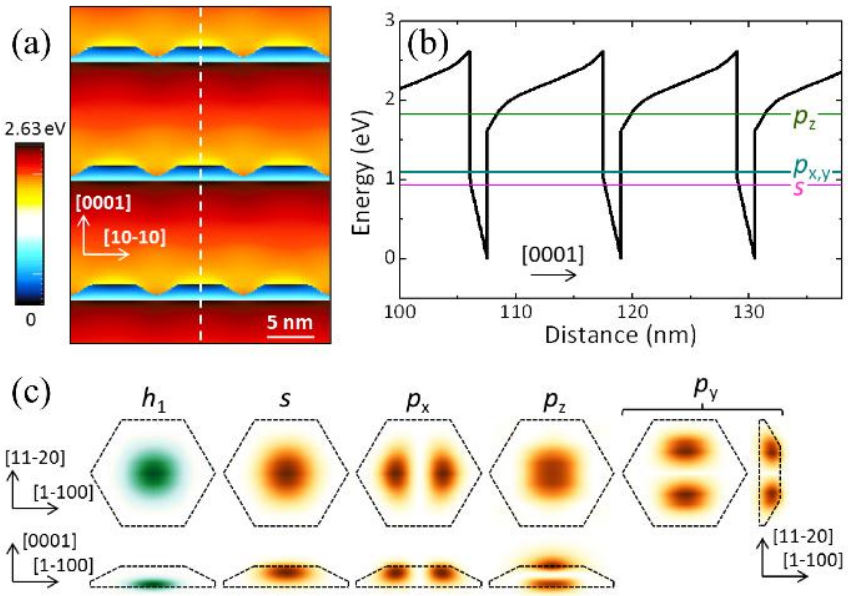

Figure 4.23: (a) Cross-sectional view of the conduction band of 3 QD layers in the stack described in Figure 4.22(a). (b) Conduction band profile along the growth axis passing though the center of the QDs (dashed line in (a)). The energetic position of the electronic levels s, p_x, p_y and p_z are indicated in the figure. (c) Probability density distribution, $|\Psi(r)|^2$, for the first hole state in the valence band (h_1), the three lowest electron states of the conduction band (s, p_x, p_y), and the first excited electron state due to confinement along the growth axis (p_z).

Figure 4.23(c) presents cross-sectional views of the square wave function, $|\Psi(r)|^2$, for the first hole state in the valence band (h_1), the three lowest electron states (s, p_x, p_y), and the first excited state with a secondary node along the growth axis (p_z). As a result of the polarization-induced internal electric field, s is shifted towards the top of the QD, whereas h_1 is confined in the wetting layer, as previously described in GaN QDs [232], [233].

Figure 4.24 displays the evolution of the s-p_z intraband transition as a function of the s-h_1 interband transition, comparing various nanostructures. In the case of QWs, experimental data correspond to FTIR and PL measurements of GaN/AlN QWs with 3-4 nm AlN barriers and various QW thicknesses (data in ref. [119]). An increase of the QW width results in a red shift of both interband and intraband transitions. The solid line corresponds to one-dimensional calculations using the Nextnano^3 Schrödinger-Poisson solver with the parameters in ref. [119], assuming that the final strain state of the structure corresponds to the minimum-energy configuration independent of the substrate, as experimentally observed [234]. Since the interband transition is more sensitive to the strain state and electric field whereas the excited levels are more sensitive to the confinement (see Figs. 3 and 4 in ref. [235]), the good fit between theory and experiment in Figure 4.24 confirms that our model provides a good description of the structure as a whole.

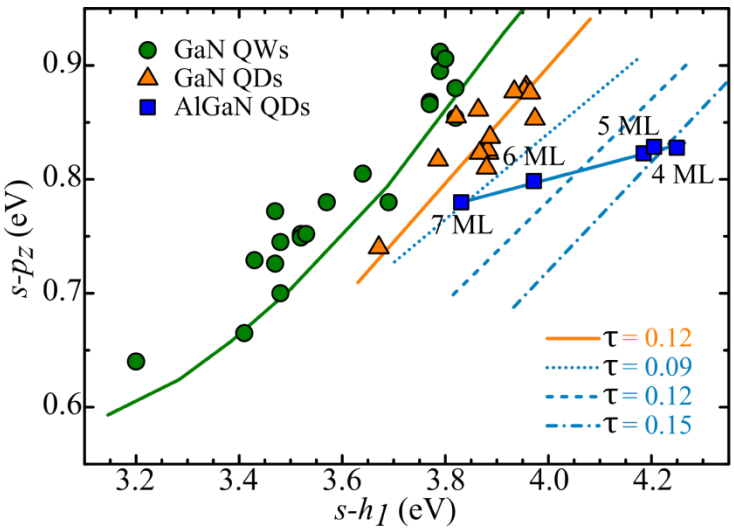

Figure 4.24: Evolution of the s-p_z intraband transition energy as a function of the s-h_1 interband transition in various nanostructures. Experimental points represent peak intraband absorption energy vs. peak PL energy for GaN/AlN QWs [217], GaN/AlN QDs [131], and the AlGaN/AlN QD samples in this study. The solid lines are theoretical calculations. In the case of GaN/AlN QDs, calculations assume an aspect ratio τ = 0.12. In the case of AlGaN/AlN QDs, the solid line is a guide for the eye, and dashed/dotted lines are calculations assuming various aspect ratios.

In the case of GaN/AlN QDs, experimental data correspond to FTIR and PL measurements of Stranski-Krastanov GaN/AlN QDs with 3-4 nm AlN barriers, the dots being deposited under N-rich conditions varying the growth temperature or the amount of GaN in the QD layer (data in ref. [131]). The experimental GaN QD data are well fitted by the solid line which is obtained from 3D calculations that consider a strain distribution extracted by elastic energy minimization. The aspect ratio used for the 3D calculations is 0.12, following the results of Adelmann *et al*. in similarly grown structures [225]. The QD intraband transition is blue shifted in comparison to QWs due, on the one hand, to the lateral confinement in the QDs, and, on the other hand, to the additional compressive strain along <0001> imposed by the AlN matrix, as observed in Figure 4.22(c).

The data corresponding to the $Al_{0.1}Ga_{0.9}N$/AlN QDs in this study are further blue shifted in terms of interband transition due to the introduction of Al in the QDs. However, the experimental intraband vs. interband trend cannot be fitted using a unique aspect ratio value. Data is rather consistent with a decrease of the aspect ratio for increasing amount of AlGaN deposited, obtaining good fits for 4 ML QDs with $\tau = 0.15$, whereas 7 ML QDs require $\tau = 0.09$. These values are within the large error bars of microscopy characterization. Therefore, in the case of AlGaN QDs (in this case Al content is ~10%), the variation of aspect ratio when changing the amount of deposited AlGaN cannot be neglected in the interpretation of the optical data.

Using this information of aspect ratio, I have re-calculated the strain distribution in the QDs under study (for each sample, I have considered the geometry (QD height and diameter) that provides a better fit to PL and intraband absorption), obtaining e_{zz}/e_{xx} as summarized in Table 4.4. By applying these values of strain to the calculation of c'_{GaN} in Eq. (4.6), I extract a more precise estimation of the average QD alloy compositions (10.6±0.8% for all the samples) and layer thicknesses, also presented in Table 4.4. The obtained d_{QD} values correspond to (85±5)% of the nominal amounts of AlGaN. These deviations of d_{QD} and the difference between the measured Al mole fraction and the metal flux ratio ($\Phi_{Al}/\Phi_{metal} = 0.09$) can be explained by the fact that Ga desorption is active at the growth temperature, and by the etching of GaN observed during AlN overgrowth [226].

In conclusion, I have demonstrated the PA-MBE growth of AlGaN/AlN QDs with various amounts of AlGaN in each QD layer. The structural characterization has shown that the AlGaN QD density increases with the amount of deposited material, and saturates at ~9×10^{11} cm^{-2}. XRD confirms that the AlGaN QDs grow pseudomorphic in the AlN matrix for deposited thickness up to 7 ML. XRD measurements point to an Al incorporation in the ~11%, slightly higher than the Al-to-metal flux ratio due to Ga desorption. The interband emission of the QDs was studied by PL and CL, and the *s*-p_z intra-conduction-band transition was identified by FTIR. By comparing interband and intraband characterization with 3D modeling of the electronic structure accounting for the elastic energy minimization, I conclude that the QDs strain distribution deviates significantly from the biaxial strain configuration, and a decrease of the QD height/base diameter ratio takes place when increasing the amount of deposited AlGaN. Best room-temperature emission intensity is obtained for QDs formed by deposition of 5 ML of AlGaN, due to a compromise between internal quantum efficiency and QD density.

4.5 Target-wavelength approaching

In the previous section, I determined that the best optical performance which was achieved by deposition of 5 ML of AlGaN to form each QD layer. However, in this experiment, the thicknesses of AlGaN were fixed at 4 ML which is the condition that provide best IQE, since the experiments were parallel done before I have a conclusion of 5 ML-maximum luminescence. The samples of 80 periods of AlGaN QDs with 5-nm-thick AlN

barriers were synthesized by PAMBE on 1-µm-thick (0001)-oriented AlN-on-sapphire templates. The Φ_N was set at 0.38 ML/s. The AlGaN QD was performed under N-rich conditions [131], [213], i.e. the $\Phi_{metal} < \Phi_N = 0.38$ ML/s. The QDs were Si-doped in the 10^{19} cm^{-3} range. The Φ_{Al}/Φ_{metal} of the first sample was set at 0.11 and was systematically increased to 0.14 and 0.18. The substrate temperature was fixed at 720°C, and was progressively increased to 730 and 740°C. Schematic of the grown structure in this section is illustrated in Figure 4.25, the growth parameters for all the samples are presented in Table 4.5.

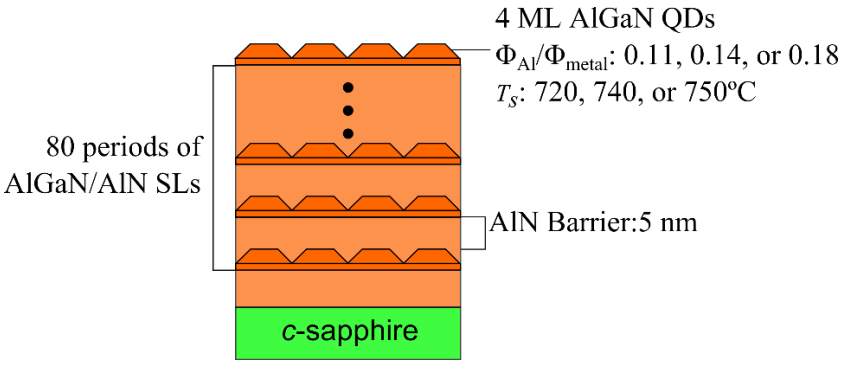

Figure 4.25: The structure of the grown samples for section 4.5, consisting of 80 periods of AlGaN/AlN QD SLs. The thicknesses of AlGaN QDs and AlN barriers were set at 4 ML and 5 nm, respectively, while the Al contents (Φ_{Al}/Φ_{metal}) were varied from 0.11, 0.14 to 0.18, and the substrate temperatures were varied from 720, 740 to 750°C.

sample	Φ_{Al}/Φ_{metal}	AlGaN QDs thickness (ML)	Substrate temperature (°C)	Peak emission wavelength (nm)
E3274	0.11	4	720	295
E3273	0.11	4	730	291
E3275	0.11	4	740	280
E3277	0.14	4	740	274
E3278, E3279	0.18	4	740	261

Table 4.5: Description of the AlGaN QD samples under study: growth parameters, peak emission wavelength at room temperature.

As illustrated in Table 4.5, the spectral response of E3274 peaks at 295 nm. The sample was grown with the same AlGaN QD thickness (4 ML) and approximately the same nominal Al content (~10%) as E3179 (see Table 4.3 in section 4.4) which peaks at 276 nm. I attribute the red-shift of E3274 to the lower growth temperature than that used for E3179. Increasing substrate temperature results in two phenomena, i.e. increasing Ga desorption rate from the growth structure (higher Al content QDs is obtained) and/or enhancing adatom mobility (larger QDs are generated). The higher Al content blue shifts emission spectrum, whereas the larger QDs, due to the weaker carrier confinement, red-shifts emission spectrum. Thus, in

my case, the higher Al content overwhelmed the shape evolution of the dots when increasing temperature.

The increasing of Al content and substrate temperature were done, in order to blue shift the peak to the peak emission wavelength to (λ_{RT} = 260-270 nm) for water purification. From our experimental results, increasing the substrate temperature from 720 to 740 ºC monotonously blue shifts peak emission spectrum from 295 to 280 nm as shown in Figure 4.26, which indicates that the effect of Ga desorption overwhelmed that of QD-shape evolution when increasing the substrate temperature.

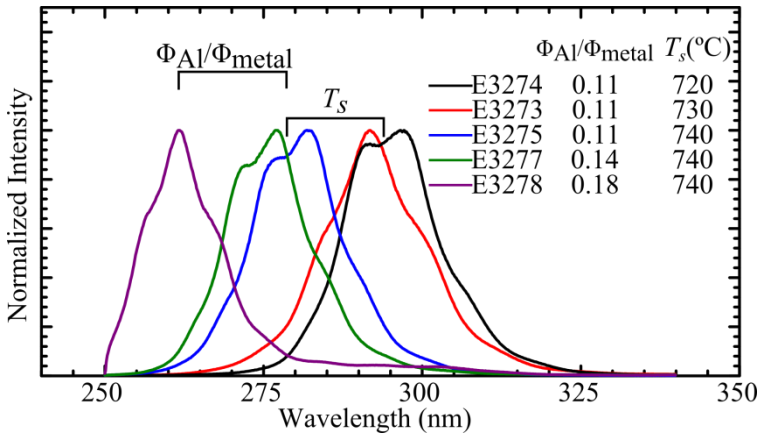

Figure 4.26: Room-temperature PL spectra of AlGaN QDs in Table 4.5

It was reported [236] that at very high growth temperature (~758 ºC), GaN QDs are not well-formed and display very broad size distribution which might result in broad emission linewidth. To avoid entering that regime, I decided to stop increasing T_s, but increasing Φ_{Al}/Φ_{metal} instead, to further blue shift the peak emission spectra. As shown in Table 4.5, increasing the Φ_{Al}/Φ_{metal} from 0.11 to 0.14, and 0.18% shifts peak emission spectra from 280 to 261 nm. Eventually, the growth condition of E3278, which provides peak emission spectrum at 261 nm, were set as the condition to fabricate the prototype active region for water purification.

4.6 Post-growth dice shaping

Despite finding the optimum growth parameters to acquire highly efficient active media, post-growth processes must be applied to enhance the light extraction. Since all the growth was performed on AlN-on-sapphire substrates, the transparency of the sample allows multiple-pass configurations to extract the light from the medium. Processes can be applied

to improve light extraction from a transparent medium, i.e. material shaping, metallizing and surface texturing [237]. The material shaping into a truncated-inverted-pyramid (TIP) geometry [238] combined with an external back mirror and surface texturing techniques have led to an external quantum efficiency of 50% for GaP-based LEDs [239].

I have performed a study of the effect shaping and back-metallizing the active region, using stacks of 80 periods of AlGaN/AlN QDs. The dots were deposited under N-rich conditions, and the substrate temperature, Al-to-metal flux ratio, and amount of AlGaN in each QD layer were set at $T_S = 720°C$, $\Phi_{Al}/\Phi_{metal} = 0.12$, and $d_{QD} = 3$ ML, respectively. The sample was diced into 8 pieces of 4 mm × 4 mm, namely A, B, C, D, E, F and G, which were characterized by PL. Subsequently, different treatments were applied to the various pieces, as summarized in Table 4.6.

Sample	Back polishing	Edge polishing	Metallizing	Improvement factor (%)
A			✓	-2
B				0
C	✓			-19
D		✓		-11
E		✓	✓	11
F	✓	✓		-10
G	✓	✓	✓	22
H	✓		✓	31

Table 4.6: Applied processes to the samples (back polishing, edge polishing, and metallizing) and their improvement factors.

The edge polishing of the samples was performed at a 45° angle. The metallization consisted in the deposition of 200 nm of aluminum by e-beam metallization. One of the samples (B) was kept as a reference of as-grown conditions. After the treatments, all the samples were measured by PL in order to assess the improvement factors due to each treatment, as illustrated in Figure 4.27.

Against the report on GaP based LEDs [238], back and edge polishings (A, D, and F) in our experiment did not improve but slightly degraded the light extraction efficiency. This might attribute to the annihilation of the bottom surface roughening of the sapphire substrate, which primitively assists in light randomization (promoting multiple pass light). However, the treatments of metallizing on the polished samples (E, G, and H) resulted in the improvement factors of 12-31%. Thus, in our case, the back-metallization helps improving the light extraction efficiency if and only if performing it on the polished surfaces.

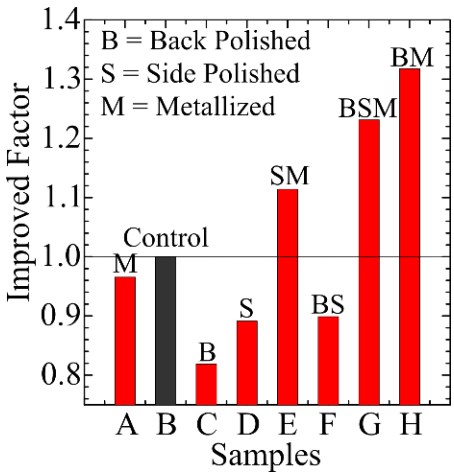

Figure 4.27: Improvement factor of samples after Back polishing, Edge polishing and Metallizing treatments.

4.7 The growth on SiC substrate

In the previous sections, the growths of AlGaN/AlN QD structures were performed on sapphire substrates. Being ultraviolet-transparent, sapphire presents advantages in terms of light extraction. However, its high resistivity and low thermal conductivity are drawbacks for some applications, involving electron-pumped devices. As an alternative, SiC is almost lattice matched with AlN and present advantages over the sapphire substrate in terms of thermal and electrical conductivity, although sacrificing the substrate transparency (6H-SiC band gap at 3.23 eV [240], i.e. 384 nm). However, the main factor that limits the use of SiC today is the price of high-quality SiC substrates.

In order to illustrate the possibility to transfer the growth process to SiC, I synthesized AlGaN/AlN QDs samples on both sapphire and SiC substrates using the same growth conditions as E3279 for acquiring a peak emission spectrum of 260-270 nm. The growth of 80 periods of AlGaN/AlN QDs with 5-nm-thick AlN barriers was performed simultaneously on both AlN-on-sapphire and SiC substrates. The Φ_N was set at 0.38 ML/s. The AlGaN QD was performed under N-rich condition, and the dots were Si-doped in the 10^{19} cm^{-3} range. The Φ_{Al} /Φ_{metal} was set at 0.18 and the substrate temperature was fixed at 740°C (68% of heater). As illustrated in Figure 4.28(a), the peak emission spectrum of active medium grown on SiC was characterized by PL, showing emission peak at 270 nm, slightly red shifted from that grown on AlN-on-sapphire. Both spectra show comparable full width at half maximum (12-14 nm) and luminescence intensity (~12,000 counts/sec).

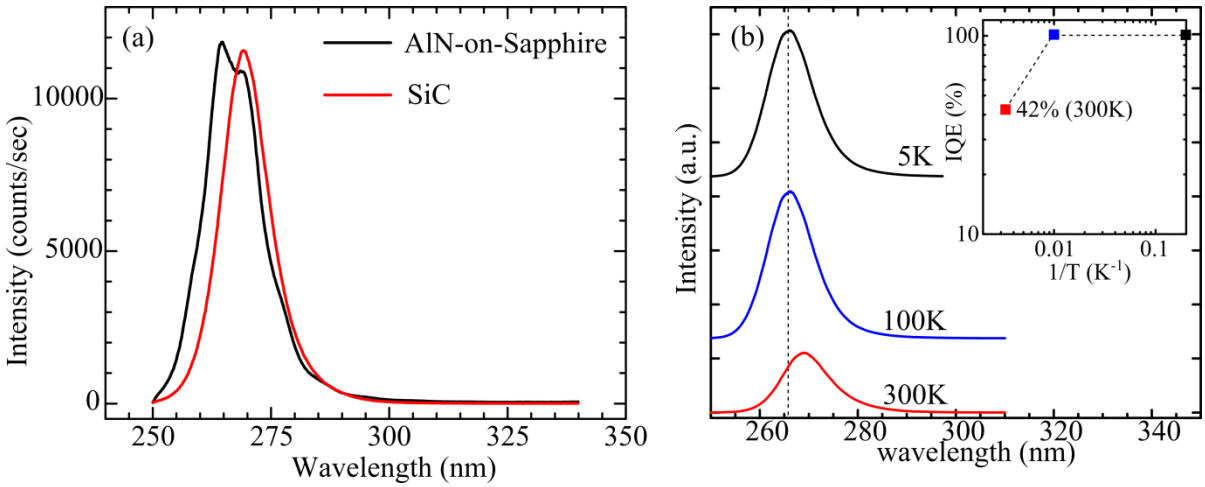

Figure 4.28 (a) Room-temperature PL spectra of AlGaN QDs grown on AlN-on-saphhire and SiC substrates. (b) Evolution of the integrated PL intensity from AlGaN/AlN QDs grown on SiC with temperature.

The IQE of AlGaN/AlN QDs grown on SiC was estimated by the ratio of integrated intensity measured at room and low (5K) temperatures, providing the IQE of 42% as displayed in Figure 4.28(b), which is in the range of all the presented samples that were grown on AlN-on-sapphire (20-60%). The spectrum at 100K was added to prove that the integrated intensities were constant at low temperature region, to assure the validity of the probed IQE.

4.8 Conclusions

The first experiment aimed at identifying the penetration depth of the electrons at the acceleration voltage of 5kV which can set the minimum active region thickness, consisting of AlGaN QD layers and AlN barriers, at 400 nm. The minimum AlN barrier thickness of 4-5 nm was subsequently designed, in order to achieve surface planarization, confirmed by the streaky RHEED patterns, and to prevent QD vertical correlation. Such AlN barrier thickness is assured to have a good carrier collection from the structure since it is lower than the maximum AlN barrier thickness which was defined from the carrier diffusion length measurement.

The efficient amount of AlGaN in each QD layer (5 ML QDs) was explored in section 4.4. It is the AlGaN QD thickness condition that provides maximum luminescence at room-temperature which compromise between the conditions of best IQE of 60% (4 ML QDs) and

highest QD density of $(9\pm1)\times10^{11}$ cm^{-2} (6 ML QDs). Furthermore, from the fitting of theoretical calculations performed by Nextnano^3 solver to the experimental information, the evolution of QD shape was discovered. I found that the QD ratio (height/base diameter) decreases when increasing the amount of deposited AlGaN.

By knowing the competent thicknesses of AlN barriers and AlGaN QDs and the active region thickness, the periods of superlattices can be further designed (~80 periods). The peak emission spectra were illustrated that they can be adjusted by applying 3 main growth parameters, namely the substrate temperature, Φ_{Al}/Φ_{metal}, and the amount of AlGaN in each QD layer. After the AlGaN QD thickness was set to obtain the maximum efficiency. Approaching the targeted wavelength at 260 nm was performed by systematically adjusting the Φ_{Al}/Φ_{metal}, and substrate temperature. Despite active region optimization, post–growth technique, i.e. polishing and metalizing are shown to increase the luminescence efficiency for 30% from as-grown sample as illustrated in the section 4.6.

Because I have been working on electron injecting devices, the high resistivity and low thermal conductivity of sapphire are important drawbacks. At the last section, I perform the growth on SiC to demonstrate that it can be synthesized without any degradation in terms of spectral response as shown in section 4.7. The choice of SiC substrate can be made when a good thermal conductivity is required, however sacrificing the substrate transparency.

Chapter 5

5 AlGaN/AlN Nanodisks on GaN Nanowires

In this chapter, I present a study of AlGaN sections on GaN nanowires and use this know-how as a foundation for the fabrication of AlGaN/AlN nanodisks. The main challenge to grow ternary alloys in nanowire geometry is the chemical inhomogeneity which is experimentally evidenced by structural and optical characterization. This inhomogeneity is correlated with the misfit strain distribution by performing strain calculations using the Nextnano^3 solver.

5.1 Introduction

For a decade, nanowires (NWs) have been considered as an attractive building block for III-N optoelectronics especially for light emitting devices since this nanostructure provides a solution for well-known problems of III-nitrides such as defects and dislocations. There are two ways to fabricate NW light emitting diodes (LEDs), either via top–down or bottom–up approaches. The first one is usually performed by etching a planar III-N LED structure into a rod-like morphology. Ramesh *et al*. [241] showed that the internal quantum efficiency (IQE) of top–down NWs created by etching the InGaN/GaN quantum wells (QWs) was improved up to 60% while the luminescence peak was controlled by adjusting the InGaN QW thickness. However, the drawback of the top-down NW is the etching process that is tedious and might deteriorate the material quality. Such problems could be possibly avoided by using bottom-up NWs.

Up to now, several research teams have developed the LEDs based on self-assembly NWs. Those nano-devices can be synthesized by different growth methods [135], [137], [242], [243]. For instance, Kim *et al*. [242] reported self-assembly GaN NW LEDs grown by hybride vapor phase epitaxy. In their case, the active region was InGaN/GaN QWs which provided the emission peak at 466 nm. Hersee *at al*. [243] realized the GaN NWs LEDs using selective-area growth via metalorganic vapor phase epitaxy, showing the spectrum peak at 372 nm. For molecular beam epitaxy (MBE), Kikuchi *et al*. [137] demonstrated the NW LEDs using InGaN/GaN nanodisks (NDs) as an active region, with the luminescence

peak locating at ~580 nm. Later on, Lin *et al*. [135] presented a realization of phosphor-free mixed-color white light emission LEDs by fabricating InGaN/GaN NDs on GaN NWs. Luminescence from such devices was obtained by collecting various locally monochromatic emissions due to the statistical distribution of GaN NW diameter in the range of 10-25 nm.

Generally, to tune the emission wavelength of NW LEDs, the bandgap of their active region should be engineered by heterostructuring and alloying the NWs. In catalyst-free growth, it is straightforward to create nanodisks by tailoring the bandgap along the wire axis. Several groups showed a feasibility to adjust the luminescence spectra from the III-N NDs using the quantum confinement determined by the ND height [244], [245].

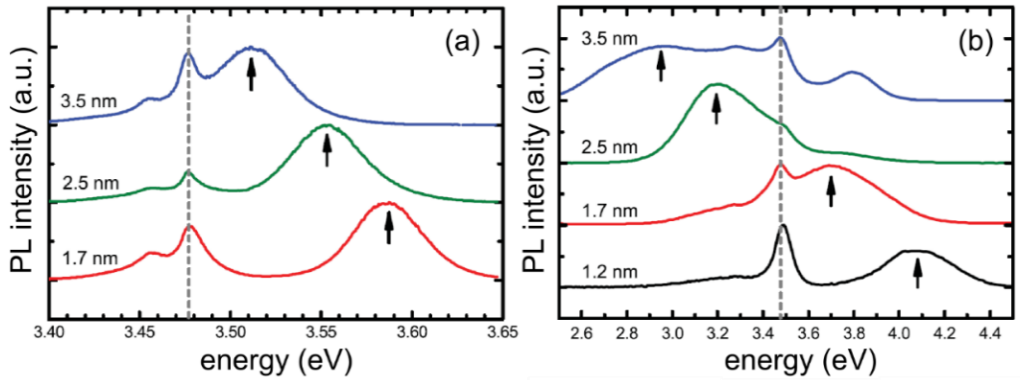

Figure 5.1: 4K-Photoluminescence spectra of NDs with different height (d_{ND}). The ND related emissions are indicated by arrows. The dotted line at 3.477 eV indicates the near-band-edge emission from the GaN base region. (a) Three GaN/$Al_xGa_{1-x}N$ NW samples with x = 0.14 and d_{ND} = 1.7, 2.5, and 3.5 nm. (b) Four GaN/AlN NW samples with d_{ND} = 1.2, 1.7, 2.5, and 3.5 nm [244].

Renard *et al*. [245] show that the spectral peak of GaN/AlN NDs was tuned from 458 to 322 nm (2.71 to 3.85 eV) when the ND thickness was decreased from 4 to 1 nm. Later on, Furtmayr *et al*. extensively studied the luminescence characteristics of GaN/Al(Ga)N NDs [244]. The influences of quantum confinement and polarization-induced internal electric field allow them to tune the emission wavelength of GaN/$Al_{0.14}Ga_{0.86}N$ NDs from 353 to 345 nm (3.51 to 3.59 eV) when the ND thickness was decreased from 3.5 to 1.7 nm (Figure 5.1(a)). In the case of GaN/AlN NDs, they were able to tune the emission wavelength from 2.95 to 4.10 eV by decreasing ND thickness from 3.5 to 1.2 nm as illustrated in Figure 5.1 (b). In this manuscript, I focus on synthesizing the III-N NDs that could luminesce in the ultraviolet (UV) -C spectral region. A shorter wavelength range in comparison to what has been achieved motivates the study of AlGaN/AlN NDs.

5.2 $Al_xGa_{1-x}N$ sections on GaN nanowires

In this section, I present the plasma-assisted (PA-MBE) growth of $Al_xGa_{1-x}N$ sections on GaN NWs. The know-how from this section is used as a foundation for the growth of AlGaN/AlN NDs. The studied growth parameters are the alloy composition and the growth temperature as described in the following sections (5.2.1 and 5.2.2).

5.2.1 Effect of the Al content

AlGaN sections were grown on the top of catalyst-free GaN NWs, whose growth process is presented in section 3.4.5. The $Al_xGa_{1-x}N$ sections were grown by fixing Ga flux (Φ_{Ga}) at 0.1 monolayer per second (ML/s), and N flux (Φ_N) at 0.34 or 0.44 ML/s, while Al flux (Φ_{Al}) was varied between 0.07 and 0.40 ML/s. The nominal Al content (x) was defined as Φ_{Al}/Φ_N. The deposition time of AlGaN sections was set at 40 min for the samples grown with Φ_N = 0.34 ML/s, and at 27 min for the samples grown with Φ_N = 0.44 ML/s. The Al, Ga, and N shutters were simultaneously opened during the growth of AlGaN sections.

Sample	Φ_{Al} (ML/s)	Φ_{Ga} (ML/s)	$\Phi_{Ga,3D}$ (ML/s)	Φ_N (ML/s)	x	$\Phi_{2D,metal}$:Φ_N	$\Phi_{3D,metal}$:Φ_N
E2915	0.07	0.10	0.25	0.34	0.21	$\Phi_{Al}+\Phi_{Ga}<\Phi_N$	$\Phi_{Al}+\Phi_{Ga,3D}<\Phi_N$
E2916	0.10	0.10	0.25	0.34	0.29	$\Phi_{Al}+\Phi_{Ga}<\Phi_N$	$\Phi_{Al}+\Phi_{Ga,3D}>\Phi_N$
E2917	0.12	0.10	0.25	0.34	0.36	$\Phi_{Al}+\Phi_{Ga}<\Phi_N$	$\Phi_{Al}+\Phi_{Ga,3D}>\Phi_N$
E2918	0.15	0.10	0.25	0.34	0.44	$\Phi_{Al}+\Phi_{Ga}<\Phi_N$	$\Phi_{Al}+\Phi_{Ga,3D}>\Phi_N$
E2921	0.17	0.10	0.25	0.34	0.50	$\Phi_{Al}+\Phi_{Ga}<\Phi_N$	$\Phi_{Al}+\Phi_{Ga,3D}>\Phi_N$
E3218	0.22	0.10	0.20	0.44	0.50	$\Phi_{Al}+\Phi_{Ga}<\Phi_N$	$\Phi_{Al}+\Phi_{Ga,3D}<\Phi_N$
E3219	0.31	0.10	0.20	0.44	0.70	$\Phi_{Al}+\Phi_{Ga}<\Phi_N$	$\Phi_{Al}+\Phi_{Ga,3D}>\Phi_N$
E3220	0.40	0.10	0.20	0.44	0.90	$\Phi_{Al}+\Phi_{Ga}>\Phi_N$	$\Phi_{Al}+\Phi_{Ga,3D}>\Phi_N$

Table 5.1: Description of $Al_xGa_{1-x}N$ sections grown on GaN NWs samples under study: deposited fluxes, nominal Al content (x), $\Phi_{2D,metal}$:Φ_N comparison, $\Phi_{3D,metal}$:Φ_N comparison.

In order to identify the growth regime at the surface of the NW top, the three-dimensional (3D) metal flux ($\Phi_{Al}+\Phi_{3D,Ga}$) must be compared with Φ_N. 3D Ga flux ($\Phi_{3D,Ga}$) is the amount of Ga atoms available on the NW top during the GaN NW growth, which is derived by dividing the GaN NW length with the deposition time. This value is higher than Φ_{Ga} because the amount of Ga atoms on the NW top surface is associated with the combination of the direct deposited Ga flux, Ga adatoms diffusion, and Ga desorption. In contrast, the amount of Al and N atoms on the NW top surface is similar to the direct deposition flux (Φ_{Al} and Φ_N) because of their short diffusion length [169], [178], [246]. All the growth parameters of $Al_xGa_{1-x}N$ sections on GaN NWs were summarized in Table 5.1.

Note that the comparison between the two-dimensional (2D) metal flux ($\Phi_{2D,metal} = \Phi_{Al}+\Phi_{Ga}$) and Φ_N is also provided to compare the NW growth conditions with the 2D layer growth.

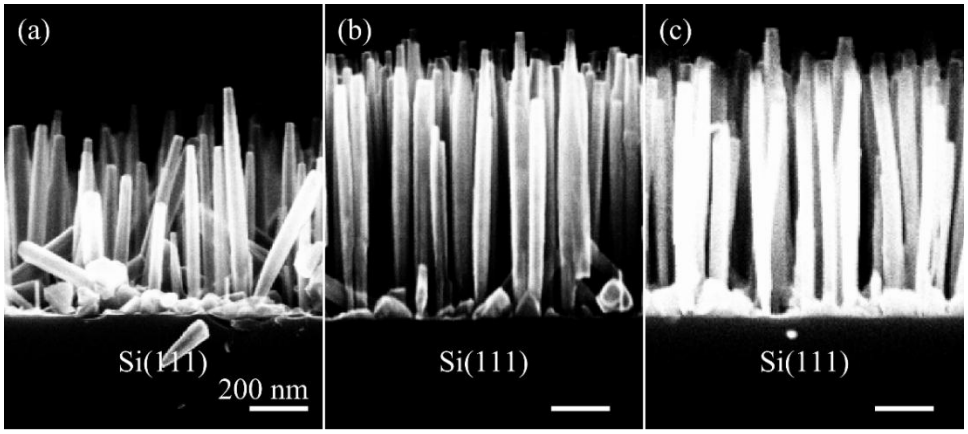

Figure 5.2: SEM images of (a) GaN NWs, and of $Al_xGa_{1-x}N$ sections grown on GaN NWs with (b) x=0.21, and (c) x=0.50.

After the growth, the structural properties were characterized by field emission scanning electron microscopy (FE-SEM) using a Zeiss Ultra55. Detailed structural properties were measured by high angle annular dark field scanning transmission electron microscopy (HAADF-STEM) using a probe-corrected FEI Titan operated at 300 kV. The SEM images shown in Figure 5.2(a)-(c) illustrate the morphology of GaN NWs without (Figure 5.2(a)) and with (Figure 5.2(b)-(c)) AlGaN sections on the NW tops. From the SEM images, the lengths of AlGaN sections ~200 nm were deduced for all the samples.

Figure 5.3(a) displays the HAADF-STEM image of $Al_{0.50}Ga_{0.50}N$ section on the GaN NW base. The bright contrast corresponds to the Ga-rich area while the darker contrast is the area with higher Al composition. Although the Al, Ga, and N shutters were simultaneously opened during the AlGaN growth, Figure 5.3(a) shows various regions in AlGaN sections which have different alloy distributions. Figure 5.3(b) displays the intensity profile taken along the wire axis of Figure 5.3(a). Deduced from HAADF-STEM images of several wires, the average length of the AlGaN sections on the GaN NW is ~180 nm. This value corresponds to an AlGaN growth rate $\Phi_{AlGaN,3D}$ ~0.30 ML/s, independent of Φ_{Al} and nearly equal to Φ_N, indicating that the AlGaN growth was limited by Φ_N [178]. Moreover, $\Phi_{AlGaN,3D}$ is larger than the 2D-metal flux (0.27 ML/s). This fact confirms that in addition to the direct material deposition on the NW top, the adatom diffusion along the NW sidewall contributes to the NW growth. The lower growth rate than the Φ_N (0.34 ML/s) is attributed to the decomposition of the material at the wire growth temperature [178], [247].

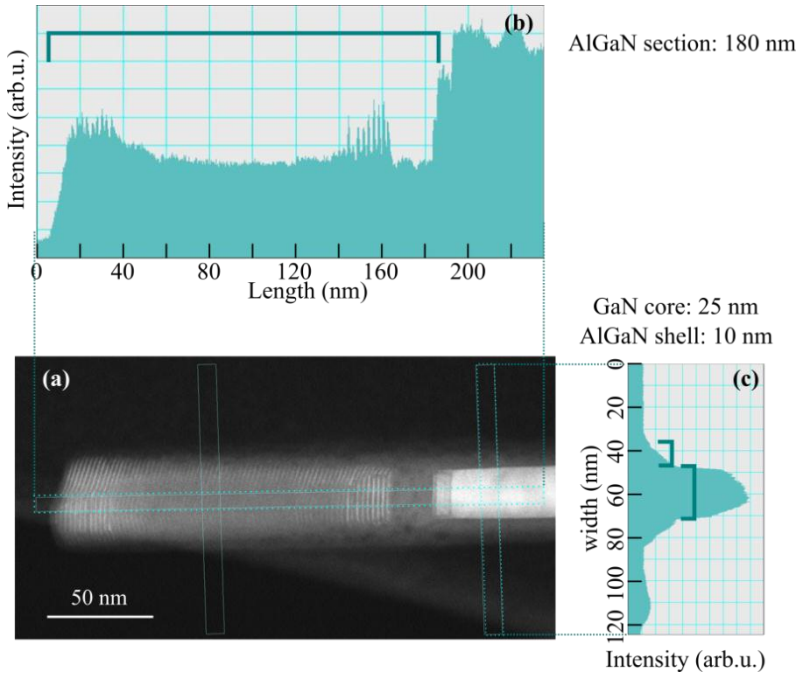

Figure 5.3:(a) HAADF-STEM image of E2921 showing GaN NWs with AlGaN section on top. Bright contrast represents Ga-rich area while the darker contrast represents the area which consists of Al-atoms. Intensity profile is taken along the axis (b) and radius (c) from the delimited areas of the NW shown in (a).

Figure 5.3(c) shows the intensity profile taken along the wire radius, which demonstrates the GaN core diameter of 25 nm, and the thickness of 10 nm-high-Al content AlGaN shell. This high-Al content shell is observed in all our growth conditions, i.e. various metal/N ratios and growth temperatures. The spontaneous core-shell formation is explained by the higher incorporation rate of Al at the sidewalls caused by the shorter diffusion length of the Al adatoms than that of Ga atoms [248], [249].

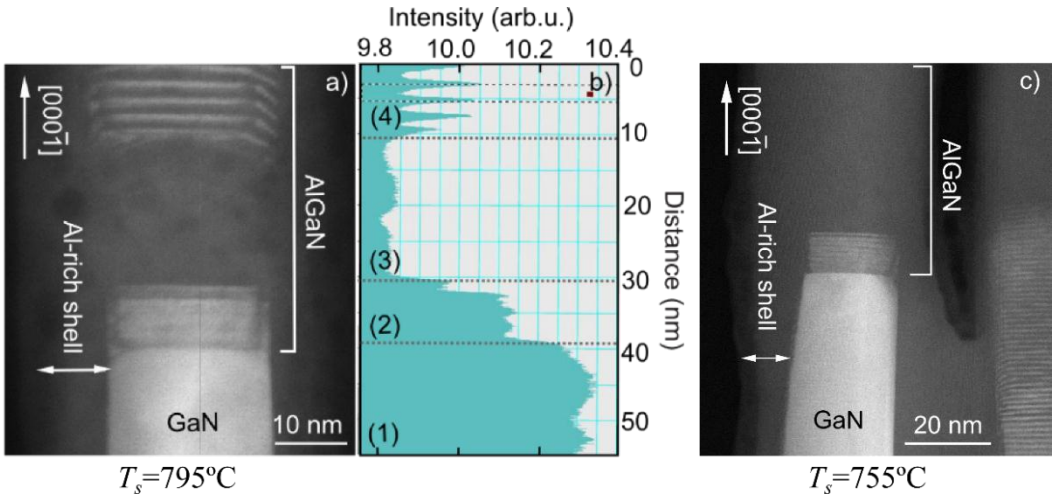

Figure 5.4:(a) HAADF-STEM image of a single $Al_{0.50}Ga_{0.50}N$ /GaN NW grown at 795°C (E2921) (b) Corresponding image contrast profile taken at the center of the NW shown in (a). (c) HAADF-STEM image of a single $Al_{0.50}Ga_{0.50}N$ /GaN NW grown at 755°C.

Figures 5.4(a) and (b) present zoom-in HAADF-STEM image of an $Al_{0.5}Ga_{0.5}N$ section grown at substrate temperature, T_s=795°C on a GaN NW and the contrast profile taken at the center along the wire axis. Most of the investigated NWs show a transition zone (Figure 5.4(b)–labeled (2)) between the GaN stem (Figure 5.4(b)–labeled (1)) and the AlGaN section. The typical thickness of this area with a lower Al content is ~10 nm. By reducing the growth temperature of AlGaN sections from 795°C to 755°C, the HAADF-STEM images (Figures 5.4(a) and (c)) show negligible changes in this zone in terms of chemical contrast and thickness. This fact indicates that the formation of this zone is not related to a surface reservoir of Ga atoms at the NW sidewalls, as Ga desorption/diffusion is highly temperature dependent in the range of our growth temperatures. After the transition zone, an Al-rich area (Figure 5.4(b)–labeled (3)) was found, followed by an area displaying chemical ordering (Figure 5.4(b)–labeled (4)). The lengths of these two regions fluctuate from wire to wire. In the labeled (4)–region, I usually find the 1:1 ratio ordering with the thickness of Al-rich and Ga-rich layers of about ~3 ML. However, it is difficult to precisely determine the Al content in both regions. The spontaneous chemical ordering is similar to what was observed in AlGaN [250]–[252] and InGaN films [253]. Theoretically, the ordering in wurtzite $Al_xGa_{1-x}N$ was suggested to be driven by the different binding energy of Al-N bond and Ga-N bond [254], [255]. The adatom surface diffusion generally allows the incorporation of Al and Ga atoms at their different preferential sites, leading to the ordering sequence of Al-rich and Ga-rich areas along the growth axis. Such description is a highly probable for the AlGaN growth in NWs where the contribution of adatom diffusion is significant.

To understand the transition zone formation, an AlN/GaN NW superlattice was investigated by HAADF-STEM, as shown in Figure 5.5(a). The image contrast reveals a transition zone with a length of ~8 nm at the first AlN/GaN interface (label (1) in Figure 5.5(a)). The transition zones at the second, third and the fourth interfaces (Labels (2), (3) and (4)) are significantly shorter. From the image contrast, these regions should be Al-Ga intermixing areas. Besides, the intermixing process is seemingly more pronounced on the top of GaN rather than at the interface below them.

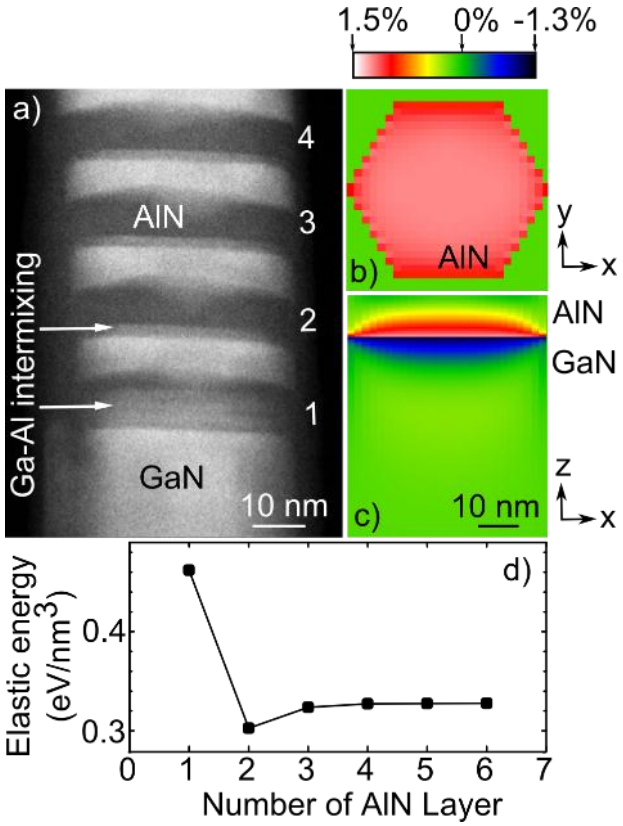

Figure 5.5: (a) HAADF-STEM image of a GaN NW with an AlN/GaN superlattice. The arrows indicate the transition zone at the AlN/GaN interfaces. (b)-(c) Contour e_{xx} plots in a GaN NW with an AlN section on top: (b) in-plane view of the interface at the AlN side, and (c) cross-section at the center of GaN NW. (d) Plot of the elastic energy density measured at the topmost AlN/GaN interface on the AlN sides as a function of the number of AlN layers in the stack.

In view of these results, I propose that the intermixing at the AlN/GaN interface forms in order to partially relieve the strain induced by the lattice mismatch between AlN and GaN. I have explored the role of the strain via 3D strain calculations using NextNano^3 solver. The strain distribution was obtained by the minimization of the elastic strain energy through the application of zero-stress boundary conditions at the NW surface, which allows the NW to deform in all three spatial directions. The structure of interest is a 50 nm-diameter hexagonal GaN NW overgrown by various periods of 10-nm-GaN/10-nm-AlN, i.e. the geometry corresponding to the structure in Figure 5.5(a). The formation of an Al shell is not considered as it is not clearly visible in this HAADF-STEM image. The number of GaN/AlN periods in the simulation was increased sequentially, to assess the strain distribution at the topmost AlN/GaN interface after the deposition of each period. Note that the Al-Ga intermixing at the AlN/GaN interface was not taken into account for the simulation.

Figure 5.5(b) and (c) present the color map of the strain in x direction (e_{xx}) in a hexagonal GaN NW capped with a single AlN layer. Figure 5.5(b) illustrates the in-plane

distribution of tensile strain at the interface of GaN NW and AlN layer on the AlN side. The cross section in Figure 5.5(c) shows the high degree of compressive strain (blue contrast) at the interface in the GaN region, and the tensile strain (red contrast) in the AlN region. From the simulation, the first AlN layer is strongly tensile strained by the GaN NW base. Figure 5.5(d) describes the elastic energy density at the topmost AlN/GaN interface on the AlN side taken at the center of a GaN NW (■), plotted as a function of the number of AlN sections in the stack.

The stronger tensile strain in the first AlN layer probably enhances Al-Ga intermixing at the AlN/GaN interface. As the NW growth proceeds, the higher AlN barriers are less strained, thus giving lower driving force for the intermixing process, and consequently a shorter transition zone. The lower intermixing effect at the interface below each GaN layer than the one above them is possibly caused by the higher binding energy of the Al-N bond with respect to the Ga-N bond.

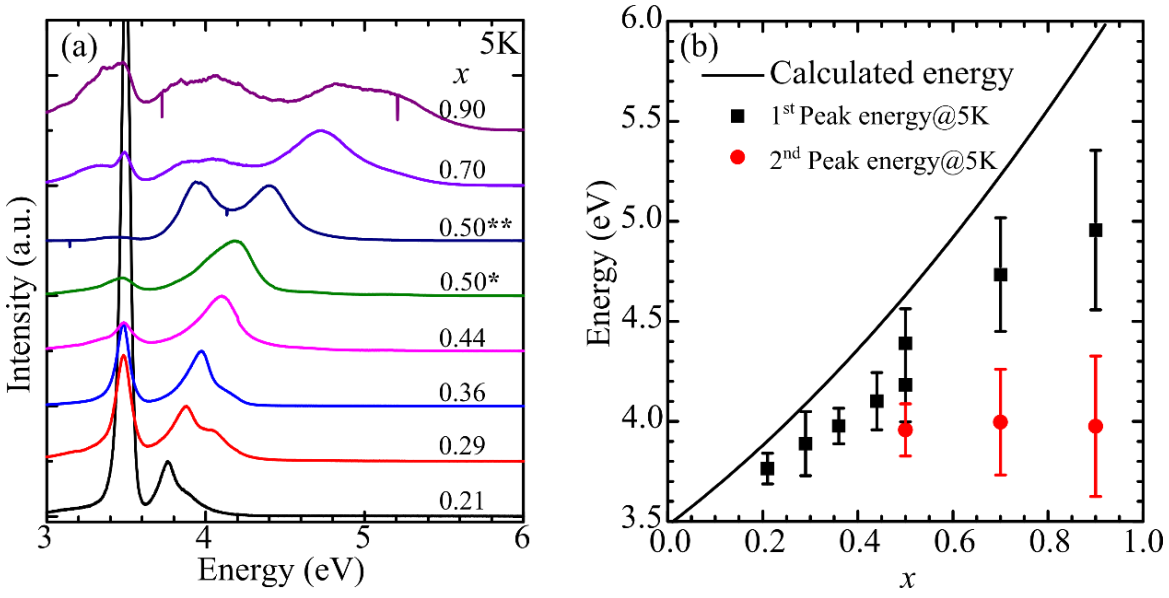

Figure 5.6: (a) CL spectra of $Al_xGa_{1-x}N$ sections on GaN NWs with various x = 0.21(E2915), 0.29(E2916), 0.36(E2917), 0.44(E2918), 0.50(E2921, E3218**), 0.70(E3219), and 0.90(E3220)) measured at 5K. E3218 is the sample that was grown using lower $\Phi_{Ga,3D}$ than that of E2921. (b) Evolutions of the higher (■) and lower (●) energy CL peak energy position at 5K, comparing with the calculated band gap value at 5K (solid line).The error bars represent the FWHMs of CL spectra. Note that the second peak appears for the $Al_xGa_{1-x}N$ sections with x>0.50.*

The optical characteristics of $Al_xGa_{1-x}N$ sections on GaN NWs were assessed by cathodoluminescence (CL). Figure 5.6(a) shows CL spectra measured at 5K from the ensemble $Al_xGa_{1-x}N$ sections on GaN NWs grown at 795°C where x = 0.21, 0.29, 0.36, 0.44, 0.50, 0.70, and 0.90. The peak which remains constant at ~3.48 eV is assigned to the

luminescence from the GaN NWs base, whereas the peak at higher energy that blue shifts with increasing Al content is attributed to the luminescence from $Al_xGa_{1-x}N$ sections. I also observed a second emission line when $x > 0.50$, in the range of 3.96–4.00 eV and stable with x. Even though the origin of this second peak is unclear, the luminescence from the defect band in AlGaN which changes with x [256] is excluded [249].

Despite having the same nominal Al content (x = 0.5), E2921 and E3218 possess different luminescence characteristic. E2921 shows a single spectral peak which centers at 4.18 eV whereas E3218 shows two spectral peaks which center at 3.96 and 4.38 eV, indicating that the latter sample contains higher Al content in AlGaN section. From the growth conditions, the $\Phi_{Ga,3D}$ used in E2921 was 0.25 ML/s, higher than that used in E3218 which was 0.20 ML/s. As a result, the growth regime on the NW top surface in E2921 is N-limited regime ($\Phi_{Al}+\Phi_{Ga,3D}>\Phi_N$), but the one in E3218 is N-rich regime ($\Phi_{Al}+\Phi_{Ga,3D}<\Phi_N$). The growth in N-rich regime on the NW top of sample E3218 could be an explanation of the higher Al content in this sample.

Figure 5.6(b) summarized the evolution of the peak emission energy (■) as a function of x, showing that the emission peaks of $Al_xGa_{1-x}N$ sections systematically blue shift from 3.77 to 4.96 eV with increasing nominal Al content. The linewidth was derived by fitting the CL spectra with Gaussian function and presented as an error bar in the figure. These observed linewidths also increase from 150 to 800 meV as a function of nominal Al content and larger than those reported in AlGaN 2D films [257]. The emission energies are systematically lower than the expected energy gaps defined by equation 2.3 (the black solid line in Figure 5.6(b)), when x increases. The maximum deviation from the calculated value was observed at x = 0.90. I attribute this deviation to the alloy inhomogeneity in AlGaN as it could strongly affect the band gap of semiconductor [258]. The second spectral peaks center in the 3.96-4.00eV (●) from the sample with $x > 0.50$ were also summarized in this figure with their full width at half maximum (FWHM) of 260-700 meV.

To investigate in detail the optical characteristics of $Al_xGa_{1-x}N$ sections on GaN NWs, the temperature dependence PL was performed on $Al_xGa_{1-x}N$ sections on GaN NWs samples where = 0.21(E2915), 0.35(E2917), and 0.50(E2921). Figure 5.7(a) shows the normalized integrated PL intensity as a function of temperature. Since all the intensities are stable at low temperatures, therefore the IQE can be approximated using Eqs.(4.1), and (4.2). Different from the cases of AlGaN quantum dots (QDs) [231], [259] , the second activation energy is

required for a good fit [260] which is similar to the case of AlGaN/AlN QWs [130] and GaN/AlGaN NDs in GaN NWs [261]. In this case, the IQE is represented by:

$$IQE=1/((1+ae^{-Ea1/kT})\,(1+be^{-Ea2/kT})) \quad (5.1)$$

where a and b are fitting parameters, kT is the thermal energy, and E_{a1} and E_{a2} are the activation energies. The extracted E_{a1} in the range of 75-135 meV is attributed to the localization energy corresponding to the potential barriers which confine the carriers in Ga-rich area of $Al_xGa_{1-x}N$ section. The E_{a2} with the value in the range of 15-20 meV could represent the activation energy accounting for the de-trapping of excitons from the interface roughness fluctuation in the ordered alloy. The extracted IQE of AlGaN section increases from 0.7 to 5 % when x increases, indicating the higher carrier localization of the sample at higher Al content.

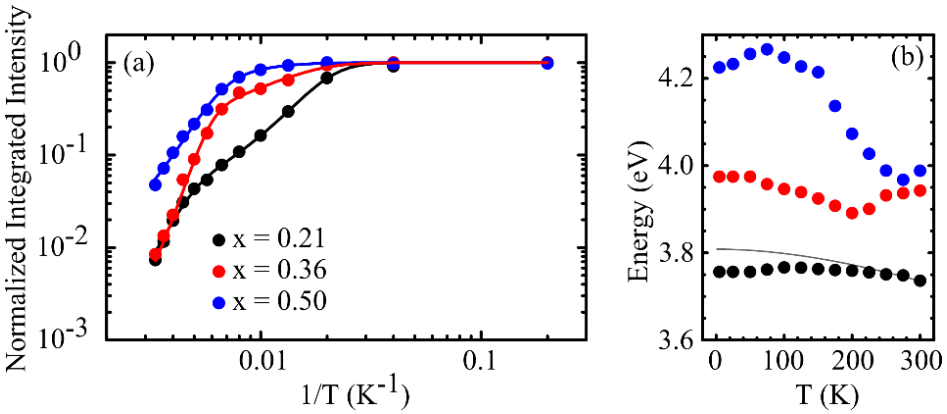

Figure 5.7: (a) Normalized integrated PL intensity as a function of temperature for $Al_xGa_{1-x}N$ sections on GaN NWs. (b) Temperature dependent PL peak position for $Al_xGa_{1-x}N$ sections with x = 0.21, 0.36 and 0.50. The solid line represents the shift expected from the Varshini's equation.

Figure 5.7(b) depicts the evolution of PL peak energy as a function of temperature, showing an *s*-shape behavior which deviates significantly from Varshni's equation [64]. This trend, which can provide information on the carrier localization in alloy potential fluctuations, is explained by the exciton freeze-out in the alloy local potential minima at low temperatures, followed by the onset of exciton thermalization with increasing temperature. The deviation becomes more pronounced with increasing *x,* similar to the case of AlGaN 2D films [219]. This *s*-shape was also reported in AlGaN thin films [125], [219], [221], [256], AlGaN/GaN QWs [222], [223], and InGaN/GaN QDs [130]. Potential fluctuations in ternary alloys can reduce the probability of carrier capture by nonradiative recombination centers. Therefore, the higher IQE in $Al_xGa_{1-x}N$ sections with larger Al content (in this case, $0<x<0.5$) could be associated to the larger alloy inhomogeneity.

In the next section, I study the $Al_{0.5}Ga_{0.5}N$ sections on GaN NWs grown at different temperatures in order to optimize the growth condition to achieve high quality AlGaN sections on GaN NWs.

5.2.2 Effect of the Growth temperature

In this study, I grew $Al_{0.50}Ga_{0.50}N$ sections using various growth temperatures on GaN NWs. The initial growth conditions of this study (E2958) were set similar to those of E2921, i.e. the $Al_{0.50}Ga_{0.50}N$ sections were grown by depositing Φ_{Al}, Φ_{Ga}, and Φ_N at 0.17, 0.10 and 0.34 ML/s, respectively, on the GaN NWs at T_s = 795°C. The deposition time of the AlGaN sections was set at 40 min. The only varied parameter in this study was the growth temperature that was changed from 795°C (E2958), to 760°C (E2955), 755 °C (E2965), 747°C (E2969), 740°C (E2967), and to 735 °C (E2966). After the growth, the structural properties were characterized by SEM and HAADF-STEM while the optical properties were investigated by PL.

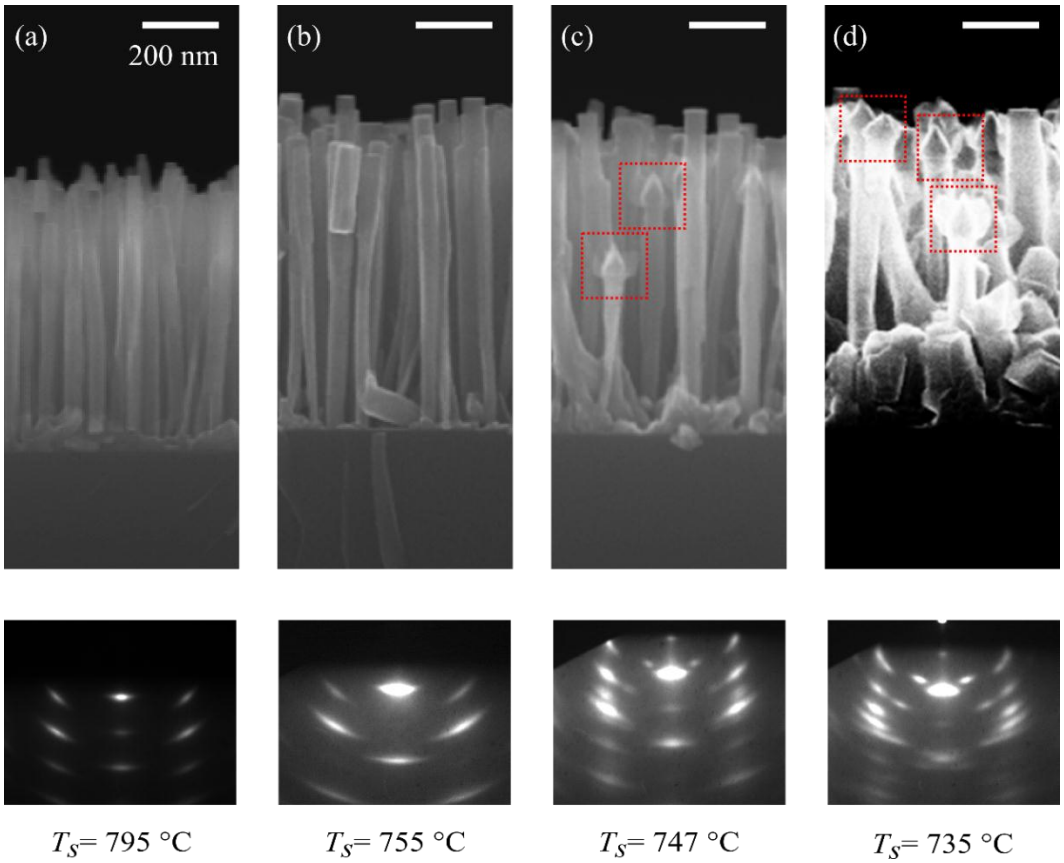

Figure 5.8: SEM of AlGaN sections grown at various growth temperatures at (a) 795°C, (b) 755°C, (c) 747°C, and (d) 735°C on GaN NWs and their corresponding RHEED patterns.

Figure 5.8 shows the morphologies of GaN NWs covered by AlGaN sections grown at different growth temperatures and their corresponding reflection high energy electron diffraction (RHEED) patterns. At T_s = 795°C and 755°C, SEM images show flat-top NWs with a typical RHEED pattern of GaN NWs [158]. On the contrary, I observe a pyramid-like structure at the NW tops for the growth temperature of 747°C and 735°C. The corresponding RHEED pattern of NW shows a ring-like characteristic that distorted from the standard RHEED pattern of wurtzite GaN NWs (see Figure 3.17 in chapter 3), indicating the formation of different NW orientation and crystal structure.

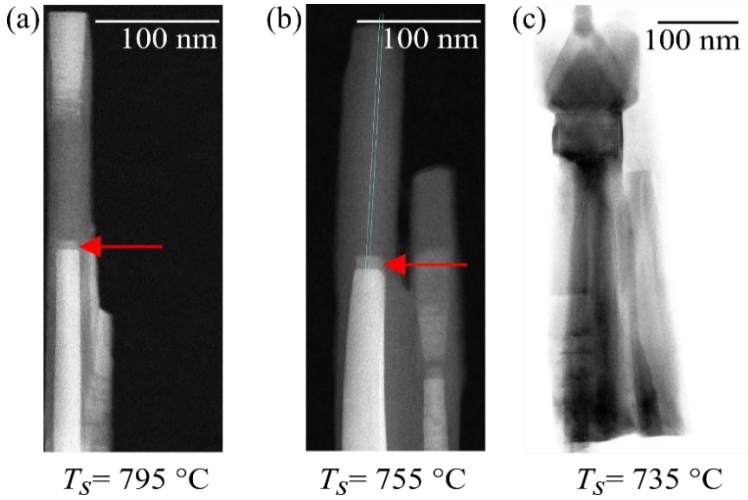

Figure 5.9: HAADF-SEM of AlGaN sections grown at (a) 795 °C, (b) 755 °C, and (c) BF-STEM of AlGaN sections grown at 735 °C

Figure 5.9(a)–(b) show HAADF-STEM while (c) shows Bright Field (BF)–STEM of the NWs grown at 795°C, 755°C and 735°C, respectively. By reducing the growth temperature from 795°C to 755°C, the structural properties of the NW do not change significantly. Total lengths of AlGaN section in both cases remains 180 nm, revealing that the AlGaN growth was limited by Φ_N [178]. The transition zone at the AlGaN/GaN interfaces (red arrows in the figures) as well as chemical ordering was generally observed. For the samples which were grown at T_s = 735°C, stacking faults become visible in NWs as shown in Figure 5.9(c).

Figure 5.10(a) shows normalized PL from $Al_{0.50}Ga_{0.50}N$ sections grown at different growth temperatures on GaN NWs. The peak located at around 3.50 eV for all samples is assigned to the luminescence from GaN NW base while the peak locates in the 4.35-4.60eV range corresponds to the luminescence of $Al_{0.50}Ga_{0.50}N$ sections. By gradually decreasing the growth temperature of $Al_{0.50}Ga_{0.50}N$ sections from 795 to 735°C, the luminescence of AlGaN sections systematically red shifts from 4.60 to 4.35eV. The red shifting is attributed to the

larger amount of Ga atoms incorporated in AlGaN sections at the lower growth temperatures because of the suppression of Ga desorption process.

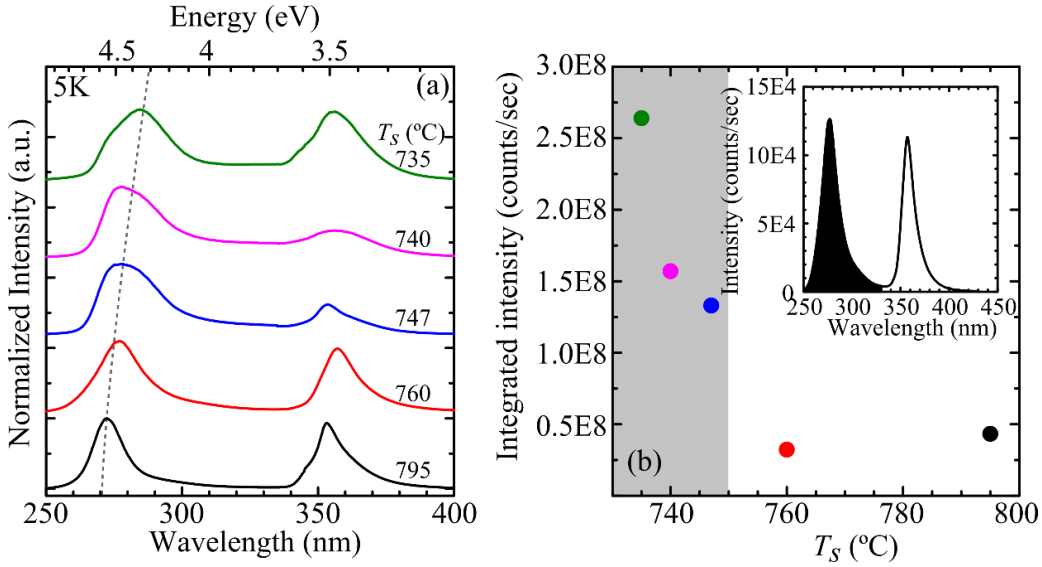

Figure 5.10: (a) Normalized PL spectra measured at 5K and (b) PL integrated intensity of $Al_{0.50}Ga_{0.50}N$ sections grown at different growth temperatures on GaN NWs. Inset of (b) illustrates the integrated intensity obtained from the interval area (250nm<wavelength<330nm) for E2958.

Figure 5.10(b) presents the evolution of integrated PL intensity of $Al_{0.50}Ga_{0.50}N$ sections as a function of grown temperature. To ensure the accuracy of intensity comparison, all the samples were placed side by side in the cryostat and were concurrently characterized by using the same excitation power while all the optical paths were preserved. Obtained Spectra exhibit two peaks which correspond to the luminescence of GaN NWs and AlGaN sections. Only the luminescence concerning to the AlGaN sections (250nm<λ<330nm) was integrated as shown in inset of Figure 5.10(b) and plotted as a function of growth temperature. The integrated PL intensity for the AlGaN sections monotonically increases when the growth temperature was lower than 760°C. Seemingly, the intensity enhancement occurs along with the modification of NW morphology which presented as a shaded-area in Figure 5.10(b).

5.3 $Al_xGa_{1-x}N$/AlN nanodisks on GaN nanowires

In this section, I study the growth of $Al_xGa_{1-x}N$/AlN NDs on GaN NWs by applying knowledge of AlGaN sections on GaN NWs. I firstly report the growth regime of $Al_xGa_{1-x}N$/AlN NDs on GaN NWs that suits for the UV-C emission target. Later on, the peak emission spectra of $Al_xG_{1-x}N$ NDs were varied by changing growth temperature, Al content, and ND thickness. 3D strain distribution was also calculated by performing it on the

assimilated growth structure dynamics in order to interpret the effect of the strain to the structural and optical characteristics.

5.3.1 AlGaN/AlN nanodisk growth regime: metal rich ($\Phi_{Al}+\Phi_{Ga}\geq\Phi_N$) and nitrogen rich ($\Phi_{Al}+\Phi_{Ga}<\Phi_N$)

This section aims to study the effect of the growth regime (metal rich or nitrogen rich) of $Al_xGa_{1-x}N$/AlN NDs that influences different structural and optical properties, in order to effectively apply it for the corresponding requirements.

Two different regimes: 2D-metal rich and 2D-nitrogen rich of 30 periods of $Al_xGa_{1-x}N$/AlN NDs were grown on the top of catalyst free GaN NWs at T_s = 795°C. The $Al_xGa_{1-x}N$ NDs were grown by varying Φ_{Al} from 0.10 to 0.23 ML/s whereas Φ_N was set at 0.34 ML/s, providing nominal Al contents ($x = \Phi_{Al}/\Phi_N$) in the 0.29-0.68 range. Φ_{Ga} was adjusted into 2 different values, those are 0.24 and 0.09 ML/s in order to switch the growth regime into 2D-metal rich and 2D-nitrogen rich regime, respectively. The deposition time of NDs was set at 12 s. All the growth parameters for $Al_xGa_{1-x}N$ NDs in this study were summarized in Table 5.2. For the AlN barriers, the Φ_{Al} and deposition time were set at 0.19 ML/s and 84 s for all the samples.

Sample	Φ_{Al} (ML/s)	Φ_{Ga} (ML/s)	$\Phi_{Ga,3D}$ (ML/s)	Φ_N (ML/s)	x	$\Phi_{2D,metal}$:Φ_N	$\Phi_{3D,metal}$:Φ_N
E2849	0.10	0.24	0.30	0.34	0.29	$\Phi_{Al}+\Phi_{Ga}\geq\Phi_N$	$\Phi_{Al}+\Phi_{Ga,3D}>\Phi_N$
E2850	0.12	0.24	0.30	0.34	0.35	$\Phi_{Al}+\Phi_{Ga}\geq\Phi_N$	$\Phi_{Al}+\Phi_{Ga,3D}>\Phi_N$
E2851	0.16	0.24	0.30	0.34	0.47	$\Phi_{Al}+\Phi_{Ga}\geq\Phi_N$	$\Phi_{Al}+\Phi_{Ga,3D}>\Phi_N$
E2852	0.20	0.24	0.30	0.34	0.59	$\Phi_{Al}+\Phi_{Ga}\geq\Phi_N$	$\Phi_{Al}+\Phi_{Ga,3D}>\Phi_N$
E2853	0.23	0.24	0.30	0.34	0.68	$\Phi_{Al}+\Phi_{Ga}\geq\Phi_N$	$\Phi_{Al}+\Phi_{Ga,3D}>\Phi_N$
E2879	0.10	0.09	0.22	0.34	0.29	$\Phi_{Al}+\Phi_{Ga}\leq\Phi_N$	$\Phi_{Al}+\Phi_{Ga,3D}\sim\Phi_N$
E2880	0.12	0.09	0.22	0.34	0.35	$\Phi_{Al}+\Phi_{Ga}\leq\Phi_N$	$\Phi_{Al}+\Phi_{Ga,3D}\sim\Phi_N$
E2881	0.16	0.09	0.22	0.34	0.47	$\Phi_{Al}+\Phi_{Ga}\leq\Phi_N$	$\Phi_{Al}+\Phi_{Ga,3D}>\Phi_N$
E2882	0.20	0.09	0.22	0.34	0.59	$\Phi_{Al}+\Phi_{Ga}\leq\Phi_N$	$\Phi_{Al}+\Phi_{Ga,3D}>\Phi_N$
E2883	0.23	0.09	0.22	0.34	0.68	$\Phi_{Al}+\Phi_{Ga}\leq\Phi_N$	$\Phi_{Al}+\Phi_{Ga,3D}>\Phi_N$

Table 5.2: Description of 30 periods of $Al_xGa_{1-x}N$ NDs on GaN NWs under study: deposited fluxes, nominal Al content (x), $\Phi_{2D,metal}$:Φ_N comparison, $\Phi_{3D,metal}$:Φ_N comparison.

Unlike the study of AlGaN sections whose regime was three-dimensionally (3D) defined by taking into account the Ga diffusion and desorption, the regime in this section is 2D identified by comparing $\Phi_{Al}+\Phi_{Ga}$ and Φ_N. 2D regime is used in this case to be able to compare with Stranski-Krastanov (SK)-QDs growth atmosphere. Additionally, the 3D

regime comparison is obscure in this case since all the samples were grown in 3D-metal rich regime ($\Phi_{Al}+\Phi_{Ga,3D}>\Phi_N$) as illustrated in Table 5.2.

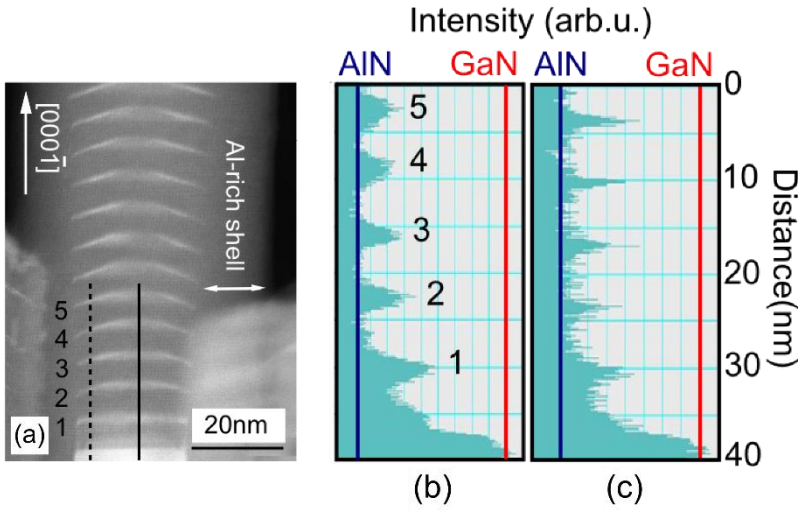

Figure 5.11: Cross-sectional HAADF-STEM images of $Al_{0.35}Ga_{0.65}N$/AlN NDs when the disk were grown in (a) 2D-nitrogen rich regime(E2880). (b) Image contrast taken along the center (black solid line shown in (a)) and (c) image constrast taken along the edge (black dash line shown in (a)) of the AlGaN NDs.

In this section, I perform HAADF-STEM measurements on $Al_{0.35}Ga_{0.65}N$ NDs on NWs grown in 2D-nitrogen rich condition (E2880) in order to study the chemical distribution in the structure. NWs were dispersed on silicon nitride membrane to be individually investigated with a probe-corrected FEI Titan operated at 300 kV. Figure 5.11(b) depicts HAADF-STEM image which shows AlGaN ND thickness in the range of 1-2 nm, whereas that of the AlN barriers is ~5 nm. The diameter of the first AlGaN ND is similar to the one of GaN NW stem. Due to the lateral growth of AlN barrier, the ND diameter progressively increases along the growth axis. Moreover, the shape of the NDs evolves to the pyramid-like shape with {1-103} facets, similar to GaN SK QDs [262]. The contrast profile taken at the center of the NW in Figure 5.11(c) reveals that the Al composition at the center of the NDs gradually increases along the growth axis (the image contrast become darker) and finally saturates at the third ND. In addition, the contrast profile in Figure 5.11(d) taken at the edge of the NW shows that the Ga-rich area becomes better defined. By comparing the contrast profiles between the center and the edge of ND in each layer, I observe that the degree of lateral phase separation is more pronounced in the higher ND layer. Note that the HAADF-STEM of NDs grown under 2D-metal rich conditions show similar structural characteristics.

From our data, I suggest that the strain can modify the shape, the axial and the radial distribution of Al composition of the AlGaN NDs. I performed 3D strain simulations of a 25 nm- diameter hexagonal GaN NW with various periods of 2 nm $Al_{0.35}Ga_{0.65}N$/ 4 nm AlN, to imitate our result shown in Figure 5.11(a). In this case, I consider the formation of the Al shell which encapsulates NDs and NW. To follow the real growth sequence, I performed the strain simulations on the 5 different structures; that is, the number of periods in the simulation was increased sequentially, to assess the strain distribution after the growth of an AlN barrier, following 0, 1, 2, 3 periods of $Al_{0.35}Ga_{0.65}N$/AlN ND. For simplicity, I assume random alloy in the AlGaN NDs with rectangular shape. Figure 5.12(a) presents the cross-section contour plot of e_{xx} taken at the center of the NW after the growth of the 4th AlN barrier.

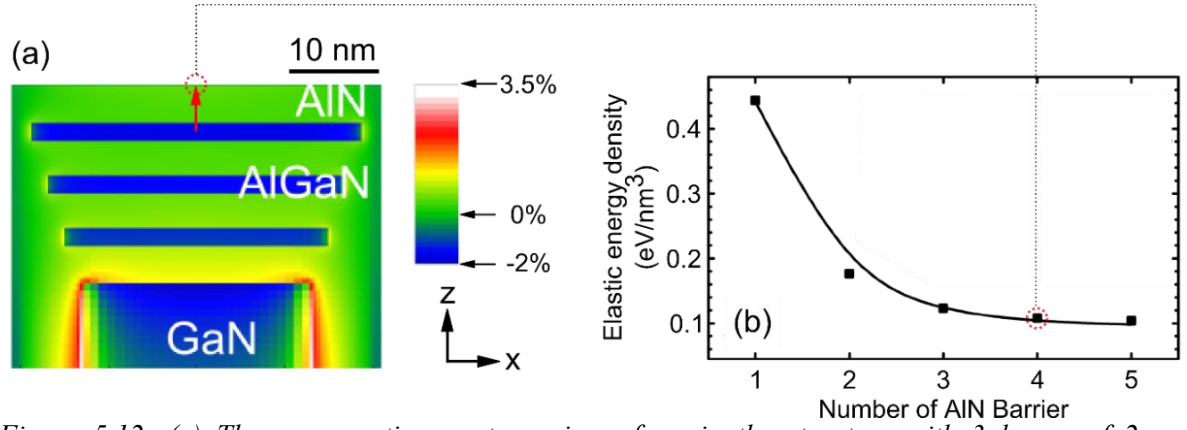

Figure 5.12: (a) The cross-section contour view of e_{xx} in the structure with 3 layers of 2-nm-$Al_{0.35}Ga_{0.65}N$/4-nm-AlN on the first AlN barrier on GaN NW stem. (b) The plot of the elastic energy density, taken at the center of the NW on the surface of the topmost 4-nm AlN barrier prior to the growth of the $Al_{0.35}Ga_{0.65}N$ ND, as a function of the number of AlN barriers.

Figure 5.12(b) shows the elastic energy density that was taken at the topmost surface of AlN barrier at the center of NW of 5 different simulated structures and were plotted as a function of the number of AlN barrier. The first simulated structure, 4-nm AlN on GaN NW stem, shows highly tensile strained by the GaN NW base. Then, the strain gradually decreases and saturates after the fourth AlN layer. I propose that the higher tensile strain in the first AlN barrier should facilitate Ga incorporation in the first $Al_{0.35}Ga_{0.65}N$ ND. As the NW growth proceeds, the tensile strain in the AlN barriers monotonically decreases which enhances the Al incorporation at the center of the $Al_xGa_{1-x}N$ NDs. Radially, the efficient strain relaxation at the edge of the NDs possibly results in the higher accumulation of Ga atoms at that area. From the simulations, I suggest that the strain can modify the shape, the

axial and radial distribution of Al composition in AlGaN NDs as illustrated in the structural results.

Figure 5.13(a) and (b) show CL spectra obtained from AlGaN NDs grown in 2D-metal rich and 2D-nitrogen rich regime, respectively. Despite similar detailed structural results, luminescence spectra show different characteristics for the samples grown in different regimes. CL spectra from all the samples grown in 2D-metal rich regime show the peaks located at 300 nm as illustrated in Figure 5.13(a). However, there are components at shorter wavelengths centerd at 240 nm and 260 nm with low intensities. The variation of these peak emission spectra does not depend on the nominal Al content. In contrast, luminescence of the peaks center at 240 and 260 nm become more pronounced for the samples grown under 2D-nitrogen rich regime as shown in Figure 5.13(b).

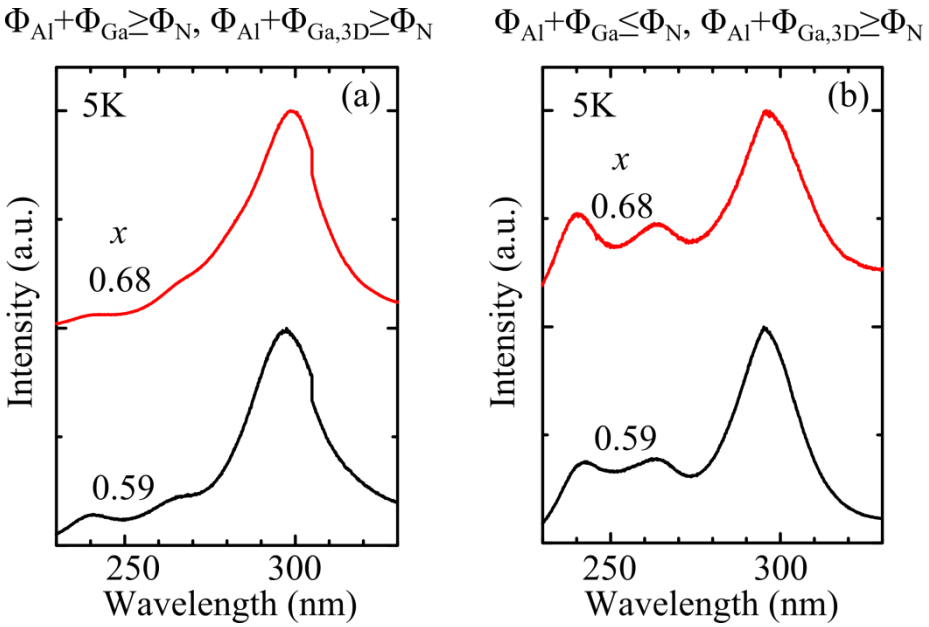

Figure 5.13: CL spectra measured at 5K of $Al_xGa_{1-x}N$/AlN NDs on GaN NWs samples grown in (a) 2D-metal rich regimes and (b) 2D-nitrogen rich regimes.

By considering the luminescent results, I further investigate the growth of AlGaN/AlN NDs in 2D-nitrogen rich conditions since they show a potential to control the emission wavelength to λ = 260-270 nm. However, the challenge of this growth regime is the broad and multi-peak spectral response.

5.3.2 Effect of the growth temperature

Based on the results from the section 5.2.2, I define the growth temperature regime which preserves the flat top morphology of NWs to be above 755°C. In this section, I present the effect of the growth temperature to the luminescence of AlGaN NDs, while the growth temperature was varied from 795°C to 755°C.

I grew 30 periods of $Al_xGa_{1-x}N$/AlN NDs on the top of catalyst free GaN NWs. The $Al_xGa_{1-x}N$ NDs were grown by setting Φ_{Al} and Φ_N at 0.13 and 0.32 ML/s, providing nominal Al content = 0.4 throughout the series. The Φ_{Ga} was kept at 0.13 ML/s which corresponds to $\Phi_{Ga,3D}$ = 0.26 ML/s, deducing from the structural results. The AlGaN NDs deposition time of NDs was set at 20s. The growth temperature of AlGaN NDs was changed from 795 to 755°C. The growth parameters for $Al_{0.40}Ga_{0.60}N$ NDs in this study were summarized in Table 5.3. While the AlN barriers were grown for 4 nm by depositing Φ_{Al} = 0.18 ML/s for 84 s.

Sample	Φ_{Al} (ML/s)	Φ_{Ga} (ML/s)	$\Phi_{Ga,3D}$ (ML/s)	Φ_N (ML/s)	x	$\Phi_{2D,metal}$:Φ_N	$\Phi_{3D,metal}$:Φ_N	T_s (°C)	t_d (s)
E3017	0.13	0.14	0.26	0.32	0.40	$\Phi_{Al}+\Phi_{Ga}<\Phi_N$	$\Phi_{Al}+\Phi_{Ga,3D}\sim\Phi_N$	795	20
E3018	0.13	0.14	0.26	0.32	0.40	$\Phi_{Al}+\Phi_{Ga}<\Phi_N$	$\Phi_{Al}+\Phi_{Ga,3D}>\Phi_N$	780	20
E3019	0.13	0.14	0.26	0.32	0.40	$\Phi_{Al}+\Phi_{Ga}<\Phi_N$	$\Phi_{Al}+\Phi_{Ga,3D}>\Phi_N$	765	20
E3021	0.13	0.14	0.26	0.32	0.40	$\Phi_{Al}+\Phi_{Ga}<\Phi_N$	$\Phi_{Al}+\Phi_{Ga,3D}>\Phi_N$	755	20

Table 5.3: Description of 30 periods of $Al_{0.40}Ga_{0.60}N$ NDs: deposited fluxes, nominal Al content (x), $\Phi_{2D,metal}$:Φ_N comparison, $\Phi_{3D,metal}$:Φ_N comparison, growth temperatures, and ND deposition time.

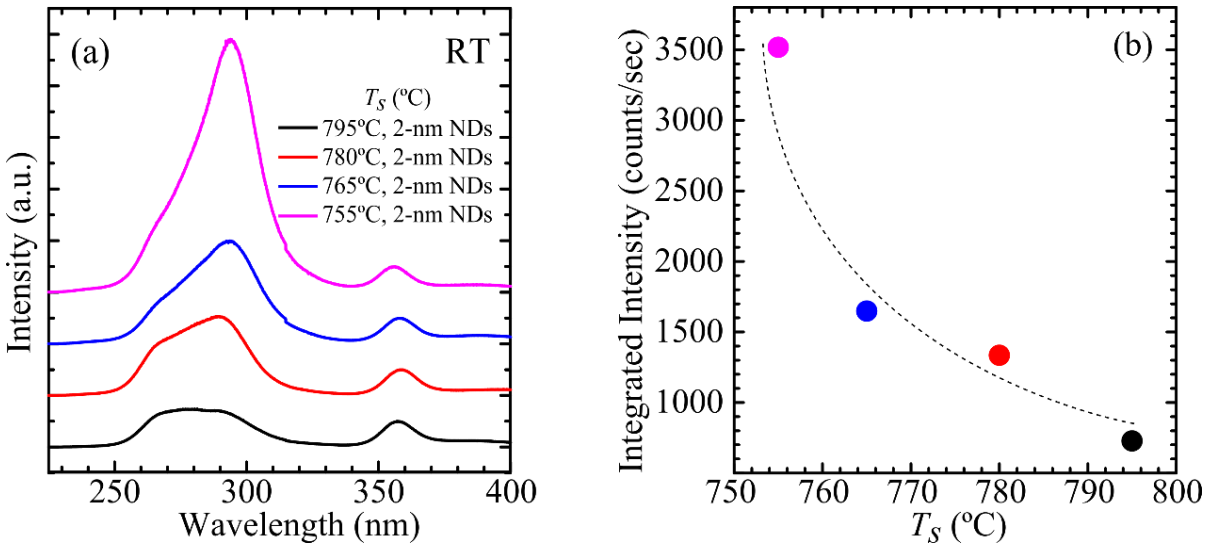

Figure 5.14: (a) Room-temperature CL spectra of $Al_{0.40}Ga_{0.60}N$/AlN NDs grown with various temperatures on GaN NWs. (b) CL integrated intensity of $Al_{0.40}Ga_{0.60}N$/AlN NDs obtained from integrate interval area (250nm<λ<340nm)

Figure 5.14(a) presents the room-temperature CL spectra of $Al_{0.40}Ga_{0.60}N$/AlN NDs grown at various temperatures. The emission intensity of AlGaN NDs progressively increases while the peak position systematically red shifts from 282 to 292 nm when the growth temperature was decreased from 795 to 755°C. The slightly red shift of the luminescence spectra is associated to the suppression of desorption and dissociation processes at low growth temperature, leading to a higher Ga incorporations in AlGaN NDs.

5.3.3 Wavelength tunability: Al content, nanodisk thickness

In this section, I demonstrate the potential to adjust the emission spectrum of AlGaN/AlN NDs by adjusting the ND thickness and Al content. Their CL spectra measured at 300K are presented in Figure 5.15. By increasing *x* from 0 to 0.4 and/or reducing the ND thickness from 4 to 1 nm, the CL peak emission can be adjusted from 350 nm to 240 nm, with a FWHM in the range of 50-500 meV. Interestingly, each AlGaN/AlN NDs shows the luminescence peak located ~4.13eV which does not shift as a function of ND thickness and Al content. The higher-energy luminescence peaks which locate at 4.78 and/or 5.17eV (λ = 260 and 240 nm) appear when the ND thickness was reduced and the nominal Al content was increased. As illustrated, the blue-shifting is achieved along with the generating of multi-peaks characteristic which is attributed to the alloy inhomogeneity in the AlGaN NDs.

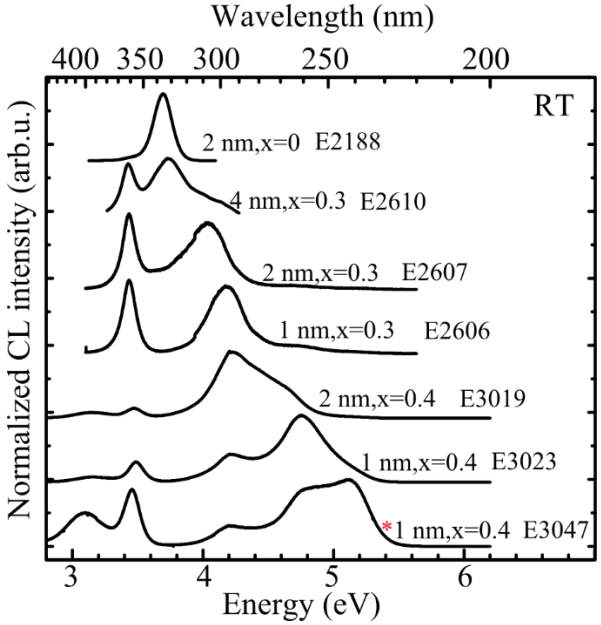

Figure 5.15: Room-temperature CL spectra of GaN/AlGaN NDs(E2188) and $Al_xGa_{1-x}N$/AlN NDs grown with different $Al_xGa_{1-x}N$ ND thicknesses and Al contents. E3047 (*) is grown with lower Φ_{Ga} (=0.13 ML/s) than E3023 and E3019 (Φ_{Ga} = 0.14 ML/s).

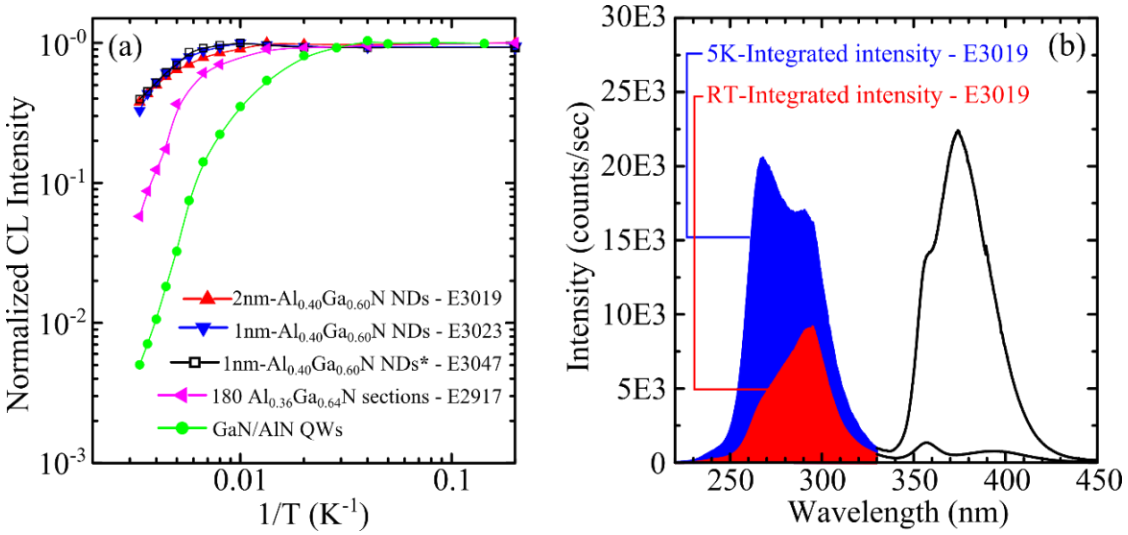

*Figure 5.16: (a) Integrated CL intensity as a function of temperature of a 180 nm-$Al_{0.4}Ga_{0.6}N$ section, 1- nm and 2-nm-$Al_{0.4}Ga_{0.6}N$/AlN NDs, in comparison to that of GaN/AlN QWs. Note that * represents $Al_xGa_{1-x}N$/AlN NDs which were grown by changing Φ_{Ga} from 0.14 to 0.13 ML/s. (b) 5K and RT CL spectra of of 2-nm-$Al_{0.40}Ga_{0.60}N$/AlN NDs (E3019), Blue- and red-shaded show the areas where integrated intensities for each sample were calculated.*

Figure 5.16(a) shows integrated CL intensity as a function of temperature of 2 nm-$Al_{0.40}Ga_{0.60}N$/AlN NDs (E3019), 1nm-$Al_{0.40}Ga_{0.60}N$/AlN NDs (E3023), and 1 nm-$Al_{0.40}Ga_{0.60}N$/AlN NDs grown with adapted Φ_{Ga} from 0.14 to 0.13 ML/s (E3047). In comparison, integrated CL intensity as a function of temperature of 180 nm-$Al_{0.36}Ga_{0.64}N$ sections on GaN NWs and of GaN/AlN QWs were provided. Figure 5.16(b) shows the luminescence spectra of 2nm-$Al_{0.40}Ga_{0.60}N$/AlN NDs on GaN NWs (E3019) to illustrate how the integrated intensity was calculated. For the structure grown on GaN NWs, luminescence from the sample generally shows peak emission spectra correspond to GaN NWs stem and structure on the wire tops. As depicted in Figure 5.16(b), the blue- and red-shaded spectra belong to the luminescence from AlGaN/AlN NDs while the peaks center 360-370 nm belong to that from GaN NWs. In such case, only shaded areas were summarized as the integrated CL intensity.

The IQEs of AlGaN/AlN NDs shown in Figure 5.16(a) are in the range of 30-40%, progressively higher than the IQE of 180 nm-$Al_{0.36}Ga_{0.64}N$ sections and GaN/AlN QWs which provides IQE at 5% and 0.5%, respectively, showing the efficient carrier confinement of the ND structure. The thickness of AlGaN ND was adjusted by controlling the deposited fluxes and deposition time of materials while the ND lateral dimension is governed by GaN NWs diameter which generally reports at 60 nm. The possibility of enhanced lateral confinement are investigated in the next section by applying the SK-QD conditions to the

GaN NWs heterostructuring, since the diameter of the reported SK-QDs is ~10 nm less than that of GaN NWs.

5.4 AlGaN/AlN heterostructuring via SK-QD growth conditions

In this section, I investigate the possibility to apply the growth conditions of SK-QDs to the synthesis of AlGaN/AlN heterostructures on a GaN NWs since an enhanced lateral confinement can be acquired from the structure.

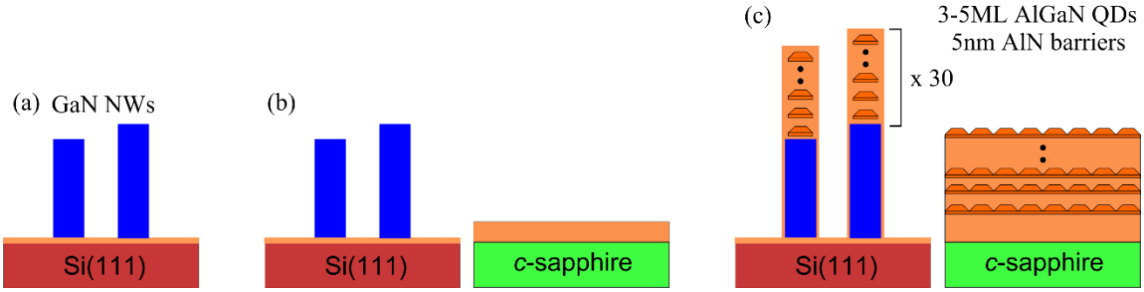

Figure 5.17: Process of the simultaneous growth of AlGaN/AlN QD SLs: (a) GaN NWs on AlN buffer layer on Si(111). (b) Sample from (a) was taken from the growth chamber, AlN-on-sapphire template substrate was placed next to the sample (a) and re-entered to the growth chamber. (c) AlGaN/AlN QD SLs were grown simultaneously on GaN NWs and on AlN-on-sapphire substrates.

The growth of QDs was simultaneously performed on GaN NWs and AlN-on-sapphire templates, as the schematic shown in Figure 5.17. First, ~600 nm of GaN NWs was grown on Si(111) substrate. After the NWs growth, the sample holder was taken out of the growth chamber. A piece of AlN-on-sapphire was attached next to the GaN NWs sample on the same sample holder which was subsequently re-entered to the growth chamber. 30 periods of AlGaN QDs were grown by keeping T_s = 720°C. Φ_{Al}, Φ_{Ga}, and Φ_N were kept at 0.035, 0.35, and 0.44 ML/s, respectively. The Al content in this section was calculated using $x = \Phi_{Al}/(\Phi_{Ga}+\Phi_{Al})$ = 9%, as the AlGaN QDs were grown in N-rich regime at T_s = 720°C, where Ga desorption and diffusion is not crucial. The amount of deposited AlGaN was varied from 3 ML(E3209) to 4 ML(E3211), and 5 ML(E3212) in the series. The growth parameters for this study are summarized in the Table 5.4. For the growth of AlN barriers, Φ_{Al} and deposition time were kept at ~0.44 ML/s and 45 s.

Figure 5.18(a)-(b) shows the morphology of AlGaN/AlN SLs grown by using SK-QDs growth conditions on the top of GaN NWs. The growth at low temperature (720°C) enhances lateral growth, makes NWs progressively widen along the growth axis as depicted Figure

5.18(a), this widening might eventually cause the merging at the NW sidewalls, subsequently triggering the dislocations which deteriorate the luminescence. I also observe (in Figure 5.18(b)) that NW top morphology deviates from the flat top surface to a faceted structure, similar to the case of AlGaN sections grown on GaN NWs at low temperature range (735°C-750°C) (See 5.2.2).

Sample	Φ_{Al} (ML/s)	Φ_{Ga} (ML/s)	Φ_N (ML/s)	Al content $\Phi_{Al}/(\Phi_{Al}+\Phi_{Ga})$	Amount of deposited AlGaN (ML)
E3209	0.035	0.35	0.44	9%	3
E3211	0.035	0.35	0.44	9%	4
E3212	0.035	0.35	0.44	9%	5

Table 5.4: Description of AlGaN SK-QDs grown simulaneously on AlN-on-sapphire and GaN NWs on Si(111): deposited fluxes, Al content, and the amount of deposited AlGaN.

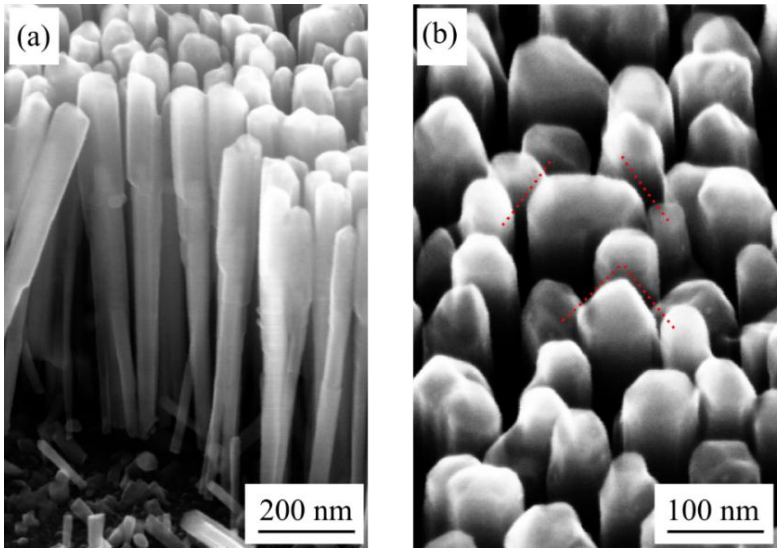

Figure 5.18: (a) SEM and (b) zoomed SEM images of 5ML-AlGaN/AlN-SLs grown on GaN NWs (E3212) using SK-QDs growth conditions.

Figure 5.19(a) shows spectral response of AlGaN QDs grown on the AlN-on-sapphire template. All the spectra show single-Gaussian characteristic with the peak blue-shift from 4.17 eV to 4.69 eV (with FWHMs ~250 meV) when the amount of AlGaN is decreased from 5 ML to 3 ML. This result is comparable to samples E3180 (3ML AlGaN QDs), E3179(4ML AlGaN QDs), and E3178(5ML AlGaN QDs) reported in section 4.4, which were grown using the same growth conditions. In contrast, the luminescence from the AlGaN/AlN SLs on GaN NWs show a much larger linewidth in the range of 500-750 meV as displayed in Figure 5.19(b). Interestingly, for a deposited AlGaN amount of 3 ML, the luminescence shows favourable emitting positions at 4.25, 4.78 and 5.17 eV, i.e. at the same spectral positions of AlGaN NDs grown on GaN NWs (see Figure 5.15).

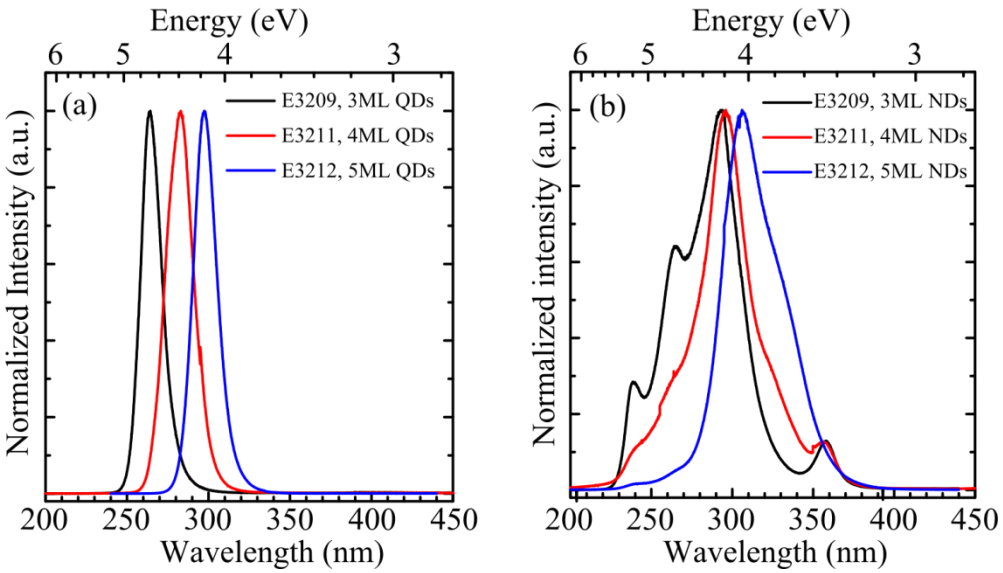

Figure 5.19: (a) Normalized room temperature CL spectra of AlGaN SK-QD SLs grown on (a) AlN-on-sapphire and on (b) GaN NWs on Si(111).

These preliminary results show that the GaN NW heterostructuring can be performed using SK-QDs growth conditions, leading to the optical characteristics (linewidth, spectral distribution) similar to those of AlGaN/AlN NDs grown on GaN NWs.

5.5 Conclusions

I firstly present the study of AlGaN sections (~180 nm long) on GaN NWs. Structural investigations show the alloy inhomogeneity in AlGaN sections which does not strongly depend on the growth temperature in the 795-755°C range. The alloy inhomogeneity leads to potential fluctuations that induce carrier localization, which determines their optical behavior, i.e. red shift of the emission, *s*-shaped temperature dependence and linewidth broadening. The Al-Ga intermixing at the GaN NW and Al(Ga)N section interface is attributed to strain relaxation process interpreted by the strain calculations performed using Nextnano[3] solver on the simulated 3D structure. I exclude the growth dynamics as the origin of such intermixing since the structural results show the same characteristic at different growth temperatures.

For the study of AlGaN/AlN NDs, I define the suitable growth regime to be 2D-nitrogen rich in order to obtain short wavelength emission spectra. Structural characterization of AlGaN NDs shows that the ND shape evolves from flat top and down interfaces to a pyramidal shape with {1-103} facets. Axially, the Al composition at the center of the NDs

gradually increases along the growth axis, and radially a Ga-rich area is generated at the edge of the NDs. The radial phase separation is more pronounced in the topmost ND layers. These structural results are correlated to the strain evolution which was solved using 3D strain calculations. Despite the challenge to control the alloy inhomogeneity, I demonstrate that the emission peak wavelength of AlGaN NDs can be tuned from 240 to 350 nm with IQE = 30-40% by adjusting the ND thickness and Al content. Nonetheless, the short wavelength approaching was obtained along with multi-peaks, thus producing a large FWHM whereas the growth at low temperature (755°C) enhances the long wavelength line by suppressing the Ga desorption processes.

Integrating the AlGaN/AlN SLs inside GaN NWs by using SK-QD growth conditions was proved possible, in spite of a widening of the NW that can eventually result in NW-sidewall merging. The optical characteristic grants the luminescence with a broad linewidth associated to alloy and structural inhomogeneity, similar to the case of AlGaN/AlN NDs grown on GaN NWs.

Chapter 6

6 The electron-pumped ultraviolet emitter

In this chapter, I first describe the growth and characterization of the active medium selected for the first prototype of electron-pumped ultraviolet (EPUV) emitter, consisting of an AlGaN/AlN quantum dot superlattice deposited on 6H-SiC. Then, I describe the device fabrication and characterization of the device. To complete the study, a final test is set by exposing E-coli bacteria to the prototype emission in order to evaluate its purification ability.

This chapter reports on the first prototype of electron-pumped ultraviolet (EPUV) emitter, integrating the carbon nanotube (CNT) electron emitter, the vacuum tube, and the active medium. The prototype fabrication characterization was performed by the group of Prof. S. Purcell at Université Claude Bernard Lyon1.

6.1 The active medium

For the active medium, I fabricated an $Al_xGa_{1-x}N$/AlN quantum dot (QD) superlattice (SL) on 6H-SiC using the optimized parameters reported in chapter 4. The active medium consists of 80 periods of 4-monolayer (ML)-thick AlGaN QDs and 5-nm-thick AlN barriers deposited on 100-nm-thick AlN grown by plasma-assisted molecular beam epitaxy (PA-MBE) on a 6H-SiC substrate. The choice of 6H-SiC was made to exploit the advantages of thermal and electrical conductivity of such substrate to favour the heat and charge evacuation, which might be main challenges in EPUV devices. The growth of AlGaN QDs was performed at a substrate temperature of 740°C, using a Ga flux Φ_{Ga} = 0.3 ML/s, Al flux Φ_{Al} = 0.064 ML/s, and N flux Φ_N = 0.38 ML/s. The AlGaN QDs were Si-doped in the 10^{19} cm^{-3} range to favor charge evacuation under electron injection. The schematic of the grown sample is depicted in Figure 6.1.

The efficiency of such sample was evaluated in terms of internal quantum efficiency (IQE) and external quantum efficiency (EQE). An IQE of 42% was estimated by the ratio of

integrated photoluminescence (PL) intensity measured at room and low temperature (5 K), as displayed in Figure 6.2(a).

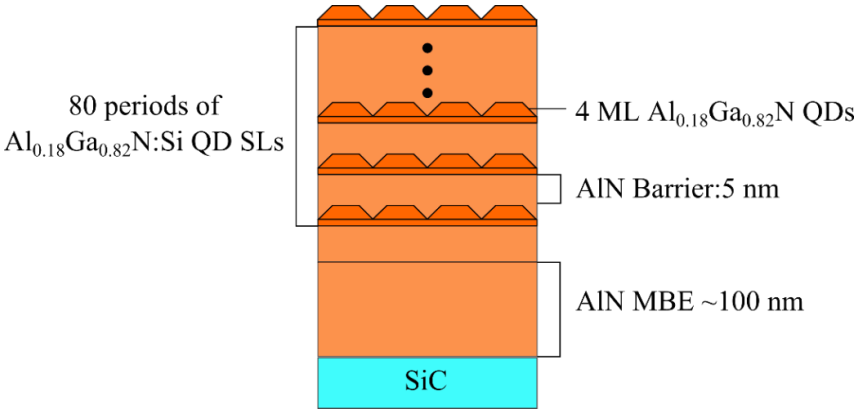

Figure 6.1: The schematic of the grown prototype sample, consisting of 80 periods of $Al_{0.18}Ga_{0.82}N$/AlN QDs. The thickness of AlGaN QDs and AlN barriers were set at 4 ML and 5 nm, respectively.

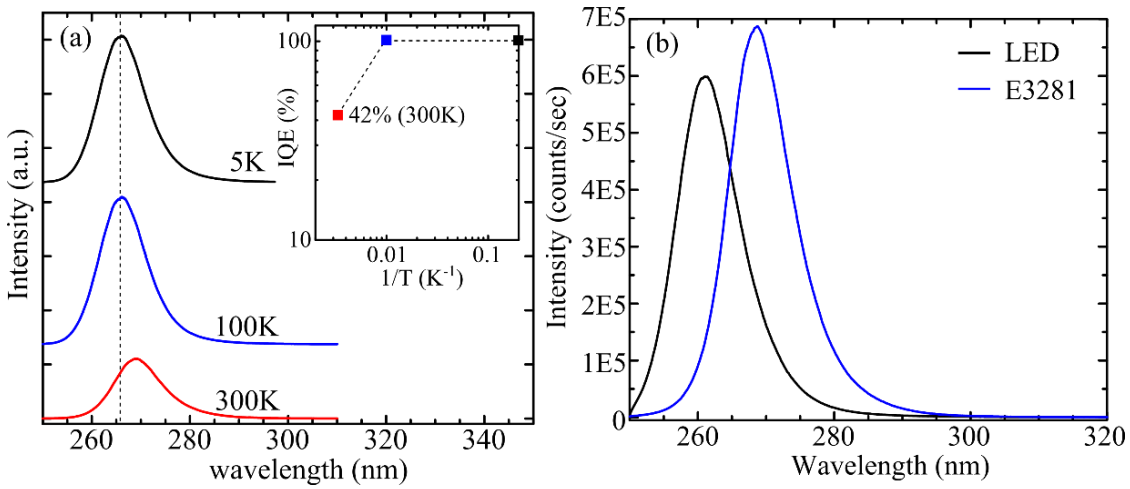

Figure 6.2 (a) PL spectra from AlGaN/AlN QDs grown on SiC measured at 5 K, 100 K, and 300 K. The spectrum measured at 100K was added in order to prove that the integrated intensities were constant at low temperature region, to assure the validity of the probed IQE. Inset: Evolution of the integrated PL intensity from the prototype sample with temperature. (b) PL spectrum of the prototype sample measured at room temperature compare with that of commercial UV-C LED.

The EQE was evaluated by quantifying the PL intensity by comparison with a commercial UV-C light emitting diode (LED) ($\lambda = 260$ nm). First, the LED optical power was measured with a calibrated silicon detector, obtaining $P_{out,LED} = 7.54$ µW. Then, using the same input current, the electroluminescence of the LED was collected by a monochromator equipped with a UV-enhanced charge-couple device (CCD) camera which provided the LED spectrum shown as the black solid line in Figure 6.2(b). The blue solid line spectrum in Figure 6.2(b) is the emission from the QD SL when excited with Ar^+ laser at

an incident power P_{in} = 1.1 mW. Using the LED as a reference, the emission of the sample is estimated to P_{out} = 8.7 µW. Then, the EQE calculated from the ratio between the radiant flux (P_{out}) and the input power (P_{in}) is 0.79%, higher than the wall-plug efficiency (WPE) of the commercial UV-C LED which was estimated at 0.15% using the equation:

$$Wall - Plug\ Efficiency\ (WPE)\ (\%) = \frac{P_{out,LED}}{P_{in,LED}} \times 100\% \qquad (6.1)$$

where $P_{in,LED}$ is the electrical input power of the LED.

6.2 The prototype

EPUV device (Figure 6.3) was fabricated by attaching the as-grown AlGaN/AlN QD SLs active medium on the copper block with indium, to help dissipating the generated heat. The CNT field emitter was optimized by Dr. M. Choueib and K. Naji from the group of Prof. S. Purcell. The source cathode was connected to the CNTs whereas the source anode was connected to the copper block which the active medium was placed on. Thus the CNTs were induced to emit electrons that are accelerated towards the active medium. Due to the requirement of operating under high vacuum, the vacuum tube was preserved under 10^{-6} Torr over the entire operation by the dynamic pump.

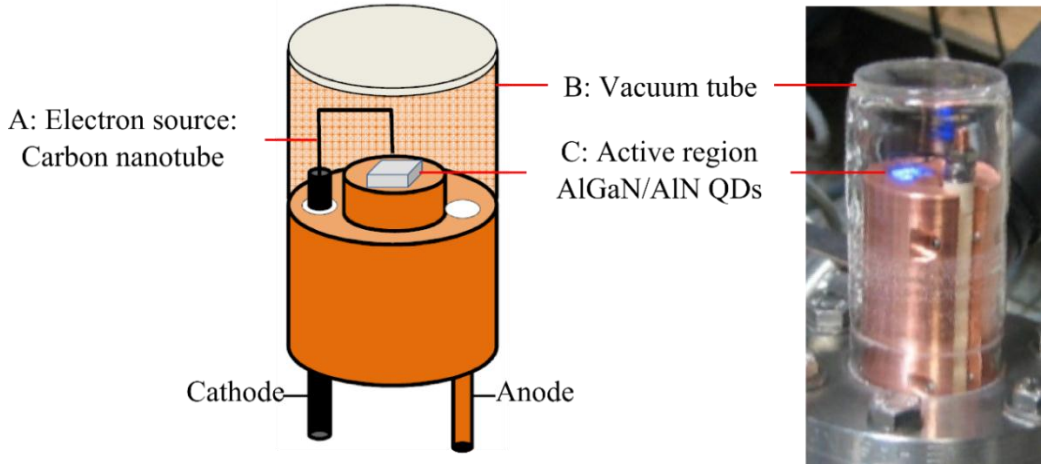

Figure 6.3: Schematic of UV emitter along with the first prototype of EPUV lamp, showing the major components including, A: the CNT field emission source, B: the vacuum tube, and C: the AlGaN/AlN QD SL active medium.

Figure 6.4(a) shows emission spectra of the AlGaN/AlN QD SL. The electron beam energy was set at 5keV, while the excitation current was scanned from 12 to 250 µA. CL measurements were carried out at room temperature in HV chamber with a base pressure ~10^{-8} torr. The electron beam energy from a thermionic field emitter can be varied between

1-20 keV and the emitted current from 1 µA to 1 mA. To measure the angular distribution of the UV emission, a UV photodetector (GaP) has been attached to a rotator in the chamber (the system has been installed by Prof. C. Dujardin).

The inset of Figure 6.4(a) shows the evolution of the peak emission intensity as a function of excitation current. The linearity of the emission points to efficient heat and charge evacuation. The angular distribution of the luminescence was also explored, as illustrated in Figure 6.4(b). The highest intensity is emitted normal to the sample surface, whereas the total emission angle was defined to be in the range of ±45° normal to the surface. These emission characteristics both in terms of non-saturated emission intensity with the excitation current and the moderate emission angle are sufficient to set up the UV-C purification testing to examine the purification performance.

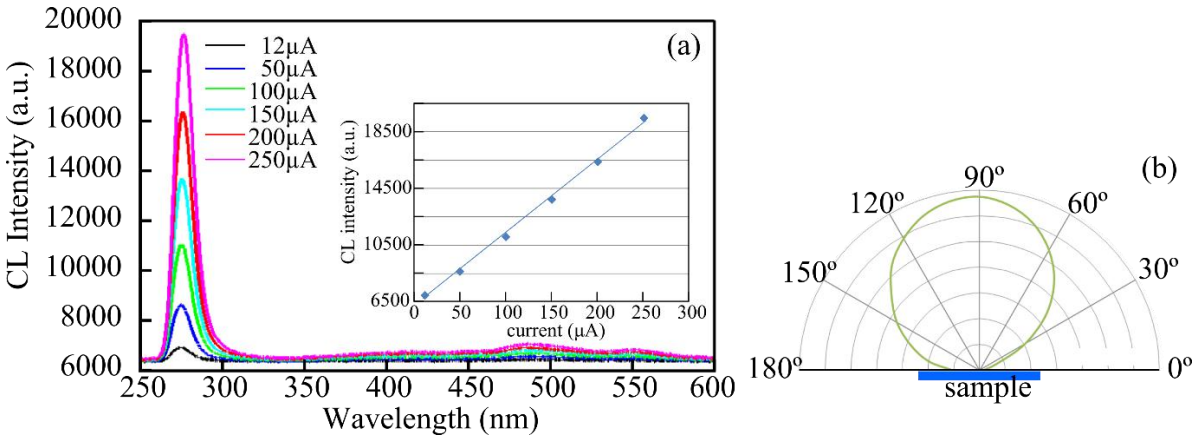

Figure 6.4:(a) CL spectra from the AlGaN/AlN QDs grown on SiC (prototype sample) exciting with a thermionic field emitter accelerated at 5 kV with various excitation currents. Inset: Evolution of CL peak intensity as a function of excitation current. (b) Measurement of the angular distribution of the luminescence angle of the prototype sample under electron excitation.

The UV-C purification testing was performed by Dr. M. Choueib in the group of Prof. S. Purcell and in collaboration with Prof. N. Cote-Pattat director of the MAP laboratory at Université Claude Bernard Lyon1. Different samples of E-coli bacteria were prepared and irradiated by exposing to our EPUV emitter. It was decided to work at low current and low acceleration voltage to prevent any degradation of the active media during the test, even if that increased the required irradiation time (field emitter current = 300 µA, acceleration voltage = 4 kV, optical power P_{out} = 38 µW). As the emission is distributed over 45° (Fig. 6.4(b)), all the UV light should be absorbed by the bacteria if they are placed at a distance of l cm to the EPUV source on a beaker with a diameter of 3.5 cm (see Fig 6.5)

The irradiated time, *t* was estimated from the output optical power of the EPUV emitter

and the purification class required after the treatment. We target the purification class 5, i.e. order of magnitude from initial condition $log\frac{N_0}{N} = 5$ where N_0 is the initial concentration and N is the concentration after irradiation. Such purification class is reported to require an irradiation dose of 10 mWcm^{-2}s, defined as:

$$Dose = \frac{P_{out} \times t}{Surface} \tag{6.2}$$

An irradiated time ~40 min was estimated from equation 6.2 using P_{out} = 38 µW and the surface of the beaker = 9.62 cm^2.

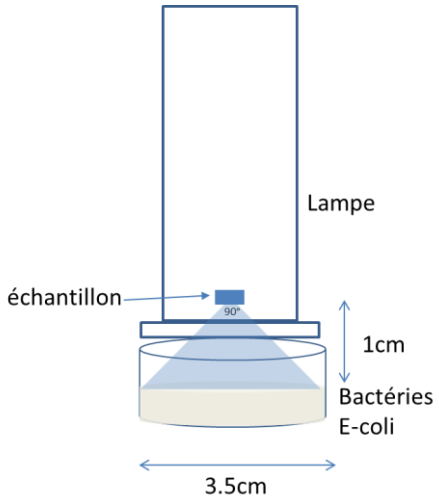

Figure 6.5: Schematic description of the experiment of UV irradiation of E-coli bacteria.

Three specimens of bacteria were prepared in a phosphate-buffered saline (PBS) solution, one as a reference, one to be irradiated for 40 min and one to be irradiated for one hour. After irradiation, specimens with various bacteria concentrations (non-diluted, 10^{-1}, 10^{-2}, 10^{-3}, and 10^{-4} diluted) were prepared for counting. For reliability, 9 specimens were cultivated on nutrient agar petri dishes. After 24 hours, it is possible to count the bacterial colonies that grew in each petri dish. In the reference beakers, the bacteria were uncountable for high concentrations, and 100-200 for the 10^{-3} diluted condition (see Figure 6.6(a) and Table 6.1). Tracing back to the non-dilute condition, the amount of bacteria should be 1-2×10^5. Then, from the design of purification class, the quantity of bacteria left from the non-diluted condition after treating for 40 min should be 1-2 bacteria.

Table 6.1 shows experimental results of the purification test, the numbers illustrate the amount of bacteria left from each testing condition. Different digit after 40 min treatment shows the quantity of bacteria from the 3 different specimens used for the same test

conditions. For instance, the result of 40 min treatment of non-dilute condition is 4 4 4, meaning that there were 4 bacteria left from the first, the second, and the third specimen. This is the only test condition where bacteria can be observed after the irradiation, as illustrated in Figure 6.6(b). For any other conditions, all the bacteria were killed. The experimental result of 4 bacteria left is in agreement with the expected calculation.

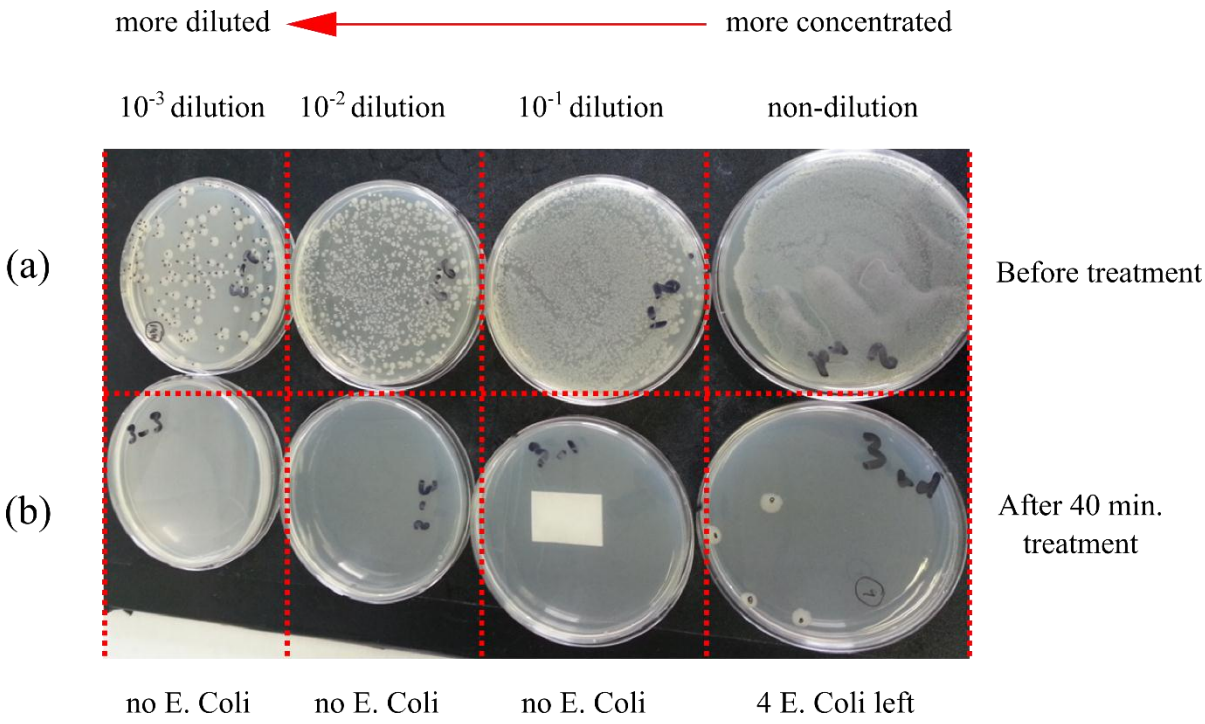

Figure 6.6: Various concentrations of bacteria, i.e. non-dilution, 10^{-1}, 10^{-2}, 10^{-3}, and 10^{-4} dilutions (a) before UV-C treatment and (b) after UV-C treatment.

	Non-diluted	10^{-1} diluted	10^{-2} diluted	10^{-3} diluted	10^{-4} diluted
Before Treatment	Uncountable	Uncountable	Uncountable	>100 bacteria	<10 bacteria
After 1 hour treatment	0 0 0	0 0 0	0 0 0	0 0 0	0 0 0
After 40 min treatment	4 4 4	0 0 0	0 0 0	0 0 0	0 0 0

Table 6.1: Amount of bacteria in each diluted condition before and after purification treatment.

6.3 Conclusions

In summary, I fabricated the active medium for the first prototype EPUV emitter. The active medium consists of an 80-period $Al_{0.18}Ga_{0.82}N$/AlN QD SL grown on 100-nm-thick

AlN on 6H-SiC. The pre-assembly efficiency of the active medium was assessed in terms of IQE (42%) and EQE (0.79%).

The prototype was fabricated under the supervision of Prof. S. Purcell at Université Claude Bernard Lyon1, by integrating the active medium with a CNT electron emitter in a vacuum tube. After the fabrication, the performance of the device was evaluated by driving the thermionic electron emitter at various currents and observing emission characteristic from the active medium. The emission intensity that increases linearly with the excitation current confirms the heat and charge evacuation efficiency.

The prototype EPUV emitter was used for a UV-C purification test which was performed by Dr. M. Choueib in collaboration with Prof. N. Cote-Pattat. The test was carried out by irradiating E-coli bacteria with EPUV emitter with various testing conditions (various exposition times), showing that all the specimens were successfully purified at the predicted UV dose.

Chapter 7

7 Conclusions and perspectives

7.1 Conclusions

The aim of this thesis was to investigate an active media for electron-pumped ultraviolet (EPUV) emitters targeting operation at 260-270 nm for water purification. Two structures were proposed, namely AlGaN/AlN quantum dots (QDs) grown by the Stranski-Krastanov (SK) method on AlN, and AlGaN/AlN nanodisks (NDs) on GaN nanowires (NWs) synthesized on Si(111) substrates. I have investigated the growth and performance of both kinds of nanostructures with the following conclusions.

Regarding AlGaN/AlN QD superlattices (SLs), I have demonstrated that by modifying the composition and geometry of the QDs, the peak emission wavelength can be shifted from 340 nm to 235 nm while keeping the internal quantum efficiency (IQE) larger than 35%. The efficient carrier confinement is confirmed by the stability of the photoluminescence (PL) intensity and decay time, from low temperature up to 100 K. Above this threshold, the PL intensity decreases and the radiative lifetime increases due to carrier thermalization.

I propose a design for the AlGaN/AlN QD SLs active region, taking into account:

- *Active region thickness:* A minimum thickness of 400 nm is obtained by measuring the electron penetration depth, with the acceleration voltage fixed at 5 kV to minimize x-ray emissions.
- *AlN barrier thickness:* A minimum AlN barrier thickness of 4-5 nm is necessary to achieve surface planarization after the deposition of each QD layer, and to prevent QD vertical correlation. Utilizing such AlN barrier thickness is assured to have a good carrier collection from the structure, since it is lower than the maximum AlN barrier thickness (~18 nm) which was defined from measurements of carrier diffusion length.
- *Amount of AlGaN in each QD layer:* An optimum amount of 5 monolayer (ML) of AlGaN provides maximum luminescence at room-temperature. This value is a compromise between the conditions of best IQE of 60% (4 ML) and highest QD density

of (9±1)×10^{11} cm^{-2} (6 ML). The evolution of QD shape is also discovered from the fitting of theoretical calculations performed by Nextnano^3 solver to the experimental results, I discover that the QD ratio (height/base diameter) decreases when increasing the amount of deposited AlGaN.

- Remaining AlGaN QD growth parameters, namely the growth temperature, and the Al content provide room for design—*adjusting peak emission wavelength to support specific applications*.
- *Post-growth treatments*—polishing, metalizing to enhance the device efficiency up to 30% is also reported.
- *Substrate options:* Although most of my work was performed on AlN-on-sapphire templates, with the advantage of being transparent in the UV range, I have also verified that the AlGaN/AlN QD SLs can be synthesized on 6H-SiC substrate without any degradation in terms of spectral response. The choice of SiC substrate is to be made when thermal/electrical conductivity becomes a limiting factor, although SiC implies sacrificing the substrate transparency.

Concerning AlGaN/AlN NW heterostructures synthesized on Si(111), I firstly investigated AlGaN sections on GaN NWs to set a foundation for the study of ND heterostructure. For the AlGaN sections grown on GaN NWs, I generally observe *alloy inhomogeneity* in the AlGaN sections, with appearance of a *transition zone* between Al(Ga)N sections and GaN NWs. The *alloy inhomogeneity and transition zone characteristics are insensitive to the growth temperature* in the range of 750-795°C. However, decreasing the growth temperature below 750°C, instead of improving alloy inhomogeneity and/or modifying transition zone, switches NW morphology to a triangle-like shape at the NW tops. The *transition zone is associated to the strain relaxation process*, which is confirmed by strain calculations using Nextnano^3 solver. The involvement of dynamic processes is excluded because the transition zone characteristic does not depend on the growth temperature. From the optical point of view, *enhanced IQE and more deviated peak emission from the calculated value are obtained when Al content of the AlGaN sections is increased*, evidencing that the alloy inhomogeneity progressively play a role when depositing higher Al contents.

For AlGaN/AlN NDs on GaN NWs, I propose the growth under *2D-nitrogen rich conditions* when the emission in UV-C range is required. *The peak emission wavelength of AlGaN NDs was tuned from 240 to 350 nm with IQE 30-40%* by adjusting the ND thickness

and Al content. I found that the *ND shape evolves* from the flat surface to the pyramidal shape with {1-103} facets when increasing the number of ND layers. *Axial and radial phase separations occur in the ND structure*. Al composition at the center of the NDs gradually increases along the growth axis, and radially a Ga-rich area is generated at the edge of NDs. The radial phase separation is more pronounced in the topmost ND layers. *The ND structural evolutions are attributed to the effect of strain evolutions* which were solved using strain calculations by Nextnano^3 solver for the structure that imitates the real growth sequences.

This thesis ends with the 1st prototype fabrication which was implemented using SK-QDs (80-period $Al_{0.18}Ga_{0.82}N$/AlN QD SL grown on 100-nm-thick AlN on 6H-SiC), integrated with the CNT electron emitter in a vacuum tube. Prior the fabrication, optical performance of the active medium was assessed in terms of IQE (42%) and EQE (0.79%). After the fabrication, the luminescence grants an emission angle of ±45° with a linearly dependent to the excitation current, revealing a good thermal and charge evacuations of the device. A water purification test was carried out by irradiating the E-coli bacteria with the prototype emitter. The results show that all the specimens were successfully purified at the nominal dose.

7.2 Perspectives

In view of the fabrication of competitive EPUV emitters, I have identified the prioritary lines of work for both types of proposed active media.

Regarding the **AlGaN/AlN QD SLs**, the 1st prototype device was fabricated using 6H-SiC as a substrate since the charge and heat evacuations were a concern. However, SiC is sometimes abstained because of its high-priced and opaqueness. Thus, I propose further investigations on the AlGaN/AlN QD SLs grown on sapphire substrates which are:

- *Evaluation of charge and heat evacuation* on sapphire substrates. This is a requirement to know whether or not this substrate disturbs the luminescence characteristics. If charge evacuation were a problem, it could be solved by the insertion of a conductive buffer layer between the AlN-on-sapphire template and the active region. Heat dissipation could be improved, for instance, by thinning the sapphire substrate or defining some deep etching areas to be filled with metal.

- *Post-growth treatments*, namely polishing, metalizing, and/or surface patterning need to be investigated to enhance the luminescence. For instance, it has been shown [263] that the optical output power of the sample increases for 2.2 times (at a forward current of 20 mA) when one-side surface patterning is performed. These treatments would be more efficient in the case of using sapphire substrates due to their transparency in the emission spectral range.

Despite the discussed advantages of the **AlGaN/AlN NDs on GaN NWs**, the reason of refraining it for the prototype fabrication was the distinct alloy inhomogeneity which induces the challenge of a broad-multiple spectrum especially in UV-C range. These facts has influenced the following views:

- *Correlated microscopic-scale luminescence and structural investigations of single* NWs should be studied in order to better understand the effect of alloy characteristics on the linewidth broadening and *further design proper structures and growth conditions*.
- *Selective-area growth*, which provides extremely uniform GaN NW diameters and adjustable density [264], is proposed. This method can minimize the shadowing effect and the wire geometry distribution, which are critical parameters that broaden the luminescence lines. Furthermore, the homogeneity of the ternary alloys under such conditions has not been studied yet. The change of polarity and growth kinetics might result in significant changes in comparison to the self-assemble NW structures described in this thesis.
- Despite the targeted UV-C application set as a basis for this manuscript, the luminescence characteristics of (Al)GaN/AlN NDs on GaN NWs are convincing to realize *devices which operate in UV-B range*. Note that the EPUV emitters are worth to investigate only these ranges (UV-B, UV-C) where the problems of doping and contacts introduce a dramatic limitation for current LED technology.

References

[1] F. Fichter, "Über Aluminiumnitride," *Z Anorg Chem*, vol. 54, p. 322, 1907.

[2] W. C. Johnson, J. B. Parson, and M. C. Crew, "Nitrogen Compounds of Gallium. III," *J. Phys. Chem.*, vol. 36, no. 10, pp. 2651–2654, Jan. 1931.

[3] R. Juza and H. Hahn, "Über die Kristallstrukturen von Cu3N, GaN und InN Metallamide und Metallnitride," *Z. Für Anorg. Allg. Chem.*, vol. 239, no. 3, pp. 282–287, Oct. 1938.

[4] H. P. Maruska, "THE PREPARATION AND PROPERTIES OF VAPOR-DEPOSITED SINGLE-CRYSTAL-LINE GaN," *Appl. Phys. Lett.*, vol. 15, no. 10, p. 327, 1969.

[5] J. Bauer, L. Biste, and D. Bolze, "Optical properties of aluminium nitride prepared by chemical and plasmachemical vapour deposition," *Phys. Status Solidi A*, vol. 39, no. 1, pp. 173–181, Jan. 1977.

[6] H. M. Manasevit, F. M. Erdmann, and W. I. Simpson, "The Use of Metalorganics in the Preparation of Semiconductor Materials," *J. Electrochem. Soc.*, vol. 118, no. 11, p. 1864, 1971.

[7] S. Yoshida, S. Misawa, and A. Itoh, "Epitaxial growth of aluminum nitride films on sapphire by reactive evaporation," *Appl. Phys. Lett.*, vol. 26, no. 8, p. 461, 1975.

[8] H. Amano, N. Sawaki, I. Akasaki, and Y. Toyoda, "Metalorganic vapor phase epitaxial growth of a high quality GaN film using an AlN buffer layer," *Appl. Phys. Lett.*, vol. 48, no. 5, p. 353, 1986.

[9] H. Amano, M. Kito, K. Hiramatsu, and I. Akasaki, "P-Type Conduction in Mg-Doped GaN Treated with Low-Energy Electron Beam Irradiation (LEEBI)," *Jpn. J. Appl. Phys.*, vol. 28, no. Part 2, No. 12, pp. L2112–L2114, Dec. 1989.

[10] S. Nakamura, T. Mukai, and M. Senoh, "Candela-class high-brightness InGaN/AlGaN double-heterostructure blue-light-emitting diodes," *Appl. Phys. Lett.*, vol. 64, no. 13, p. 1687, 1994.

[11] S. Nakamura, M. Senoh, S. Nagahama, N. Iwasa, T. Yamada, T. Matsushita, H. Kiyoku, and Y. Sugimoto, "InGaN Multi-Quantum-Well-Structure Laser Diodes with Cleaved Mirror Cavity Facets," *Jpn. J. Appl. Phys.*, vol. 35, no. Part 2, No. 2B, pp. L217–L220, Feb. 1996.

[12] M. Asif Khan, J. N. Kuznia, D. T. Olson, W. J. Schaff, J. W. Burm, and M. S. Shur, "Microwave performance of a 0.25 µm gate AlGaN/GaN heterostructure field effect transistor," *Appl. Phys. Lett.*, vol. 65, no. 9, p. 1121, 1994.

[13] H.-S. Lee, D. Piedra, M. Sun, X. Gao, S. Guo, and T. Palacios, "3000-V 4.3-Omega . cm(2) InAlN/GaN MOSHEMTs With AlGaN Back Barrier," *IEEE Electron Device Lett.*, vol. 33, no. 7, pp. 982–984, Jul. 2012.

[14] M. Sun, H.-S. Lee, B. Lu, D. Piedra, and T. Palacios, "Comparative Breakdown Study of Mesa- and Ion-Implantation-Isolated AlGaN/GaN High-Electron-Mobility Transistors on Si Substrate," *Appl. Phys. Express*, vol. 5, no. 7, p. 074202, Jul. 2012.

[15] M. Razeghi and A. Rogalski, "Semiconductor ultraviolet detectors," *J. Appl. Phys.*, vol. 79, no. 10, p. 7433, 1996.

[16] E. Monroy, F. Omn s, and F. Calle, "Wide-bandgap semiconductor ultraviolet photodetectors," *Semicond. Sci. Technol.*, vol. 18, no. 4, pp. R33–R51, Apr. 2003.

[17] J. R. Lang, C. J. Neufeld, C. A. Hurni, S. C. Cruz, E. Matioli, U. K. Mishra, and J. S. Speck, "High external quantum efficiency and fill-factor InGaN/GaN heterojunction solar cells grown by NH[sub 3]-based molecular beam epitaxy," *Appl. Phys. Lett.*, vol. 98, no. 13, p. 131115, 2011.

[18] R. M. Farrell, C. J. Neufeld, S. C. Cruz, J. R. Lang, M. Iza, S. Keller, S. Nakamura, S. P. DenBaars, U. K. Mishra, and J. S. Speck, "High quantum efficiency InGaN/GaN multiple quantum well solar cells with spectral response extending out to 520 nm," *Appl. Phys. Lett.*, vol. 98, no. 20, p. 201107, 2011.

[19] S. Valdueza-Felip, A. Mukhtarova, L. Grenet, C. Bougerol, C. Durand, J. Eymery, and

E. Monroy, “Improved conversion efficiency of as-grown InGaN/GaN quantum-well solar cells for hybrid integration,” *Appl. Phys. Express*, vol. 7, no. 3, p. 032301, Mar. 2014.

[20] M. Mori, S. Yamamoto, Y. Kuwahara, T. Fujii, T. Sugiyama, M. Iwaya, T. Takeuchi, S. Kamiyama, I. Akasaki, and H. Amano, “Concentrating properties of nitride-based solar cells using GaInN/GaInN superlattices,” 2012, p. 82620Z–82620Z–8.

[21] M. Beeler, E. Trichas, and E. Monroy, “III-nitride semiconductors for intersubband optoelectronics: a review,” *Semicond. Sci. Technol.*, vol. 28, no. 7, p. 074022, Jul. 2013.

[22] B. F. Levine, “Quantum-well infrared photodetectors,” *J. Appl. Phys.*, vol. 74, no. 8, p. R1, 1993.

[23] J. Faist, F. Capasso, D. L. Sivco, C. Sirtori, A. L. Hutchinson, and A. Y. Cho, “Quantum Cascade Laser,” *Science*, vol. 264, no. 5158, pp. 553–556, Apr. 1994.

[24] K. Motoki, T. Okahisa, R. Hirota, S. Nakahata, K. Uematsu, and N. Matsumoto, “Dislocation reduction in GaN crystal by advanced-DEEP,” *J. Cryst. Growth*, vol. 305, no. 2, pp. 377–383, Jul. 2007.

[25] M. K. Kelly, R. P. Vaudo, V. M. Phanse, L. Görgens, O. Ambacher, and M. Stutzmann, “Large Free-Standing GaN Substrates by Hydride Vapor Phase Epitaxy and Laser-Induced Liftoff,” *Jpn. J. Appl. Phys.*, vol. 38, no. Part 2, No. 3A, pp. L217–L219, Mar. 1999.

[26] R. Dwiliński, R. Doradziński, J. Garczyński, L. P. Sierzputowski, A. Puchalski, Y. Kanbara, K. Yagi, H. Minakuchi, and H. Hayashi, “Excellent crystallinity of truly bulk ammonothermal GaN,” *J. Cryst. Growth*, vol. 310, no. 17, pp. 3911–3916, Aug. 2008.

[27] “mercury spectral linewidths.”

[28] G. Derra, H. Moench, E. Fischer, H. Giese, U. Hechtfischer, G. Heusler, A. Koerber, U. Niemann, F.-C. Noertemann, P. Pekarski, J. Pollmann-Retsch, A. Ritz, and U. Weichmann, “UHP lamp systems for projection applications,” *J. Phys. Appl. Phys.*, vol. 38, no. 17, pp. 2995–3010, Sep. 2005.

[29] J. Reader, C. J. Sansonetti, and J. M. Bridges, “Irradiances of spectral lines in mercury pencil lamps,” *Appl. Opt.*, vol. 35, no. 1, p. 78, Jan. 1996.

[30] A. Khan, K. Balakrishnan, and T. Katona, “Ultraviolet light-emitting diodes based on group three nitrides,” *Nat. Photonics*, vol. 2, no. 2, pp. 77–84, Feb. 2008.

[31] T. Mukai, S. Nagahama, N. Iwasa, M. Senoh, and T. Yamada, “Nitride light-emitting diodes,” *J. Phys. Condens. Matter*, vol. 13, no. 32, pp. 7089–7098, Aug. 2001.

[32] K. Akita, T. Kyono, Y. Yoshizumi, H. Kitabayashi, and K. Katayama, “Characteristics of InGaN light-emitting diodes on GaN substrates with low threading dislocation densities,” *Phys. Status Solidi A*, vol. 204, no. 1, pp. 246–250, Jan. 2007.

[33] F. Bernardini, V. Fiorentini, and D. Vanderbilt, “Spontaneous polarization and piezoelectric constants of III-V nitrides,” *Phys. Rev. B*, vol. 56, no. 16, pp. R10024–R10027, Oct. 1997.

[34] K. B. Nam, M. L. Nakarmi, J. Li, J. Y. Lin, and H. X. Jiang, “Mg acceptor level in AlN probed by deep ultraviolet photoluminescence,” *Appl. Phys. Lett.*, vol. 83, no. 5, p. 878, 2003.

[35] M. Kneissl, T. Kolbe, C. Chua, V. Kueller, N. Lobo, J. Stellmach, A. Knauer, H. Rodriguez, S. Einfeldt, Z. Yang, N. M. Johnson, and M. Weyers, “Advances in group III-nitride-based deep UV light-emitting diode technology,” *Semicond. Sci. Technol.*, vol. 26, no. 1, p. 014036, Jan. 2011.

[36] T. Oto, R. G. Banal, K. Kataoka, M. Funato, and Y. Kawakami, “100 mW deep-ultraviolet emission from aluminium-nitride-based quantum wells pumped by an electron beam,” *Nat. Photonics*, vol. 4, no. 11, pp. 767–770, Nov. 2010.

[37] C. A. Klein, “Bandgap Dependence and Related Features of Radiation Ionization Energies in Semiconductors,” *J. Appl. Phys.*, vol. 39, no. 4, p. 2029, 1968.

[38] K. Watanabe, T. Taniguchi, T. Niiyama, K. Miya, and M. Taniguchi, “Far-ultraviolet plane-emission handheld device based on hexagonal boron nitride,” *Nat. Photonics*,

vol. 3, no. 10, pp. 591–594, Oct. 2009.
[39] H. S. Nalwa, Ed., *Handbook of nanostructured materials and nanotechnology*. San Diego: Academic Press, 2000.
[40] C.-Y. Yeh, Z. Lu, S. Froyen, and A. Zunger, "Predictions and systematizations of the zinc-blende–wurtzite structural energies in binary octet compounds," *Phys. Rev. B*, vol. 45, no. 20, pp. 12130–12133, May 1992.
[41] B. Daudin, G. Feuillet, J. Hubner, Y. Samson, F. Widmann, A. Philippe, C. Bru-Chevallier, G. Guillot, E. Bustarret, G. Bentoumi, and A. Deneuville, "How to grow cubic GaN with low hexagonal phase content on (001) SiC by molecular beam epitaxy," *J. Appl. Phys.*, vol. 84, no. 4, p. 2295, 1998.
[42] X. L. Sun, Y. T. Wang, H. Yang, L. X. Zheng, D. P. Xu, J. B. Li, and Z. G. Wang, "Strain and photoluminescence characterization of cubic (In,Ga)N films grown on GaAs(001) substrates," *J. Appl. Phys.*, vol. 87, no. 8, p. 3711, 2000.
[43] A. F. Wright, "Basal-plane stacking faults and polymorphism in AlN, GaN, and InN," *J. Appl. Phys.*, vol. 82, no. 10, p. 5259, 1997.
[44] H. Morkoc¸, S. Strite, G. B. Gao, M. E. Lin, B. Sverdlov, and M. Burns, "Large-band-gap SiC, III-V nitride, and II-VI ZnSe-based semiconductor device technologies," *J. Appl. Phys.*, vol. 76, no. 3, p. 1363, 1994.
[45] I. Vurgaftman and J. R. Meyer, "Band parameters for nitrogen-containing semiconductors," *J. Appl. Phys.*, vol. 94, no. 6, p. 3675, 2003.
[46] O. Ambacher, "Growth and applications of Group III-nitrides," *J. Phys. Appl. Phys.*, vol. 31, no. 20, pp. 2653–2710, Oct. 1998.
[47] T. Sasaki and T. Matsuoka, "Substrate-polarity dependence of metal-organic vapor-phase epitaxy-grown GaN on SiC," *J. Appl. Phys.*, vol. 64, no. 9, p. 4531, 1988.
[48] M. Asif Khan, J. N. Kuznia, D. T. Olson, and R. Kaplan, "Deposition and surface characterization of high quality single crystal GaN layers," *J. Appl. Phys.*, vol. 73, no. 6, p. 3108, 1993.
[49] M. Seelmann-Eggebert, J. L. Weyher, H. Obloh, H. Zimmermann, A. Rar, and S. Porowski, "Polarity of (00.1) GaN epilayers grown on a (00.1) sapphire," *Appl. Phys. Lett.*, vol. 71, no. 18, p. 2635, 1997.
[50] A. W. Stevenson, S. W. Wilkins, M. S. Kwietniak, and G. N. Pain, "Polarity determination of single-crystal epitaxial layers by x-ray diffraction," *J. Appl. Phys.*, vol. 66, no. 9, p. 4198, 1989.
[51] R. D. Horning and B. L. Goldenberg, "AlxGa1−xN polarity determination by x-ray diffraction," *Appl. Phys. Lett.*, vol. 55, no. 17, p. 1721, 1989.
[52] D. C. Meyer, K. Richter, H. G. Krane, W. Morgenroth, and P. Paufler, "Determination of polarity in noncentrosymmetric layer/substrate systems," *J. Appl. Crystallogr.*, vol. 32, no. 5, pp. 854–858, Oct. 1999.
[53] F. A. Ponce, D. P. Bour, W. T. Young, M. Saunders, and J. W. Steeds, "Determination of lattice polarity for growth of GaN bulk single crystals and epitaxial layers," *Appl. Phys. Lett.*, vol. 69, no. 3, p. 337, 1996.
[54] B. Daudin, J. L. Rouvière, and M. Arlery, "The key role of polarity in the growth process of (0001) nitrides," *Mater. Sci. Eng. B*, vol. 43, no. 1–3, pp. 157–160, Jan. 1997.
[55] D. Li, M. Sumiya, K. Yoshimura, Y. Suzuki, Y. Fukuda, and S. Fuke, "Characteristics of the GaN Polar Surface during an Etching Process in KOH Solution," *Phys. Status Solidi A*, vol. 180, no. 1, pp. 357–362, Jul. 2000.
[56] V. Ramachandran, R. M. Feenstra, W. L. Sarney, L. Salamanca-Riba, J. E. Northrup, L. T. Romano, and D. W. Greve, "Inversion of wurtzite GaN(0001) by exposure to magnesium," *Appl. Phys. Lett.*, vol. 75, no. 6, p. 808, 1999.
[57] I. Remediakis and E. Kaxiras, "Band-structure calculations for semiconductors within generalized-density-functional theory," *Phys. Rev. B*, vol. 59, no. 8, pp. 5536–5543, Feb. 1999.
[58] L. Cláudio de Carvalho, A. Schleife, F. Fuchs, and F. Bechstedt, "Valence-band

splittings in cubic and hexagonal AlN, GaN, and InN," *Appl. Phys. Lett.*, vol. 97, no. 23, p. 232101, 2010.

[59] Y. Li, Y. Lu, H. Shen, M. Wraback, M. G. Brown, M. Schurman, L. Koszi, and R. A. Stall, "Temperature dependence of energy gap in GaN thin film studied by thermomodulation," *Appl. Phys. Lett.*, vol. 70, no. 18, p. 2458, 1997.

[60] S. Tripathy, R. K. Soni, H. Asahi, K. Iwata, R. Kuroiwa, K. Asami, and S. Gonda, "Optical properties of GaN layers grown on C-, A-, R-, and M-plane sapphire substrates by gas source molecular beam epitaxy," *J. Appl. Phys.*, vol. 85, no. 12, p. 8386, 1999.

[61] Q. Guo and A. Yoshida, "Temperature Dependence of Band Gap Change in InN and AlN," *Jpn. J. Appl. Phys.*, vol. 33, no. Part 1, No. 5A, pp. 2453–2456, May 1994.

[62] G. Steude, D. M. Hofmann, B. K. Meyer, H. Amano, and I. Akasaki, "The Dependence of the Band Gap on Alloy Composition in Strained AlGaN on GaN," *Phys. Status Solidi B*, vol. 205, no. 1, pp. R7–R8, Jan. 1998.

[63] S. R. Lee, A. F. Wright, M. H. Crawford, G. A. Petersen, J. Han, and R. M. Biefeld, "The band-gap bowing of Al[sub x]Ga[sub 1−x]N alloys," *Appl. Phys. Lett.*, vol. 74, no. 22, p. 3344, 1999.

[64] Y. P. Varshni, "Temperature dependence of the energy gap in semiconductor.," *Physica*, vol. 34, pp. 149–154.

[65] P. Perlin, E. Litwin-Staszewska, B. Suchanek, W. Knap, J. Camassel, T. Suski, R. Piotrzkowski, I. Grzegory, S. Porowski, E. Kaminska, and J. C. Chervin, "Determination of the effective mass of GaN from infrared reflectivity and Hall effect," *Appl. Phys. Lett.*, vol. 68, no. 8, p. 1114, 1996.

[66] M. Drechsler, D. M. Hofmann, B. K. Meyer, T. Detchprohm, H. Amano, and I. Akasaki, "Determination of the Conduction Band Electron Effective Mass in Hexagonal GaN," *Jpn. J. Appl. Phys.*, vol. 34, no. Part 2, No. 9B, pp. L1178–L1179, Sep. 1995.

[67] J. S. Im, A. Moritz, F. Steuber, V. Härle, F. Scholz, and A. Hangleiter, "Radiative carrier lifetime, momentum matrix element, and hole effective mass in GaN," *Appl. Phys. Lett.*, vol. 70, no. 5, p. 631, 1997.

[68] M. Suzuki, T. Uenoyama, and A. Yanase, "First-principles calculations of effective-mass parameters of AlN and GaN," *Phys. Rev. B*, vol. 52, no. 11, pp. 8132–8139, Sep. 1995.

[69] A. Salvador, G. Liu, W. Kim, O. Aktas, A. Botchkarev, and H. Morkoc, "Properties of a Si doped GaN/AlGaN single quantum well," *Appl. Phys. Lett.*, vol. 67, no. 22, p. 3322, 1995.

[70] C. Merz, M. Kunzer, U. Kaufmann, I. Akasaki, and H. Amano, "Free and bound excitons in thin wurtzite GaN layers on sapphire," *Semicond. Sci. Technol.*, vol. 11, no. 5, pp. 712–716, May 1996.

[71] J. L. Pankove, S. Bloom, and G. Harbeke, "Optical properties of GaN.," *RCA Rev.*, vol. 36, no. 163, 1975.

[72] I. Vurgaftman, J. R. Meyer, and L. R. Ram-Mohan, "Band parameters for III–V compound semiconductors and their alloys," *J. Appl. Phys.*, vol. 89, no. 11, p. 5815, 2001.

[73] K. Kim, W. Lambrecht, B. Segall, and M. van Schilfgaarde, "Effective masses and valence-band splittings in GaN and AlN," *Phys. Rev. B*, vol. 56, no. 12, pp. 7363–7375, Sep. 1997.

[74] Y. Takagi, M. Ahart, T. Azuhata, T. Sota, K. Suzuki, and S. Nakamura, "Brillouin scattering study in the GaN epitaxial layer," *Phys. B Condens. Matter*, vol. 219–220, pp. 547–549, Apr. 1996.

[75] A. Polian, M. Grimsditch, and I. Grzegory, "Elastic constants of gallium nitride," *J. Appl. Phys.*, vol. 79, no. 6, p. 3343, 1996.

[76] M. Yamaguchi, T. Yagi, T. Azuhata, T. Sota, K. Suzuki, S. Chichibu, and S. Nakamura, "Brillouin scattering study of gallium nitride: elastic stiffness constants," *J. Phys.*

Condens. Matter, vol. 9, no. 1, pp. 241–248, Jan. 1997.

[77] C. Deger, E. Born, H. Angerer, O. Ambacher, M. Stutzmann, J. Hornsteiner, E. Riha, and G. Fischerauer, "Sound velocity of Al[sub x]Ga[sub 1−x]N thin films obtained by surface acoustic-wave measurements," *Appl. Phys. Lett.*, vol. 72, no. 19, p. 2400, 1998.

[78] K. Kim, W. Lambrecht, and B. Segall, "Elastic constants and related properties of tetrahedrally bonded BN, AlN, GaN, and InN," *Phys. Rev. B*, vol. 53, no. 24, pp. 16310–16326, Jun. 1996.

[79] A. F. Wright, "Elastic properties of zinc-blende and wurtzite AlN, GaN, and InN," *J. Appl. Phys.*, vol. 82, no. 6, p. 2833, 1997.

[80] L. E. McNeil, M. Grimsditch, and R. H. French, "Vibrational Spectroscopy of Aluminum Nitride," *J. Am. Ceram. Soc.*, vol. 76, no. 5, pp. 1132–1136, May 1993.

[81] A. Zoroddu, F. Bernardini, P. Ruggerone, and V. Fiorentini, "First-principles prediction of structure, energetics, formation enthalpy, elastic constants, polarization, and piezoelectric constants of AlN, GaN, and InN: Comparison of local and gradient-corrected density-functional theory," *Phys. Rev. B*, vol. 64, no. 4, Jul. 2001.

[82] F. Bernardini and V. Fiorentini, "Nonlinear Behavior of Spontaneous and Piezoelectric Polarization in III–V Nitride Alloys," *Phys. Status Solidi A*, vol. 190, no. 1, pp. 65–73, 2002.

[83] V. Fiorentini, F. Bernardini, and O. Ambacher, "Evidence for nonlinear macroscopic polarization in III–V nitride alloy heterostructures," *Appl. Phys. Lett.*, vol. 80, no. 7, p. 1204, 2002.

[84] F. Bernardini and V. Fiorentini, "Nonlinear macroscopic polarization in III-V nitride alloys," *Phys. Rev. B*, vol. 64, no. 8, Aug. 2001.

[85] O. Ambacher, B. Foutz, J. Smart, J. R. Shealy, N. G. Weimann, K. Chu, M. Murphy, A. J. Sierakowski, W. J. Schaff, L. F. Eastman, R. Dimitrov, A. Mitchell, and M. Stutzmann, "Two dimensional electron gases induced by spontaneous and piezoelectric polarization in undoped and doped AlGaN/GaN heterostructures," *J. Appl. Phys.*, vol. 87, no. 1, p. 334, 2000.

[86] X. H. Wu, L. M. Brown, D. Kapolnek, S. Keller, B. Keller, S. P. DenBaars, and J. S. Speck, "Defect structure of metal-organic chemical vapor deposition-grown epitaxial (0001) GaN/Al2O3," *J. Appl. Phys.*, vol. 80, no. 6, p. 3228, 1996.

[87] X. J. Ning, F. R. Chien, P. Pirouz, J. W. Yang, and M. A. Khan, "Growth defects in GaN films on sapphire: The probable origin of threading dislocations," *J. Mater. Res.*, vol. 11, no. 03, pp. 580–592, Mar. 1996.

[88] E. V. Etzkorn and D. R. Clarke, "Cracking of GaN films," *J. Appl. Phys.*, vol. 89, no. 2, p. 1025, 2001.

[89] F. Semond, P. Lorenzini, N. Grandjean, and J. Massies, "High-electron-mobility AlGaN/GaN heterostructures grown on Si(111) by molecular-beam epitaxy," *Appl. Phys. Lett.*, vol. 78, no. 3, p. 335, 2001.

[90] W. G. Perry, M. . Bremser, T. Zheleva, K. . Linthicum, and R. . Davis, "Biaxial strain in AlxGa1−xN/GaN layers deposited on 6H-SiC," *Thin Solid Films*, vol. 324, no. 1–2, pp. 107–114, Jul. 1998.

[91] J. E. Northrup, "Theory of the (12$\bar{1}$0) prismatic stacking fault in GaN," *Appl. Phys. Lett.*, vol. 72, no. 18, p. 2316.

[92] V. Potin, P. Ruterana, and G. Nouet, "HREM study of stacking faults in GaN layers grown over sapphire substrate," *J. Phys. Condens. Matter*, vol. 12, no. 10301, 2000.

[93] P. Vermaut, G. Nouet, and P. Ruterana, "Observation of two atomic configurations for the {12$\bar{1}$0} stacking fault in wurtzite (Ga, Al) nitrides," *Appl. Phys. Lett.*, vol. 74, no. 5, p. 694, 1999.

[94] D. S. Li, H. Chen, H. B. Yu, X. H. Zheng, Q. Huang, and J. M. Zhou, "Anisotropy of a-plane GaN grown on r-plane sapphire by metalorganic chemical vapor deposition," *J. Cryst. Growth*, vol. 265, no. 1–2, pp. 107–110, Apr. 2004.

[95] R. Liu, A. Bell, F. A. Ponce, C. Q. Chen, J. W. Yang, and M. A. Khan, "Luminescence

from stacking faults in gallium nitride," *Appl. Phys. Lett.*, vol. 86, no. 2, p. 021908, 2005.

[96] R. C. Powell, N.-E. Lee, and J. E. Greene, "Growth of GaN(0001)1×1 on Al2O3(0001) by gas-source molecular beam epitaxy," *Appl. Phys. Lett.*, vol. 60, no. 20, p. 2505, 1992.

[97] R. C. Powell, N.-E. Lee, Y.-W. Kim, and J. E. Greene, "Heteroepitaxial wurtzite and zinc-blende structure GaN grown by reactive-ion molecular-beam epitaxy: Growth kinetics, microstructure, and properties," *J. Appl. Phys.*, vol. 73, no. 1, p. 189, 1993.

[98] W. Qian, M. Skowronski, M. De Graef, K. Doverspike, L. B. Rowland, and D. K. Gaskill, "Microstructural characterization of α-GaN films grown on sapphire by organometallic vapor phase epitaxy," *Appl. Phys. Lett.*, vol. 66, no. 10, p. 1252, 1995.

[99] K. Hiramatsu, S. Itoh, H. Amano, I. Akasaki, N. Kuwano, T. Shiraishi, and K. Oki, "Growth mechanism of GaN grown on sapphire with AlN buffer layer by MOVPE," *J. Cryst. Growth*, vol. 115, pp. 628–633, 1991.

[100] B. Heying, X. H. Wu, S. Keller, Y. Li, D. Kapolnek, B. P. Keller, S. P. DenBaars, and J. S. Speck, "Role of threading dislocation structure on the x-ray diffraction peak widths in epitaxial GaN films," *Appl. Phys. Lett.*, vol. 68, no. 5, p. 643, 1996.

[101] N.-E. Lee, "Molecular beam epitaxy of GaN(0001) utilizing NH3 and/or NH+x ions: Growth kinetics and defect structure," *J. Vac. Sci. Technol. Vac. Surf. Films*, vol. 13, no. 5, p. 2293, Sep. 1995.

[102] L. T. Romano, B. S. Krusor, and R. J. Molnar, "Structure of GaN films grown by hydride vapor phase epitaxy," *Appl. Phys. Lett.*, vol. 71, no. 16, p. 2283, 1997.

[103] Z. Liliental-Weber, C. Kisielowski, S. Ruvimov, Y. Chen, J. Washburn, I. Grzegory, M. Bockowski, J. Jun, and S. Porowski, "Structural characterization of bulk GaN crystals grown under high hydrostatic pressure," *J. Electron. Mater.*, vol. 25, no. 9, pp. 1545–1550, Sep. 1996.

[104] C. Stampfl and C. Van de Walle, "Energetics and electronic structure of stacking faults in AlN, GaN, and InN," *Phys. Rev. B*, vol. 57, no. 24, pp. R15052–R15055, Jun. 1998.

[105] Y. Arroyo Rojas Dasilva, M. P. Chauvat, P. Ruterana, L. Lahourcade, E. Monroy, and G. Nataf, "Defect structure in heteroepitaxial semipolar (11\bar {2} 2) (Ga, Al)N," *J. Phys. Condens. Matter*, vol. 22, no. 35, p. 355802, Sep. 2010.

[106] J. Villain and A. Pimpinelli, *Physique de la croissance Cristalline*, Eyrolles. Paris, 1995.

[107] Y. Saito, *Statiscal Physics of Crystal Growth*, World Scienctic. Singapore, 1996.

[108] I. V. Markov, *Crystal Growth for Beginners*, World Scientific. Singapore, 1995.

[109] A. L. Barabási and H. E. Stanley, *Fractal Concepts in Surface Growth*. Cambridge University Press, 1995.

[110] P. Politi, G. Grenet, A. Marty, A. Ponchet, and J. Villain, "Instabilities in crystal growth by atomic or molecular beams," *Phys. Rep.*, vol. 324, no. 5–6, pp. 271–404, Feb. 2000.

[111] I. Daruka and A.-L. Barabási, "Dislocation-Free Island Formation in Heteroepitaxial Growth: A Study at Equilibrium," *Phys. Rev. Lett.*, vol. 79, no. 19, pp. 3708–3711, Nov. 1997.

[112] I. Daruka and A.-L. Barabási, "Equilibrium phase diagrams for dislocation free self-assembled quantum dots," *Appl. Phys. Lett.*, vol. 72, no. 17, p. 2102, 1998.

[113] F. Tinjod and H. Mariette, "Self-assembled quantum dot formation induced by surface energy change of a strained two-dimensional layer," *Phys. Status Solidi B*, vol. 241, no. 3, pp. 550–557, Mar. 2004.

[114] A. Y. Cho, "Film Deposition by Molecular-Beam Techniques," *J. Vac. Sci. Technol.*, vol. 8, no. 5, p. S31, Sep. 1971.

[115] J. E. Mahan, "A review of the geometrical fundamentals of reflection high-energy electron diffraction with application to silicon surfaces," *J. Vac. Sci. Technol. Vac. Surf. Films*, vol. 8, no. 5, p. 3692, Sep. 1990.

[116] B. A. Joyce, P. J. Dobson, J. H. Neave, K. Woodbridge, J. Zhang, P. K. Larsen, and B. Bôlger, "RHEED studies of heterojunction and quantum well formation during MBE growth — from multiple scattering to band offsets," *Surf. Sci.*, vol. 168, no. 1–3, pp. 423–438, Mar. 1986.

[117] C. Adelmann, J. Brault, G. Mula, B. Daudin, L. Lymperakis, and J. Neugebauer, "Gallium adsorption on (0001) GaN surfaces," *Phys. Rev. B*, vol. 67, no. 16, Apr. 2003.

[118] B. Heying, R. Averbeck, L. F. Chen, E. Haus, H. Riechert, and J. S. Speck, "Control of GaN surface morphologies using plasma-assisted molecular beam epitaxy," *J. Appl. Phys.*, vol. 88, no. 4, p. 1855, 2000.

[119] P. K. Kandaswamy, F. Guillot, E. Bellet-Amalric, E. Monroy, L. Nevou, M. Tchernycheva, A. Michon, F. H. Julien, E. Baumann, F. R. Giorgetta, D. Hofstetter, T. Remmele, M. Albrecht, S. Birner, and L. S. Dang, "GaN/AlN short-period superlattices for intersubband optoelectronics: A systematic study of their epitaxial growth, design, and performance," *J. Appl. Phys.*, vol. 104, no. 9, p. 093501, 2008.

[120] J. Neugebauer, T. Zywietz, M. Scheffler, J. Northrup, H. Chen, and R. Feenstra, "Adatom Kinetics On and Below the Surface: The Existence of a New Diffusion Channel," *Phys. Rev. Lett.*, vol. 90, no. 5, Feb. 2003.

[121] R. M. Feenstra, J. E. Northrup, and J. Neugebauer, "Review of Structure of Base and Adsorbate-Covered GaN(0001) surfaces," *MRS Internet J. Nitride Semicond. Res.*, vol. 7, no. 3, 2002.

[122] J. Northrup, J. Neugebauer, R. Feenstra, and A. Smith, "Structure of GaN(0001): The laterally contracted Ga bilayer model," *Phys. Rev. B*, vol. 61, no. 15, pp. 9932–9935, Apr. 2000.

[123] M. Hermann, E. Monroy, A. Helman, B. Baur, M. Albrecht, B. Daudin, O. Ambacher, M. Stutzmann, and M. Eickhoff, "Vertical transport in group III-nitride heterostructures and application in AlN/GaN resonant tunneling diodes," *Phys. Status Solidi C*, vol. 1, no. 8, pp. 2210–2227, Jul. 2004.

[124] G. Koblmueller, R. Averbeck, L. Geelhaar, H. Riechert, W. Hösler, and P. Pongratz, "Growth diagram and morphologies of AlN thin films grown by molecular beam epitaxy," *J. Appl. Phys.*, vol. 93, no. 12, p. 9591, 2003.

[125] E. Monroy, B. Daudin, E. Bellet-Amalric, N. Gogneau, D. Jalabert, F. Enjalbert, J. Brault, J. Barjon, and L. S. Dang, "Surfactant effect of In for AlGaN growth by plasma-assisted molecular beam epitaxy," *J. Appl. Phys.*, vol. 93, no. 3, p. 1550, 2003.

[126] E. Iliopoulos and T. D. Moustakas, "Growth kinetics of AlGaN films by plasma-assisted molecular-beam epitaxy," *Appl. Phys. Lett.*, vol. 81, no. 2, p. 295, 2002.

[127] B. Damilano, N. Grandjean, F. Semond, J. Massies, and M. Leroux, "From visible to white light emission by GaN quantum dots on Si(111) substrate," *Appl. Phys. Lett.*, vol. 75, no. 7, p. 962, 1999.

[128] N. Gogneau, E. Sarigiannidou, E. Monroy, S. Monnoye, H. Mank, and B. Daudin, "Surfactant effect of gallium during the growth of GaN on AlN(0001) by plasma-assisted molecular beam epitaxy," *Appl. Phys. Lett.*, vol. 85, no. 8, p. 1421, 2004.

[129] J. Brown, F. Wu, P. M. Petroff, and J. S. Speck, "GaN quantum dot density control by rf-plasma molecular beam epitaxy," *Appl. Phys. Lett.*, vol. 84, no. 5, p. 690, 2004.

[130] Z. Gačević, A. Das, J. Teubert, Y. Kotsar, P. K. Kandaswamy, T. Kehagias, T. Koukoula, P. Komninou, and E. Monroy, "Internal quantum efficiency of III-nitride quantum dot superlattices grown by plasma-assisted molecular-beam epitaxy," *J. Appl. Phys.*, vol. 109, no. 10, p. 103501, 2011.

[131] F. Guillot, E. Bellet-Amalric, E. Monroy, M. Tchernycheva, L. Nevou, L. Doyennette, F. H. Julien, L. S. Dang, T. Remmele, M. Albrecht, T. Shibata, and M. Tanaka, "Si-doped GaN/AlN quantum dot superlattices for optoelectronics at telecommunication wavelengths," *J. Appl. Phys.*, vol. 100, no. 4, p. 044326, 2006.

[132] F. Glas, "Critical dimensions for the plastic relaxation of strained axial heterostructures in free-standing nanowires," *Phys. Rev. B*, vol. 74, no. 12, Sep. 2006.

[133] A. B. Greytak, C. J. Barrelet, Y. Li, and C. M. Lieber, "Semiconductor nanowire laser

and nanowire waveguide electro-optic modulators," *Appl. Phys. Lett.*, vol. 87, no. 15, p. 151103, 2005.

[134] W. Guo, M. Zhang, A. Banerjee, and P. Bhattacharya, "Catalyst-Free InGaN/GaN Nanowire Light Emitting Diodes Grown on (001) Silicon by Molecular Beam Epitaxy," *Nano Lett.*, vol. 10, no. 9, pp. 3355–3359, Sep. 2010.

[135] H.-W. Lin, Y.-J. Lu, H.-Y. Chen, H.-M. Lee, and S. Gwo, "InGaN/GaN nanorod array white light-emitting diode," *Appl. Phys. Lett.*, vol. 97, no. 7, p. 073101, 2010.

[136] L. Rigutti, M. Tchernycheva, A. De Luna Bugallo, G. Jacopin, F. H. Julien, L. F. Zagonel, K. March, O. Stephan, M. Kociak, and R. Songmuang, "Ultraviolet Photodetector Based on GaN/AlN Quantum Disks in a Single Nanowire," *Nano Lett.*, vol. 10, no. 8, pp. 2939–2943, Aug. 2010.

[137] A. Kikuchi, M. Kawai, M. Tada, and K. Kishino, "InGaN/GaN Multiple Quantum Disk Nanocolumn Light-Emitting Diodes Grown on (111) Si Substrate," *Jpn. J. Appl. Phys.*, vol. 43, no. No. 12A, pp. L1524–L1526, Nov. 2004.

[138] R. S. Wagner and W. C. Ellis, "VAPOR-LIQUID-SOLID MECHANISM OF SINGLE CRYSTAL GROWTH," *Appl. Phys. Lett.*, vol. 4, no. 5, p. 89, 1964.

[139] L. Geelhaar, C. Chèze, W. M. Weber, R. Averbeck, H. Riechert, T. Kehagias, P. Komninou, G. P. Dimitrakopulos, and T. Karakostas, "Axial and radial growth of Ni-induced GaN nanowires," *Appl. Phys. Lett.*, vol. 91, no. 9, p. 093113, 2007.

[140] L. T. T. Giang, C. Bougerol, H. Mariette, and R. Songmuang, "Intrinsic limits governing MBE growth of Ga-assisted GaAs nanowires on Si(111)," *J. Cryst. Growth*, vol. 364, pp. 118–122, Feb. 2013.

[141] M. F. Bailon-Somintac, J. J. Ibañez, R. B. Jaculbia, R. A. Loberternos, M. J. Defensor, A. A. Salvador, and A. S. Somintac, "Low temperature photoluminescence and Raman phonon modes of Au-catalyzed MBE-grown GaAs–AlGaAs core–shell nanowires grown on a pre-patterned Si (111) substrate," *J. Cryst. Growth*, vol. 314, no. 1, pp. 268–273, Jan. 2011.

[142] M. J. Tambe, S. Ren, and S. Gradečak, "Effects of Gold Diffusion on n-Type Doping of GaAs Nanowires," *Nano Lett.*, vol. 10, no. 11, pp. 4584–4589, Nov. 2010.

[143] T. Kuykendall, P. J. Pauzauskie, Y. Zhang, J. Goldberger, D. Sirbuly, J. Denlinger, and P. Yang, "Crystallographic alignment of high-density gallium nitride nanowire arrays," *Nat. Mater.*, vol. 3, no. 8, pp. 524–528, Aug. 2004.

[144] S. Han, W. Jin, T. Tang, C. Li, D. Zhang, X. Liu, J. Han, and C. Zhou, "Controlled growth of gallium nitride single-crystal nanowires using a chemical vapor deposition method," *J. Mater. Res.*, vol. 18, no. 02, pp. 245–249, Feb. 2003.

[145] J. Goldberger, R. He, Y. Zhang, S. Lee, H. Yan, H.-J. Choi, and P. Yang, "Single-crystal gallium nitride nanotubes," *Nature*, vol. 422, no. 6932, pp. 599–602, Apr. 2003.

[146] A. Colli, S. Hofmann, A. C. Ferrari, C. Ducati, F. Martelli, S. Rubini, S. Cabrini, A. Franciosi, and J. Robertson, "Low-temperature synthesis of ZnSe nanowires and nanosaws by catalyst-assisted molecular-beam epitaxy," *Appl. Phys. Lett.*, vol. 86, no. 15, p. 153103, 2005.

[147] Y. Ohno, T. Shirahama, S. Takeda, A. Ishizumi, and Y. Kanemitsu, "Fe-catalytic growth of ZnSe nanowires on a ZnSe(001) surface at low temperatures by molecular-beam epitaxy," *Appl. Phys. Lett.*, vol. 87, no. 4, p. 043105, 2005.

[148] E. Janik, J. Sadowski, P. Dłużewski, S. Kret, L. T. Baczewski, A. Petroutchik, E. Łusakowska, J. Wróbel, W. Zaleszczyk, G. Karczewski, T. Wojtowicz, and A. Presz, "ZnTe nanowires grown on GaAs(100) substrates by molecular beam epitaxy," *Appl. Phys. Lett.*, vol. 89, no. 13, p. 133114, 2006.

[149] J. Basu, R. Divakar, J. Nowak, S. Hofmann, A. Colli, A. Franciosi, and C. B. Carter, "Structure and growth mechanism of ZnSe nanowires," *J. Appl. Phys.*, vol. 104, no. 6, p. 064302, 2008.

[150] X. T. Zhang, Z. Liu, Y. P. Leung, Q. Li, and S. K. Hark, "Growth and luminescence of zinc-blende-structured ZnSe nanowires by metal-organic chemical vapor deposition," *Appl. Phys. Lett.*, vol. 83, no. 26, p. 5533, 2003.

[151] X. T. Zhang, "Luminescence of ZnSe nanowires grown by metalorganic vapor phase deposition under different pressures," *J. Appl. Phys.*, vol. 95, no. 10, p. 5752, 2004.
[152] U. Philipose, T. Xu, S. Yang, P. Sun, H. E. Ruda, Y. Q. Wang, and K. L. Kavanagh, "Enhancement of band edge luminescence in ZnSe nanowires," *J. Appl. Phys.*, vol. 100, no. 8, p. 084316, 2006.
[153] R. Koester, J. S. Hwang, C. Durand, D. Le Si Dang, and J. Eymery, "Self-assembled growth of catalyst-free GaN wires by metal–organic vapour phase epitaxy," *Nanotechnology*, vol. 21, no. 1, p. 015602, Jan. 2010.
[154] M. Yoshizawa, A. Kikuchi, M. Mori, N. Fujita, and K. Kishino, "Growth of Self-Organized GaN Nanostructures on $\bf Al_{2}O_{3}(0001)$ by RF-Radical Source Molecular Beam Epitaxy," *Jpn. J. Appl. Phys.*, vol. 36, no. Part 2, No. 4B, pp. L459–L462, Apr. 1997.
[155] M. Yoshizawa, A. Kikuchi, N. Fujita, K. Kushi, H. Sasamoto, and K. Kishino, "Self-organization of GaN/Al0.18Ga0.82N multi-layer nano-columns on (0001) Al2O3 by RF molecular beam epitaxy for fabricating GaN quantum disks," *J. Cryst. Growth*, vol. 189–190, pp. 138–141, Jun. 1998.
[156] M. A. Sanchez-Garcia, E. Calleja, E. Monroy, F. J. Sanchez, F. Calle, E. Muñoz, and R. Beresford, "The effect of the III/V ratio and substrate temperature on the morphology and properties of GaN- and AlN-layers grown by molecular beam epitaxy on Si(1 1 1)," *J. Cryst. Growth*, vol. 183, no. 1–2, pp. 23–30, Jan. 1998.
[157] J. Grandal, M. A. Sánchez-García, E. Calleja, E. Luna, and A. Trampert, "Accommodation mechanism of InN nanocolumns grown on Si(111) substrates by molecular beam epitaxy," *Appl. Phys. Lett.*, vol. 91, no. 2, p. 021902, 2007.
[158] R. Songmuang, O. Landré, and B. Daudin, "From nucleation to growth of catalyst-free GaN nanowires on thin AlN buffer layer," *Appl. Phys. Lett.*, vol. 91, no. 25, p. 251902, 2007.
[159] A. Ohtani, K. S. Stevens, and R. Beresford, "Microstructure and photoluminescence of GaN grown on Si(111) by plasma-assisted molecular beam epitaxy," *Appl. Phys. Lett.*, vol. 65, no. 1, p. 61, 1994.
[160] E. Calleja, M. . Sánchez-García, F. . Sánchez, F. Calle, F. . Naranjo, E. Muñoz, S. . Molina, A. . Sánchez, F. . Pacheco, and R. García, "Growth of III-nitrides on Si(111) by molecular beam epitaxy Doping, optical, and electrical properties," *J. Cryst. Growth*, vol. 201–202, pp. 296–317, May 1999.
[161] J. Ristić, E. Calleja, S. Fernández-Garrido, L. Cerutti, A. Trampert, U. Jahn, and K. H. Ploog, "On the mechanisms of spontaneous growth of III-nitride nanocolumns by plasma-assisted molecular beam epitaxy," *J. Cryst. Growth*, vol. 310, no. 18, pp. 4035–4045, Aug. 2008.
[162] S. Fernández-Garrido, J. Grandal, E. Calleja, M. A. Sánchez-García, and D. López-Romero, "A growth diagram for plasma-assisted molecular beam epitaxy of GaN nanocolumns on Si(111)," *J. Appl. Phys.*, vol. 106, no. 12, p. 126102, 2009.
[163] C.-W. Hu, H. Hibino, T. Ogino, and I. S. T. Tsong, "Hysteresis in the (1×1)-(7×7) first-order phase transition on the Si(111) surface," *Surf. Sci.*, vol. 487, no. 1–3, pp. 191–200, Jul. 2001.
[164] W. Telieps and E. Bauer, "The (7 × 7) ↔ (1 × 1) phase transition on Si(111)," *Surf. Sci.*, vol. 162, no. 1–3, pp. 163–168, Oct. 1985.
[165] P. A. Bennett and M. W. Webb, "The Si(111) 7 × 7 TO '1 × 1' transition," *Surf. Sci.*, vol. 104, no. 1, pp. 74–104, Mar. 1981.
[166] K. Takayanagi, "Structural analysis of Si(111)-7×7 by UHV-transmission electron diffraction and microscopy," *J. Vac. Sci. Technol. Vac. Surf. Films*, vol. 3, no. 3, p. 1502, May 1985.
[167] O. Landré, C. Bougerol, H. Renevier, and B. Daudin, "Nucleation mechanism of GaN nanowires grown on (111) Si by molecular beam epitaxy," *Nanotechnology*, vol. 20, no. 41, p. 415602, Oct. 2009.
[168] V. Consonni, M. Knelangen, L. Geelhaar, A. Trampert, and H. Riechert, "Nucleation

mechanisms of epitaxial GaN nanowires: Origin of their self-induced formation and initial radius," *Phys. Rev. B*, vol. 81, no. 8, Feb. 2010.

[169] R. Calarco, R. J. Meijers, R. K. Debnath, T. Stoica, E. Sutter, and H. Lüth, "Nucleation and Growth of GaN Nanowires on Si(111) Performed by Molecular Beam Epitaxy," *Nano Lett.*, vol. 7, no. 8, pp. 2248–2251, Aug. 2007.

[170] C. Ratsch and J. A. Venables, "Nucleation theory and the early stages of thin film growth," *J. Vac. Sci. Technol. Vac. Surf. Films*, vol. 21, no. 5, p. S96, 2003.

[171] M. Arlery, J. L. Rouvière, F. Widmann, B. Daudin, G. Feuillet, and H. Mariette, "Quantitative characterization of GaN quantum-dot structures in AlN by high-resolution transmission electron microscopy," *Appl. Phys. Lett.*, vol. 74, no. 22, p. 3287, 1999.

[172] M. Korytov, M. Benaissa, J. Brault, T. Huault, T. Neisius, and P. Vennéguès, "Effects of capping on GaN quantum dots deposited on Al[sub 0.5]Ga[sub 0.5]N by molecular beam epitaxy," *Appl. Phys. Lett.*, vol. 94, no. 14, p. 143105, 2009.

[173] I. Daruka, J. Tersoff, and A.-L. Barabási, "Shape Transition in Growth of Strained Islands," *Phys. Rev. Lett.*, vol. 82, no. 13, pp. 2753–2756, Mar. 1999.

[174] J. Tersoff, B. Spencer, A. Rastelli, and H. von Känel, "Barrierless Formation and Faceting of SiGe Islands on Si(001)," *Phys. Rev. Lett.*, vol. 89, no. 19, Oct. 2002.

[175] K. A. Bertness, A. Roshko, L. M. Mansfield, T. E. Harvey, and N. A. Sanford, "Nucleation conditions for catalyst-free GaN nanowires," *J. Cryst. Growth*, vol. 300, no. 1, pp. 94–99, Mar. 2007.

[176] L. Lymperakis and J. Neugebauer, "Large anisotropic adatom kinetics on nonpolar GaN surfaces: Consequences for surface morphologies and nanowire growth," *Phys. Rev. B*, vol. 79, no. 24, Jun. 2009.

[177] T. Zywietz, J. Neugebauer, and M. Scheffler, "Adatom diffusion at GaN (0001) and (000$\bar{1}$) surfaces," *Appl. Phys. Lett.*, vol. 73, no. 4, p. 487, 1998.

[178] R. Songmuang, T. Ben, B. Daudin, D. González, and E. Monroy, "Identification of III–N nanowire growth kinetics via a marker technique," *Nanotechnology*, vol. 21, no. 29, p. 295605, Jul. 2010.

[179] J. Ristić, E. Calleja, M. Sánchez-García, J. Ulloa, J. Sánchez-Páramo, J. Calleja, U. Jahn, A. Trampert, and K. Ploog, "Characterization of GaN quantum discs embedded in AlxGa1-xN nanocolumns grown by molecular beam epitaxy," *Phys. Rev. B*, vol. 68, no. 12, Sep. 2003.

[180] J. Ristić, C. Rivera, E. Calleja, S. Fernández-Garrido, M. Povoloskyi, and A. Di Carlo, "Carrier-confinement effects in nanocolumnar GaN/AlxGa1−xN quantum disks grown by molecular-beam epitaxy," *Phys. Rev. B*, vol. 72, no. 8, Aug. 2005.

[181] J. Ristić, E. Calleja, A. Trampert, S. Fernández-Garrido, C. Rivera, U. Jahn, and K. Ploog, "Columnar AlGaN/GaN Nanocavities with AlN/GaN Bragg Reflectors Grown by Molecular Beam Epitaxy on Si(111)," *Phys. Rev. Lett.*, vol. 94, no. 14, Apr. 2005.

[182] N. Grandjean, J. Massies, F. Semond, S. Y. Karpov, and R. A. Talalaev, "Erratum: 'GaN evaporation in molecular beam epitaxy environment' [Appl. Phys. Lett. 74, 1854 (1999)]," *Appl. Phys. Lett.*, vol. 75, no. 19, p. 3035, 1999.

[183] A. J. Ptak, M. R. Millecchia, T. H. Myers, K. S. Ziemer, and C. D. Stinespring, "The relation of active nitrogen species to high-temperature limitations for (000$\bar{1}$) GaN growth by radio-frequency-plasma-assisted molecular beam epitaxy," *Appl. Phys. Lett.*, vol. 74, no. 25, p. 3836, 1999.

[184] S. D. Carnevale, J. Yang, P. J. Phillips, M. J. Mills, and R. C. Myers, "Three-Dimensional GaN/AlN Nanowire Heterostructures by Separating Nucleation and Growth Processes," *Nano Lett.*, vol. 11, no. 2, pp. 866–871, Feb. 2011.

[185] H. Iwanaga, A. Kunishige, and S. Takeuchi, "Anisotropic thermal expansion in wurtzite-type crystals," *J. Mater. Sci.*, vol. 35, pp. 2451–2454, 2000.

[186] A. Alemu, M. Julier, J. Campo, B. Gil, D. Scalbert, J.-P. Lascaray, and S. Nakamura, "Optical anisotropy in GaN grown onto A–plane sapphire," *Mater. Sci. Eng. B*, vol. 59, no. 1–3, pp. 159–162, May 1999.

[187] C. R. Eddy, T. D. Moustakas, and J. Scanlon, "Growth of gallium nitride thin films by electron cyclotron resonance microwave plasma-assisted molecular beam epitaxy," *J. Appl. Phys.*, vol. 73, no. 1, p. 448, 1993.

[188] K. Iwata, H. Asahi, K. Asami, R. Kuroiwa, and S. Gonda, "Gas Source Molecular Beam Epitaxy Growth of GaN on C-, A-, R- and M-Plane Sapphire and Silica Glass Substrates," *Jpn. J. Appl. Phys.*, vol. 36, no. Part 2, No. 6A, pp. L661–L664, Jun. 1997.

[189] T. J. Baker, B. A. Haskell, F. Wu, J. S. Speck, and S. Nakamura, "Characterization of Planar Semipolar Gallium Nitride Films on Sapphire Substrates," *Jpn. J. Appl. Phys.*, vol. 45, no. No. 6, pp. L154–L157, Feb. 2006.

[190] M. J. Kappers, J. L. Hollander, C. McAleese, C. F. Johnston, R. F. Broom, J. S. Barnard, M. E. Vickers, and C. J. Humphreys, "Growth and characterisation of semi-polar InGaN/GaN MQW structures," *J. Cryst. Growth*, vol. 300, no. 1, pp. 155–159, Mar. 2007.

[191] G. Binnig and C. F. Quate, "Atomic Force Microscope," *Phys. Rev. Lett.*, vol. 56, no. 9, pp. 930–933, Mar. 1986.

[192] R. Wiesendanger, *Scanning probe microscopy and spectroscopy*. Cambridge University Press, 1994.

[193] J. O. Tegenfeldt and L. Montelius, "Image widening not only a question of tip sample convolution," *Appl. Phys. Lett.*, vol. 66, no. 9, p. 1068, 1995.

[194] M. T. Postek, K. S. Howard, A. H. Johnson, and K. L. McMichael, *Scanning electron microscopy: a student's handbook. Williston, VT: Ladd Research Industries, Inc*. Ladd Research Ind., Inc.: Williston, VT, 1980.

[195] C. E. Lyman, Ed., *Scanning electron microscopy, X-ray microanalysis, and analytical electron microscopy: a laboratory workbook*. New York: Plenum Press, 1990.

[196] A. Bhattacharyya, T. D. Moustakas, L. Zhou, D. J. Smith, and W. Hug, "Deep ultraviolet emitting AlGaN quantum wells with high internal quantum efficiency," *Appl. Phys. Lett.*, vol. 94, no. 18, p. 181907, 2009.

[197] M. Shatalov, J. Yang, W. Sun, R. Kennedy, R. Gaska, K. Liu, M. Shur, and G. Tamulaitis, "Efficiency of light emission in high aluminum content AlGaN quantum wells," *J. Appl. Phys.*, vol. 105, no. 7, p. 073103, 2009.

[198] W. Zhang, A. Y. Nikiforov, C. Thomidis, J. Woodward, H. Sun, C.-K. Kao, D. Bhattarai, A. Moldawer, L. Zhou, D. J. Smith, and T. D. Moustakas, "Molecular beam epitaxy growth of AlGaN quantum wells on 6H-SiC substrates with high internal quantum efficiency," *J. Vac. Sci. Technol. B Microelectron. Nanometer Struct.*, vol. 30, no. 2, p. 02B119, 2012.

[199] G. Rajanna, W. Feng, S. Sohal, V. V. Kuryatkov, S. A. Nikishin, A. A. Bernussi, and M. Holtz, "Temperature and excitation intensity dependence of photoluminescence in AlGaN quantum wells with mixed two-dimensional and three-dimensional morphology," *J. Appl. Phys.*, vol. 110, no. 7, p. 073512, 2011.

[200] H.-M. Huang, C.-Y. Chang, Y.-P. Lan, T.-C. Lu, H.-C. Kuo, and S.-C. Wang, "Ultraviolet emission efficiency enhancement of a-plane AlGaN/GaN multiple-quantum-wells with increasing quantum well thickness," *Appl. Phys. Lett.*, vol. 100, no. 26, p. 261901, 2012.

[201] J. Renard, P. K. Kandaswamy, E. Monroy, and B. Gayral, "Suppression of nonradiative processes in long-lived polar GaN/AlN quantum dots," *Appl. Phys. Lett.*, vol. 95, no. 13, p. 131903, 2009.

[202] J. Verma, P. K. Kandaswamy, V. Protasenko, A. Verma, H. Grace Xing, and D. Jena, "Tunnel-injection GaN quantum dot ultraviolet light-emitting diodes," *Appl. Phys. Lett.*, vol. 102, no. 4, p. 041103, 2013.

[203] J. Brault, B. Damilano, B. Vinter, P. Vennéguès, M. Leroux, A. Kahouli, and J. Massies, "AlGaN-Based Light Emitting Diodes Using Self-Assembled GaN Quantum Dots for Ultraviolet Emission," *Jpn. J. Appl. Phys.*, vol. 52, no. 8S, p. 08JG01, Aug. 2013.

[204] J. Verma, S. M. Islam, V. Protasenko, P. Kumar Kandaswamy, H. (Grace) Xing, and D. Jena, "Tunnel-injection quantum dot deep-ultraviolet light-emitting diodes with polarization-induced doping in III-nitride heterostructures," *Appl. Phys. Lett.*, vol. 104, no. 2, p. 021105, Jan. 2014.

[205] J. Simon, V. Protasenko, C. Lian, H. Xing, and D. Jena, "Polarization-Induced Hole Doping in Wide-Band-Gap Uniaxial Semiconductor Heterostructures," *Science*, vol. 327, no. 5961, pp. 60–64, Jan. 2010.

[206] K. Kanaya and S. Okayama, "Penetration and energy-loss theory of electrons in solid targets," *J. Phys. Appl. Phys.*, vol. 5, no. 1, pp. 43–58, Jan. 1972.

[207] M. Toth and M. R. Phillips, "Monte Carlo modeling of cathodoluminescence generation using electron energy loss curves," *Scanning*, vol. 20, no. 6, pp. 425–432, Dec. 2006.

[208] P. Hovington, D. Drouin, and R. Gauvin, "CASINO: A new monte carlo code in C language for electron beam interaction -part I: Description of the program," *Scanning*, vol. 19, no. 1, pp. 1–14, Dec. 2006.

[209] D. Drouin, P. Hovington, and R. Gauvin, "CASINO: A new monte carlo code in C language for electron beam interactions-part II: Tabulated values of the mott cross section," *Scanning*, vol. 19, no. 1, pp. 20–28, Dec. 2006.

[210] P. Hovington, D. Drouin, R. Gauvin, D. C. Joy, and N. Evans, "CASINO: A new monte Carlo code in C language for electron beam interactions-part III: Stopping power at low energies," *Scanning*, vol. 19, no. 1, pp. 29–35, Dec. 2006.

[211] N. Gogneau, F. Fossard, E. Monroy, S. Monnoye, H. Mank, and B. Daudin, "Effects of stacking on the structural and optical properties of self-organized GaN/AlN quantum dots," *Appl. Phys. Lett.*, vol. 84, no. 21, p. 4224, 2004.

[212] V. Chamard, T. Schülli, M. Sztucki, T. Metzger, E. Sarigiannidou, J.-L. Rouvière, M. Tolan, C. Adelmann, and B. Daudin, "Strain distribution in nitride quantum dot multilayers," *Phys. Rev. B*, vol. 69, no. 12, Mar. 2004.

[213] B. Daudin, F. Widmann, G. Feuillet, Y. Samson, M. Arlery, and J. Rouvière, "Stranski-Krastanov growth mode during the molecular beam epitaxy of highly strained GaN," *Phys. Rev. B*, vol. 56, no. 12, pp. R7069–R7072, Sep. 1997.

[214] F. Ross, J. Tersoff, and R. Tromp, "Coarsening of Self-Assembled Ge Quantum Dots on Si(001)," *Phys. Rev. Lett.*, vol. 80, no. 5, pp. 984–987, Feb. 1998.

[215] A. Rosa and J. Neugebauer, "First-principles calculations of the structural and electronic properties of clean GaN(0001) surfaces," *Phys. Rev. B*, vol. 73, no. 20, May 2006.

[216] M. Leroux, N. Grandjean, B. Beaumont, G. Nataf, F. Semond, J. Massies, and P. Gibart, "Temperature quenching of photoluminescence intensities in undoped and doped GaN," *J. Appl. Phys.*, vol. 86, no. 7, p. 3721, 1999.

[217] P. Lefebvre, T. Taliercio, A. Morel, J. Allègre, M. Gallart, B. Gil, H. Mathieu, B. Damilano, N. Grandjean, and J. Massies, "Effects of GaAlN barriers and of dimensionality on optical recombination processes in InGaN quantum wells and quantum boxes," *Appl. Phys. Lett.*, vol. 78, no. 11, p. 1538, 2001.

[218] F. Rol, S. Founta, H. Mariette, B. Daudin, L. Dang, J. Bleuse, D. Peyrade, J.-M. Gérard, and B. Gayral, "Probing exciton localization in nonpolar GaN⁄AlN quantum dots by single-dot optical spectroscopy," *Phys. Rev. B*, vol. 75, no. 12, Mar. 2007.

[219] E. Kuokstis, W. H. Sun, M. Shatalov, J. W. Yang, and M. Asif Khan, "Role of alloy fluctuations in photoluminescence dynamics of AlGaN epilayers," *Appl. Phys. Lett.*, vol. 88, no. 26, p. 261905, 2006.

[220] N. Nepal, J. Li, M. L. Nakarmi, J. Y. Lin, and H. X. Jiang, "Exciton localization in AlGaN alloys," *Appl. Phys. Lett.*, vol. 88, no. 6, p. 062103.

[221] C. J. Collins, A. V. Sampath, G. A. Garrett, W. L. Sarney, H. Shen, M. Wraback, A. Y. Nikiforov, G. S. Cargill, and V. Dierolf, "Enhanced room-temperature luminescence efficiency through carrier localization in Al[sub x]Ga[sub 1−x]N alloys," *Appl. Phys. Lett.*, vol. 86, no. 3, p. 031916, 2005.

[222] I. Friel, "Investigation of excitons in AlGaN/GaN multiple quantum wells by lateral photocurrent and photoluminescence spectroscopies," *J. Appl. Phys.*, vol. 95, no. 7, p. 3495, 2004.

[223] M. Esmaeili, H. Haratizadeh, B. Monemar, P. P. Paskov, P. O. Holtz, P. Bergman, M. Iwaya, S. Kamiyama, H. Amano, and I. Akasaki, "Photoluminescence study of MOCVD-grown GaN/AlGaN MQW nanostructures: influence of Al composition and Si doping," *Nanotechnology*, vol. 18, no. 2, p. 025401, Jan. 2007.

[224] S. Birner, T. Zibold, T. Andlauer, T. Kubis, M. Sabathil, A. Trellakis, and P. Vogl, "nextnano: General Purpose 3-D Simulations," *IEEE Trans. Electron Devices*, vol. 54, no. 9, pp. 2137–2142, Sep. 2007.

[225] C. Adelmann, B. Daudin, R. Oliver, G. Briggs, and R. Rudd, "Nucleation and growth of GaN/AlN quantum dots," *Phys. Rev. B*, vol. 70, no. 12, Sep. 2004.

[226] N. Gogneau, D. Jalabert, E. Monroy, E. Sarigiannidou, J. L. Rouvière, T. Shibata, M. Tanaka, J. M. Gerard, and B. Daudin, "Influence of AlN overgrowth on structural properties of GaN quantum wells and quantum dots grown by plasma-assisted molecular beam epitaxy," *J. Appl. Phys.*, vol. 96, no. 2, p. 1104, 2004.

[227] M. Miyamura, K. Tachibana, and Y. Arakawa, "High-density and size-controlled GaN self-assembled quantum dots grown by metalorganic chemical vapor deposition," *Appl. Phys. Lett.*, vol. 80, no. 21, p. 3937, 2002.

[228] M. J. Hÿtch, E. Snoeck, and R. Kilaas, "Quantitative measurement of displacement and strain fields from HREM micrographs," *Ultramicroscopy*, vol. 74, no. 3, pp. 131–146, Aug. 1998.

[229] J. L. Rouvière, A. Mouti, and P. Stadelmann, "Measuring strain on HR-STEM images: application to threading dislocations in Al $_{0.8}$ In $_{0.2}$ N," *J. Phys. Conf. Ser.*, vol. 326, p. 012022, Nov. 2011.

[230] D. Simeonov, E. Feltin, J.-F. Carlin, R. Butté, M. Ilegems, and N. Grandjean, "Stranski-Krastanov GaN/AlN quantum dots grown by metal organic vapor phase epitaxy," *J. Appl. Phys.*, vol. 99, no. 8, p. 083509, 2006.

[231] C. Himwas, R. Songmuang, Le Si Dang, J. Bleuse, L. Rapenne, E. Sarigiannidou, and E. Monroy, "Thermal stability of the deep ultraviolet emission from AlGaN/AlN Stranski-Krastanov quantum dots," *Appl. Phys. Lett.*, vol. 101, no. 24, p. 241914, 2012.

[232] A. Andreev and E. O'Reilly, "Theory of the electronic structure of GaN/AlN hexagonal quantum dots," *Phys. Rev. B*, vol. 62, no. 23, pp. 15851–15870, Dec. 2000.

[233] V. Ranjan, G. Allan, C. Priester, and C. Delerue, "Self-consistent calculations of the optical properties of GaN quantum dots," *Phys. Rev. B*, vol. 68, no. 11, Sep. 2003.

[234] P. K. Kandaswamy, C. Bougerol, D. Jalabert, P. Ruterana, and E. Monroy, "Strain relaxation in short-period polar GaN/AlN superlattices," *J. Appl. Phys.*, vol. 106, no. 1, p. 013526, 2009.

[235] L. Lahourcade, P. K. Kandaswamy, J. Renard, P. Ruterana, H. Machhadani, M. Tchernycheva, F. H. Julien, B. Gayral, and E. Monroy, "Interband and intersubband optical characterization of semipolar (1122)-oriented GaN/AlN multiple-quantum-well structures," *Appl. Phys. Lett.*, vol. 93, no. 11, p. 111906, 2008.

[236] P. K. Kandaswamy, "Nanostructures Al(Ga)N/GaN pour l'optoélectronique intersousbande dans l'infrarouge proche et moyen," Université de Grenoble.

[237] M. R. Krames, O. B. Shchekin, R. Mueller-Mach, G. O. Mueller, L. Zhou, G. Harbers, and M. G. Craford, "Status and Future of High-Power Light-Emitting Diodes for Solid-State Lighting," *J. Disp. Technol.*, vol. 3, no. 2, pp. 160–175, Jun. 2007.

[238] M. R. Krames, M. Ochiai-Holcomb, G. E. Hofler, C. Carter-Coman, E. I. Chen, I.-H. Tan, P. Grillot, N. F. Gardner, H. C. Chui, J.-W. Huang, S. A. Stockman, F. A. Kish, M. G. Craford, T. S. Tan, C. P. Kocot, M. Hueschen, J. Posselt, B. Loh, G. Sasser, and D. Collins, "High-power truncated-inverted-pyramid (Al[sub x]Ga[sub 1−x])[sub 0.5]In[sub 0.5]P/GaP light-emitting diodes exhibiting >50% external quantum efficiency," *Appl. Phys. Lett.*, vol. 75, no. 16, p. 2365, 1999.

[239] K. Streubel, "Osram Opto Semiconductors," *private communication*, Regensburg, Germany, 2006.
[240] M. E. Levinshteĭn, S. L. Rumyantsev, and M. Shur, Eds., *Properties of advanced semiconductor materials: GaN, AlN, InN, BN, SiC, SiGe*. New York: Wiley, 2001.
[241] V. Ramesh, A. Kikuchi, K. Kishino, M. Funato, and Y. Kawakami, "Strain relaxation effect by nanotexturing InGaN/GaN multiple quantum well," *J. Appl. Phys.*, vol. 107, no. 11, p. 114303, 2010.
[242] H.-M. Kim, Y.-H. Cho, H. Lee, S. I. Kim, S. R. Ryu, D. Y. Kim, T. W. Kang, and K. S. Chung, "High-Brightness Light Emitting Diodes Using Dislocation-Free Indium Gallium Nitride/Gallium Nitride Multiquantum-Well Nanorod Arrays," *Nano Lett.*, vol. 4, no. 6, pp. 1059–1062, Jun. 2004.
[243] S. D. Hersee, M. Fairchild, A. K. Rishinaramangalam, M. S. Ferdous, L. Zhang, P. M. Varangis, B. S. Swartzentruber, and A. A. Talin, "GaN nanowire light emitting diodes based on templated and scalable nanowire growth process," *Electron. Lett.*, vol. 45, no. 1, p. 75, 2009.
[244] F. Furtmayr, J. Teubert, P. Becker, S. Conesa-Boj, J. R. Morante, A. Chernikov, S. Schäfer, S. Chatterjee, J. Arbiol, and M. Eickhoff, "Carrier confinement in GaN/Al_{x}Ga_{1−x}N nanowire heterostructures (0<x≤ 1)," *Phys. Rev. B*, vol. 84, no. 20, Nov. 2011.
[245] J. Renard, R. Songmuang, G. Tourbot, C. Bougerol, B. Daudin, and B. Gayral, "Evidence for quantum-confined Stark effect in GaN/AlN quantum dots in nanowires," *Phys. Rev. B*, vol. 80, no. 12, Sep. 2009.
[246] R. K. Debnath, R. Meijers, T. Richter, T. Stoica, R. Calarco, and H. Lüth, "Mechanism of molecular beam epitaxy growth of GaN nanowires on Si(111)," *Appl. Phys. Lett.*, vol. 90, no. 12, p. 123117, 2007.
[247] O. Ambacher, "Thermal stability and desorption of Group III nitrides prepared by metal organic chemical vapor deposition," *J. Vac. Sci. Technol. B Microelectron. Nanometer Struct.*, vol. 14, no. 6, p. 3532, Nov. 1996.
[248] R. F. Allah, T. Ben, R. Songmuang, and D. González, "Imaging and Analysis by Transmission Electron Microscopy of the Spontaneous Formation of Al-Rich Shell Structure in Al$_{x}$Ga$_{1-x}$N/GaN Nanowires," *Appl. Phys. Express*, vol. 5, no. 4, p. 045002, Mar. 2012.
[249] A. Pierret, C. Bougerol, S. Murcia-Mascaros, A. Cros, H. Renevier, B. Gayral, and B. Daudin, "Growth, structural and optical properties of AlGaN nanowires in the whole composition range," *Nanotechnology*, vol. 24, no. 11, p. 115704, Mar. 2013.
[250] D. Korakakis, K. F. Ludwig, and T. D. Moustakas, "Long range order in Al[sub x]Ga[sub 1−x]N films grown by molecular beam epitaxy," *Appl. Phys. Lett.*, vol. 71, no. 1, p. 72, 1997.
[251] I. Levin, L. H. Robins, M. D. Vaudin, J. A. Tuchman, E. Lakin, M. J. Sherman, and J. Ramer, "Spontaneous compositional modulation in the AlGaN layers of a thick AlGaN/GaN multilayer structure," *J. Appl. Phys.*, vol. 89, no. 1, p. 188, 2001.
[252] M. Gao, Y. Lin, S. T. Bradley, S. A. Ringel, J. Hwang, W. J. Schaff, and L. J. Brillson, "Spontaneous compositional superlattice and band-gap reduction in Si-doped Al[sub x]Ga[sub 1−x]N epilayers," *Appl. Phys. Lett.*, vol. 87, no. 19, p. 191906, 2005.
[253] D. Doppalapudi, S. N. Basu, K. F. Ludwig, and T. D. Moustakas, "Phase separation and ordering in InGaN alloys grown by molecular beam epitaxy," *J. Appl. Phys.*, vol. 84, no. 3, p. 1389, 1998.
[254] M. Benamara, L. Kirste, M. Albrecht, K. W. Benz, and H. P. Strunk, "Pyramidal-plane ordering in AlGaN alloys," *Appl. Phys. Lett.*, vol. 82, no. 4, p. 547, 2003.
[255] M. Albrecht, L. Lymperakis, J. Neugebauer, J. Northrup, L. Kirste, M. Leroux, I. Grzegory, S. Porowski, and H. Strunk, "Chemically ordered AlxGa1−xN alloys: Spontaneous formation of natural quantum wells," *Phys. Rev. B*, vol. 71, no. 3, Jan. 2005.
[256] N. Nepal, M. L. Nakarmi, J. Y. Lin, and H. X. Jiang, "Photoluminescence studies of

impurity transitions in AlGaN alloys," *Appl. Phys. Lett.*, vol. 89, no. 9, p. 092107, 2006.

[257] K. B. Nam, J. Li, M. L. Nakarmi, J. Y. Lin, and H. X. Jiang, "Unique optical properties of AlGaN alloys and related ultraviolet emitters," *Appl. Phys. Lett.*, vol. 84, no. 25, p. 5264, 2004.

[258] S. Dudiy and A. Zunger, "Optical consequences of long-range order in wurtzite AlxGa1-xN alloys," *Phys. Rev. B*, vol. 68, no. 4, Jul. 2003.

[259] C. Himwas, M. den Hertog, E. Bellet-Amalric, R. Songmuang, F. Donatini, L. Si Dang, and E. Monroy, "Enhanced room-temperature mid-ultraviolet emission from AlGaN/AlN Stranski-Krastanov quantum dots," *J. Appl. Phys.*, vol. 116, no. 2, p. 023502, Jul. 2014.

[260] M. S. Minsky, S. Watanabe, and N. Yamada, "Radiative and nonradiative lifetimes in GaInN/GaN multiquantum wells," *J. Appl. Phys.*, vol. 91, no. 8, p. 5176, 2002.

[261] R. Songmuang, D. Kalita, P. Sinha, M. den Hertog, R. André, T. Ben, D. González, H. Mariette, and E. Monroy, "Strong suppression of internal electric field in GaN/AlGaN multi-layer quantum dots in nanowires," *Appl. Phys. Lett.*, vol. 99, no. 14, p. 141914, 2011.

[262] E. Sarigiannidou, E. Monroy, B. Daudin, J. L. Rouvière, and A. D. Andreev, "Strain distribution in GaN/AlN quantum-dot superlattices," *Appl. Phys. Lett.*, vol. 87, no. 20, p. 203112, 2005.

[263] J.-H. Lee, J.-T. Oh, S.-B. Choi, Y.-C. Kim, H.-I. Cho, and J.-H. Lee, "Enhancement of InGaN-Based Vertical LED With Concavely Patterned Surface Using Patterned Sapphire Substrate," *IEEE Photonics Technol. Lett.*, vol. 20, no. 5, pp. 345–347, 2008.

[264] K. Kishino, H. Sekiguchi, and A. Kikuchi, "Improved Ti-mask selective-area growth (SAG) by rf-plasma-assisted molecular beam epitaxy demonstrating extremely uniform GaN nanocolumn arrays," *J. Cryst. Growth*, vol. 311, no. 7, pp. 2063–2068, Mar. 2009.

Publications and conference contributions

PUBLICATIONS IN INTERNATIONAL JOURNALS

[1] **Thermal stability of the deep ultraviolet emission from AlGaN/AlN Stranski-Krastanov quantum dots**
C. Himwas, R. Songmuang, Le Si Dang, J. Bleuse, L. Rapenne, E. Sarigiannidou, and E. Monroy
Appl. Phys. Lett. 101, 241914 (2012)

[2] **AlGaN/AlN quantum dots for UV light emitters**
C. Himwas, M. den Hertog, F. Donatini, Le Si Dang, L. Rapenne, E. Sarigiannidou, R. Songmuang, and E. Monroy
Phys. Stat. Sol. C 10, pp. 285–288 (2013)

[3] **Enhanced room-temperature mid-ultraviolet emission from AlGaN/AlN Stranski-Krastanov quantum dots**
C. Himwas, M. den Hertog, E. Bellet-Amalric, R. Songmuang, F. Donatini, Le Si Dang, and E. Monroy
J. Appl. Phys. 116, 023502 (2014)

[4] **Alloy inhomogeneity and carrier localization in AlGaN sections and AlGaN/AlN nanodisks in nanowires with 240-350 nm emission**
C Himwas, M Hertog, LS Dang, E Monroy, R Songmuang
Appl. Phys. Lett 105, 241908 (2014)

[5] **Effect of the quantum well thickness on the performance of InGaN photovoltaic cells**
L. Redaelli, A. Mukhtarova, S. Valdueza-Felip, A. Ajay, C. Bougerol, C. Himwas, J. Faure-Vincent, C. Durand, J. Eymery, and E. Monroy
Appl. Phys. Lett. 105, 131105 (2014)

[6] **Optical properties of as-grown and annealed InAs quantum dots on InGaAs cross-hatch patterns.**
C. Himwas, S. Panyakeow, and S. Kanjanachuchai.
Nanoscale Res. Lett. 6, 496 (2011)

CONTRIBUTIONS TO INTERNATIONAL CONFERENCES

[1] (Poster) **AlGaN/AlN quantum dots for UV light emitters**
C. Himwas, M. den Hertog, F. Donatini, Le Si Dang, L. Rapenne, E. Sarigiannidou, R. Songmuang, and E. Monroy
4th Int. Symposium on the Growth of III-Nitrides (ISGN4). St. Petersburg, Russia. July 2012

[2] (Oral) **UV emission from AlGaN/AlN nanostructures with high internal quantum efficiency**
C. Himwas, M. den Hertog, F. Donatini, Le Si Dang, L. Rapenne, E. Sarigiannidou, R. Songmuang, and E. Monroy
21st European Workshop on Heterostructure Technology (HETECH 2012), Barcelone, Spain. Nov. 2012

[3] (Oral) **Optical properties of AlGaN/AlN Stranski-Krastanov quantum dots**
C. Himwas, M. den Hertog, F. Donatini, Le Si Dang, R. Songmuang, and E. Monroy
E-MRS Spring Meeting 2013 Strasbourg, France. May 2013

[4] (Poster) **Deep ultraviolet emission from AlGaN/AlN nanodisks in nanowires**
C. Himwas, M. den Hertog, F. Donatini, Le Si Dang, E. Monroy, and R. Songmuang
10th International Conference on Nitride Semiconductors (ICNS10), Washington, US. Aug. 2013

[5] (Oral) **Optimization of AlGaN/AlN quantum dot superlattices for electron-pumped UV emitters**
C. Himwas, M. Den Hertog, F. Donatini, Le Si Dang, R. Songmuang, G. Schmidt, M. Müller, P. Veit, F. Bertram, J. Christen, and E. Monroy
10th International Conference on Nitride Semiconductors (ICNS10), Washington, US. Aug. 2013

[6] (Oral) **AlGaN/AlN Stranski-Krastanov quantum dots with improved luminescence internal quantum efficiency**
C. Himwas, M. den Hertog, F. Donatini, Le Si Dang, R. Songmuang, and E. Monroy
E-MRS Spring Meeting 2014, Lille, France. May 2014

[7] (Poster) **Electron-Pumped Mid-UV Emission using AlGaN/AlN Quantum Dot Superlattices**
C. Himwas, M. den Hertog, R. Songmuang, M. Choueib, K. Naji, H-Lin, S. T. Purcell, F. Donatini, Le Si Dang, and E. Monroy
International Workshop on Nitride Semiconductors (IWN-2014), Wroclaw, Poland. Aug. 2014

[8] (Oral) **Electron-Pumped Mid-UV Emitters using AlGaN/AlN Quantum Dots as active media**
C. Himwas, M. den Hertog, M. Choueib, K. Naji, H-Lin, S. Purcell, Le Si Dang, and E. Monroy
10th International Symposium on Semiconductor Light Emitting Devices (ISSLED 2014). Kaohsiung, Taiwan. Dec. 2014.

[9] (Oral) **Luminescence properties of as-grown and annealed InGaAs quantum dots on cross-hatch patterns**
C. Himwas, S. Panyakeow, and S. Kanjanachuchai
2011 IEEE 4th International NanoElectronics Conference (2011 INEC).Tao-Yuan, Taiwan. Jun. 2011.

This work reports on the design, epitaxial growth, and the structural, and optical characterization of two types of nanostructures, namely AlGaN/AlN Stranski-Krastanov quantum dots (SK-QD) and AlGaN/AlN nanodisks (NDs) on GaN nanowires (NWs). These nanostructures were grown using plasma-assisted molecular beam epitaxy (PA-MBE) and were conceived to be the active media of electron-pumped ultraviolet (EPUV) emitters for water purification, operating in mid-ultraviolet range.

The peak emission wavelength of three-dimensional SK-QD can be tuned in mid-ultraviolet range while keeping high internal quantum efficiency (IQE > 35%) by modifying the Al composition and the QD geometry. The efficient carrier confinement was confirmed by the stability of the photoluminescence intensity and decay time with temperature. The optimal deposited amount of AlGaN in AlGaN/AlN QDs which grants maximum luminescence at room temperature was determined by finding a compromise between the designs providing maximum IQE and maximum QD density. The effect of the variation of the QD height/base-diameter ratio on the interband and intraband optical properties was explored by fitting the experimental data with three-dimensional calculations of the band diagram and quantum levels.

Regarding AlGaN/AlN NDs on GaN NWs, the Al-Ga intermixing at Al(Ga)N/GaN interfaces and the alloy inhomogeneity in AlGaN/AlN NDs are attributed to the strain relaxation process. This interpretation was proved by correlation of experimental data with three-dimensional strain distribution calculations performed on structures that imitate the real growth sequence. Despite the challenge of inhomogeneity, the emission wavelength of AlGaN/AlN NDs can be tuned in mid-ultraviolet range while preserving high IQE by adjusting the ND thickness and Al content.

A prototype of EPUV emitter was fabricated using the AlGaN/AlN SK-QDs active region with proposed optimal design of active region thickness, AlN barrier thickness, and amount of AlGaN in each QD layer. For this first device, SiC was used as a substrate to prevent problems associated to charge or heat evacuation. A water purification test by such prototype EPUV emitter was carried out by irradiating E-coli bacteria, showing that all the specimens were successfully purified at the predicted ultraviolet dose.

Keywords: III-nitrides, quantum dots, nanowires, molecular beam epitaxy, ultraviolet

---

Ce travail porte sur la conception, l'épitaxie, et la caractérisation structural et optique de deux types de nanostructures, à savoir des boîtes quantiques AlGaN/AIN et des nanodisques AlGaN/AIN sur nanofils GaN. Ces nanostructures ont été synthetisées par épitaxie par jets moléculaires assistée par plasma (PA-MBE) et ont été conçues pour être le matériau actif d'une lampe ultraviolette à pompage électronique (EPUV) pour la purification de l'eau.

En modifiant la composition Al et la géométrie des boîtes quantiques AlGaN/AlN, leur longueur d'onde d'émission peut être réglée dans la gamme 320-235 nm tout en gardant une grande efficacité quantique interne (> 35%). Le confinement quantique a été confirmé par la stabilité de l'intensité et du temps de déclin de la photoluminescence avec la température. La quantité optimale d'AlGaN dans les boîtes pour obtenir une luminescence maximale à la température ambiante est un compromis entre densité de boîtes quantiques et rendement quantique interne. L'effet de la variation du rapport hauteur/diamètre de base sur les transitions interbande et intrabande dans les boîtes a été explorée par ajustement des données expérimentales à des calculs tridimensionnels du diagramme de bande et des niveaux quantiques.

En ce qui concerne les nanodisques d'AlGaN sur nanofils GaN, l'interdiffusion Al-Ga aux interfaces et l'hétérogénéité de l'alliage ternaire sont attribuées aux processus de relaxation des contraintes. Cette interprétation a été prouvée par la corrélation des données expérimentales avec des calculs de distribution déformation en trois dimensions effectuées sur des structures qui imitent la séquence de croissance réelle. Malgré le défi du manque d'homogénéité, la longueur d'onde d'émission des nanodisques AlGaN/AIN peut être réglée dans la gamme ultraviolette en préservant une haute efficacité quantique interne.

Un prototype de lampe EPUV a été fabriqué en utilisant une région active à base de boîtes quantiques AlGaN/AIN avec les valeurs optimals d'épaisseur de la région active, d'épaisseur de la barrière AlN, et de quantité d'AlGaN dans chaque couche de boîtes. Pour ce premier dispositif, le SiC a été utilisé comme substrat pour éviter les problèmes associés à l'évacuation de charge ou de chaleur. Un essai de purification de l'eau par une telle lampe a été réalisé. Tous les échantillons ont été purifiés avec succès à la dose prévue.

Mots-clés: Nitrures III-V, boîtes quantiques, nanofils, épitaxie par jets moléculaires, ultraviolet.